2018

Nanoparticle-Electromagnetic Radiation Interaction: Implications and Applications

Parth Nalin Vakil

FLORIDA STATE UNIVERSITY

COLLEGE OF ARTS AND SCIENCES

NANOPARTICLE – ELECTROMAGNETIC RADIATION INTERACTION: IMPLICATIONS AND APPLICATIONS

By

PARTH NALIN VAKIL

A Dissertation submitted to the
Department of Chemistry and Biochemistry
in partial fulfillment of the
requirements for the degree of
Doctor of Philosophy

2018

Parth Nalin Vakil defended this dissertation on July 13, 2018.
The members of the supervisory committee were:

Geoffrey F. Strouse
Professor Directing Dissertation

Subramanian Ramakrishnan
University Representative

Joseph B. Schlenoff
Committee Member

Lei Zhu
Committee Member

The Graduate School has verified and approved the above-named committee members, and certifies that the dissertation has been approved in accordance with university requirements.

ACKNOWLEDGMENTS

This thesis has been a culmination of several years of work that would not have been possible without all the amazing people who have supported me throughout this journey. I would like to firstly thank Dr. Strouse for the wonderful opportunity that allowed me to delve further into the ’nano-world’ and to learn about the intricacies and applications of nanostructures. His mentorship and support throughout the PhD helped me develop my skills as a competent scientist and independent thinker, and I will forever be thankful for all his guidance. I would like to also thank my PhD committee members for their invaluable insight and advice that they have provided for my research work throughout the years. I want to thank my loving, supporting family for allowing me to explore and find my passions in life, and for helping me achieve my dreams that include this doctorate degree. Despite being two intercontinental flights away, their encouragement and constant communication with me has kept them close. There are not enough words to express the gratitude and love I have for them. This research experience would also not have been possible without the fantastic lab members (former - Dr. Megan M., Dr. Ryan R., Dr. Megan F., Dr. Bridgett A., Dr. David C., and current - Kate, David H., Chris, Tony, Matt, Eddie and Rodney), department colleagues and staff (especially Dr. Su for all the TEM images), as well as all the collaborators I have worked with. I cannot thank them enough for making this PhD a great experience.I would like to thank Faheem Muhammed (Dr. Ramakrishnan’s Group) for his help with the nanocomposites project and for teaching me some concepts about additive manufacturing and dielectrics. Last but not the least, I would like to thank the most amazing, inspiring, and patient friends I have found in Tallahassee who have been with me through the tough times and the great times. They made this PhD life experience at FSU quite memorable.

TABLE OF CONTENTS

Appendix

LIST OF TABLES

LIST OF FIGURES

LIST OF SYMBOLS

Å	Angstrom
°C	degrees Celcius
K	Kelvin
T	Temperature
r	Radius
V	Volume
d	Diameter
ω_p	Plasma frequency
d_p	Penetration depth
T_B	Blocking temperature
Q_eff	Quenching efficiency
d_0	50% quenching distance
ϵ_λ	Extinction coefficient of the NP at the maximum emission wavelength of dye
N_A	Avogadro's number
V_{cm^3}	volume of the nanoparticle in cm^3
ϕ	Quantum yield of the donor dye
λ	Emission wavelength maximum for the donor
n_r	refractive index of the metal
ε_m	Solvent dielectric
ε_2	Complex dielectric function of the metal
ϵ'	Real component of the complex dielectric function
ϵ'_f	Real component of the complex dielectric function of the filler
ϵ'_m	Real component of the complex dielectric function of the matrix
ϵ''	Imaginary component of the complex dielectric function
T_B	Blocking Temperature
n^*	Complex refractive index
W	Watt
s	Seconds
σ	Standard deviation
q	Scattering vector
χ^2	Chi-squared

LIST OF ABBREVIATIONS

1-ODE	1-Octadecene
AP	Anton Paar
AR	Aspect ratio
AuNP	Gold nanoparticle
bp	Base pair
BSPP	Bis(p-sulfonatophenyl)phenylphosphine
com	Commercial
CO	Carbon monoxide
CTAB	Hexadecyltrimethylammonium bromide
dev	Deviation
DLS	Dynamic light scattering
DNA	Deoxyribonucleic acid
DSC	Differential scanning calorimetry
dsDNA	Double stranded deoxyribonucleic acid
DyLt680	Dylight680
EDS	Energy dispersive X-ray spectroscopy
EM	Electromagnetic
EMI	Electromagnetic interference shielding
EMR	Electromagnetic radiation
fcc	face centered cubic
FDM	Fused-deposit modeling
Fe_3O_4	Iron (II, III) oxide, magnetite
FRET	Forster resonance energy transfer
FTIR	Fourier transform infrared spectroscopy
GHz	Gigahertz
hcp	Hexagonal close packed
HRTEM	High resolution transmission electron microscopy
LSPR	Localized surface plasmon resonance
M	Molar
MALDI-TOF	Matrix -assisted laser desorption/ionization- Time of flight
MeOH	Methanol
min	Minute
MHz	Megahertz
ml	Milli-liter
mm	Millimeter
mmol	Millimol
MW	Microwave
M-W	Maxwell-Wagner
$Ni(acac)_2$	nickel (II) acetylacetonate
NiNP	Nickel nanoparticle

nm	nanometer
NPs	nanoparticles
NSET	Nanometal surface energy transfer
OAc	Oleic acid
OAm	Oleylamine
pXRD	Powder X-ray diffraction
rpm	Rounds per minute
SAXS	Small angle X-ray scattering
SEM	Scanning electron microscopy
SET	Surface energy transfer
ssDNA	single stranded deoxyribonucleic acid
SQUID	Super-conducting quantum interference device
std	Standard
syn	Synthetic
TCEP	Tris(2-carboxyethyl)phosphine
TEM	Transmission electron microscopy
T_g	Glass transition temperature
TGA	Thermogravimetric analysis
T_m	Melting temperature
TOA	Trioctylamine
UV-Vis	Ultraviolet-Visible
XRF	X-ray Fluorescence

ABSTRACT

Nanotechnology is a new frontier for the advancement of science and technology. Nanomaterials are playing a crucial role and that they will continue to do so is beyond doubt. They are being used in electronic, magnetic, optical and catalytic applications where the unique interactions of nanostructured materials with electromagnetic radiation is of great benefit. While significant progress in understanding fundamental nanoparticle–electromagnetic radiation interactions has been made, and has improved practical technology applications, there is plenty left to be fully understood. This dissertation aims to further probe nanoparticle–electromagnetic radiation interactions and unveil details previously not known. More specifically, this dissertation looks at how microwaves can aid in the synthesis of anisotropic magnetic nickel nanoparticles, how small sized nanoparticles can be used in tuning the dielectric properties of polymer-nanocomposites, and how core-shell nanoparticles can be used for high quenching of fluorescence red dyes. An overview of chapters section that provides a more detailed content summary for each chapter is found at the end of the introduction chapter.

CHAPTER 1

INTRODUCTION

1.1 Nanoscience and Nanotechnology

Materials with structural dimensions on the nanometer scale, or nanomaterials, exhibit unique and interesting properties. These properties can include optical, electronic, magnetic, physical and mechanical properties that are beneficial for various applications.[1, 2] A number of commercially available products today already apply the benefits nanomaterials provide. These products range from air-filters and antimicrobial clothing, to color televisions and medical diagnostic instruments to name a few. Traditionally, the most prominent feature, or benefit, of nanomaterials was the significantly larger surface area to volume ratio compared to bulk structures. While the surface area to volume ratio is beneficial in certain applications, sitting in a regime in between the atomic scale and bulk scale, nanoscale material properties (optical, magnetic, electronic, mechanical) can be tuned by simply changing the size or shape of the nanomaterial.[3, 4] Working at the nanoscale also allows formation of certain structures that do not occur naturally or at the bulk scale. The scientists, engineers and biomedical experts in the multidisciplinary field of nanoscience and nanotechnology are a group of people that are trying to synthesize various nanomaterials and understand their properties with the objective of translating the nanomaterials into new technologies. While nanomaterials may provide better performance, scaling their production from a laboratory bench-top synthesis to an economically viable industry-scale synthesis brings its own challenge and hinders the rapid application of many nanomaterials in everyday life. There is plenty of room left in the mastery of nanomaterials. This thesis contributes to that pursuit.

The majority of nanomaterials that exist today are synthesized, but nanotechnology has existed in a number of naturally occurring systems that have reaped the benefits of the nanoscale.[5, 6] The most iconic examples are the super-hydrophobic lotus leaves and the iridescent colorful wings of the blue morpho butterfly [7, 8]. In the first case, the presence of nanometer hair structures on the leaf surface prevent adhesion of water droplets which reduces water retention on the surface, while in the latter case, well arranged nanostructures that comprise the wing cause the incident light on the wing to undergo constructive and destructive interference before being reflected back. The lotus leaf effect has lead to production of nanotechnology-based water-proof surfaces and self-cleaning surfaces[9], and the photonic crystal structure of the butterfly wing has created new counterfeit technology.[10] These fascinating examples open up questions of how are such intricate nanostructures created and how do they interact with matter or light to fulfill a certain function. This thesis focuses on the synthesis of nanomaterials, the interaction of nanomaterials with electromagnetic radiation, and how such nanoparticle-electromagnetic radiation interaction can benefit the synthesis of nanomaterials and their application in certain technologies.While the research presented in this thesis does not involve naturally occurring nanostructures, it does focus on the synthesis of certain types of nanomaterials, the interaction of such nanomaterials with electromagnetic radiation, and how such nanoparticle-electromagnetic radiation interaction can be beneficial in both, the synthesis of and the application of nanomaterials.

1.2 Metallic and Magnetic Nanoparticles

Nanomaterials can be classified in a number of categories based on the constituent materials, properties, or application in a certain type of technology. The nanomaterials studied in this research can be classified as metallic and/or magnetic nanoparticles. In certain context within the nanoworld, the term nanoparticle, typically refers to spherical structures between 1 and 100 nm, but for this thesis, the term nanoparticle is used broadly for materials that have at least one dimension between 1 and 100 nm.[11] These nanoparticle structures can be isotropic spheres or anisotropic shapes such as rods (nanorods) and branched or star-like structures (multipods) to name a few.

From band theory, metals are classified as materials that have electrons that fill the valence band and (partially) the conduction band.[12, 13] The ‘sea of electrons’ allow metals to be good conductors of electricity and give rise to a number of properties exhibited by metals.[14] As structures get smaller in dimension, the continuum of states in the valence and conduction band of the material become more and more discreet as the atomic size is approached.[13] The metallic nanoparticles such as gold nanoparticles (AuNPs) or nickel nanoparticles (NiNPs) being discussed can be still viewed as structures that have a ’sea of electrons’ that can be described by the Drude model.[14, 15] Quantum confinement effects on the nanoscale allow metallic nanoparticles to present unique properties such as the localized surface plasmon resonance (LSPR) in AuNPs which arises when the confined sea of electrons responds to incident electromagnetic radiation as seen in figure 1.1 for a spherical 3.5 nm AuNP. The absorptive and scattering properties of spherical nanoparticles can be described by Mie theory.[15]

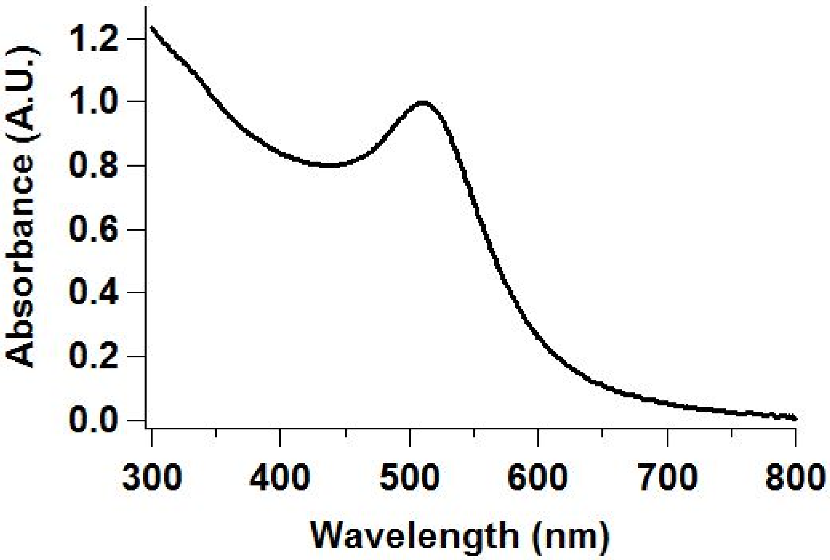

Figure 1.1: UV-Vis absorption spectrum of citrate-functionalized 3.5 nm AuNPs exhibiting a LSPR feature centered at 511 nm

Metallic nanoparticles of noble elements such as gold show greater resistance to oxidation which make them the most widely studied (and used) materials for a range of applications where the metal properties are beneficial.[16] However, AuNPs tend to have a higher price disadvantage. Nickel (an earth-abundant element) nanoparticles on the other hand are not as inert as AuNPs and are known to form a surface oxide layer that inhibits further oxidation of the material.[17–19] Other metallic nanoparticles such as iron nanoparticles are highly reactive and oxidize immediately to form iron oxide nanoparticles when exposed to air.[20] The resistance of metal nanoparticles to oxidization therefore is important to their properties and applications, especially when the majority of atoms of small nanoparticles are surface atoms.

Paramagnetic materials, materials with unpaired electron spins which produce a magnetic dipole, are typically associated with most of the magnetic nanoparticles that are being studied. Paramagnetic nanoparticles can be grouped into ferromagnets, ferrimagnets or antiferromagnets.

Materials that exhibit ferromagnetism include Ni, Fe and Co where the equal magnitude magnetic moments are parallel to each other and produces a net magnetic dipole. Magnetite iron oxide (Fe_3O_4) on the other hand is a ferrimagnetic material where the presence of unequal magnitude magnetic moments in an anti-parallel fashion to each other giving rise to a magnetic moment but weaker than that in a ferromagnet.[20–23]

The magnetism exhibited by materials also depends on the size of the structure because of the existence of magnetic domains or Weiss domains.[21–23] Magnetic domains are volumes of ferromagnetic material where magnetic spins are aligned in the same direction and have a certain size.[21] These domain sizes vary depending on the material, and when nanomaterials are of a size that falls under the size of a magnetic domain, they are known as single domain nanostructures. These structures exhibit coercivity, the ability of the material to resist changes in magnetization by an external field, but when the nanostructure size becomes even smaller, they show no coercivity and become superparamagnetic. An example of this behavior is shown in figure 1.2 for 11 nm Fe_3O_4 nanoparticles.[21, 23]

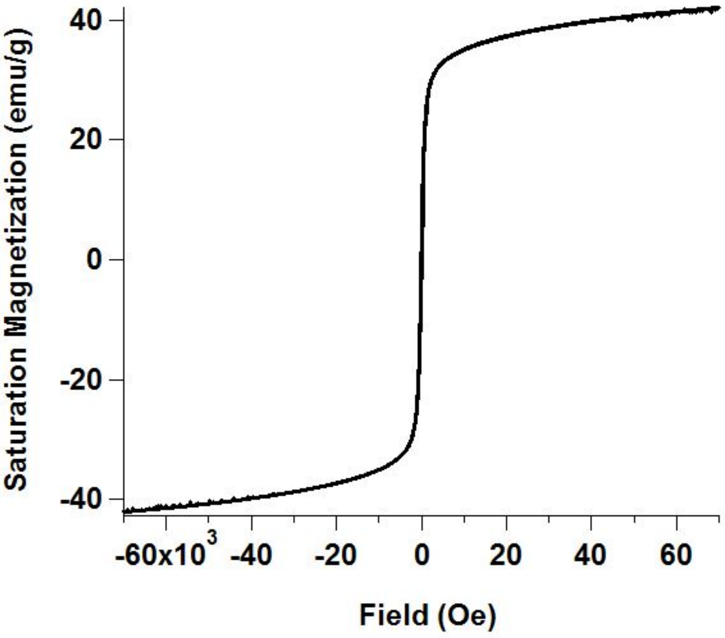

Figure 1.2: 300K Field-sweep magnetization curve of superparamagnetic 11 nm Fe_3O_4 nanoparticles

Superparamagnetic nanoparticles act as a single magnetic dipole but show higher susceptibility than a single paramagntic atom and have temperature dependent magnetic behavior defined by the blocking temperature (T_B).[23, 24] The blocking temperature is defined as transition temperature above which thermal energy overcomes the magnetic interaction between individual superparamagnetic nanoparticles.[20] Above the blocking temperature, the collection of superparamagnetic nanoparticles moments are oriented in random directions and show no net magnetic moment. The size dependent blocking temperature is given as [23]

$$T_B = \frac{K_{eff}V}{25k_b} \tag{1.1}$$

where K_{eff} is the effective magnetic anisotropy of the nanoparticle, V is the volume of the nanoparticle, k_b is the Boltzmann constant and T is the temperature in Kelvin.[23] The magnetic anisotropy of materials is a combination of magnetocrystalline, shape and stress anisotropy.[23, 24] Therefore the blocking temperature of a magnetic nanoparticle will be influenced by the type of crystalline structure and the morphology it is made up of.

1.3 Interaction of Electromagnetic Radiation with Matter

The properties of a material to understand its interactions with electromagnetic radiation can be linked to the permittivity and permeability of the material. The permittivity of a material is related to how the material interacts with electric fields while the permeability corresponds to the interaction with magnetic fields. These properties are complex functions with a real component (ϵ' or μ') and an imaginary component (ϵ'' or μ'') that are both frequency- and temperature-dependent functions that vary with the type of material.[24] For nanoscale materials, these functions are also size-dependent.[14, 15, 24] In relation to this research, these parameters affect the heating of materials in microwave reactors, and on how the nanoparticles can affect the properties of the nanocomposite they are embedded in, or in the ability of the nanoparticles to quench the fluorescence of dye molecules.

The complex permittivity, also referred to as the dielectric function, can be expressed as:

$$\epsilon^* = \epsilon' - i\epsilon'' \tag{1.2}$$

while the complex permeability can be expressed as:

$$\mu^* = \mu' - i\mu'' \tag{1.3}$$

The real part of the dielectric function, ϵ', is a positive value that describes the ability of the material to absorb or allow the electric field to penetrate the material while the ϵ'' component describes how easily this energy is lost (that can occur through conversion to thermal losses).[24] The dielectric response of a material is based upon the response of its electrons, charges and dipoles. The electric field, depending on the frequency will affect how the components of the material will react. For a typical dielectric material (not a pure metal), various responses can be observed as illustrated in figure 1.3 adapted from the review from Kohl.[25] The ratio of the loss component over the absorptive component is referred to as the loss tangent (tan $\delta_\epsilon = \epsilon'' \ / \ \epsilon'$). The more 'lossy' a material is, the higher the tan δ.(Note: The magnetic loss tangent is denoted by tan δ_μ and is the ratio equal to $\mu'' \ / \ \mu'$)

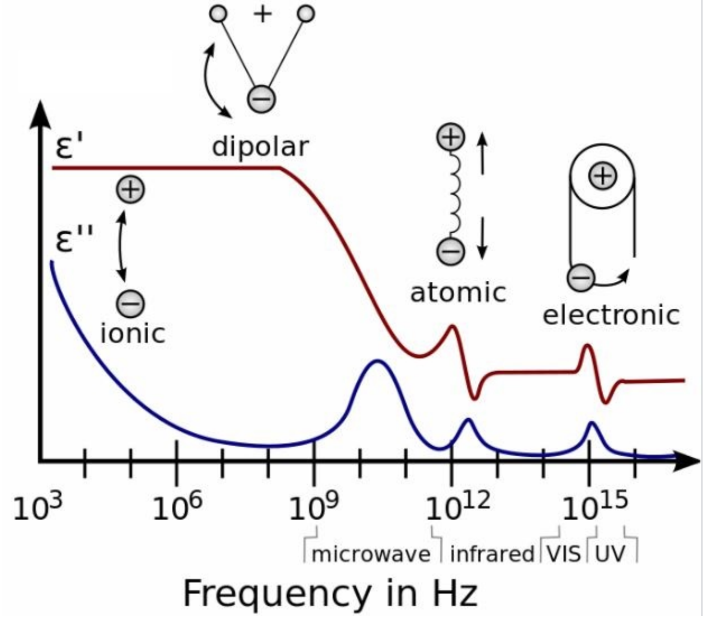

Figure 1.3: Frequency dependent permittivity of a dielectric material (Source: Low-Dielectric Constant Insulators for Future Integrated Circuits and Packages)

In the case of bulk metals, the ϵ' is a negative value for EM radiation of low frequencies (below the plasma frequency (ω_p)) which make them reflect EM radiation.[14, 26] However, once the frequency of the incident EM radiation is higher than the plasma frequency (which is in the deep UV-range), the ability of the metal to negate the EM radiation is decreased and the metal can be penetrated by the EM radiation.[14] The penetration depth (d_p) of materials (or skin depth for metals) is defined as the distance from the surface of the material at which the amplitude of the wave (or electric/magnetic field) drops to a value of 1/e of its original value within the material.[24] The penetration depth of a material depends on the frequency of the radiation as well as the permittivity and permeability properties of the material.[24, 27, 28] Metallic elements that also have magnetic characteristics such as nickel and iron are able to attenuate EM radiation even better because of their high permeability values, with loss mechanisms related to the magnetic nature of the material (hysteresis, Eddy current, domain wall resonance and ferromagnetic resonance).[29] This is why many EMI shielding materials developed (such as Mu-metal) incorporate magnetic elements as well. For 99% decay of the wave/field, a thickness equivalent to five penetration depths is typically required.[24] The skin depth of metals ranges from centimeters to nanometers depending on the frequency, which means that when metals are on the nanoscale, they will indeed be interacting with the impingent electromagnetic radiation.

For metallic nanoparticles, the dielectric function can be formulated starting with the modeling of the system as being comprised of a sea of free electrons using Drude formalism. Size dependence incorporation into the Drude model and addition of dielectric contributions using an analytical Etchegoin model allows an accurate modeling of the dielectric function.[15] This dielectric dispersion curve fits well with experimental data, and can accurately help predict the scattering and absorptive properties of nanoparticles. In the quasi-static limit, where the electric field is homogeneous across a nanoparticle (that is smaller in size than the wavelength of the EM radiation), Mie theory is able to predict the scattering and absorptive properties of nanoparticles. The scattering function scales as function of the sixth power of the radius while the absorption scales as a function of the third power of the radius (cubic), and the sum of the scattering and absorption cross-sections gives the total extinction cross section of the nanoparticle.[15] Nanoparticles under 20 nm in diameter can be considered to be purely absorptive, while those above 20 nm can scatter the incident radiation much stronger. The properties of the nanoparticle however are modified by changing the shape of the nanoparticle as exemplified by gold nanorods that exhibit two plasmon resonance modes describable through Gans Theory.[30]

As in the case of the size-dependent permittivity (dielectric function) for nanoparticles as a function of frequency, a size-dependent permeability function can be described by the Landau-Lifshitz-Gilbert expression.[24] However as the magnetic field strength is much weaker than the electric field strength, the influence of the permittivity is more significant in many cases.

1.4 Synthesis of Nanoparticles

The synthesis of nanomaterials can typically be grouped into two categories: a top-down approach and a bottom-up approach.[1, 4] As the names suggest, a top-down approach involves taking a large structure and breaking it down to form materials who dimensions are on the nanometer length, while bottom-up approaches make nanostructures atom by atom. Top-down methods include expensive, time-consuming lithography (photolithograpy, electron-beam lithography) methods or cheaper mechanical attrition (ball milling)methods which do not produce high quality homogeneous nanoparticle product.[31, 32] The nanomaterials synthesized for the research in this work has been through a solution-based bottom-up approach. The following subsections delve into concepts and methods relevant to bottom-up approaches.

1.4.1 Bottom-up Approaches

As previously mentioned, bottom-up methods to synthesize nanoparticles involve the growth of the nanoparticle starting from ions, atoms or molecular units that make up the final nanoparticle. A number of bottom-up methods are currently used in the production of nanoparticles, each with advantages and disadvantages. Bottom-up approaches include synthesis via a gas or vapor phase (physical vapor deposition or chemical vapor deposition) or liquid phase synthesis (chemical synthesis, sol-gel, spray pyrolysis or microemulsion method)[11, 32]. Narrowing down the scope further, chemical synthesis of nanoparticles is the method of choice for the remainder of this section where the nanoparticles can be synthesized in either organic or aqueous media. Liquid phase chemical synthesis routes provide precise control and tunability of nanoparticle growth as the rate of growth can be easily tuned by changing concentrations, precursors, temperature and time of the reaction[1, 3, 4, 33]. This method therefore enables easier understanding of the role of the different factors used.

Classical Nucleation and Growth Theories. The growth of metallic nanoparticles in the liquid chemical synthesis method usually involves a reduction chemistry approach where three main components are used: a metal ion precursor such as a metal salt, a reducing agent (sodium borohydride for example) that can reduce the metal ion to a metal atom, and capping ligands (citrate anions)that can bind to the surface of the growing nanoparticle and stabilize it.[33, 34]

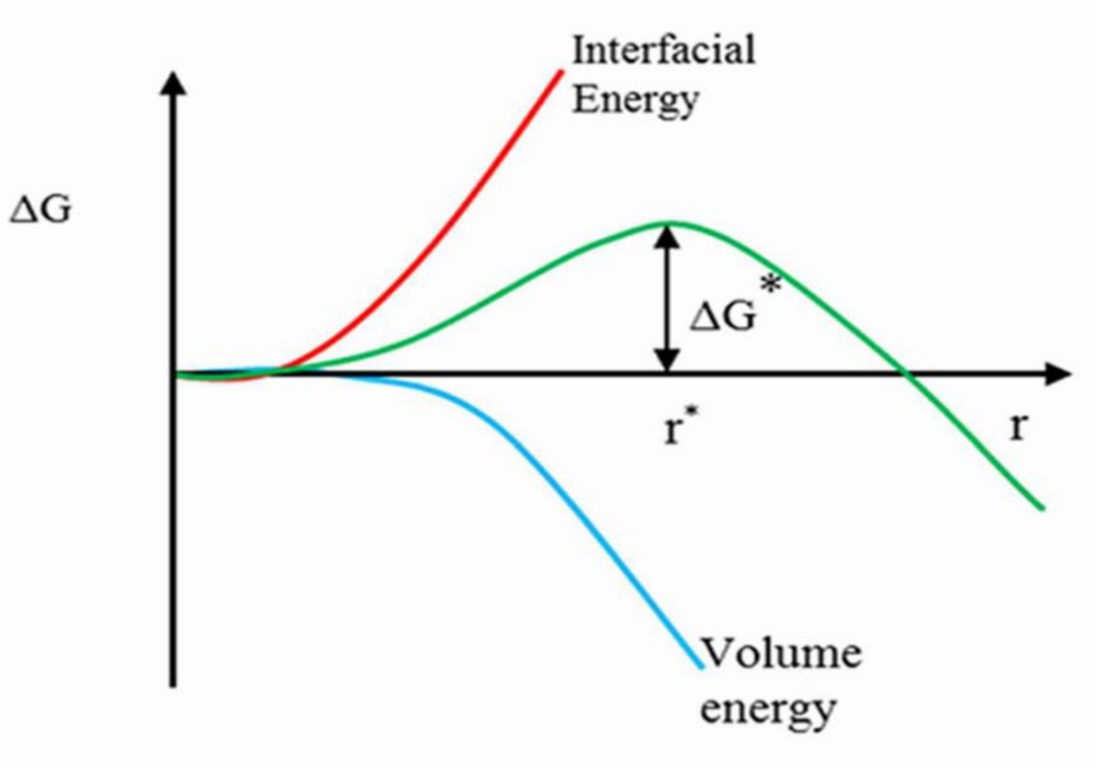

Figure 1.4: Illustration of classical nucleation theory (Reference 35)

In classical LaMer nucleation and growth theory, the first step involves the rapid formation of a high concentration of monomers (atoms) in solution. Collisions and coalescence of atoms follows and leads to the formation of stable nuclei. The nuclei have to reach a size with a critical radius (r^*) in order to prevent it from dissolving back in solution. The critical energy barrier (ΔG^*) to overcome depends on the bulk (volume) energy (red curve) and surface energy (blue curve) which scale as a function of particle size. This is illustrated in figure 1.4 where the green curve is the summation of the Gibbs free energy contributions from the interface (or surface term that scales with r^2) and volume (or bulk term that scales with r^3 shown as a blue curve) of the growing nucleus.[1, 4, 33, 35, 36]

The stable nuclei continue to grow as more atoms are added, and eventually stop growing when the available atoms in solution are depleted.[1, 4, 33, 35] Growth is favored as the free energy of the system continues to decrease with increase in volume of the nanoparticle. In other words, the growth is under thermodynamic control. Figure 1.5 helps visualize this process of nucleation and growth.[37]

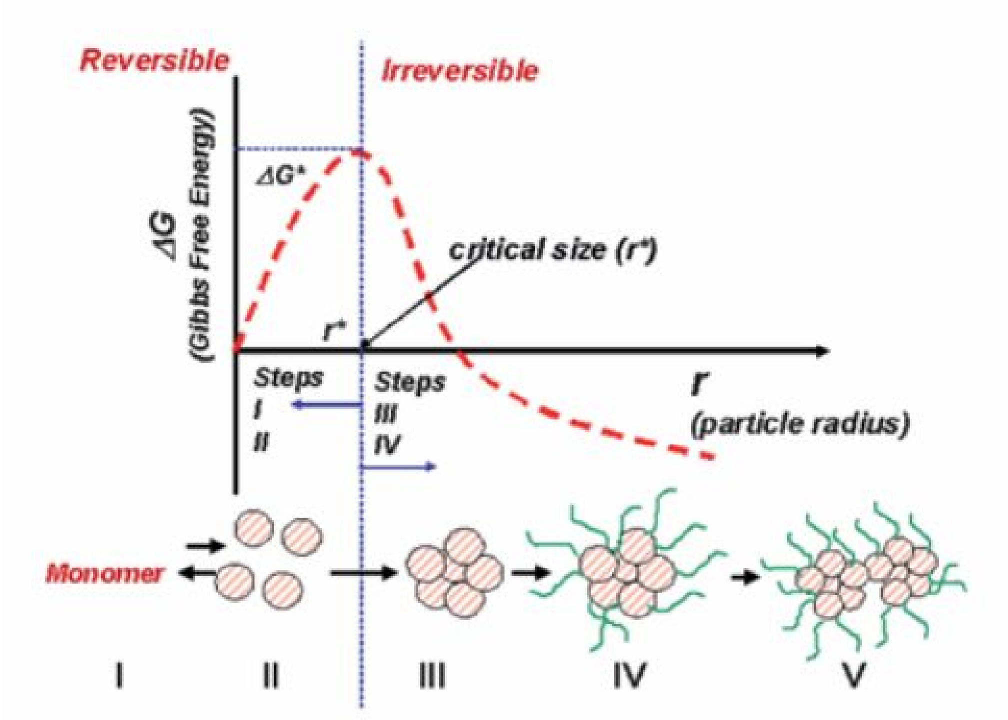

Figure 1.5: Stages of classical nucleation and growth (Reference 36)

As nuclei formed in solution compete to get larger, the final particle distribution sometimes may produce a population of nanoparticles with different sizes. Ostwald, in 1897, noted that if a colloidal solution of nanoparticles was left to sit longer in time, the size distribution narrowed.[35] This process of focusing the nanoparticle size is known as the Ostwald Ripening process where smaller and energetically unfavorable nanoparticle dissolve back and are redeposited onto the larger nanoparticle in solutions. Digestive Ripening, opposite to the Ostwald Ripening process, has also been shown to take place in certain instances.[35]

Auto-Catalytic Growth of Nanoparticles. As the understanding of nanoparticle growth has continued to grow, different growth behaviors have been observed in certain metallic systems including silver, platinum and nickel.[18, 35, 38–40] According to Finke and Watzky, the classic LaMer model is a linear process where growth follows nucleation, and the growth process of the formed nuclei becomes diffusion-limited. In the LaMer process, nucleation in solution does not occur after the initial stage of nucleation. As the LaMer mechanism was developed for sulfur sols, it may only apply to systems similar to sulfur sols and not a universal growth mechanism for all types of materials. Lastly, the LaMer model applies mainly to systems where a supersaturation of monomer in solution occurs which leads to an initial burst-nucleation process.[38]

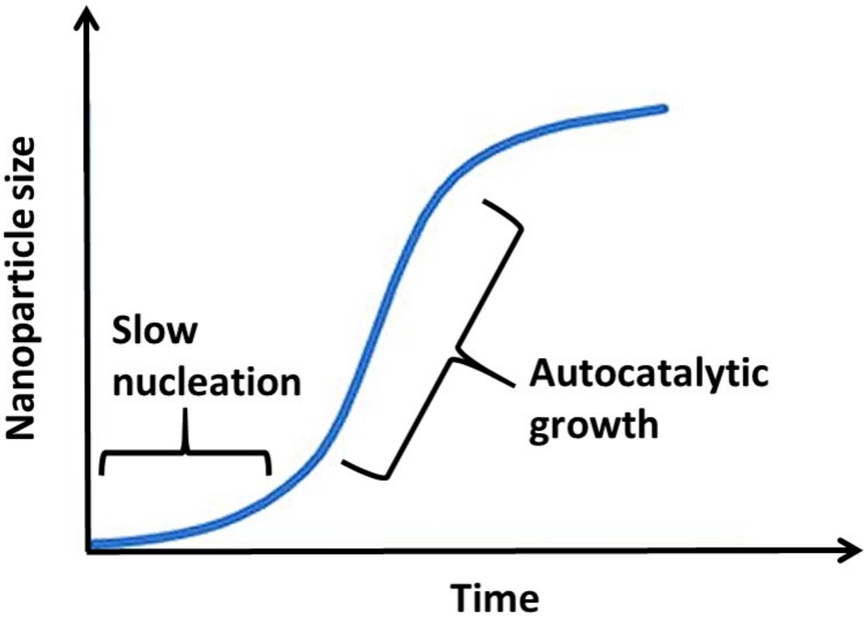

Figure 1.6: Graphical representation of sigmoidal growth behavior of nanoparticle under Finke-Watzky mechanism

A model developed by Finke and Watzky, the 2-step Finke-Watzky (F-W) model has been shown to fit many colloidal metallic systems recently. The F-W model is applicable to systems where monomer concentrations are not at supersaturation. In the F-W model, a slow process of nucleation takes place and a much faster autocatalytic surface-mediated growth occurs at the enlarging nuclei in solution. The sigmoidal growth behavior in the F-W model is also assumed to not be diffusion-limited as in the case of LaMer growth. The rate constants related to nucleation (k_1) and autocatalytic surface growth (k_2) describe the following equations [38, 41]:

$$A \xrightarrow{k_1} B \tag{1.4}$$

$$B \xrightarrow{k_2} B^* \tag{1.5}$$

where A represents the monomer (metal atom), B represents the critical metal nucleus, k_1 is nucleation step rate constant, B^* represents a larger continuously growing nucleus, and k_2 is the surface-enabled growth step rate constant. In the F-W model, $k_1 \lll k_2$. The rate of growth of the nanoparticle can be graphically represented by figure 1.6. The work by Dr. Ashley in our group has shown that the nucleation and growth of nickel nanoparticles in a microwave-assisted heating route fits the 2-step Finke-Watzky mechanism.[18]

1.4.2 Growing Anisotropic Nanoparticles

Anisotropic materials can be defined materials whose property are direction-dependent.[1] In other words, the properties of the nanoparticle vary along different axes of the structure or at different regions of the nanoparticle. Anisotropy is seen in magnetic materials where an 'easy axis' exists along which the magnetic moment prefers to align[20–22], or in gold nanorods where two (transverse and longitudinal) plasmon resonance modes arise from the different surface presented at the ends of the rods and along the length of the rod.[1] Anisotropy extends beyond magnetic and optical properties and can be easily tuned by controlling the shape of the nanoparticle. While interest (and challenge) exists in the production of zero-dimensional (0-D) isotropic nanomaterials, the growing knowledge that nanomaterial properties are only size-dependent but morphology- and surface-dependent has brought significant focus of the research community towards understanding anisotropic nanoparticle synthesis mechanisms, achieving synthetic-control over them, and evaluation of anisotropic nanomaterial performance in various applications. In crystalline structures such as metals and metal oxides, the final shape of the nanocrystal will control the presented surface crystalline facets.[42] Different crystalline facets have different surface energies as well as atomic spacing, both of which affect the ability of the surface to catalyze chemical reactions.[2, 33, 42] Additionally, complex nanostructure morphologies provide corners, steps, edges, tips, specific facets and dangling bonds that give rise to improved catalytic properties.[2, 42]

Formation of anisotropic nanomaterials of various morphologies has produced structures including nano-needles, nano-rice, nano-urchins, nano-belts, nano-popcorn, nano-cages and nano-dumbbells, which be grouped into categories of one-dimensional (1-D), two-dimensional (2-D) or three-dimensional (3-D) nanomaterials.[4] Anisotropic materials can also be mesoporous or hollow structures, or Janus-structures.[1, 43] Progress in the synthesis of anisotropic nanoparticles has revealed that precise growth control involves the interplay of a number of factors affecting solution-based synthesis including competition between thermodynamics and kinetics of growth.[44, 45] This section will focus on solution-based colloidal synthesis routes but acknowledges the existence of other methods to synthesize anisotropic structures including templated-growth (nanowires using porous membranes) and vapor-liquid-solid (VLS) growth (nanotubes as an example).[46, 47]

For nanocrystals, one of the main factors has been the crystalline nature of the material and the initial seed crystal structure.[2] Certain materials exhibit polymorphism, the ability to exist in more than one crystalline forms (fcc and hcp for some metals)that can determine the macroscopic shape of the nanomaterial.[48, 49] Crystalline nanostructures tend to evolve into thermodynamically stable morphologies as they continue to grow. These stable morphologies where surface energy was minimized was first shown by G. Wulff who proposed a theorem that could be applied to understanding the final shape of nanoparticles.[4, 33, 44, 45] Nanocrystals will tend to grow and achieve an equilibrium shape that reduces the total interfacial surface energy of the crystal; this is why certain crystal facets are predominantly displayed. In fcc systems, the surface energy is the order of $(111) < (100) < (110)$ for clean surfaces (no ligand bound).[44, 45] However, Wulff construction fails when it comes to several anisotropic structures because these structures are grown under kinetic control and not purely under thermodynamic control. During nucleation and growth, the formation of the initial nanocrystal nucleus is controlled by surface energetics as well as reaction kinetics that can be influenced by temperature, ligands and concentrations. This can produce both Wulff and non-Wulff shaped nuclei that can be either single crystalline or multiply twinned crystals. The initial crystallinity of the seeds will control subsequent growth of the nanoparticle. This has been advantageous for the seeded-growth approach where seeds of a particular shape are used to help create anisotropic structures of another material.[50] The seed shape stability is determined by the stability of maintaining the displayed facets which in turn depends on the material, surface-stabilization effect of ligands used, as well as the temperature of the system.[44]

The use of shape-directing ligands (or surfactants) and small molecules (or ions) has been another approach in obtaining anisotropic nanoparticles. Oleylamine, oleic acid, hexadecyltrimethylammonium bromide (CTAB), carbon monoxide (CO) and halides (Br^-, Cl^-) have been shown to affect the shape of the final nanomaterial.[42] They influence the evolution of the nanocrystal by exhibiting different binding affinity towards different facets of nanocrystals leading to faster addition of atoms (or surface-mediated reduction) on selective facets, and/or inhibiting growth on certain facets. As the understanding of how ligands affect shape-control continues to progress, some studies have shown that ligands not only play a role during the nanoparticle growth but modify the initial metal precursor complex before the reaction even begins.[51, 52] The reactivity of the metal precursor can have tremendous impact on the reaction pathway as it affects the nucleation rate as well as the ability of the precursor to get reduced in solution or auto-catalytically on the growing nanoparticle surface.[51] Lastly, ligands can play a role as an etching agent that will shape the nanoparticle as it grows due to selective facet reactivity.[33]

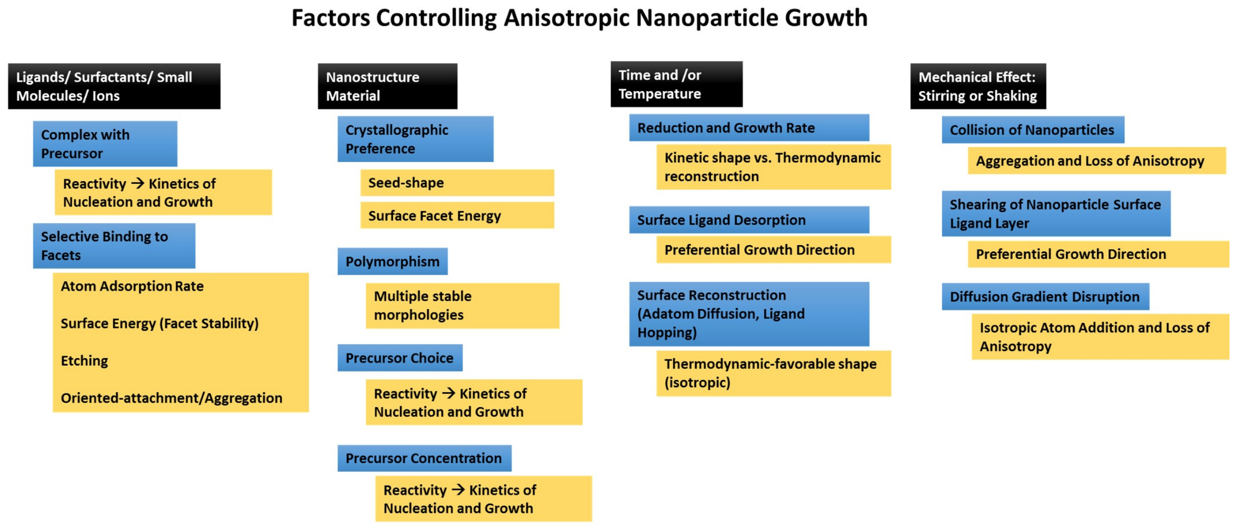

Figure 1.7: Factors influencing anisotropic nanoparticle growth

Anisotropic nanoparticles can also arise through oriented-attachment or oriented-aggregation growth mechanisms. This occurs when nanoparticles that form in solution attach to each other through specific facets and form elongated structures, typically worm-like structures or nanowires. This route to anisotropic nanoparticles is one of the newest routes to synthesizing anisotropic nanostructures. So far, oriented-attached mechanisms have been shown to depend on binding affinity of ligands and stearic hindrance on selective facets, permanent or temporary electric or magnetic dipoles interactions of nanoparticles, and crystallographic matching and surface energy reduction. Imaging the nanostructures formed using HRTEM shows that stacking faults and interfaces between smaller constituent nanoparticles can be observed that provide evidence for this mechanism of growth.[1, 4, 53]

Other kinetic and thermodynamic factors that play a role in the growth of anisotropic nanoparticles in addition to some of the previously listed parameters include concentrations (precursor, reducing agent and capping agents), reaction time and temperature, as well as mechanical effects like stirring or shaking the solution. The concentration of the chemicals in solution not only affect the type of nanocrystal seed formed as described earlier, but also affect the competition between rate of adatom addition to the growing nanocrystal and rate of surface reconstruction, the accessibility of atoms or precursor to the ligand passivated surfaces (faces, corners, tips) of the nanocrystal, and atomic diffusion gradients from the surface of the formed seeds.[54, 55] A handful of research papers have shown that the stirring of the colloidal reaction solution can be beneficial or disadvantageous to anisotropic growth. On one hand, stirring can help shear the liquid layer along certain facets to promote anisotropic gold nanorod growth[56], while on the other hand, stirring or shaking leads to reduction in aspect ratio of cobalt nanorods,loss of anisotropic arrow-head palladium nanoparticles or aggregation of polyaniline nanofibers.[57–59] Reaction time as a parameter is used to control the size of nanoparticles, and for anisotropic structures, it can allow control over the aspect ratio of nanorods or arms of multipod-like structures.[49] The temperature of the reaction is critical in many aspects as it affects the type of crystalline phase that can form, the kinetics of the reaction (solution reduction, surface-growth), the ability for surface diffusion of atoms (reconstruction) or ligands (ligand hopping), and the ability to displace ligands on the surface.[60] A summary flow chart of the various factors involved in controlling nanoparticle morphology and what effect they would have is presented in figure 1.7.

1.4.3 Microwaves and Microwave-Assisted Growth of Nanoparticles

Microwaves are electromagnetic radiation that correspond to a part of the electromagnetic spectrum that have a frequency range of 0.3 to 300 GHz, corresponding to a wavelength range of 1 mm to 1 m.[61] They are used in telecommunications, in radio astronomy, in radar technology, in heating up food, and in the synthesis and processing of nanomaterials as well.[29] The specific microwave frequency used in domestic microwave ovens is 2.45 GHz, and is typically the frequency of many laboratory based microwave reactors as well.[61] The energy possessed by a photon corresponding to 2.45 GHz frequency is 1.0 x 10^{-5} eV.[61] This small amount of energy is comparable to the rotational energies of molecules and therefore cannot directly participate in break chemical bonds (which have much higher energies).[62] However, microwave-assisted heating is very efficient in heating chemical reactions under most circumstances. This makes the technology an economical and environmentally friendly alternative to convective heating, and results in faster and reliable production of materials. Microwave-assisted heating systems can be scaled to larger production capacities and can also be incorporated in flow-reactor technologies.[63]

In order for the microwave energy to efficiently heat a material, the material must absorb the energy and convert it to thermal energy. This conversion to thermal energy can take place by the multiple mechanisms including motion of ions, rotation of molecules, Ohmic losses and Maxwell-Wagner polarization depending on the type of material in the microwave field.[63] Additionally, magnetic losses can be at play for magnetic materials interacting with EM radiation as mentioned in the previous subsection. The higher the loss tangent of the material, the greater its ability to absorb and convert the MW energy into heat. A system comprised of multiple reagents with different loss tangent values such as solvent, metal precursor and growing metallic nanoparticle will experience selective heating as the reaction proceeds due to the change in reaction temperature and the increasing dielectric properties of the larger nanoparticle being formed.[40] Selective heating allows the surface of the nanoparticle to absorb the microwave energy more effectively than other species in solution, and can enable faster autocatalytic growth or efficient shelling of cores using microwave-assisted heating.[64] Recent work from the Strouse lab has shown that the nanoparticle size can be tuned in a microwave by adjusting the power and frequency of the delivered microwave radiation to the reaction solution.[40]

1.4.4 ‘Lightning-Rod Effect’

The lightning-rod effect, not a commonly known phenomenon, describes the ability of structures with sharp tips or edges to generate a strong localized electric field (or magnetic field).[65–72] This can arise when a highly conducting material such as metal is subjected to a high frequency electromagnetic field that leads to an unequal distribution of charge within an anisotropic structure. The result of this is the generation of high surface charge densities at corners, tips and edges of the material which produces high electric fields and possible discharge from those local regions. The lightning-rod effect is a geometry-related phenomena that depends on shape of the conducting material, and benefits certain applications including (surface-enhanced Raman spectroscopy) SERS, generation of plasma, as well as in the sintering of metal. The lightning-rod effect explains the ability of anisotropic nanoparticles such as plasmonic gold nanostars to improves SERS signal and photothermal conversion for biomedical applications.[73] The more sharp the features are, or the greater the aspect ratio of arms of a multipod are, the higher the enhancement of the local charge density.[67] Through the lightning-rod effect, the sharp features of metal nanoparticles in an EM field (including microwave field) can get much hotter than the rest of the nanoparticle structure through enhanced thermal energy loss processes while responding to the changing field.[66] This temperature differential between tips and the rest of the nanoparticle surface be taken advantage of in the synthesis of anisotropic nanostructures using microwave-assisted heating as shown in this dissertation.

1.5 Manipulating Nanometal Properties Through Layering Dielectric Materials

1.5.1 Surface Energy Transfer using Plasmonic Nanoparticles

Efficient quenching of the fluorescence emission of excited dye molecules by small gold nanoparticles in the last two decades has allowed for the development of biophysical tools to enable the understanding complex structure of biological systems such as G-quadruplex folding, track cellular uptake and payload release processes, and detect biomarkers for disease more accurately.[74–82] The interaction (fluorescence quenching) of the dye molecule (treated as a dipole with a small ($<$ 20 nm diameter) gold nanoparticle (treated as a surface), is a nanoparticle-dye distant-dependent non-radiative energy transfer process that is inversely proportional to the fourth power of the distance as given by the equation:

$$Q_{eff} = \frac{1}{1 + \left(\frac{d}{d_0}\right)^4} \tag{1.6}$$

where Q_{eff} is the quenching efficiency given in percentage, d is the distance between the dye and nanoparticle surface, and d_0 is the 50% quenching distance at which fluorescence intensity of the dye is 50% quenched by the nanoparticle. Figure 1.8 shows how this function looks graphically. This was first experimentally demonstrated by the Strouse group and enables researchers to monitor structural changes in real-time.[83]

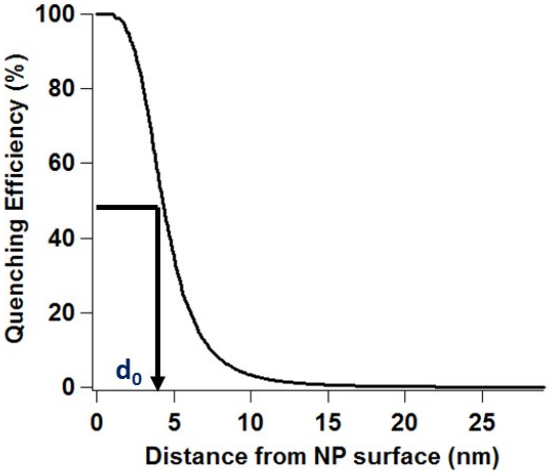

Figure 1.8: Theoretical quenching efficiency of ROX dye by a 3.5 nm AuNP as a function of distance (of dye) from nanoparticle surface. The d_0 distance indicates where the dye would be 50% quenched by the particle.

The theory behind the interaction is known as nanometal surface energy transfer (NSET) which is superior (and versatile) to other techniques such as Forster resonance energy transfer (FRET) because it allows larger distances to be probed, a single acceptor (nanoparticle) can be used to quench multiple dyes, and it does not require as stringent conditions as FRET (J overlap) to work efficiently. The NSET model was further developed and shown to predict the quenching behavior of different sizes of gold nanoparticles.[74] It takes into account the size-dependent absorptivity of the nanoparticle and can be written out as shown in equation 1.7:

$$d_0 = \frac{\alpha\lambda}{n_m}(A\phi)^{1/4}\left(\frac{n_r}{2n_m}\left(1+\frac{\varepsilon_m^2}{|\varepsilon_2|^2}\right)\right)^{1/4} \tag{1.7}$$

where d_0 is the distance from the nanoparticle surface at which the dye is 50% quenched, α is the orientation of the dye to the AuNP plasmon vector ($\alpha = (9/2)^4)/4\pi$), n_m is the solvent refractive index, A is the nanoparticle absorptivity defined in equation 1.8, ϕ is the quantum yield of the donor dye, λ is the emission wavelength maximum for the donor, n_r is the refractive index of the metal, ε_m is the solvent dielectric and ε_2 is the complex dielectric function of the metal. The reader is directed to reference [15] for the set of equations that describe the dielectric function of the metal (a sum of the Drude free electron contribution that is size-dependent, interband transition contribution and the bulk correction term).

The size-dependent absorptivity of the metal nanoparticle is given in equation 1.8:

$$A_{np} = 10^3 \ln(10)\left[\frac{\epsilon_\lambda\left(2r_{cm}\left(\frac{2r_{cm}}{\delta_{skin}}\right)\right)}{N_A V_{cm^3}}\right] \tag{1.8}$$

where ϵ_λ is the extinction coefficient of the NP at the maximum emission wavelength, r_{cm} is the radius of the nanoparticle in cm, δ_{skin} is the skin depth of the metal in cm, N_A is Avogadro's number and V_{cm^3} is the volume of the nanoparticle in cm^3.

1.5.2 Layered Dielectric Materials for Energy Transfer: Core-Shell Nanoparticles

As described in the previous sections, the dielectric properties are material-dependent as well as nanoparticle size-dependent. In order to tune the optical properties of a nanoparticle, or to incorporate other modalities into the same system (magnetic and plasmonic properties as an example), combining more than one material into the nanoparticle could be a beneficial approach. One could create an alloy[84], dope the plasmonic nanoparticle[85], or develop a core-shell nanoparticle that provides tunability of properties.[86] As gold is a material that shows plasmonic properties, is chemically stable, and is bio-compatible, a number of core-shell structures have been pursued where a shell of gold enables several benefits.[86] Some of these structures include hollow gold nanoshells[87–89], gold-shelled magnetic cores[86, 90], as well as gold-shelled silica nanoparticles.[91, 92] Core-shell structures can also be created by having a gold nanoparticle as the core material and a different material (silica, oxide, polyelectrolytes, etc.) which will result in changes in the LSPR peak position and intensity based on Mie theory.[92, 93] The use of a dielectric shell on a gold nanoparticle core has been used to tune the LSPR peak to a wavelength suitable for better spectral overlap, or as a spacer between the gold nanoparticle and fluorescing material (dye, quantum dot, fluorescent protein, lanthanide, etc.). Studies using core-shell nanoparticles with gold cores have shown distant-dependent behavior that matches NSET theory for small sizes of gold cores[92, 93], while larger size gold cores with greater scattering have observed fluorescent enhancement with short spacer distances.[91, 94] For the research work in this dissertation, the interest is in core-shell structures of small sizes (<20 nm) with a magnetic core material (nickel or iron oxide) and a gold shell that results in a magnetic plasmonic nanoparticle. These multimodal materials can be used in a number of applications such as bio-compatible MRI agents, in magnetic cell-sorting, photothermal therapy, and layered dielectric structures for fluorescence quenching.[95–98] Significant effort to synthesize such core-shell structures in a well-controlled manner and characterizing them has been taken. Some of the challenges faced include obtaining good size distributions and detailed analysis of the core-shell structure which at times consists of a very thin monolayer or two of gold.[98–100] Another body of research being done focuses on predicting the plasmonic properties of core-shell structures, and validating the predictions experimentally.[101–104]

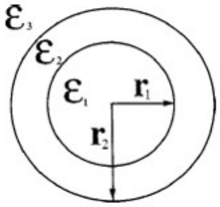

Figure 1.9: Schematic of a core-shell structure where ϵ_1 is the dielectric of the core, ϵ_2 is the dielectric of the shell, ϵ_3 is the dielectric of the media surrounding the particle, r_1 is the core radius and r_2 is the radius of the entire core-shell particle (Reference 87)

In the case of a core-shell nanoparticle, the absorptivity of the nanoparticle can be derived by taking into account the dielectric of the core, shell and surrounding medium that affects the polarizability of the particle in the presence of EM radiation, which in turn contributes to the absorption cross-section of the particle. Figure 1.9 shows the structure of what a core-shell structure looks like and the parameters used to calculate the absorption of the structure as done by the Halas group. [87]

The effect of a core-shell morphology changes the extinction spectrum of the nanoparticle, affecting both the magnitude of the extinction and position of resonance features such as the LSPR in a core-shell structure with a gold shell.[103] Figure 1.10 from the work of Wang et. al shows how changing the core dielectric properties can change the extinction of a 40 nm core with a 5 nm gold shell structure.[103] (Note: The complex refractive index ($n^* = n + ik$) is related back to the real part of permittivity by $\epsilon' = n^2 - k^2$ and to the imaginary part of the permittivity by $\epsilon'' = 2nk$)

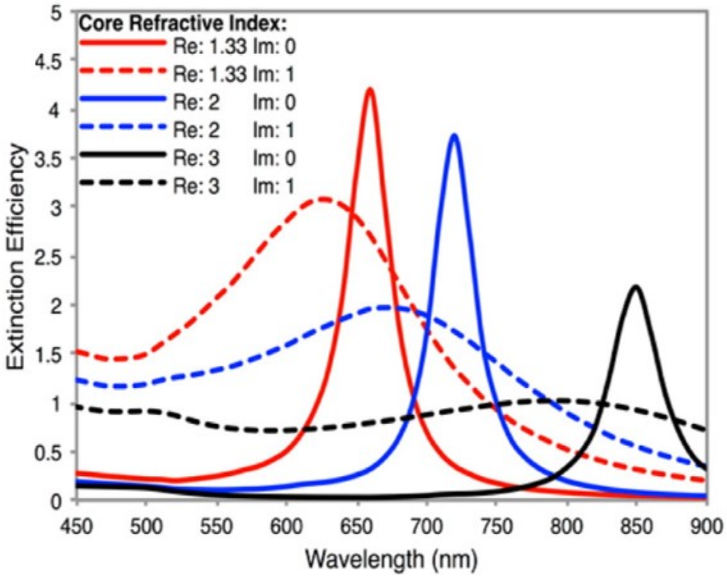

Figure 1.10: Effect of changing the dielectric properties of the 40 nm core in a core-shell structure where a 5 nm gold shell is present. (Reference 103)

By increasing the imaginary component of the dielectric for the core structure, a more 'lossy' core, the LSPR of the gold-shelled particle is dampened but increases the extinction in the red-wavelengths.[103] Furlani et al. more recently modeled the properties of gold shelled silica or iron oxide (magnetite) and provide the complex permittivity of the iron oxide.[105] Their results are consistent with that of Wang et al. and show that a more lossy core material like iron oxide does contribute to the absorption of the nanoparticle.[103] Distant-dependent quenching studies of small magnetic plasmonic core-shell structures has been very limited possibly because of challenges in making such structures, and/or because of the easy availability of well-studied gold nanoparticles. Experimental data in a 2014 article that used an iron oxide nanoparticle (no gold shell) and silica as a spacer suggests that the distance-dependent quenching behavior was linear. Permittivity data for nickel shows that it would be a good absorber of red wavelengths and could be a good candidate as a lossy core for core-shell plasmonic nanoparticles.

1.6 Overview of Dissertation Chapters

As the importance of anisotropic nanostructures and their unique surfaces continues to rise in applications including catalysis, magneto-optics and electromagnetic interference shielding, there is a need for efficient and economical synthesis routes for such nanostructures. Chapter 2 describes the application of pulsed microwave-based heating for the rapid synthesis of highly branched pure phase fcc crystalline nickel mulitpods nanostructures with >99% multipod population. By controlling the power delivery to the reaction mixture through cycling, superior control is achieved over the growth kinetics of the metallic nanostructures allowing formation of multipods consisting of arms with different aspect ratios. The multipod structures are formed under ambient conditions in a simple reaction system comprised of nickel acetylacetonate (Ni(acac)$_2$), oleylamine (OAm) and oleic acid (OAc) in a matter of minutes by selective heating at the (111) overgrowth corners on Ni nanoseeds. The selective heating at the corners leads to accelerated autocatalytic growth along the <111> direction through a lightning rod effect. The length is directly proportional to the number of cycles, while the core size is controlled by continuous power delivery. The roles of heating mode (cycling versus variable power versus convective heating) during synthesis of the materials is explored allowing a mechanism into how cycled microwave energy may allow fast multipod evolution to be proposed.

In Chapter 3, other parameters influencing the growth of nickel multipods structures in a cycled microwave power reaction are explored. This set of experiments tries to elucidate whether role of precursor concentration, precursor type, ligands used and their ratios, as well as the microwave reactor type and solution stirring rate may affect the shaped growth of the multipods in addition to the cycled microwave-power delivery. $Ni(acac)_2$ and Ni-acetate precursors show the formation of multipods but the use of $NiCl_2$ leads to the formation of a mixture of faceted particles and no multipods under similar reaction conditions suggesting a difference in precursor reactivity or effect of chloride ions. Switching the primary amine reducing agent, oleylamine, to a tertiary amine (trioctylamine) leads to a loss of anisotropic growth while removal of the other ligand component, oleic acid, also leads to isotropic growth. Ligand ratio studies using oleylamine and oleic acid show that too high of a oleylamine to oleic acid ratio ($> 5:1$) or too low of a ratio ($< 3:1$) does not produce multipod morphologies. UV-Vis spectroscopy of the starting solution for the different ligand ratio solutions suggests that the ligands not only affect the reaction during growth but may modify the initial Ni precursor complex formed. This different Ni precursor may have different reactivity and modify the kinetics of the reaction that affects multipod formation. The use of a SiC microwave vessel was shown to influence the heating profile and affect the uniformity of multipod growth. Lastly, the effect of stirring the reaction was also shown to affect the evolution of the multipods, and it maybe an underlooked factor in the growth of anisotropic nanoparticle growth.

Nanomaterial loaded thermoplastics are attractive for applications in adaptive printing methods, as the physical properties of the printed materials are dependent on the nanomaterial type and degree of dispersion. Chapter 4 compares the dispersion and the impact on the dielectric properties of two common nanoparticles, nickel and iron oxide, loaded into polystyrene as a potential printable low k dielectric polymer. Comparisons were made between commercial and synthetically prepared samples. The change in the real and imaginary dielectric was systematically studied as a function of particle type, concentration (0 to 13 volume percent), and surface coating for commercially and synthetically sourced materials to evaluate the influence of nanoparticle dispersion on polymer performance. By varying the volume percentage of filler in the matrix, it is shown that one can increase the magnetic properties of the materials while minimizing unwanted contributions to the dielectric constant and dielectric loss. The well dispersed nanoparticle systems were successfully modeled through the Looyenga dielectric theory thus giving one a predictive ability for the dielectric properties. The current experimental work coupled with modeling could facilitate future material choices, and guide design rules for printable polymer composite systems.

Chapter 5 investigates the synthesis of nickel-gold core-shell nanoparticles and their quenching efficiency of red dyes in comparison to a pure gold nanoparticles. The chapter details the synthesis of the core-shell structure and characterization of the nanoparticles using absorption spectroscopy, magnetic measurements (SQUID), powder X-ray diffraction, transmission electron microscopy (TEM) as well energy dispersive and X-ray fluorescence spectroscopy. The nickel nanoparticles synthesized in an organic solution are etched significantly during the galvanic exchange at the surface with the gold precursor assisted by a reducing agent, and exhibit magnetic and plasmonic properties corresponding to a core-shell particle with a very thin gold shell. The phase-transferred 3.3 nm diameter nanoparticles were coupled to fluorescent dyes, DyLt680 and ROX using different length dye-labeled double-stranded DNA sequences for the quenching studies. The quenching studies were carried out by monitoring fluorescence emission intensity of the coupled dye-nanoparticle system and uncoupled dye-nanoparticle system where sodium cyanide was used to etch away the nanoparticle or DTT was used to outcompete the surface-bound dye-labeled DNA. Similar studies using 3.5 nm gold nanoparticles show that the quenching of the nickel-gold core-shell structures is higher than that of gold nanoparticles, as expected from the higher absorptive nature of nickel compared to gold in the frequency range of dye emission. The quenching efficiency follows the distant-dependent behavior predicted by surface-energy transfer between a dye and an nanoparticle, but shows a higher d_0 value than that from the previously modified size-dependent NSET equation for a core-shell structure. This difference maybe attributed to the model under-predicting the absorptivity of the core.

Chapter 6 provides a brief conclusion of the significant results from this dissertation work and suggests the next directions for the projects described in the earlier chapters.

CHAPTER 2

KINETIC CONTROL OF NICKEL MULTIPODS USING CYCLED MICROWAVE POWER

Reprinted from ”Synthesis of Highly Uniform Nickel Multipods with Tunable Aspect Ratio by Microwave Power Control.” Vakil PN, Hardy DA, Strouse GF. 2018. *ACS Nano. Article ASAP*. DOI: 10.1021/acsnano.8b01992 Copyright 2018 American Chemical Society

2.1 Introduction

The growth of metal nanoparticles is known to follow an autocatalytic 2-step Finke-Watsky mechanism, where the first step involves a slow reduction step (k_1) of the cationic precursor in solution by a weak reducing agent, such as oleylamine, followed by a second fast reduction step (k_2) of the cation precursor at the surface of the growing nanoparticle.[18, 39, 52] In the autocatalytic mechanism k2 >>> k1 leading to growth being dominated by the nanoparticle surface. The nuclei morphology, the facet stability for a given metal, the reaction conditions, and face selective binding of ligands can lead to hyper-branching. While spherical particles are no doubt important materials, controlling the reaction to allow isolation of high surface area branched metal nanoparticles is attractive for catalysis and plasmonic applications.[106–115]

Recent studies have revealed for fcc metals branching is achieved by initial overgrowth on the high energy vertex and edge sites corresponding to the (111) facets. Xia, *et* al. revealed morphology control can be achieved by preferential growth along the (111) facet initiated by (111) overgrowth occurring on nucleated cubic (fcc) nanometal seeds.[107] Researchers have carried the overgrowth ideas to other metals and shown that materials with rapid metal reorganization leads to primarily isotropic structures (Au, Ag, Cu), while structures with slow reorganization can readily grow as anisotropic structures (Ni, Pd, Pt).[116, 117] The breakthrough in understanding the mechanism is resulting in new routes to achieve the desired morphology. For catalytic applications, multipod Ni-, Pt-, and Pd nanoparticles have been reported, although the systematic control of arm length and aspect ratio is poor and long reaction times limit the scalability of the reactions.[49, 54, 58, 118–120]

To truly realize the benefits of hyper-branched nanostructured materials, it is critical to develop simple, economical, scalable, reliable and efficient routes for their synthesis.

Transitioning the mechanistic understanding of growth to sustainable synthetic methods for solution processed materials, whether by flow chemistry, batch reactors, or more recently microwave assisted methods is fundamentally important as such materials are being used for catalytic and plasmonic applications.[121, 122] In the past decade, the use of microwave (MW) chemistry for nanomaterials synthesis has attracted attention due to the enhancement of reaction rates and reproducibility of the materials when carried out in a single mode MW reactor. The observed enhancement is not due to the energy absorbed per MW photon, as it does not contain enough energy to break a bond, but rather to enhanced growth rates reflecting the evolving dielectric loss tangent for the growing nanoparticle. The size dependent loss tangent reflects the repolarization of the electric field, as described within the Maxwell-Wagner (M-W) model.[40] Such polarization effects are anticipated to be enhanced at sharp tips and edges, leading to enhanced heating at these sites in a growing metal. This is referred to as a lightning rod effect, since the sharp tips and edges generate very high electric fields in their vicinity due to the surface charge density in those regions.[65–72] The size and shape dependent M-W loss tangents for a metal nanoparticle suggest selective heating of the tip under pulsed power may provide control through selective tip growth acceleration. MW pulsing as a tool in MW chemistry has been suggested by organic chemists to enhance yield of reactions, and in materials synthesis to manipulate heating rates. While the fundamental physics are well understood and the lightning rod effect has been shown to enhance electromagnetic shielding, the use in MW synthesis has not been explored.[68, 71, 123–125]

In this work, a simple and rapid microwave-assisted chemical reaction that takes minutes to produce highly crystalline metallic *fcc* nickel multipod structures is shown. Nickel is chosen as the example material as it is a highly valuable industrial catalyst in fuel cells, waste reduction, and bioprocessing technologies.[126–131] Ni multipods with arms that are 230 nm in length and 51 nm in width (aspect ratio of 4.5) can be routinely prepared by sequential pulsing (9 pulses) in a 2.45 GHz MW single mode cavity (300 W) within 10 mins. The application of single mode pulsed MW heating is demonstrated to enhance growth of the (111) facet to form multipod Ni nanoparticles with large aspect ratios. The arm length of the Ni multipod is easily controlled by the number of pulses applied during growth. This method does not need inert conditions to produce particles.

The aspect ratio is systematically reduced with fewer pulses. The resulting multipod structures are highly crystalline metallic single phase fcc nickel. The high aspect ratio samples are not achieved by continuous MW operation.

It is hypothesized that the ability to generate multipod structures selectively reflects local tip heating leading to acceleration of the (111) facet growth on the initial Ni seed crystal. As the arm grows the selective heating coupled to increased MW cross-section for the anisotropic structure results in the observed >99% selective multipod formation. Mechanistically, the accelerated growth is describable under the Finke-Watzky autocatalytic mechanism as a temperature enhanced growth rate on the (111) facet which occurs faster than atom reorganization on the seed faces. The lack of multipod formation under continuous power is ascribed to the fact that the system reaches equilibrium and the growth of the (111) facet is in competition with nanocrystal reconstruction to minimize surface energy.

The study furthers the demonstration of microwave-driven chemistry as a powerful technology providing precise control over nanomaterial growth and morphology, with lower energy consumption. [132–134] Although multipod structures can be achieved in classical convective reactions by addition of ligands that selective bind to a facet, the use of the cycled MW produces >99% multipod morphology.

2.2 Materials and Methods

2.2.1 Materials

99%, nickel acetylacetonate hydrate ($Ni(acac)_2.xH_2O$), oleic acid (OAc), oleylamine (OAm) technical grade 70%, tri-n-octylamine (TOA), toluene, methanol (MeOH), acetone and chloroform were purchased from Sigma Aldrich. The materials were used without further purification.

2.2.2 Synthesis of Nanoparticles

Microwave Synthesis of Nickel Multipods. Ni multipods were prepared by MW heating a solution containing 0.75 mmol of nickel acetylacetonate, 25 mmol of oleylamine (or tri-n-octylamine) and 5 mmol of oleic acid. The reaction was performed in a 2.45 GHz single mode Anton-Parr Monowave 300 microwave using a G30 (30 ml) Anton-Paar microwave vessel that was sealed with a silicone septa and crimp cap. The blue reaction solution was degassed under vacuum with stirring at a temperature of approx. 100 °C for 30 min using a water bath until no more bubbling was observed prior to MW heating (Note: This step is not required but carried out as standard protocol). The nanoparticles were grown by heating the reaction to 280 °C using 300 W of microwave power followed by one of three operational modes: (1) constant temperature mode (280 °C) (instrument maintains temperature by adjusting the microwave power automatically) for a fixed duration of time, (2) a custom profile where the microwave power is stepped to a lower constant power value that can maintain the temperature at an almost constant value, or (3) a custom profile where the instrument is programmed to deliver microwave power in an on/off cyclic manner. During the cycling mode, the microwave power is completely off while the reaction cools from 280 °C to 240 °C (10 seconds using automatic forced air) between the on cycles where the microwave delivers a fixed amount of power to raise the temperature back to 280 °C as illustrated by the power-temperature reaction profiles in the figures within the paper for the various reactions. The time to raise the temperature from 240 °C to 280 °C depends on the selected power (300 W 13 s, 150 W 26 s). For cycled 300W power reactions with different frequencies (2 cycles of 5 sec or 3 cycles of 3 sec), the power between cycles is reduced to 1 W instead of air cooling as the microwave system cannot respond on such short time scales without lowering the reaction temperature significantly. Following the last on cycle, the solution is cooled to 55 °C and the nanoparticles isolated by magnetic separation, followed by three repeat toluene dissolutions, methanol precipitation, magnetic isolation, and finally drying the particles under vacuum.

In the case of smaller particles that do not separate out magnetically, the nickel nanoparticles were precipitated by addition of 5mL toluene followed by 15 ml of methanol. The resulting solution was centrifuged for 5 min using a centrifuge tube. After removing the supernatant, the pellet was re-dispersed in toluene. To precipitate the NiNPs, excess methanol was added followed by isolation through centrifugation before drying under vacuum.

Synthesis of Nickel Nanoparticles by Convective Heating. Convectively prepared Ni nanoparticles were prepared using the same reaction solution in a microwave glass vessel (Anton Paar G30) heated to 280 °C from room temperature (4 °C/min) and held at 280 °C for 1 h using a heating mantle after prior degassing under vacuum at 100 °C for 30 min (the reaction was opened to air. A second reaction was also carried out where the reaction vessel was placed in a preheated aluminum block at 280°C to increase heating rate to match closely to that of the initial ramp in the microwave. The reactions were cooled down quickly to room temperature using a blower and the nanoparticles were cleaned up as described previously.

2.2.3 Transmission Electron Microscopy (TEM)

Nanoparticle samples were drop-cast, from toluene dispersion, onto 300 mesh carbon coated copper grids and left to dry under vacuum overnight. The TEM images were recorded using a JEM-ARM200cF electron microscope at 200 kV acceleration voltage.

2.2.4 Scanning Electron Microscopy (SEM)

SEM imaging was performed on aluminum mounts with nanoparticles drop-casted directly and allowed to dry. SEM imaging was performed on a FEI Nova NanoSEM 400 operating at 20 kV with a spot size of 4.0. The images were collected with an Everhart-Thornley detector (ETD).

2.2.5 Powder X-Ray Diffraction (pXRD)

The pXRD patterns for Ni nanoparticles were acquired on a Rigaku Ultima III diffractometer equipped with a Cu-K source. Data was collected at room temperature, in the 2 range of 10-84°.

2.2.6 Magnetic Measurements

Magnetic properties were studied with a superconducting quantum interference device (SQUID) magnetometer, MPMS-XL (Quantum Design). Field-dependent magnetization for nanostructures embedded in paraffin wax was measured at 300 K, with the applied field varying from 0 T to 1.5 T and back.

2.2.7 Thermogravimetric Analysis (TGA)

TGA was performed on a TA Instruments Q50 thermogravimetric analyzer. The samples were heated at a rate of 10 °C/min from room temperature to 100 °C in an alumina pan and held for 5 minutes before continuing to ramp at 10 °C/min to the final temperature (200-600 °C). The samples were held at the final temperature for 30 min. Measurements were performed under nitrogen environment.

2.3 Results and Discussion

Although Ni nanoparticle growth is well understood, controlling morphology is not as predictable with typical reactions yielding a distribution of morphologies.[49, 119, 135] In all reactions, enhancing growth at the tips (overgrowths) is key to achieves the desired selective control of (111) growth allowing larger reaction batches to be prepared in isolating anisotropic morphologies. Enhancing tip growth requires control of surface energy, which can be achieved by ligand binding or potentially selective heating. MW heating can give rise to selective heating due to the fact that MW absorption by a nanoparticle is size and shape dependent.[18, 40, 136] The interaction of the MW field will be largest at sharp edges reflecting the properties of the dielectric absorption process.[68, 71, 123–125] In systems exhibiting overgrowth, this may lead to selective heating of the tips and potentially increased reduction rates at the overgrowth sites owing to the lightning rod effect[65–72] leading to enhanced anisotropic growth at the super-heated tips as hypothesized in Figure 1. Of course, under continuous MW absorption, as the nanoparticle reaches thermal equilibrium this effect will be diminished leading to the reported spherical shapes.

The degree of experimental control achieved by pulsing vs continuous MW power is illustrated in selected electron microscopy images showing initial nucleation and growth results in cubic structures (Figure 2.1 a-c) that evolve towards (111) overgrowth (figure 2.1d) maintained under continuous power (Figure 2.1e) but leading to high aspect ratio multipod morphologies under pulsed conditions (Figure 2.1f). As detailed in the results section below, the evolution from cubic to overgrowth to high aspect ratio multipods was analyzedas a function of time (number of pulses) to produce a mechanism for growth that distinguishes autocatalytic growth observed in MW reactors for Ni under continuous heating from the onset of MW enhanced (111) facet growth under pulsed MW conditions. To evaluate the effect of MW pulsing on anisotropic growth, the nanoparticles were grown by one of two operational modes: (1) constant temperature mode (280 °C) (instrument maintains temperature with adjusting the power automatically), and (2) power and frequency dependent cycling of MW power. Comparison to heating in a convective reaction using a round bottom was carried out to evaluate the proposed growth model.

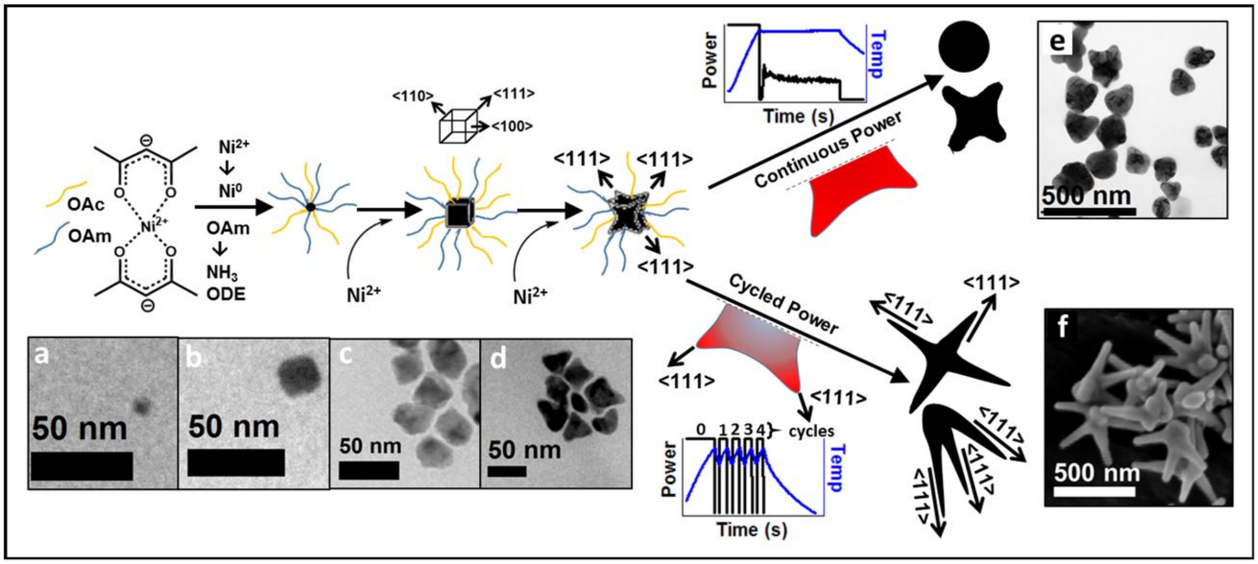

Figure 2.1: Proposed mechanism of nickel multipod growth during cycled microwave heating. The growth of Ni occurs via a 2-step autocatalytic process where Ni(acac)$_2$ is reduced in solution by the weak reducing agent, oleylamine followed by the formation of small nickel nuclei capped by oleylamine and oleic acid that continue to grow. The rates of growth are controlled by facet energy with the (111) facet being energetically favored. During the microwave on cycle, selective-heating of (111) tips on nanoparticle corners enable faster autocatalytic growth. Fastest growth of long multipod arms is therefore enabled when using high microwave power cycles that provide a greater differential temperature between arm tips and the rest of the nanoparticle surface unlike the case of the continuous power mode where particle reaches thermal equilibrium.

2.3.1 Evolution of Multipods Under Constant Temperature Mode for MW Heating (Variable Power)

The influence of time on multipod formation was evaluated under constant temperature conditions where the MW power fluctuates to maintain temperature to maintain temperature over the course of the reaction. The reactions were carried out by heating a solution of Ni(acac)$_2$ dissolved in a 5:1 (V:V) ratio of oleylamine to oleic acid to 280 °C using an initial incident power of 300 W to reach 280 °C and allowing the power to fluctuate to maintain the reaction temperature (See Figure 2.1 continuous power graphic). The reaction temperature and microwave power profile for a continuous temperature reaction and resulting particles are shown in Figure 2.2. Comparison is made to a reaction where the power is stepped from 300 W to 75 W under controlled power, as direct comparison to the constant temperature study.

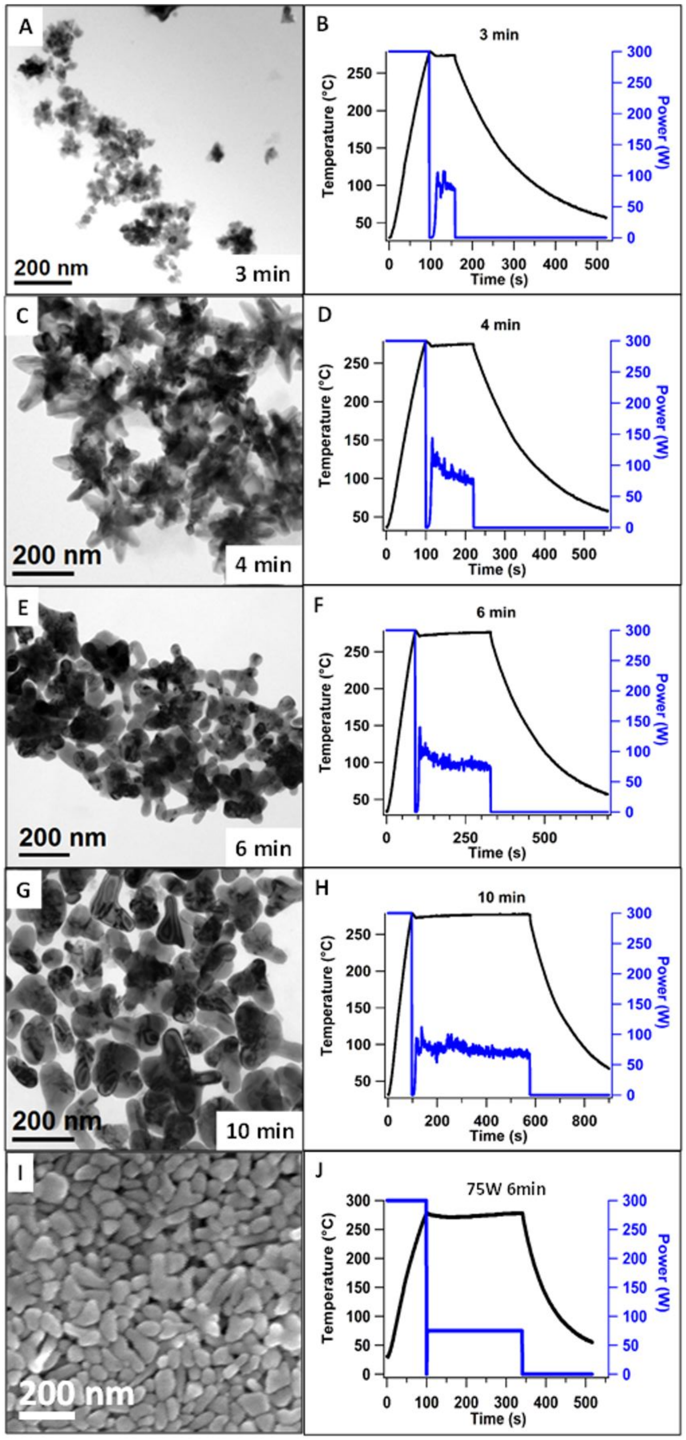

Figure 2.2: TEM of nickel multipods under constant temperature mode at different times of (A) 3 min, (C) 4 min, (E) 6 min and (G) 10 min. Temperature and microwave power profiles for the (B) 3 min, (D) 4 min, (F) 6 min and (H) 10 min reactions. SEM of nickel multipods under constant power mode for (I) 6 min and (J) corresponding temperature and microwave power profile.

Table 2.1: Multipod arm length, width, and aspect ratio with respective standard deviations for various reactions using constant temperature mode related to Figure 2.2. The reaction for constant power mode (75 W 6 min) produces sphere-like nanoparticles with diameter of 72 ± 12 nm.

Reaction	Arm Length (nm)	Arm Length std. dev. (nm)	Arm Width (nm)	Arm Width std. dev. (nm)	Aspect ratio	AR Relative std. dev.
3 min	16	7.5	14	5.1	1.1	0.59
4 min	55	19	38	10	1.4	0.44
6 min	77	26	50	13	1.6	0.43
10 min	81	31	58	10	1.4	0.42

During the Ni growth reaction under constant temperature conditions, the power cycles after 2 min dropping from 300W to 0W, with continuous power fluctuation at 50W to 100W to maintain reaction temperature. Small power fluctuations are evident in the constant temperature reaction. In contrast, under constant power (Figure 2.2J), the temperature is maintained over the course of the reaction without power fluctuations. In figure 2.2, no clear correlation is observed between the length of reaction at 280°C (constant temperature) and the appearance of multipod arms. Reactions carried out for 3 minutes (1 min beyond cycle event) during the largest variance in power produce irregular shaped nanoparticles exhibiting overgrowth but wide dispersities in size (20-100 nm). After 4 minutes (2 min beyond pulse event), the nanoparticles have grown larger and exhibit clear multipod morphology (arm aspect ratio of 1.4) with tapering arms. From 6 min to 10 min, the particles exhibit variability in the multipod morphology having large sphere-like cores with longer arms of uniform width and rounded ends extending out from the core (arm aspect ratio of 1.6-1.4).The stepped power experiment produces non-uniform shaped Ni (Figure 2.2I) consistent with the 6 to 10 min reactions.

The average arm length, arm width and aspect ratio for each time point is provided in Table 2.1 and distributions extracted from the TEM images are provided in 2.3. Arm length is reported as the length from tip to base of the arm while width is measured across the center region of the multipod arm.

The 4 min and 10 min Ni nanocrystals were investigated by high resolution TEM lattice spacing analysis to assess the crystallinity (Figure 2.4 A and B). High resolution TEM (HRTEM)

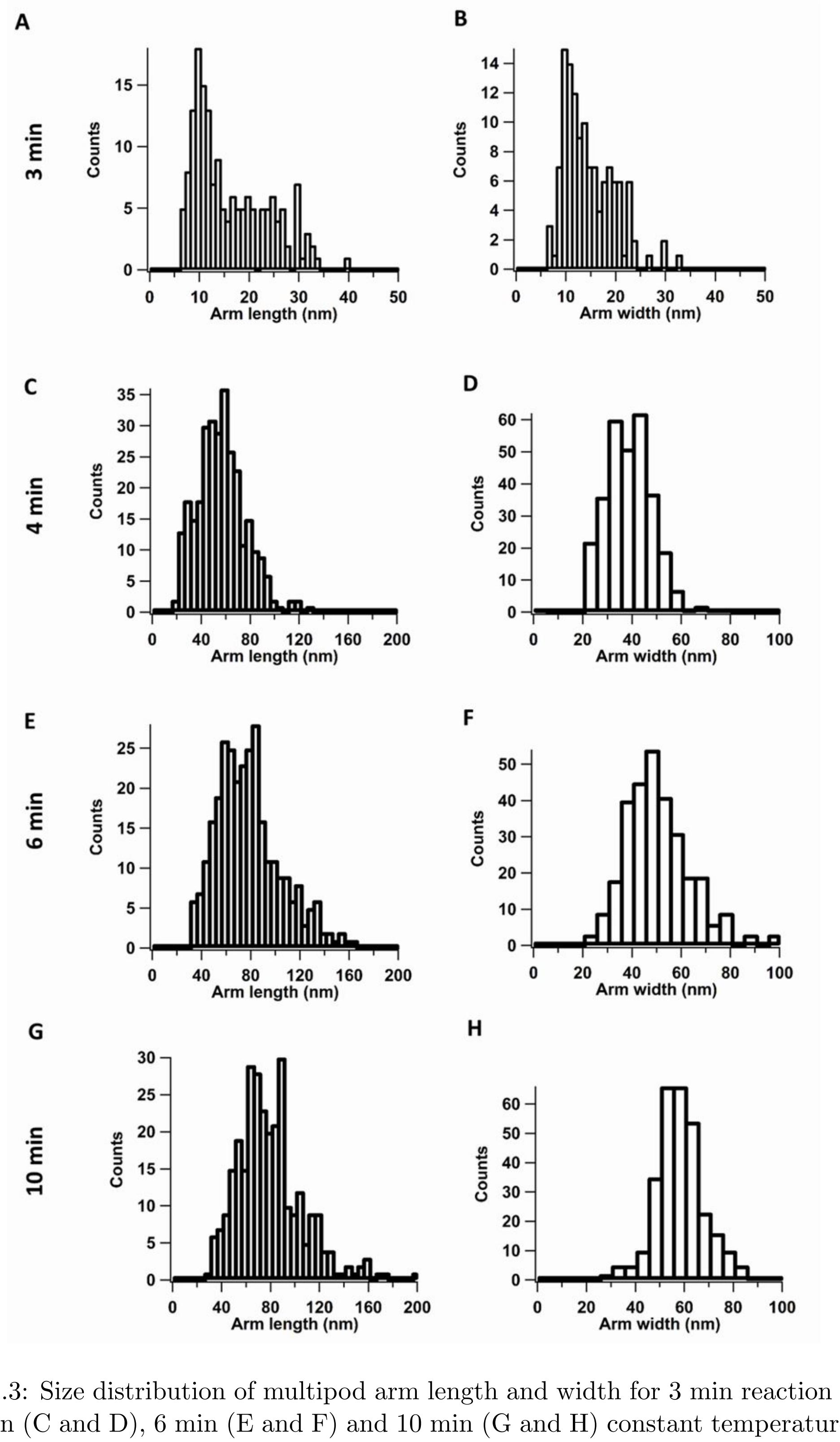

Figure 2.3: Size distribution of multipod arm length and width for 3 min reaction (A and B), 4 min (C and D), 6 min (E and F) and 10 min (G and H) constant temperature mode reactions.

of the arms in the 4 min reaction shows the arms grow along the <111> direction with a d-spacing of 0.20 nm with no visible glide plane errors. In the 10 min reaction, the overgrowths on the 10 min Ni nanoparticle also conform to the (111) plane with a d-spacing of 0.20 nm. pXRD patterns on the 10 min reaction confirms the d-spacing assignments to fcc Ni (Figure 2.5)

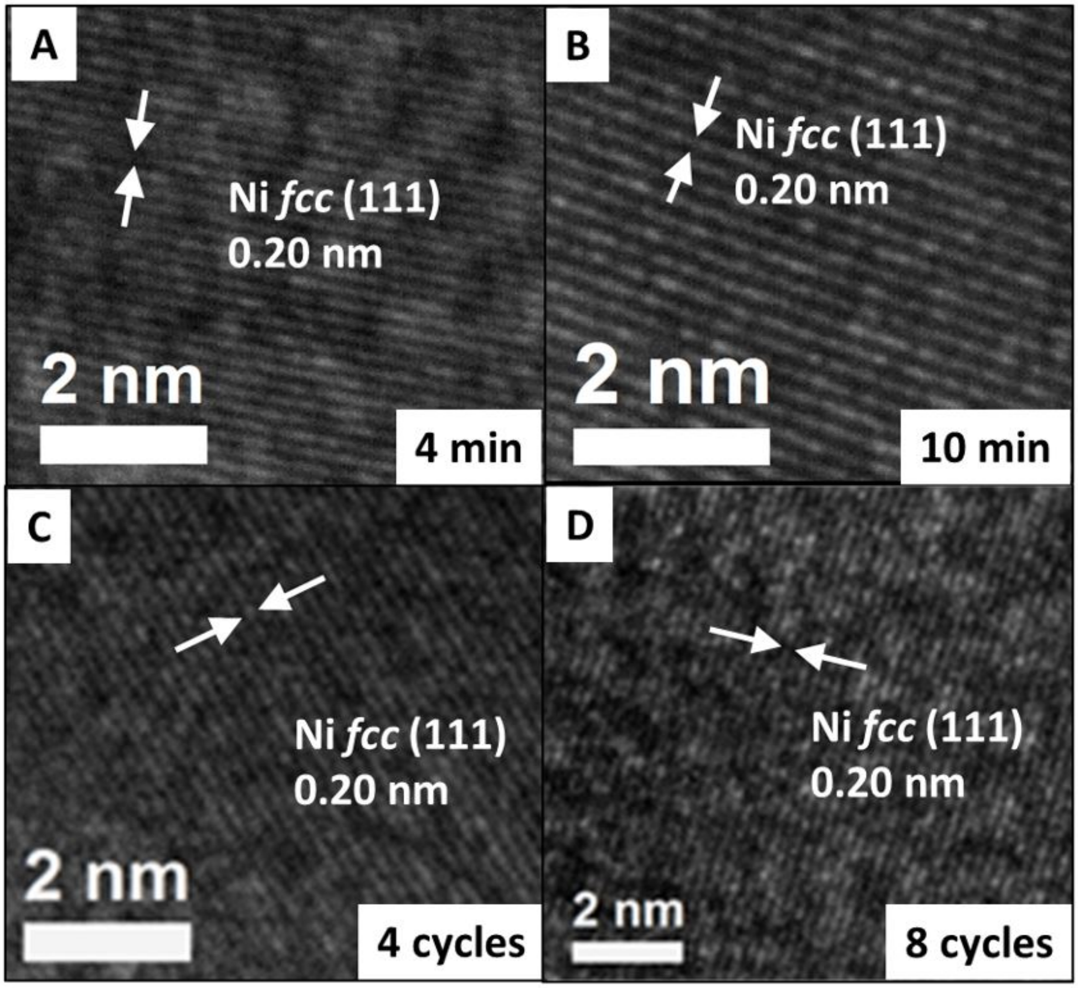

Figure 2.4: High resolution TEM (HRTEM) showing d-spacing along multipod arm of particle grown with constant temperature mode for (A) 4 min and (B) 10 min. HRTEM showing d-spacing along multipod arm for particle grown under cycled MW power mode using (C) 4 cycles and (D) 8 cycles.

The lack of a clear power or time dependence on growth behavior using constant temperature is attributed to the large fluctuation in the MW power cycle profiles. To assess the effect of MW influence, controlled convective reactions were carried out under identical reaction conditions to the constant temperature studies in Figure 2 (280 °C, 5:1 OAm:OAc, 0.08 M Ni(acac)$_2$) for 4 min in a pre-heated aluminum block and 1 h using a round-bottom flask with a heating mantle. In the convective reactions the NiNPs appear as spherical nanocrystals (Figure 2.6). The formation of overgrowth and multipod arms is not observed under convective conditions. The lack of overgrowth under the experimental conditions are consistent with reports where high temperature reactions lead to spherical nanocrystals.[117, 135, 137, 138]

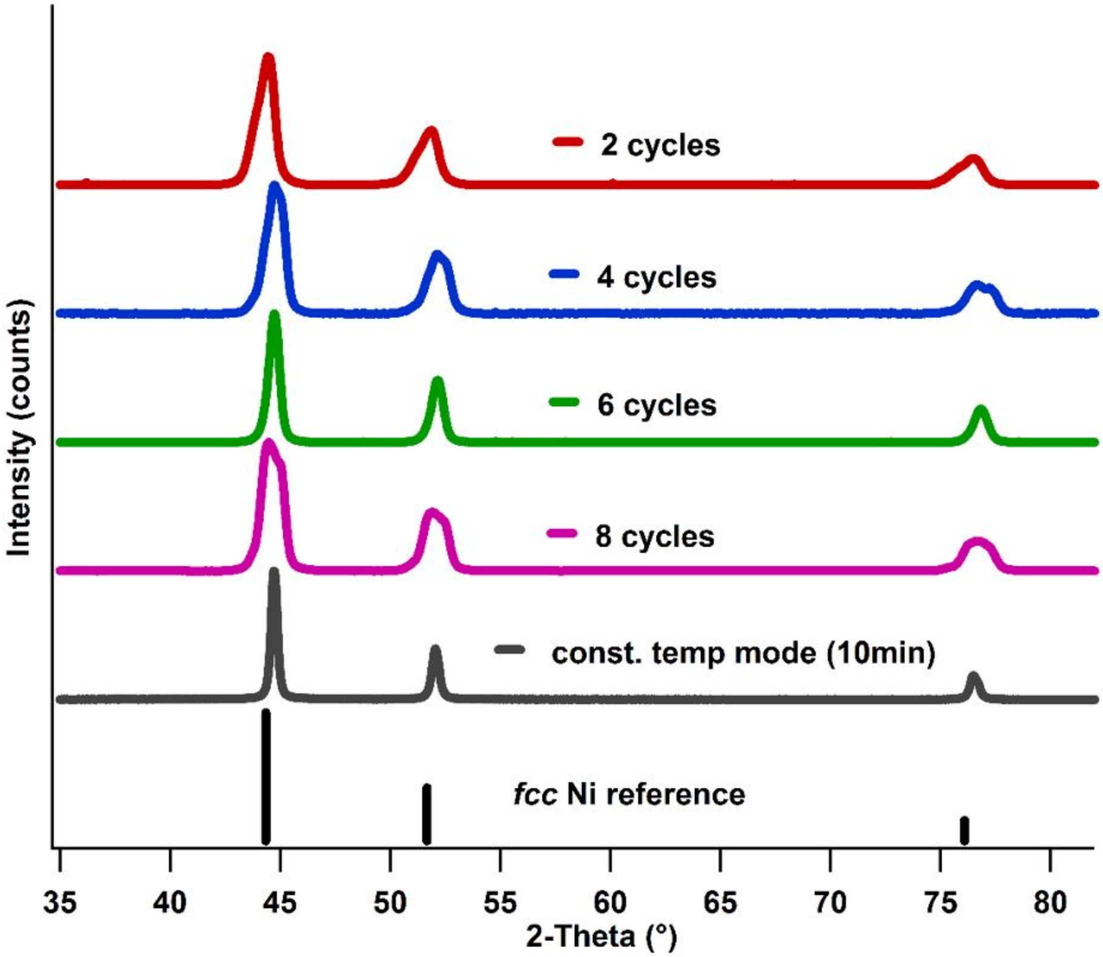

Figure 2.5: Powder-XRD patterns for various multipod structures (Cycled power for 2-, 4-, 6- and 8-cycles, and 10 min constant temperature reaction). Multipod structures show crystal structure that matches the fcc Ni reference pattern (PDF 01-087-0712).

The shapes of the Ni NPS grown under convective conditions compared to NiNPs grown in a MW are remarkably different. It is clear in Figure 2.2 that the NiNPS grown in a MW exhibit overgrowth leading to multipod structures. Inspection of the power vs. time graphs suggest the multipod formation in the MW is potentially due to the presence of pulsing.

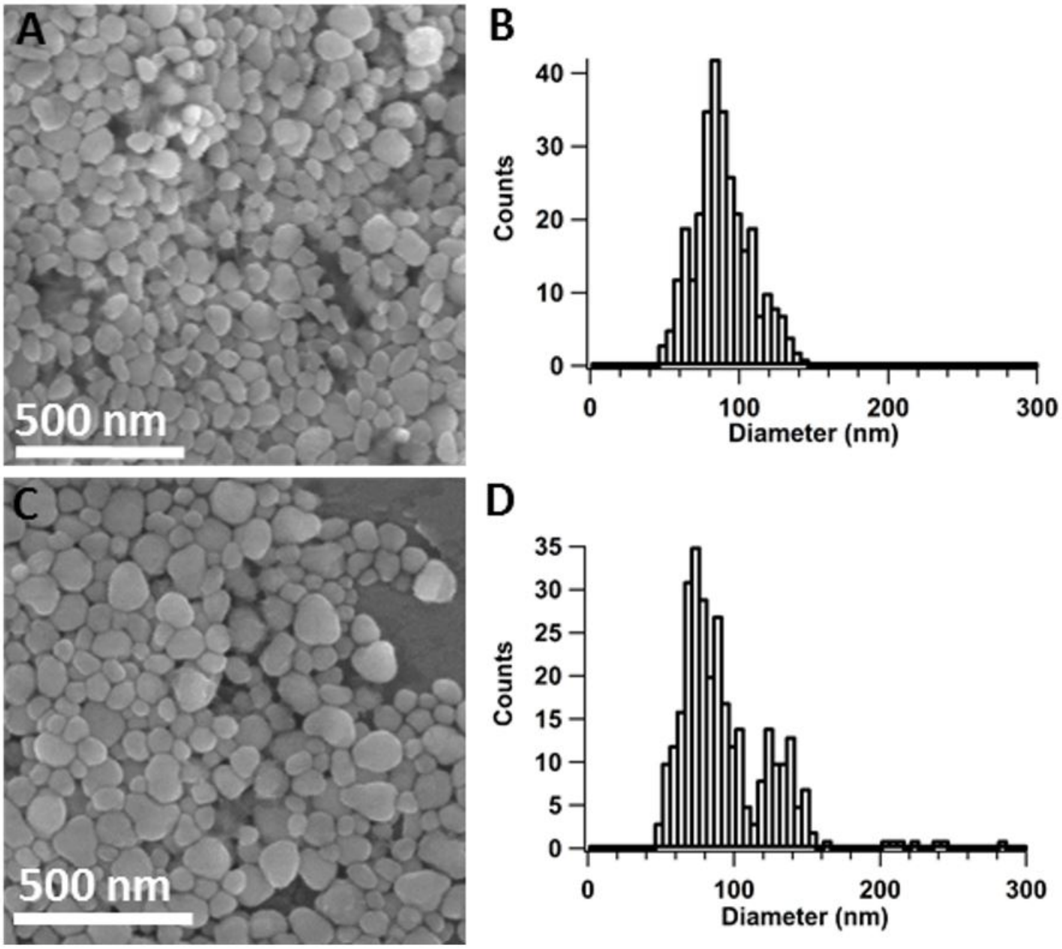

Figure 2.6: (A) SEM of nickel nanoparticle formed using convective heating in a pre-heated aluminum block at 280 °C and held for 4 min and (B) respective size distribution from the SEM analysis. (C) SEM of nickel nanoparticles formed using convective heating (heating mantle) where reaction was heated to 280 °C and held for 1 h and (D) respective size distribution from SEM analysis.

2.3.2 Evolution of Multipods Under Pulsed Microwave Power (Variable Temperature and Reaction Time)

The influence of MW power cycling on multipod formation was evaluated under variable temperature and time to evaluate whether cycling of the impingent MW field (Figure 2.7) directly correlated to the length of the arm in arm observed in the MW reactions (Figure 2.8). The cycle power and temperature profiles for the experimental conditions that produce the multipod structures in Figure 2.8 are shown in Figure 2.7.

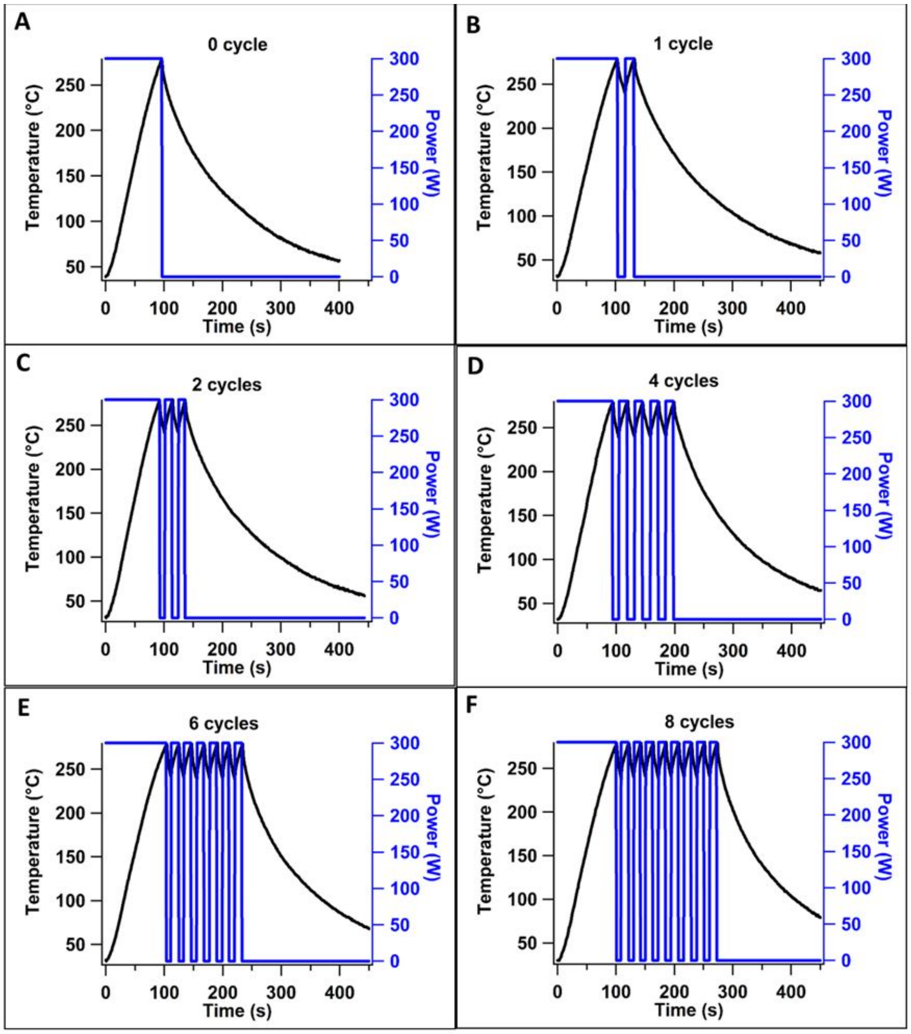

Figure 2.7: Temperature and power profiles for cycled power mode microwave reactions with (A) 0 cycle, (B) 1 cycle, (C) 2 cycles, (D) 4 cycles, (E) 6 cycles and (F) 8 cycles.

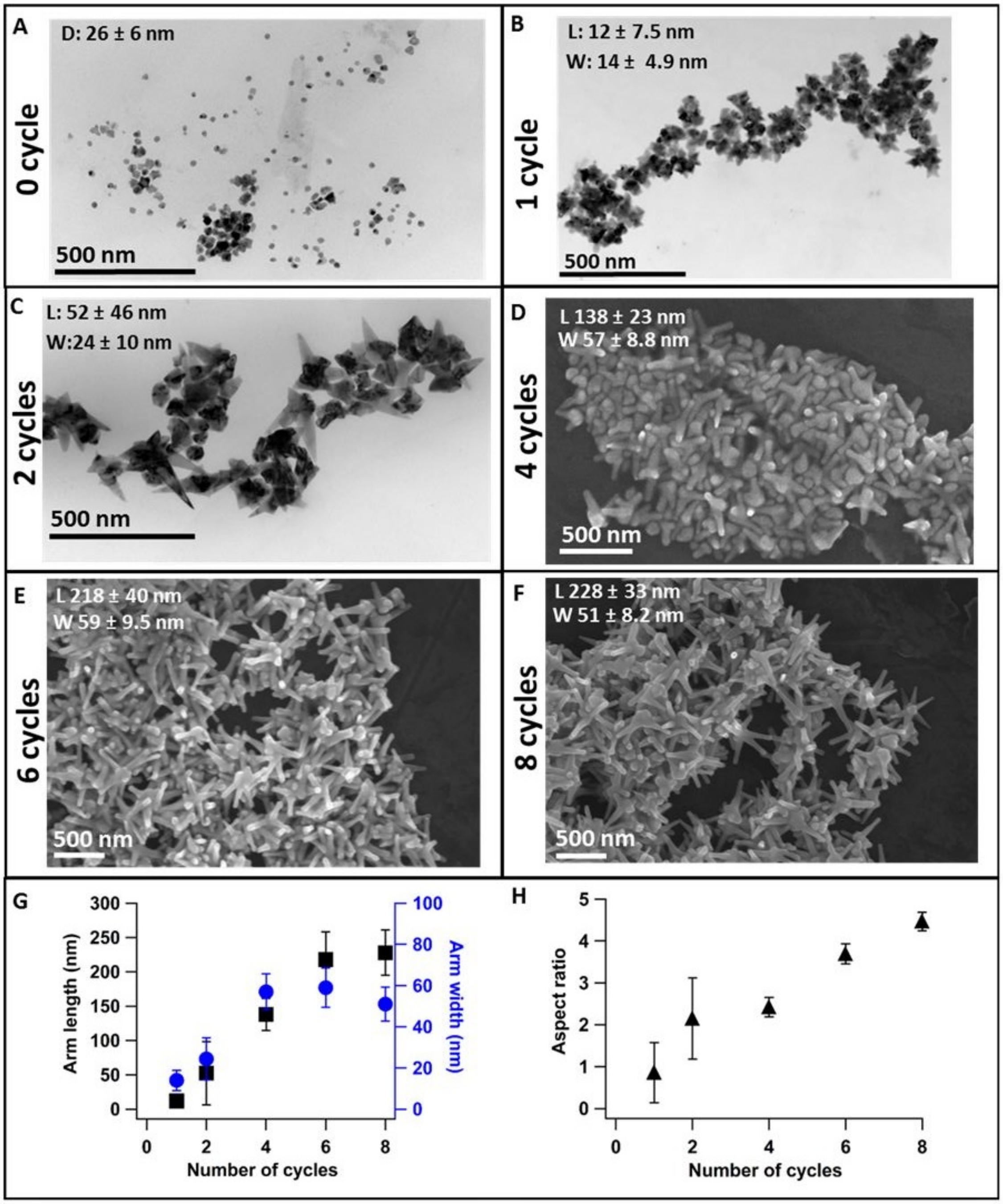

Figure 2.8: Evolution of nickel multipod structure synthesized using cycled power mode with increasing number of cycles shown by TEM for (A) 0 cycle, (B) 1 cycle, (C) 2 cycles, (D) 4 cycles, (E) 6 cycles and (F) 8 cycles. Inset 3D and 3F show high resolution TEM showing crystalline lattice of multipod arms. (G) Length and width of multipod arms as a function of number of applied after initial cycle and (H) aspect ratio of arms versus number of cycles after initial cycle.

The reactions are carried out under identical reaction conditions to the constant temperature study; however, the MW is pulsed at 300W in a controlled fashion and the temperature maximum is set to 280 °C and allowed to drop to 240 °C between pulses. In figure 2.1 cycled power graphic, the definition of cycle number is defined as it relates to the experimental data presented in Figure 2.8. The average temperature of the reaction is approximately 260°C.

The overall MW power impingent of the samples is higher than constant temperature mode (figure 2.9). For instance, an 8 cycle reaction requiring 4.5 min of reaction time has 38% higher MW power impingent on the reactants when compared to the reaction at constant reaction temperature (280°C) for the same reaction time.

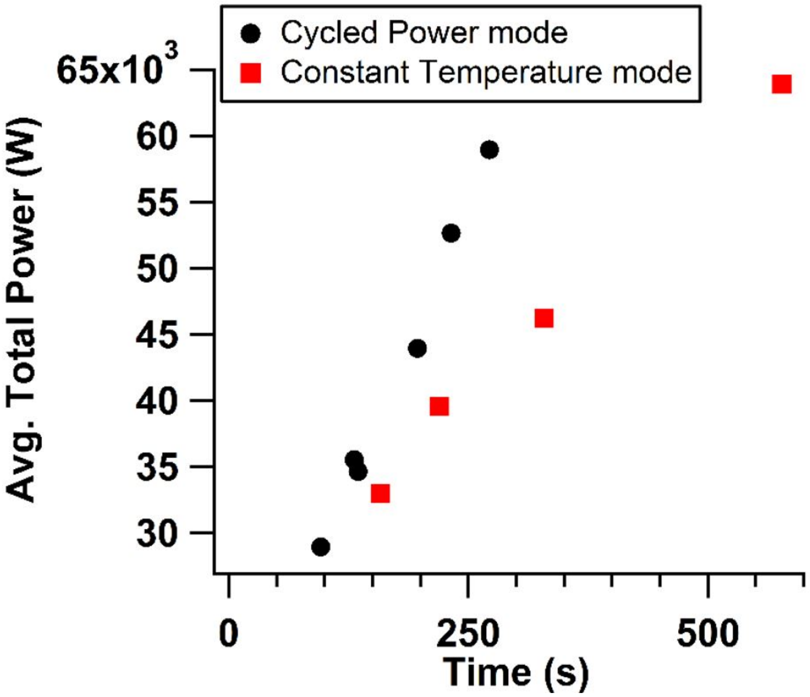

Figure 2.9: Average total microwave power delivered to reaction in pulsed power mode versus constant temperature mode in time.

At zero cycle (Figure 2.8a), cube shaped nanoparticles of 26 nm in diameter are observed (size distribution provided in figure 2.10. With increasing number of cycles (Figure 2.8B-F), anisotropic multipod structures are observed wherein the arm length and aspect ratio increases with the number of cycles. The isolated materials are fcc based on powder X-ray diffraction (Figure 2.5). A plot of the average length of the arms and widths, as well as the aspect ratio (length/width) as a function of the number of cycles is plotted in Figures 2.8 G and H. Analysis of the SEM image for the 8 cycle reaction, in Figure 2.8 demonstrates >99% multipod formation (within 2σ) with an average of four arms per multipod. The distribution is a Gaussian distribution (2.12). The length of the arms are 228 ± 33 nm with a width about 51 ± 8.2 nm resulting in an aspect ratio of 4.5.

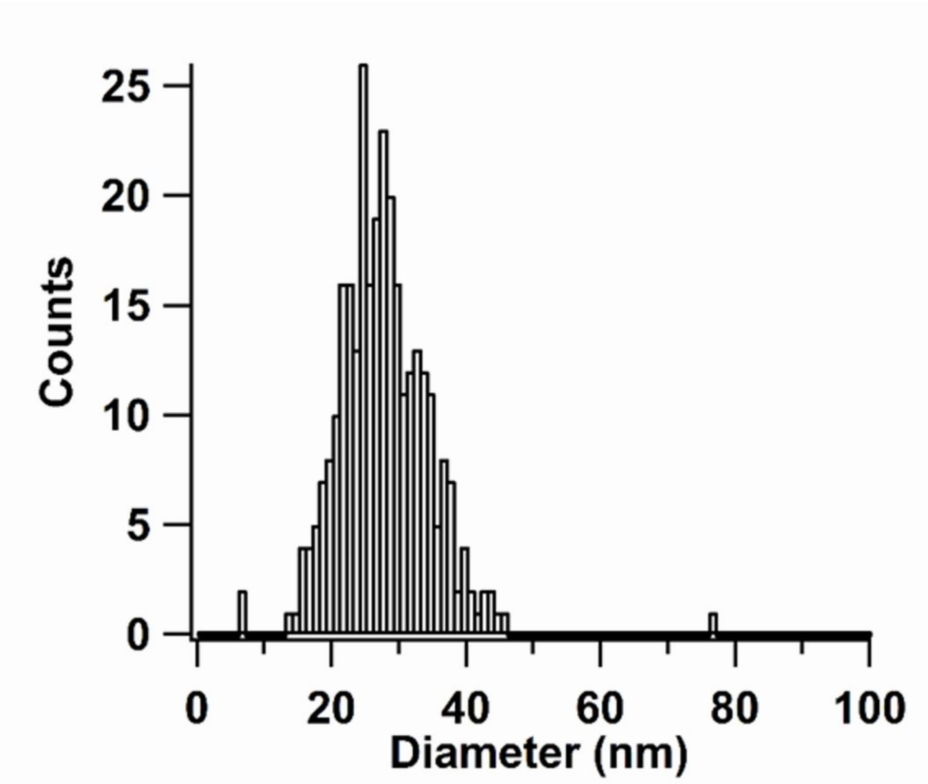

Figure 2.10: Size distribution analysis from TEM of nanoparticles from 0-cycle power mode microwave reaction.

The multipod arms exhibit no glide plane errors and grow as (111) extensions. HRTEM imaging of the 4-cycle and 8-cycle sample reveals the arms are single crystal along the <111> direction with d-spacing of 0.20 nm (2.4). HRTEM of some initially formed Ni cores (0-cycle reaction) and region near the core-arm interface for the 8-cycle reaction show defect-free single crystalline nature (Figure 2.11).

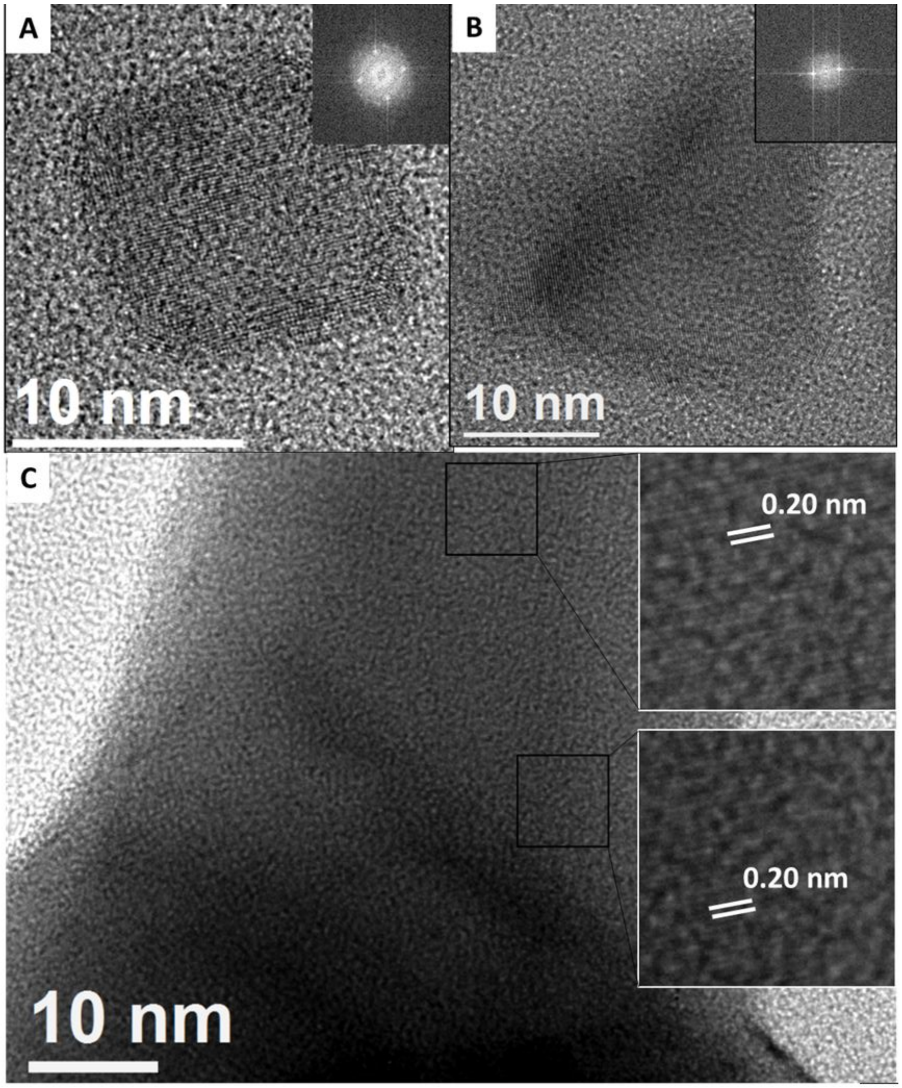

Figure 2.11: (A and B) High resolution TEM images of core structures exhibiting single-crystalline nature without defect. (Insets) Numerical electron diffraction patterns corresponding to fast Fourier transform within core region. (C) TEM of a multipod arm (8 cycle reaction) near core-arm intersection showing highly crystalline defect-free structure as observed in magnified insets in two regions with a d-spacing of 0.20 nm corresponding to the (111) planes.

The increase in the aspect ratio for the (111) arm appear is shown for the 10s MW-on cycles in Figure 2.8 G and H. The aspect ratio appears to be linear with respect to the number of cycles. The histograms for arm length and width are shown in figure 2.12 and 2.13. In Figure 2.14, the impact of shorter MW heating cycles is evaluated.

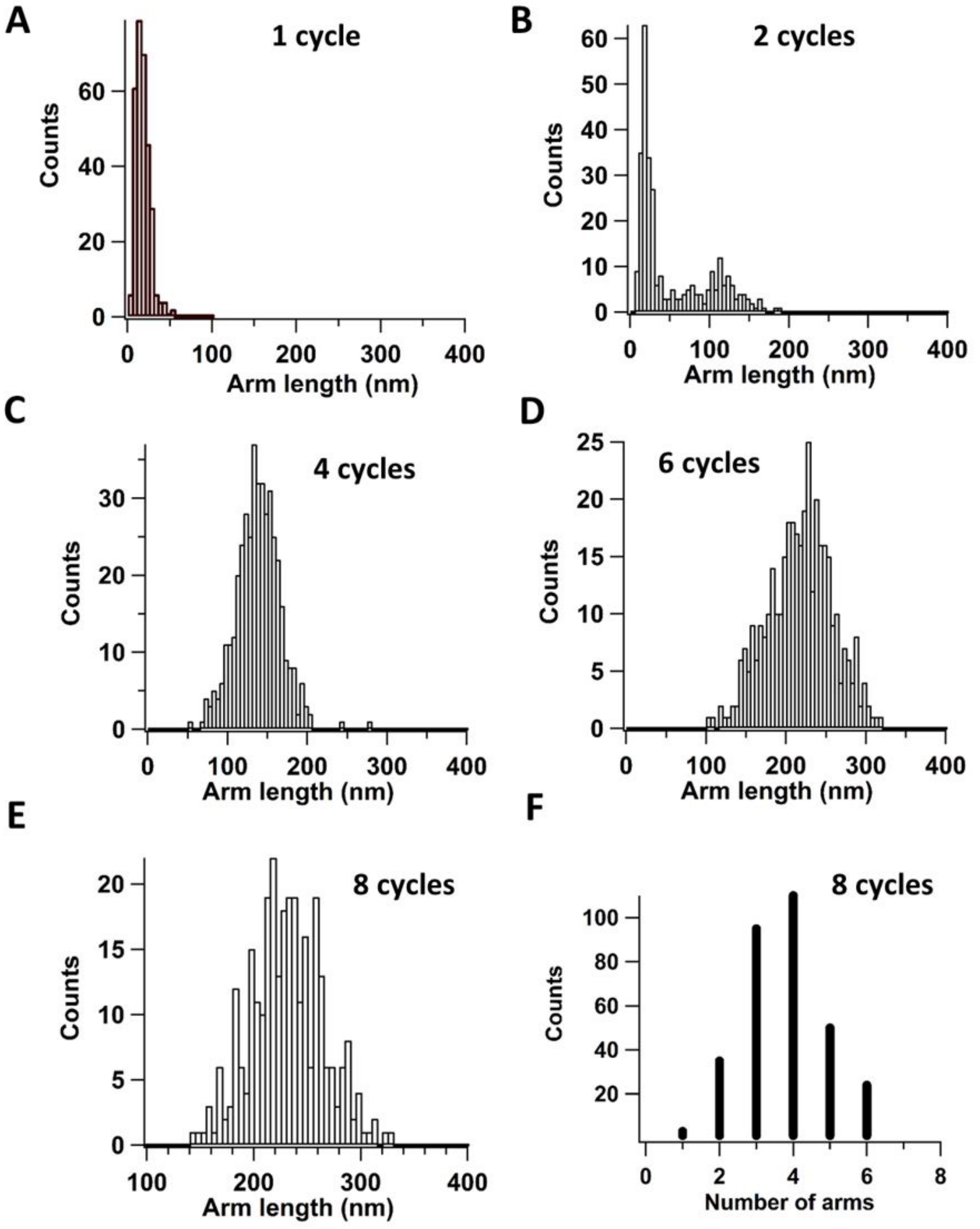

Figure 2.12: Arm length distribution analysis from TEM/SEM of multipod structures synthesized using cycled power mode using (A) 1 cycle, (B) 2 cycles, (C) 4 cycles, (D) 6-cycles and (E) 8 cycles (number of cycles after initial cycle to raise temperature to 280 °C). (F) Number of arms per multipod observed from SEM image of the 8 cycles reaction.

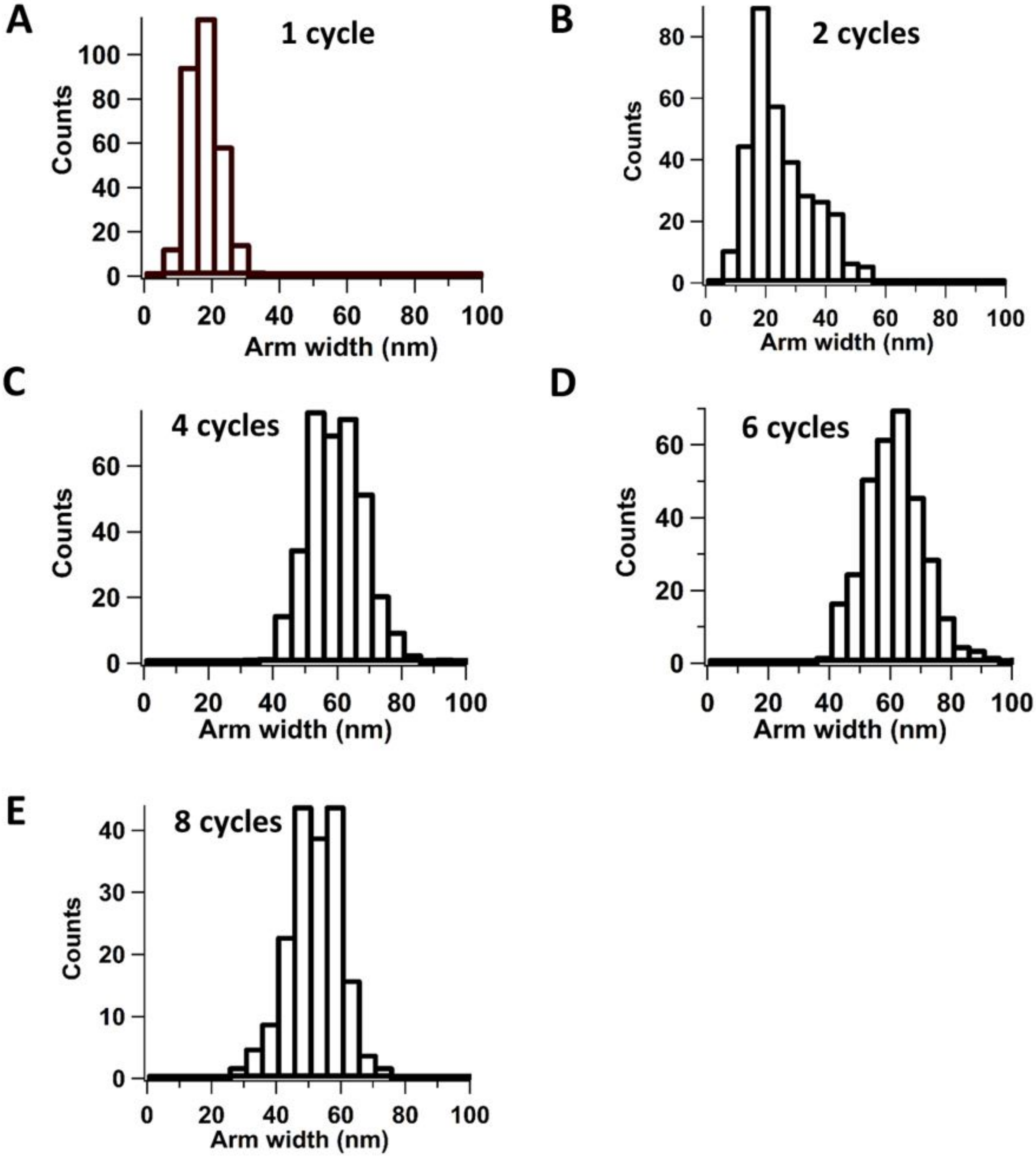

Figure 2.13: Arm width distribution of multipod structures using cycled microwave reaction using (A) 1-cycle, (B) 2-cycles, (C) 4-cycles, (D) 6-cycles and (E) 8-cycles.

Comparison of nearly equivalent heating times for a single 10s cycle, two 5s cycles, and three 3s cycles following the initial 13s MW irradiation event confirms the control of aspect ratio.

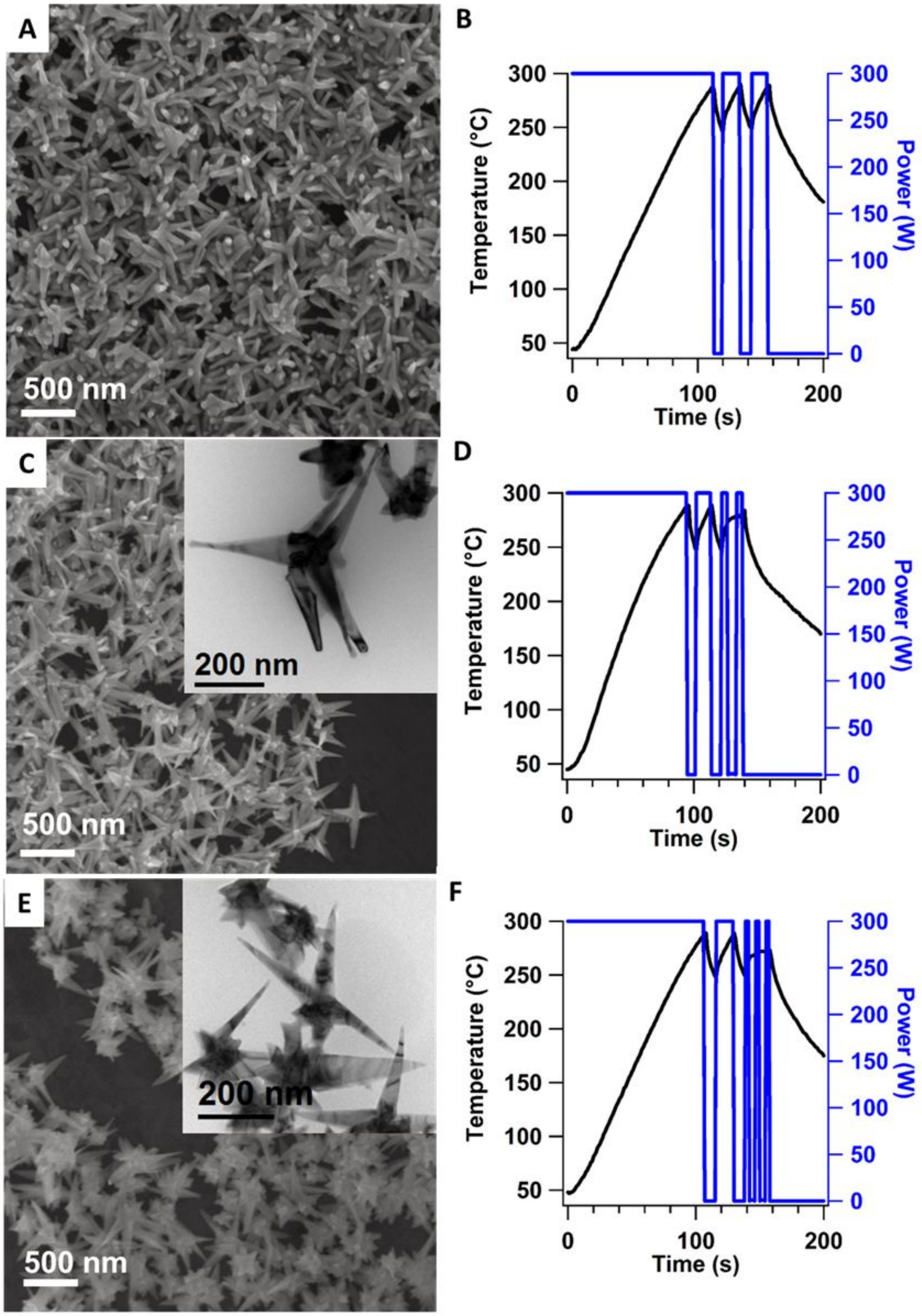

Figure 2.14: SEM of nanostructures with corresponding temperature and microwave power profile of cycled power reaction with different cycle frequencies following an initial cycle of 10 sec 300W: (A and B) 1 cycle of 300 W for 10 sec, (C and D) 2 cycles of 300W for 5 sec, and (E and F) 3 cycles of 300W for 3 sec. TEM image of multipod structure (insets C and E).

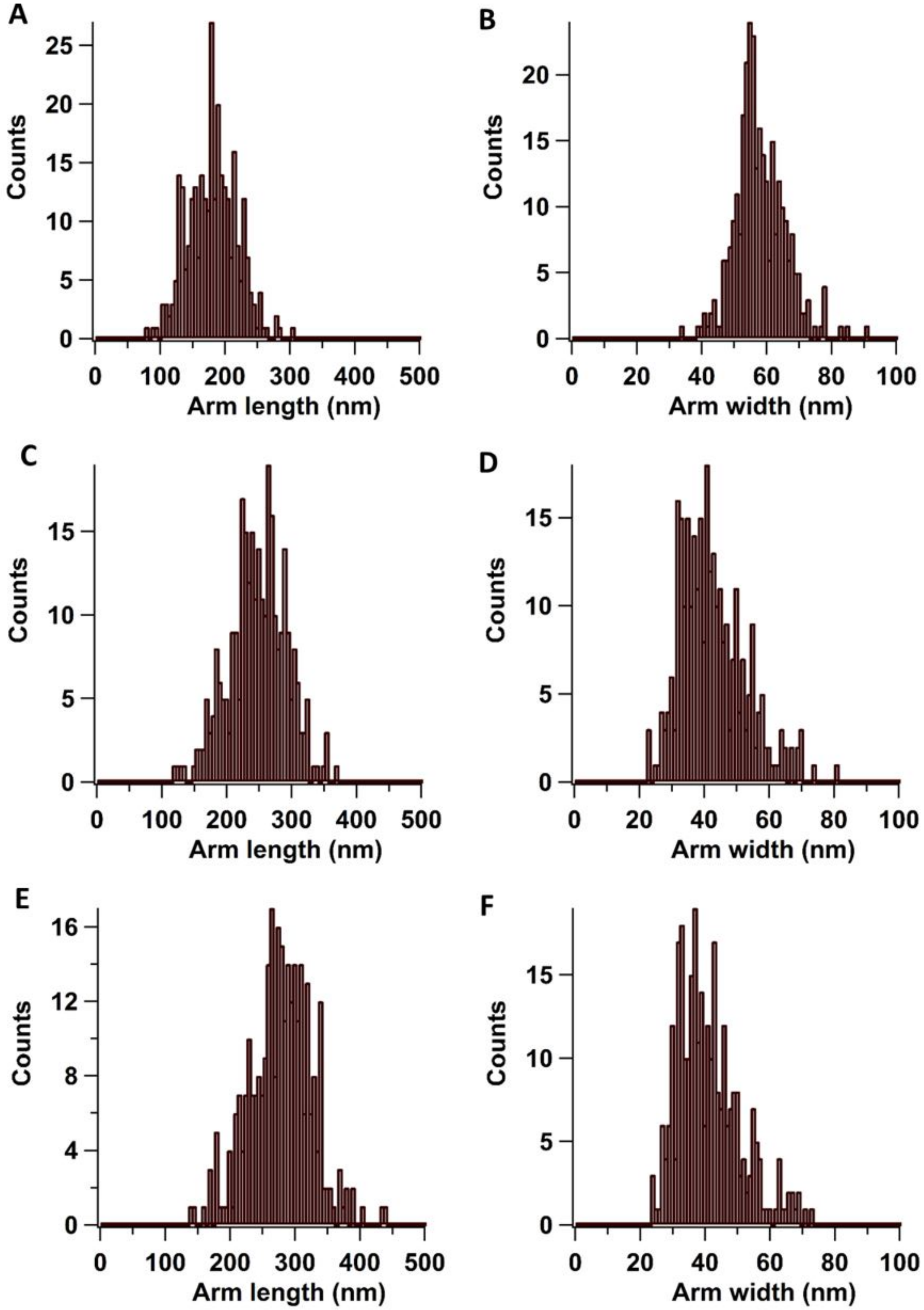

Figure 2.15: Arm length and arm width distribution of nanostructures synthesized using cycled power reaction with different cycle frequencies following an initial cycle of 13 sec 300 W: (A and B) 1 cycle of 300 W for 10 sec, (C and D) 2 cycles of 300W for 5 sec, and (E and F) 3 cycles of 300 W for 3 sec.

The arm length and width can be extracted by analysis of 300 arms in the SEM images (figure 2.15). For the 10s cycle (Figure 2.14 A) the length is 178 ± 37.9 nm and the width is 57.6 ± 7.87 nm (aspect ratio 3.1); for the two 5s MW-on cycles (Figure 2.14B) the length is 246 44.4 nm and the width is 42.2 ± 10.1 nm (aspect ratio 5.8); and for the three 3s MW-on cycles (Figure 2.14C) the length is 277 ± 49.6 nm and the arm width is 41.1 ± 10.5 nm (aspect ratio 6.8). From the cycling study it is clear that for the shorter MW-on cycle times thinner arms are observed.

The resultant multipods in the cycled experiments compared to the constant temperature reveal under cycled power conditions the uniformity of the multipods is significantly better with a higher multipod density. The observed multipod density is in fact the highest ratio reported in the literature, with >99% for experimental conditions of four or more cycles. The observed experimental data is consistent with the overgrowth model for multipod formation suggested by Xia, *et* al.[107]

2.3.3 Effect of Cycle Power on Multipod Evolution

While it would be desirable to measure the tip vs core of the Ni multipod during the MW cycle to support the lightning rod mechanism, it is not practical to measure this on the scale of the nanoparticle. The MW measures vessel temperature and not the nanoparticle temperature directly. In order to support that growth behavior is dependent on MW-on cycling leading to tip heating, a series of experiments were carried out where the influence of MW power on the growth behavior was evaluated. It is reasonable to assume the higher cycle powers will lead to hotter tips even though the average reaction temperature is nearly constant. However, the time to achieve temperature is lengthened at lower power which should lead to nanoparticle temperature equilibration. (Note: For these reactions a 10 ml reaction vessel was used which impacts the MW energy absorbed and the growth rates).

As seen in Figure 2.16A and B, by lowering the power of the 4-cycle reaction to 150 W, the population of multipods is greatly reduced, and primarily forms spherical nanoparticles (diameter 52.4 ± 13.9 nm) in comparison to the 300W 4-cycle reaction (Figure 2.16C and D) which produces well-defined multipods (arm length 73.6 ± 27.1, arm width 33.5 ± 5.6 nm. Furthermore, two other experiments were carried out where the sequential cycle power of the 4 cycles was either increased or decreased by 50 W. When the cycle power is sequentially decreased from 300 W to 150 W in a 4-cycle reaction (Figure 2.16E and F), the nanostructures formed are more rounded with very little overgrowth (arm length 22.2 ± 6.7 nm, arm width 13.9 3.4 nm. In the other case, where the

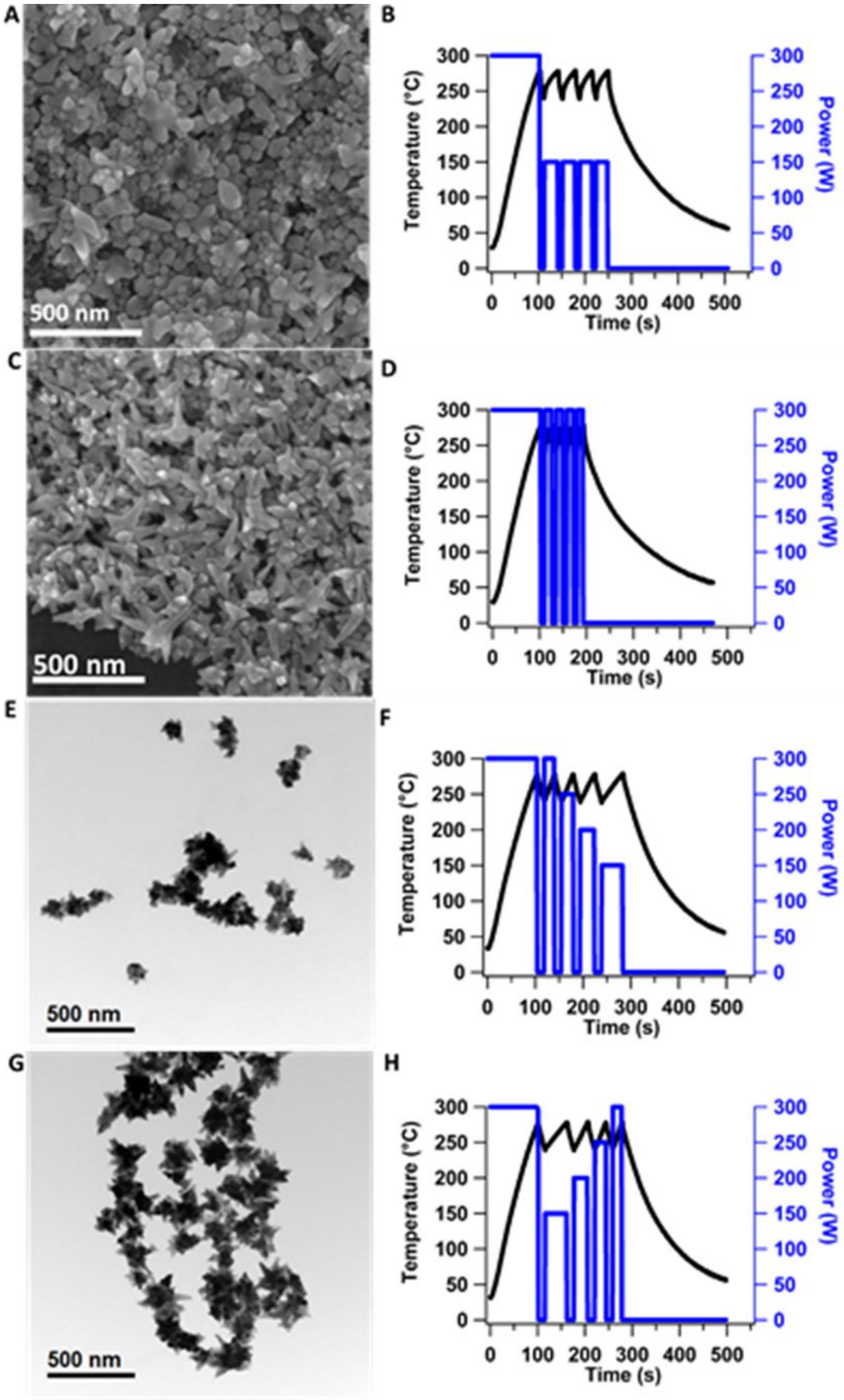

Figure 2.16: SEM of nanostructures with corresponding temperature and microwave power profile of reactions under cycled power of 150 W (A and B) and 300 W (C and D). TEM of nanostructures with corresponding temperature and microwave power profile of reactions under cycled power with sequential cycles of either decreasing power from 300 W to 150 W (E and F) or increasing power from 150 W to 300 W (G and H).

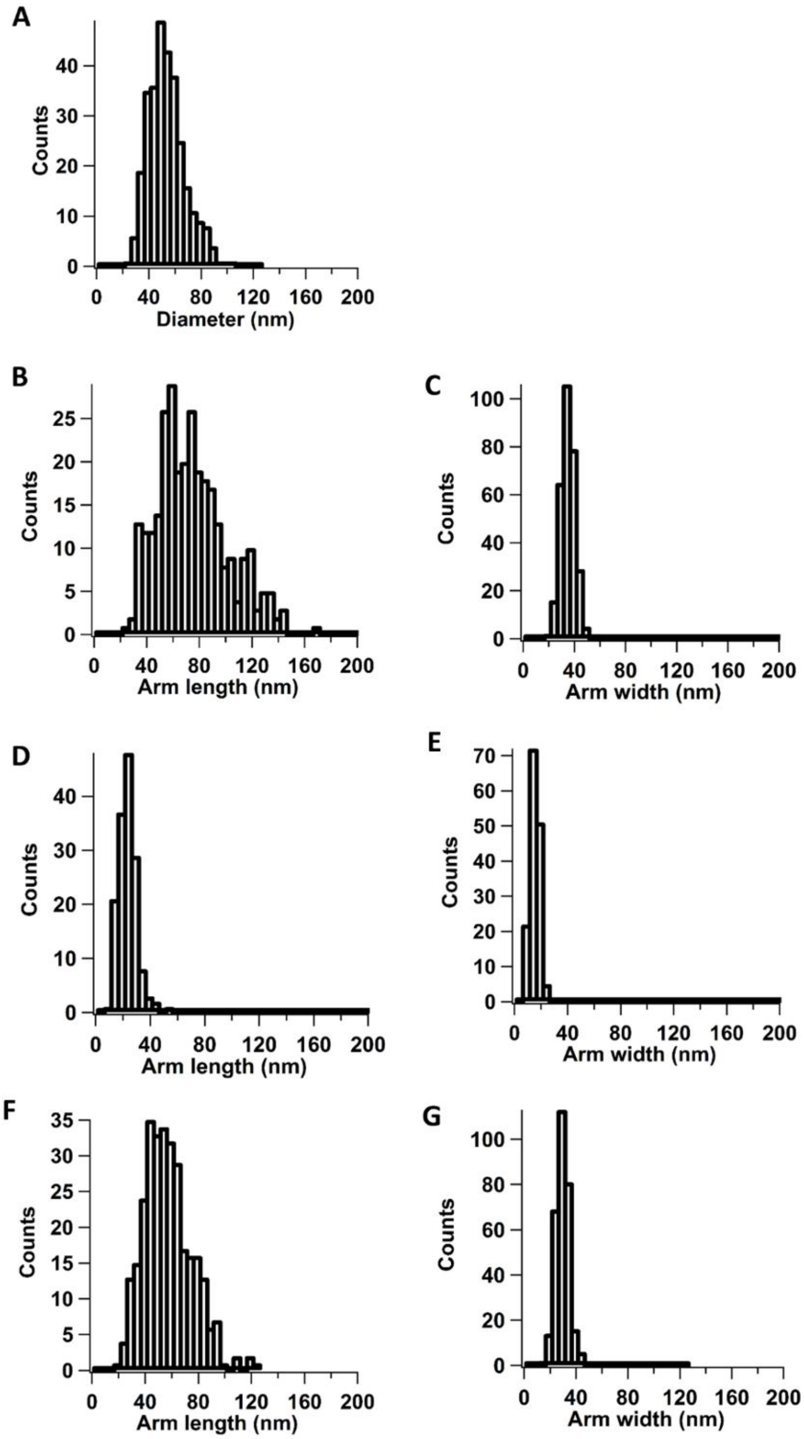

Figure 2.17: (A) Diameter of nanoparticles synthesized using cycled power where the microwave power during the 4 cycles was set to 150W. Arm length and width distributions of nanostructures synthesized using cycled power with different cycle power: (B and C) 4 cycles of 300 W, (D and E) 4 cycles of sequential decreasing power from 300 W to 150 W, and (F and G) 4 cycles of sequential increasing power from 150 W to 300 W.

MW power of sequential cycles is increased from 150W to 300W (Figure 2.16G and H), multipods with longer arms are formed (arm length 55.9 ± 18.5 nm, arm width 28.0 ± 5.2 nm). Distribution of arm lengths and arm widths are provided in figure 2.17.

The power dependent growth behavior can be ascribed to a lower temperature differential between the core and the tips when the cycle power is sequentially decreased leading to more uniform nanoparticle surface heating and growth. On the other hand, when the cycle power is increased sequentially, the initially formed overgrowths continue to be selectively heated compared to the rest of the nanoparticle surface with subsequent high-power short-time cycles as described previously.

2.3.4 Role of Ligands on Multipod Generation Under Constant Temperature and Cycled MW Power Modes

As a final check on the MWon cycle dependent growth, the influence of ligand was investigated, as it is known ligands can direct nanoparticle shaping.[52, 109, 111, 116] A set of experiments were carried out under both, constant temperature (8 min) and cycled MW power (4 cycles of 300 W), where the ratio of the OAm (reducing agent and capping agent) and OAc (capping agent) was varied (Figure 8). In addition, the effect of nanoparticle growth when the primary amine (OAm) is substituted with a tertiary amine, trioctylamine (TOA) was investigated.

As shown in Figure 2.18 C and D, reactions carried out at 5:1 OAm to OAc in the 10ml reaction vessel produce multipod structures. The formation of the multipod is likely to be enhanced by the presence of OAc, since the igand directing ability of OAc to enhance anisotropic shapes is well-documented. Reactions carried out at 1:5 or 0 :1 OAm to OAc (not shown) do not yield product due to too little reducing agent consistent with the requirement of an amine to act as a reducing agent to initiate reduction of the Ni(acac)$_2$ to initiate Ni growth.[18, 40] When the MW experiments (Figure 2.18 A and B) are carried out at 1:0 OAm to OAc, spherical-shaped nanoparticles form consistent with the requirement of OAc being present to direct nanoparticle shape. The isolated Ni spheres constant temperature conditions have a diameter of 74.5 ± 13.0 nm and following a reaction with 12 cycles at 300 W the nanoparticle diameter is 137 ± 37 nm.

Interestingly, the Ni nanoparticles formed using a 5:1 V:V TOA:OAc ratio also eliminated multipod growth under constant temperature and cycled MW power modes. Under constant

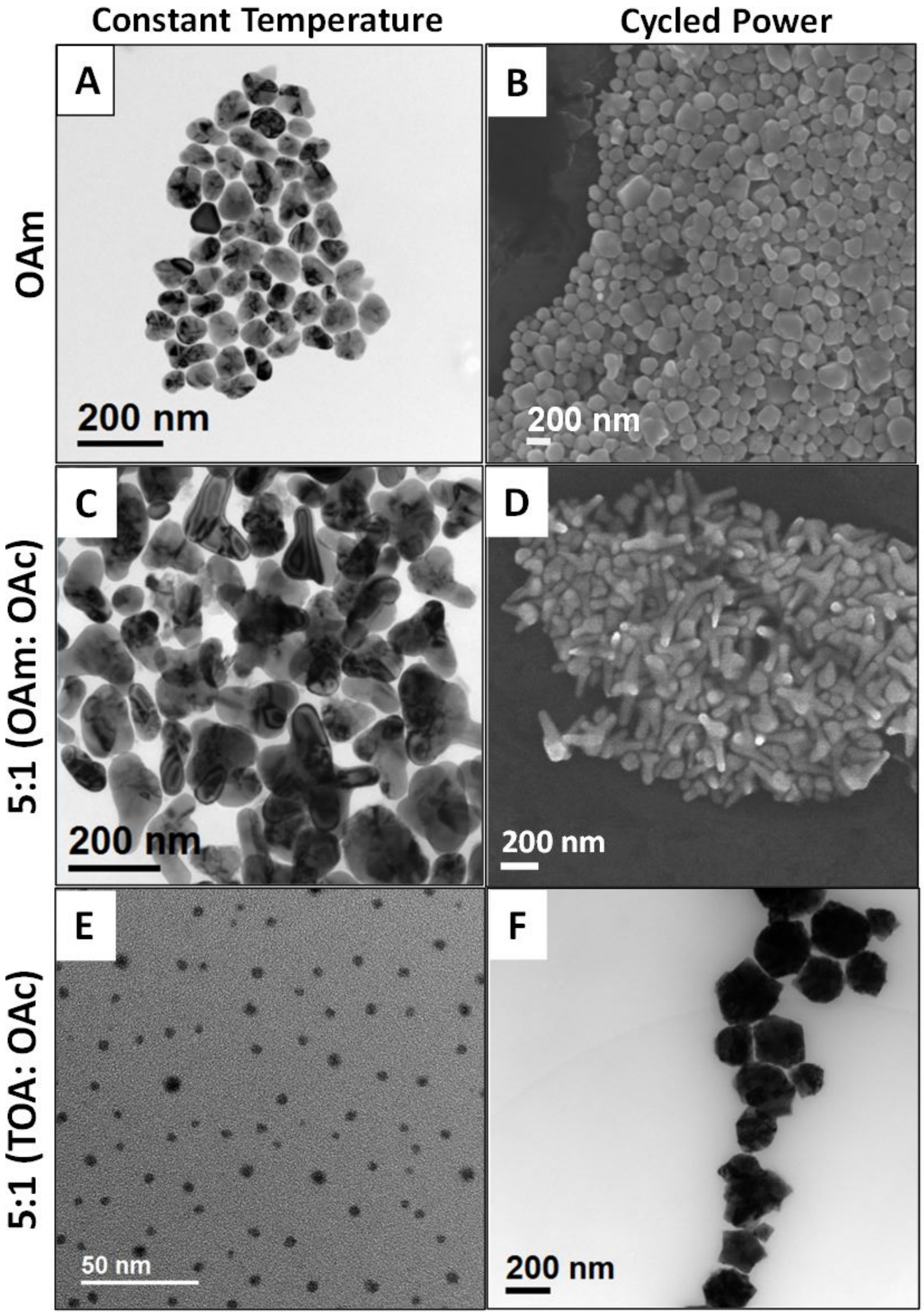

Figure 2.18: Ligand role in Ni multipod synthesis. Nanostructures formed using pure oleylamine (OAm) under (A) constant temperature mode for 10 min (TEM) and (B) cycled MW power with 12 cycles (SEM) (4 cycles did not form any product). Nanostructures formed using 5:1 V:V ratio of OAm and oleic acid (OAc) under (C) constant temperature mode for 10 min (TEM) and (D) cycled MW power with 4 cycles (SEM). Nanostructures formed using 5:1 V:V ratio of trioctylamine (TOA) to OAc under (E) constant temperature mode for 10 min (TEM) and (F) cycled MW power with 4 cycles (SEM). Reactions carried out using 1:5 V:V ratio of OAm:OAc and using pure OAc yielded no product.

temperature mode spherical nanoparticles with a diameter of 4.63 ± 1.62 nm was isolated, while cycled MW power mode produced large faceted nanoparticles with diameters of 173 ± 70 nm. The difference in growth is not understood but is under study. It is believed that the loss of the multipod structure reflects loss of packing order at the surface due to the presence of bound TOA.

The observation from the ligand studies suggest that the combination of OAm and OAc is key to the formation of a Ni core structure with overgrowths that can then be elongated most effectively through MW power cycling. Further studies are underway to explore the full role of ligand.

2.3.5 Analysis of the Magnetic and Thermal Stability Properties of Ni Multipods

The multipod structures with high anisotropic structures may have applications in a range of technical fields, including magnetism and catalysis. The magnetic characterization and thermal stability of selected multipods were analyzed for completeness. The data is provided in figures 2.19 and 2.20. It is known that shape anisotropy in magnetic materials is known to influence the magnetic properties of materials.[139, 140]

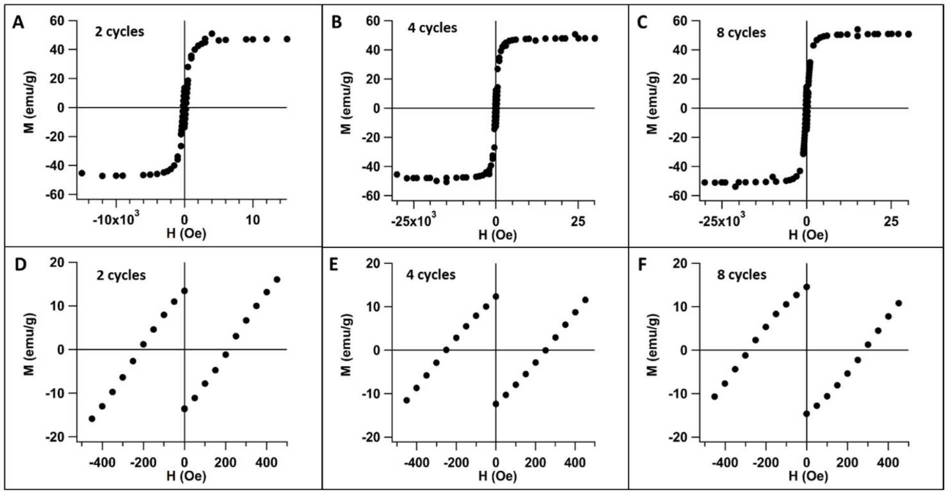

Figure 2.19: 300K field sweep saturation magnetization curves with close up near origin to show coercivity for (A and D) multipods with arms of aspect ratio 2.17 (coercivity 215 Oe), (B and E) multipods with arms of aspect ratio 2.42 (coercivity 250 Oe), and (C and F) multipods of aspect ratio 4.47 (coercivity 283 Oe) synthesized using a cycle power of 300 W (10 sec).

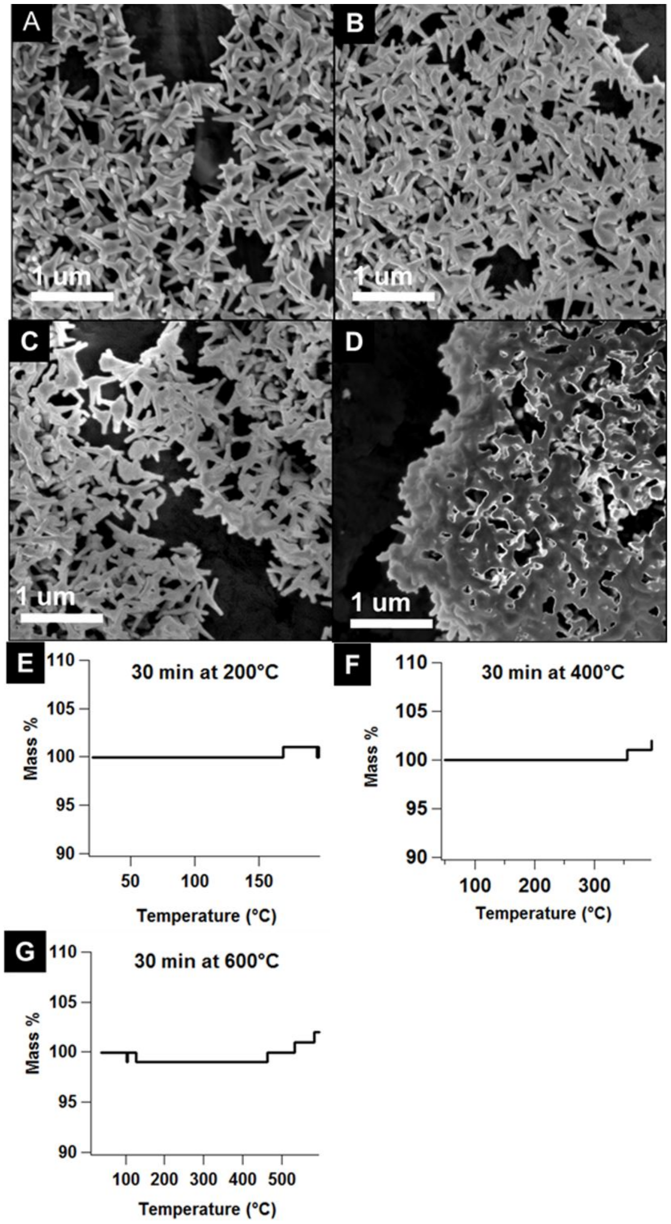

Figure 2.20: SEM images of multipods (8-cycles) (A) pre-TGA, (B) post-TGA after holding at 200 C for 30 min), (C) post-TGA after holding at 400 °C for 30 min, and (D) post-TGA after holding at 600°C for 30 min. TGA graphs for (E) sample at 200 °C for 30 min, (F) sample at 400°C for 30 min and (G) sample at 600°C for 30 min.

Results from the magnetic field-sweep studies carried out at 300K show that the anisotropic nature of the multipod arms influences the coercivity of the materials while maintaining a high saturation magnetization value (figure 2.19). The coercivity increases from 215 Oe (arm aspect ratio of 2.17) to 250 Oe (arm aspect ratio of 2.42) and finally 283 Oe (arm aspect ratio of 4.47) as the aspect ratio of the multipod arms increases. In comparison, spherical Ni fcc nanoparticles of 55 nm diameter synthesized in the lab exhibit a coercivity of only 109 Oe at 300 K. The values of coercivity at 300K for Ni multipods from the 8 cycle reaction is greater than many of the Ni nanostructures synthesized to date.[119, 141–144]

Catalytic reactions are often carried out at high temperature and the benefit of high surface area multipods are only applicable if the structures are stable. In order to probe the structural stability of the multipods at higher temperatures which are typically used for catalytic studies, a series of experiments were carried out where the multipod structures from the 300W 8-cycle reaction were thermally heated at 200 °C, 400 °C and 600 °C for 30 min in a thermogravimetric analysis (TGA) instrument and imaged by SEM post-treatment. The SEM images for the multipods pre- and post-thermal treatment show that the multipod morphology is maintained even at 400 °C without any observation of reconstruction to spherical morphology (figure 2.20). At 600 °C, the particles start to fuse with each other as ligand loss has taken place, and melting alongside surface reconstruction of the multipods seems to occur at this temperature.

2.4 Conclusion

Size-tunable nickel multipod structures were synthesized using a pulsed microwave heating approach that provided greater control over growth and produces good quality metallic nickel nanostructures with tight size distributions. Particle analysis by pXRD and TEM reveal pure fcc phase Ni structures with arms that grow along the <111> direction. The experimental results support that anisotropic growth control proposed is due to the pulsing of the microwave field as suggested in the proposed mechanism in Figure 2.1. Results from this work suggest a temperature difference between the multipod tips versus the rest of the nanoparticle achieved through selective heating of the tips during the pulse step of the reaction enables the arms to grow rapidly along the tip. During the pulsing step of the microwave, the tips of the multipods heat rapidly in comparison to the other parts of the nanoparticle owing to the lightning rod effect.[65–72, 123] Selective heating of (111) tips leads to increase in the surface mediated autocatalytic growth at the tip leading to the observed multipod structures. High power pulses provide greater differential temperature which impacts arm growth more significantly than total reaction time or average reaction temperature.

From the tapering of the multipod width from base to tip and single crystalline nature of the arms, the nanoparticle growth cannot be ascribed to oriented attachment of smaller nanoparticles formed at the initial stages of the reaction.

The use of MW power cycles to control multipod structures is advantageous as the synthesis approach uses only three reactants and can be carried out under ambient conditions within minutes. Synthesis times for even the largest multipods took less than 15 minutes with the cycled microwave approach. This cycled heating approach should apply to other material types and further illustrates the important role of microwave-matter interactions in the synthesis of materials using microwave-based heating. The catalytic properties of such highly branched structures with different arm sizes is currently being investigated.

CHAPTER 3

ELUCIDATING FACTORS CONTROLLING MULTIPOD MORPHOLOGY IN MICROWAVE-ASSISTED REACTIONS (PRECURSOR AND LIGAND CONCENTRATIONS AND TYPE, LIGAND RATIOS, MICROWAVE VESSEL TYPE AND STIRRING RATES)

3.1 Introduction

Anisotropic metallic nanoparticles exhibit improved properties for a number of applications including SERS, catalysis, EMI shielding and plasmonics.[68, 71, 106–115, 123–125] The majority of routes to synthesize such nanostructures are achieved through convectively heated bottom-up chemical approaches and require precise control of reaction parameters. Translating synthesis of such nanostructures to microwave-assisted heating routes can allow fast, reproducible and scalable production.[61] Microwave-assisted reactions have been shown to increase the reaction rates of many chemical reactions through efficient coupling of the MW field to MW absorbing solvents or reactants used, and microwave-matter interactions as the nanoparticle grows, will further impact the reaction pathway. The kinetics of a reaction impact the shape of nanostructures as described in section 1.4.2, and therefore one cannot assume that the every reaction using a convective-approach will also behave the same in a fast microwave-assisted heating setup.

In Chapter 2, the role of tip heating by the MW field via the 'lightning-rod effect' was shown to affect the growth of nickel multipods in a microwave reactor, and running the same reaction using convective heating was shown to result in different structures. The cycled-MW power approach to synthesize large aspect ratio arms is indeed more advantageous than extremely lengthy and multi-step reactions heated using convective methods. From the work done in literature, it is clear that a number of parameters influence the growth of anisotropic metallic structures including the metal used, choice and concentration of metal precursor, ligands, temperature and time. The efforts have allowed the expansion of anisotropic materials that can be made today, but a lot still remains to fully understanding and controlling anisotropic growth. The goal of the work in this chapter is to expand the understanding of anisotropic Ni multipod growth in a microwave reactor by investigating other factors that could affect the growth of the structures. In MW reactions that take minutes to complete, how critical is the concentration or type of the metal precursor, or ligand ratios and choices? What happens when the reaction takes place in a more convective-type of MW vessel (silicon carbide), or does stirring the reaction that is uniformly heated by a MW field play any role? Without understanding the influence of such parameters, translating the approach of nickel multipod growth in a microwave reactor to other materials might not work as expected.

The growth of metal nanoparticles using microwave-assisted heating has typically produced highly crystalline tight size-distribution spherical nanoparticles.[61, 62] A uniform temperature throughout the reaction solution leads to homogeneous nucleation resulting in tight size distributions.[145]

The literature on growth of anisotropic metallic nanoparticles in MW-assisted reactions however is limited. Tsuji et al. have synthesized gold nanoparticles with a high degree of twinning using a polyol process that produced a mixture of decahedral, icosahedral and plate-like structures.[62] The product population comprised of a mixture of shapes that could be tuned towards decahedron and icosahedron structures by increasing the gold salt and chloride ion concentrations. Humphrey et al. have synthesized Rh multipod structures using a microwave-assisted heating route using continuous flow setup in a multimode MW reactor. The populations are again not of tight size distributions and the particles are not tunable to a great extent [122]. In the case of nickel, icosahedral nanoparticles have been synthesized by Holmes et. al that showed enhanced magnetic properties.[141] Flower-like nickel nanostructures comprising of smaller nanoparticle aggregates have been also reported for a microwave-assisted synthesis method.[146] Most of the examples listed previously are typically aqueous-based or polyol-based reactions that do not produce the high quality anisotropic structures observed from organometallic precursor routes for anisotropic structures. Unfortunately, the solvothermal routes using organometallic precursors have not been carried out using MW reactors.

In this chapter, the results of reactions with changes in different reaction parameters carried out under cycled-MW power are presented. The sampling space of parameters includes organometallic precursor concentration and choice, ligand ratios and ligand types, microwave vessel type and mechanical stirring. It was expected that as the growth of nickel multipods is under a kinetic control regime, each of these parameters would affect the kinetics of the reaction. The precursor concentration and amount of reducing agent, OAm, would affect the nucleation and growth rates significantly. Despite having an excess (an order of magnitude) of reducing agent (OAm), the concentration of the Ni(acac)$_2$ was shown to influence the multipod evolution. Very high or very low concentrations produced spherical structures, while doubling the concentration from 0.083 M lead to multipods with lower aspect ratio arms and larger core sizes. The choice of metal precursor controls the ease of precursor reduction, which in turn will affect the reaction kinetics. Switching from Ni(acac)$_2$ to Ni(acetate)$_2$ did not have a profound impact on multipod structure, but the use of $NiCl_2$ resulted in large faceted nanoparticle that might have been as a consequence of strongly binding Cl^- ions in the solution. In terms of ligands, OAc is known to play a role in producing anisotropic structures, while both OAm and OAc have been shown to interact with the precursor and modify the kinetics. The ligand studies in this chapter showed that without using the pair of OAc and OAm, multipod generation was not possible. The OAm:OAc ratio was also critical in controlling shape, with a range of 5:1 to 3:1 V:V ratio of OAm:OAc giving multipods, and other ratios giving isotropic morphologies. Absorption spectra of the pre-reaction solutions for the ligand studies show that the nickel complex that undergoes reduction is not the starting Ni(acac)$_2$ hydrate precursor and is modified by coordination of OAm and OAc at the very beginning. These complexes react differently giving rise to a range of morphologies. While stirring has played a role in convectively-heated reactions, the impact it would have in a microwave-assisted reaction for Ni multipod growth was expected to be minor as the uniform heating within the microwave cavity would not be greatly influenced by stirring. Stirring did end up affecting the reaction dramatically, with higher stirring rates leading to loss of multipod growth in a 3 ml 4-cycle 300W reaction (10 ml vessel that cannot handle pressure generation with large number of cycles), but did not inhibit multipod growth as shown in a 9 ml 8-cycle 300W reaction (30 ml vessel). Stirring at 600rpm reduced the arm length by a factor of two approximately. Stirring experiments suggest that stirring increases the nuclei produced and therefore result in smaller multipod structures. From all the results so far, it can be concluded that cycled MW power does enable production of multipod morphologies for a set of reaction conditions, but other factors for the MW-assisted reaction do influence the final structure of the nanoparticles.

3.2 Materials and Methods

3.2.1 Materials

99%, nickel acetylacetonate hydrate ($Ni(acac)_2.xH_2O$), 99%, nickel acetate tetrahydrate ($Ni(acetate)_2.4H_2O$) 99%, nickel chloride ($NiCl_2$), oleic acid (OAc), oleylamine (OAm) technical grade 70%, tri-n-octylamine (TOA), 1-octadecene (ODE), toluene, methanol (MeOH), acetone and chloroform were purchased from Sigma Aldrich. The materials were used without further purification.

3.2.2 Synthesis of Nanoparticles

Nickel Precursor Concentration and Choice Effect. For the concentration studies, solutions of nickel precursor, $Ni(acac)_2$ (0.0415 M, 0.0834 M, 0.167 M and 0.334 M) with a 5:1 V:V ratio of OAm:OAc totaling to 3 ml was reacted. The blue reaction solution was degassed under vacuum with stirring at a temperature of approx. 100 °C for 30 min using a water bath until no more bubbling was observed prior to MW heating. The reaction was performed in a 2.45 GHz single mode Anton-Parr Monowave 300 microwave using a G10 (10 ml) Anton-Paar microwave vessel that was sealed with a silicone septa and snap cap. The nanoparticles were grown by heating the reaction to 280 °C using 300 W of microwave power followed by a 300W-4 cycle heating profile where the reaction temperature is cooled to 240 °C before applying 300W of MW power to heat the reaction to 280 °C for four consecutive times. (Note: for the 0.334 M solution, only 1 cycle of 300W MW power was applied to the reaction following the initial heating of the reaction to 280 °C as the reaction generates a significant amount of pressure (ammonia gas) due to the quantity of nickel generated through the reductive elimination mechanism of oleylamine with $Ni(acac)_2$).

Following the last on cycle, the solution is cooled to 55 °C and the nanoparticles isolated by magnetic separation, followed by three repeat toluene dissolutions, methanol precipitation, magnetic isolation, and finally drying the particles under vacuum. In the case of smaller particles that do not separate out magnetically, the nickel nanoparticles were precipitated by addition of 2mL toluene followed by 8 ml of methanol. The resulting solution was centrifuged for 5 min using a centrifuge tube. After removing the supernatant, the pellet was re-dispersed in toluene. To precipitate the NiNPs, excess methanol was added followed by isolation through centrifugation. For the precursor choice effect, the exact same conditions were used as listed above, but with fixing the

Ni precursor concentration at 0.083 M and varying the Ni precursor choice from the acac to the acetate or chloride compounds.

Ligand Ratios and Ligand Type Effect. Reactions for this set of experiments were carried out as described in the earlier section (for precursor effects) but the nickel precursor used was $Ni(acac)_2$ at 0.083 M and the ligand ratios for OAm:OAc were 1:0, 10:1 5:1, 4:1, 3:1, 2:1, 1:1, 1:5 and 0:1 V:V. An additional set of reactions were carried out for a 5:1 ratio where the OAm was substituted with TOA in one experiment (5:1 TOA:OAc) and another experiment where the OAc was replaced by ODE (5:1 OAm:ODE). All other reaction conditions were the same.

MW Vessel Type and Stirring Rate Effect. A 0.083 M $Ni(acac)_2$ solution made in a 5:1 OAm:OAc V:V ratio mixture (3 ml) was used under similar reaction conditions as described previously. For the vessel type studies, a 10ml SiC vessel (SiC10) and a 10 ml G10 vessel were used. For the stirring rate effect experiments, a 0.083 M $Ni(acac)_2$ in a 5:1 OAm:OAc V:V solution (3 ml) was added to a G10 vessel along with a 7 mm (L) x 2 mm (D) stirbar. MW reaction program was modified to set the stirring to different values (6 rpm, 60 rpm or 600 rpm). An additional set of studies was carried out using the same solution recipe in a G30 vessel with 9 ml of solution and an 8-cycle 300W heating program. A reaction with no stirbar was compared to a reaction with a stirbar, and a stir-rate of 600 rpm set on the instrument.

3.2.3 Transmission Electron Microscopy (TEM)

Nanoparticle samples were drop-cast, from toluene dispersion, onto 300 mesh carbon coated copper grids and left to dry under vacuum overnight. The TEM images were recorded using a JEM-ARM200cF electron microscope at 200 kV acceleration voltage.

3.2.4 Scanning Electron Microscopy (SEM)

SEM imaging was performed on aluminum mounts with nanoparticles drop-casted directly and allowed to dry. SEM imaging was performed on a FEI Nova NanoSEM 400 operating at 20 kV with a spot size of 4.0. The images were collected with an Everhart-Thornley detector (ETD).

3.2.5 UV-Vis Absorption Spectroscopy

Solution absorption spectra for various precursor solutions and ligands dissolved in different solvents (toluene, MeOH, deionized water) were taken using a Varian Cary 50 UV-visible spectrophotometer between 200 nm and 900 nm in a 1 cm quartz cuvette.

3.3 Results and Discussion

3.3.1 Effect of Nickel Precursor Concentration

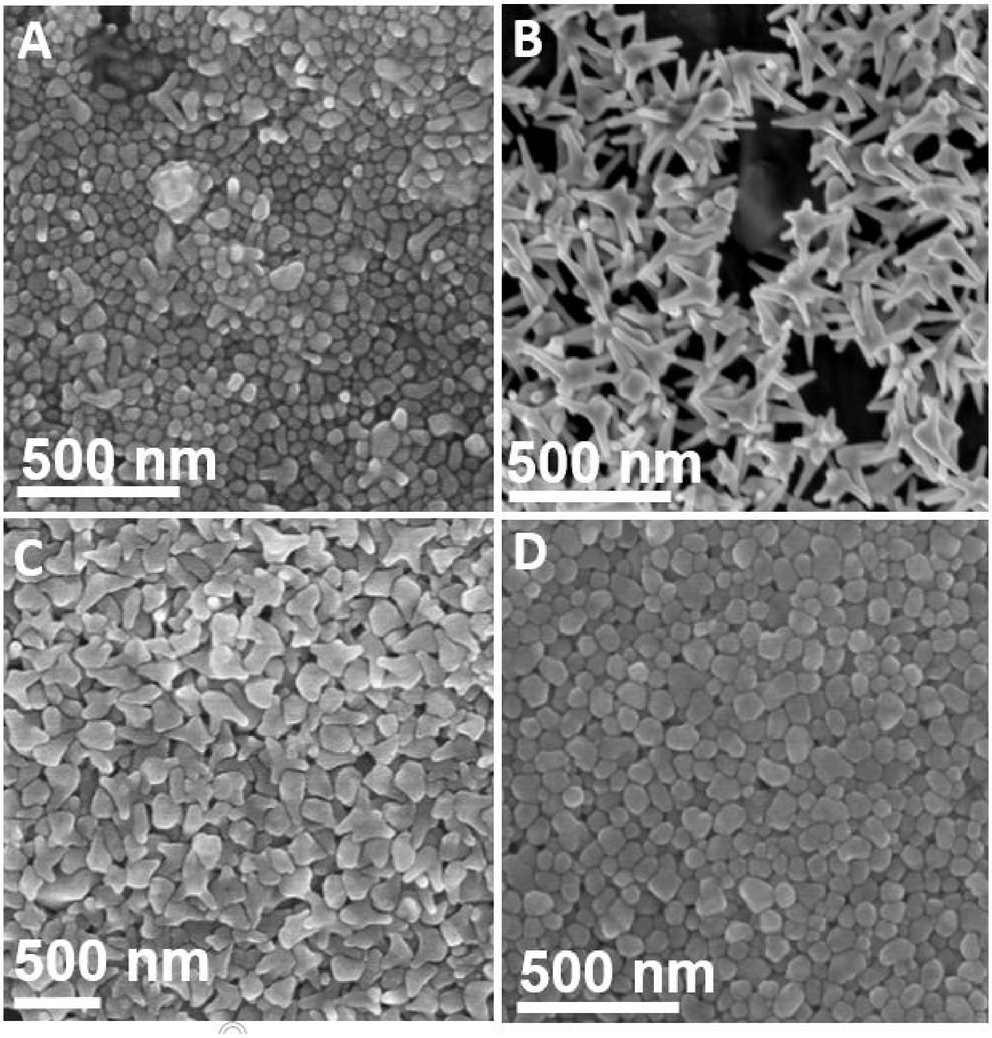

Figure 3.1: Effect of $Ni(acac)_2$ concentration on multipod morphology imaged using SEM. Reactions were carried out in a 5:1 V:V OAm:OAc ratio using (A) 0.0415 M, (B) 0.0834 M, (C) 0.167 M and (D) 0.334 M $Ni(acac)_2$.

One of the important parameters in nanoparticle synthesis is the concentration of the initial precursor. Concentration controls the rate of nucleation and growth, and the available material that will affect the final size of the nanoparticles. For an autocatalytic F-W growth mechanism, the concentration will impact the slow nucleation step and drastically affect the autocatalytic second step.[18] The results of decreasing the concentration two-fold, or increasing the concentration two-fold and four-fold from 0.0834 M impacts the nickel multipod structure significantly as shown in 3.1. At a concentration of 0.0415 M, the reaction produces spherical nanoparticles of diameter 44 ± 8.2 nm primarily while at 0.334 M (only 1 cycle 300W instead of 4-cycle 300W) the particles are also spherical with diameter of 55 (± 12) nm (figure 3.1). The reaction using 0.083 M produces multipods with small cores and high aspect ratio (2.2) arms of length 73 (± 27) nm and width 33 (± 5.9) nm in comparison to the reaction at 0.167 M that give larger core size multipods with smaller aspect ratio (1.4) arms of length 87 (± 21) nm and width of 62 (± 8.5) nm. The size analysis of the structures is shown as histograms in figure 3.2. In all cases however, the morphology of the nanoparticles seems to be quite uniform. It should be noted that in these reactions, while the concentration of the nickel precursor is changing, the ratio of the two ligands, OAm and OAc in the reaction is kept the same, and the concentrations for both are still an order of magnitude more than the nickel precursor even at the highest concentration of metal precursor. This means that the rate of reaction is significantly affect by subtle changes in the concentration of the metal precursor and not because the ratio of the precursor to the ligands is changing drastically. The fact that the reaction rate increases significantly at 0.334 M $Ni(acac)_2$ concentration (that only allows 1 cycle of 300W because of significant ammonia pressure) with the fixed concentration of reducing agent (OAm at 5.56 M) implies that the nickel precursor is the limiting reagent. Another possibility as to why the highest and lowest concentrations studied do not lead to multipod morphology is a total monomer (Ni^0) concentration and amount argument. At very low nickel precursor concentrations, the rate of nucleation is reduced due to a low monomer concentration, and the same low precursor availability prevents increase in nanoparticle size as the reaction is depleted of precursor. On the other hand, when the concentration of the precursor is very high, the rate of nucleation increases and availability of high precursor and monomer concentration in solution leads to rapid isotropic growth of the nanoparticles (through rapid addition on all nanocrystal facets) leading to spherical structures.

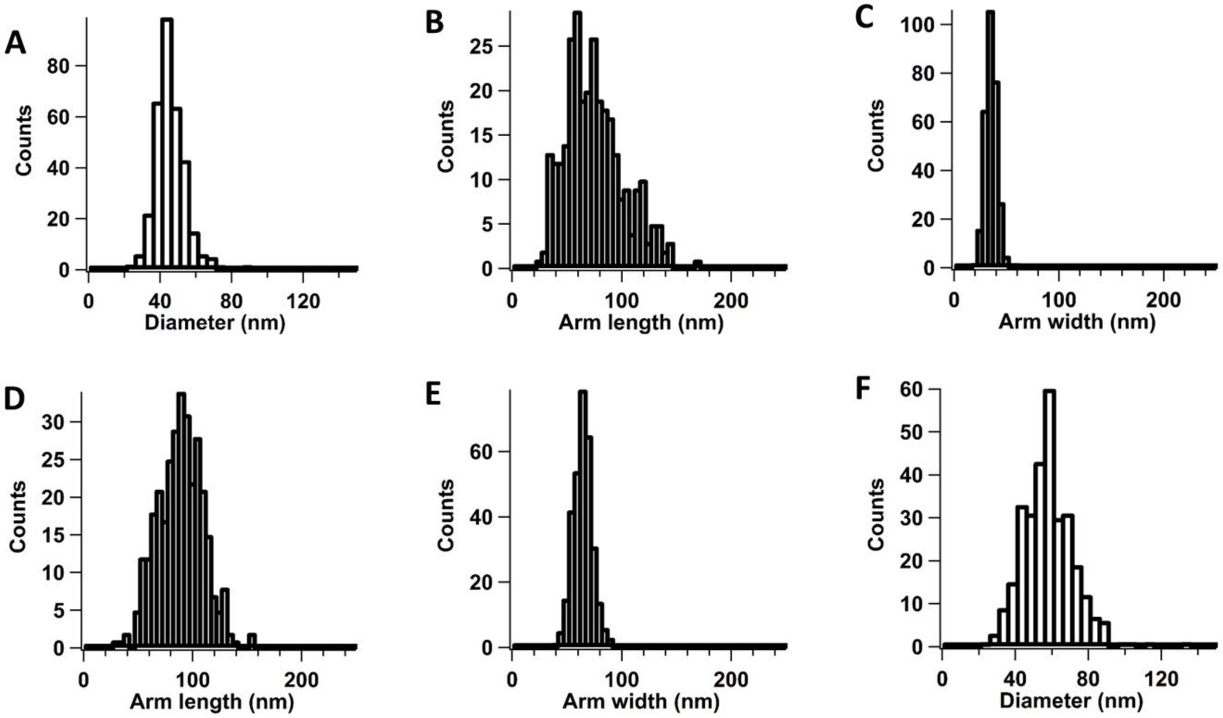

Figure 3.2: Size analysis of nanoparticles grown using different Ni(acac)$_2$ concentrations. (A) Diameter of spherical particles produced using 0.0415 M Ni(acac)$_2$, (B and C) arm length and arm width distribution of arms on nanoparticles produced using 0.0834 M Ni(acac)$_2$, (D and E) arm length and arm width distribution of arms on nanoparticles produced using 0.167 M Ni(acac)$_2$, and (F) diameter of spherical particles produced using 0.334 M Ni(acac)$_2$.

Unfortunately, the rate of reaction using 0.334 M was so high that it was not possible to evaluate if continuing the reaction for longer would result in multipod morphology at the end of 4 cycles of 300W power. The results from the concentration study are consistent with literature reports where kinetic control of anisotropic structures is affected by initial concentration of precursor.[4] The results of the precursor concentration studies under cycled microwave power show varied morphologies of uniform size, and add another parameter to control morphology of nickel multipod structures.

3.3.2 Effect of Nickel Precursor Choice

The next parameter investigated to fully comprehend the morphology control of nickel multipods in a fast microwave-assisted heating approach was the choice of the starting metal precursor.

Skrabalak et. al have shown that in the case of Pd nanoparticles, substitution of the metal precursor in convective reactions does change the reactivity of precursor.[51] The reactivity in turn will control how easily the metal ion can get reduced by the reducing agent as well as the ease at which it can be reduced at the autocatalytic surface of the growing nanoparticle. Another subtle effect that can take place is the shape-directing effect of the precursor complex ligands during the reaction after they dissociate from the metal ion or are displaced by the ligands in the solution (in this case OAm or OAc). For example, Xia et. al have demonstrated the facet-selective affinity of chloride and bromide ions that leads to control of selective surface growth on facets, edges or corners of initial nanocrystal seed.[42] As metal nanoparticle shape control using microwave-assisted heating is not vastly studied, it is justifiable to investigate how such precursors react under fast microwave heating, especially under cycled microwave power. Another difference between convective and microwave-assisted reactions is that the precursors used in the reaction can have different microwave absorption cross-sections which in turn will affect the reaction rates as shown in the past by the Strouse group.[147] Results from changing the starting precursor from Ni(acac)$_2$ to Ni(acetate)$_2$ or NiCl$_2$ are shown.

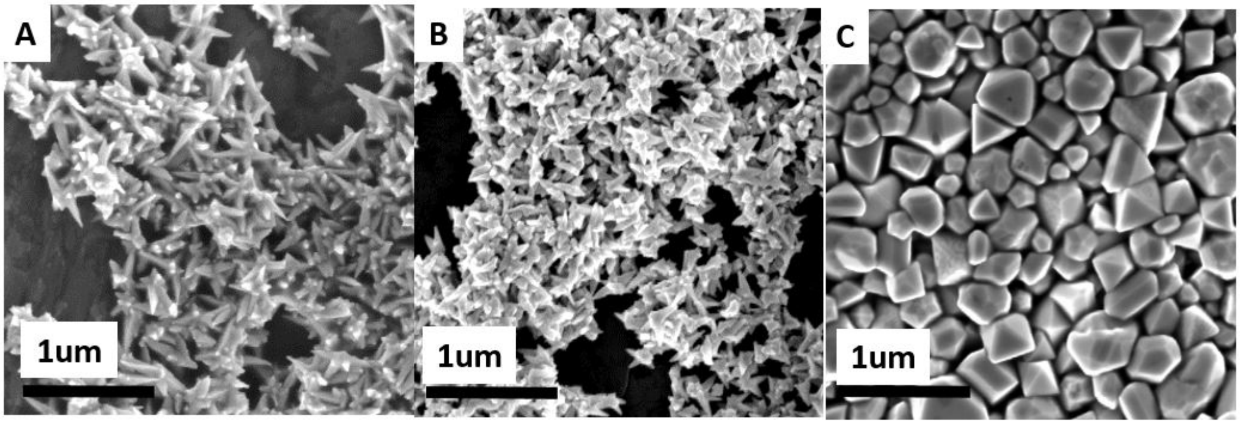

Figure 3.3: Effect of Ni precursor choice on multipod morphology imaged using SEM. Reactions were carried out in a 5:1 V:V OAm:OAc ratio using 0.083 M of (A) Ni(acac)$_2$, (B) Ni(acetate)$_2$ and (C) Ni(Cl)$_2$

In figure 3.3, the formation of multipods is achieved by use of either the Ni(acac)$_2$ or Ni(acetate)$_2$ precursor but not in the case of using NiCl$_2$ which produces a distribution of faceted morphologies of a wide size range (100 - 600 nm diameter). Particle analysis in figure 3.4 for the nanoparticles shows that the acetate precursor produces multipods with arm aspect ratio of 2.36, average length of 111 (± 18) nm and width of 47 (± 9.2) nm. These arms are larger than those produced using the acetylacetonate precursor (aspect ratio of 2.2, average length of 73 (± 27) nm and width of 33 (± 8.9) nm.

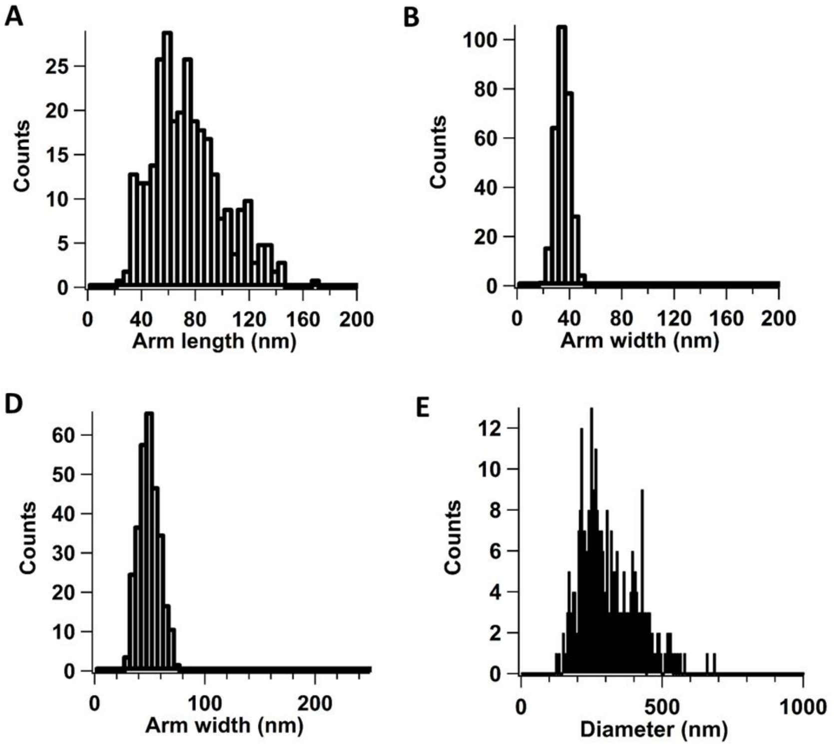

Figure 3.4: Size analysis of nanoparticles formed using different Ni precursors. (A and B) Arm length and arm width of multipods formed using $Ni(acac)_2$, (C and D) arm length and arm width of multipods formed using $Ni(acetate)_2$ and (C) diameter of faceted particles formed using $NiCl_2$

Absorption spectra for the pre-reaction solution for each type of precursor diluted in toluene shows an identical spectrum suggesting similar complexation upon addition of a 5:1 V:V ratio of OAm:OAc to the different nickel precursors. This suggests that the reaction starting with $NiCl_2$ might release Cl^- ions when the Ni^{2+} ion coordinates with the amine group of OAm and acid group of OAc. The Cl^- may affect the initial seed morphology and eventual facet stabilization of the growing nanoparticle. Generating anisotropic structures is a complex process with multiple parameters, including precursor choice. Despite heating under cycled MW power, the nanoparticle morphology is significantly affected by the type of metal precursor. Techniques to isolate and identify the actual species in the pre-reaction solution and during the reaction would greatly aid in the understanding of the growth mechanism.

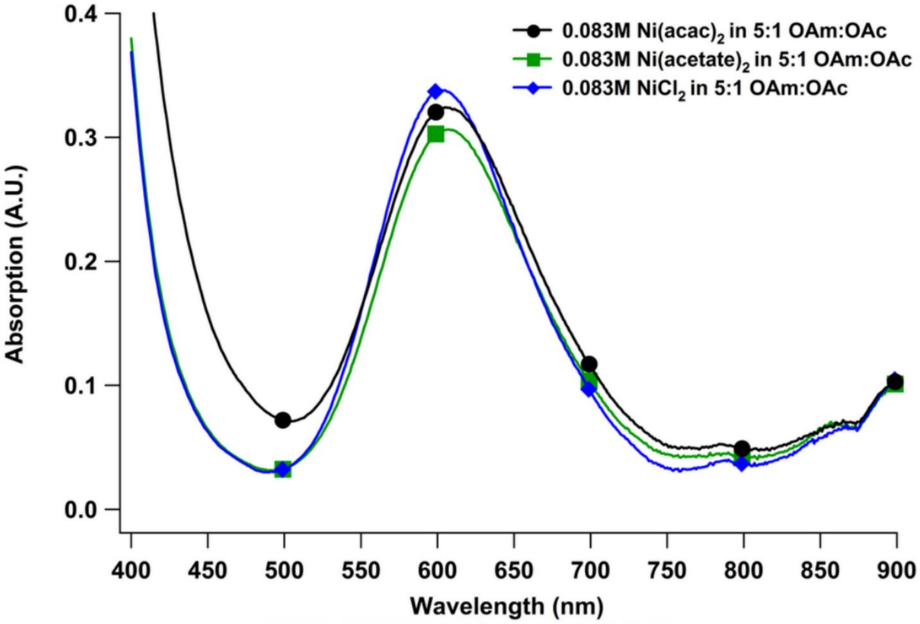

Figure 3.5: UV-Vis absorption spectra of pre-reaction solution formed using different Ni precursors (0.083 M) in 5:1 V:V OAm:OAc (diluted in toluene). Spectrum of (A) Ni(acac)$_2$, (B) Ni(acetate)$_2$ and (C) NiCl$_2$

.

3.3.3 Effect of Ligand Ratios and Types

As shown in Chapter 2 and earlier part of this chapter, the use of a 5:1 V:V ratio of OAm:OAc containing Ni(acac)$_2$ at 0.083 M results in the production of multipod nanostructures which are well controlled using cycled MW power. This section focuses on the role of the ligands, OAm and OAc, in the shape-control of multipods in the microwave-assisted approach. OAm and OAc are two of the most widely used chemicals in nanoparticle synthesis but their exact roles are still not well understood when it comes to morphology control. Both structures are 18-carbon compounds with a double-bond present in the chain and a terminal functional group (NH_2 for OAm, COOH for OAc). Marzan et. al have published a review article on the role of OAm in nanoparticle synthesis where the use of OAm in different nanoparticle synthesis is discussed.[148] As mentioned in the review, OAm can act as a high temperature solvent, a mild reducing agent, a capping agent/surfactant, or either two or all of the roles depending on reaction conditions.[148] In one instance, it was shown that not only is the amine group important, but also the double-bond present in OAm for controlling the twinning of gold nanoparticles.[149].

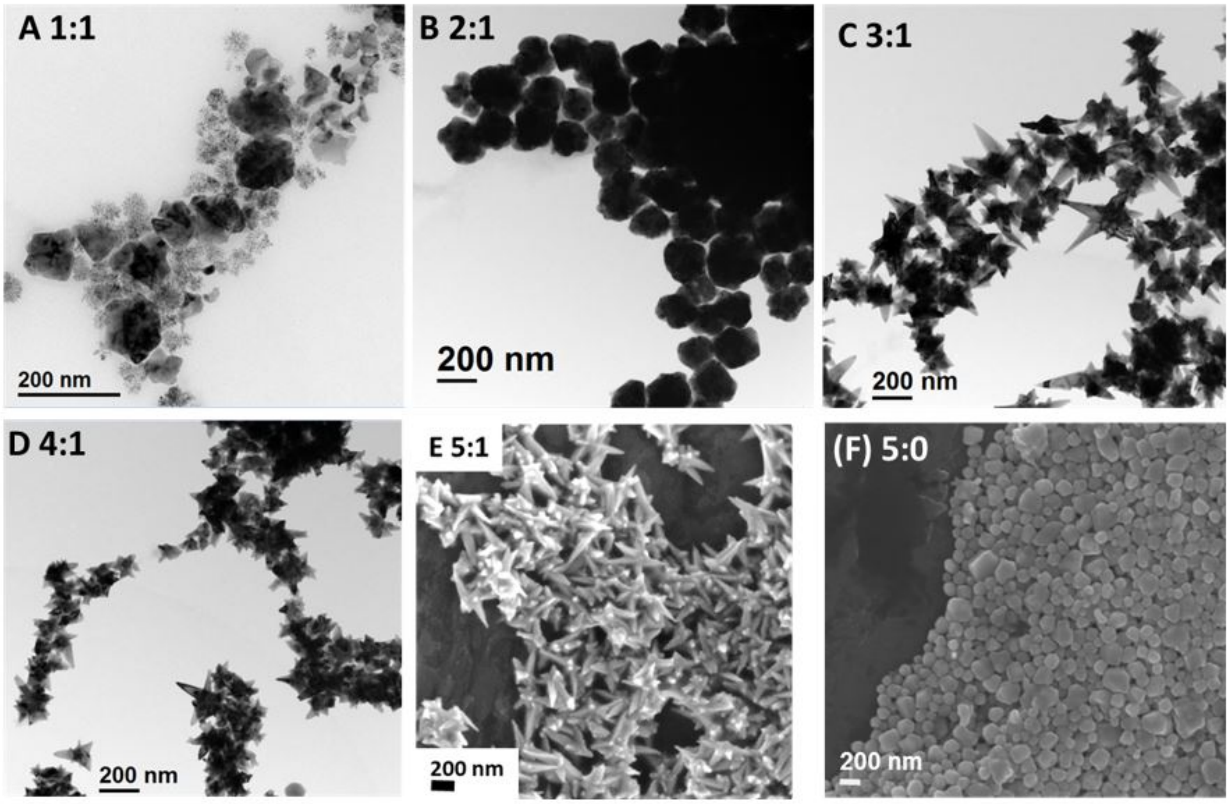

Figure 3.6: Effect of OAm:OAc ratio on multipod morphology imaged using TEM and SEM. Reactions were carried out in a in different OAm:OAc V:V ratio while keeping the $Ni(acac)_2$ concentration at 0.083 M. Particle morphology for (A) 1:1 , (B) 2:1, (C) 3:1, (D) 4:1, (E) 5:1 and (F) 1:0 OAm:OAc ratios. Reaction using 0:5 OAm:OAc ration gave no product. Note: The reaction for 1:0 required 3 rounds of 300W-4 cycle reactions to produce a reasonable quantity of product.

Further understanding of how exactly OAm can reduce the widely used metal acetylacetonate precursors was shown by Park et. al in an article looking at formation of cobalt nanoparticles. [150] With the introduction of OAc into reaction systems containing OAm and organometalic precursor, a number of parameters are modified which affect the resulting nanoparticle structure. Tilley et al. have shown that difference in binding affinity of OAm and OAc to a palladium surface results in a change in ability of monomer addition to the nanoparticle surface.[54] When OAc is present, highly branched Pd structures are formed due to kinetic control that is absent in a system of only strongly binding OAm. More recently, Yang et. al have suggested that the presence of OAm and OAc will produce populations of platinum complexes that have different reduction potentials.[52] The study suggests that $acac^-$ ligands can be substituted by OAm and OAc, and in complexes containing OAc, the fast surface autocatalytic reduction step is switched off, leading to a slow growth rate. Unfortunately, the study was unable to identify what exact Pt complexes were formed by MALDI-TOF MS. Two other articles look at how the pair of OAm and OAc interact with one another in controlling shaping of oxide nanoparticles.[151, 152] The research work to date in nanoparticle shape and size control implies the complexity of nanoparticle synthesis and validates the need for more scrutiny on exactly how two molecules like OAm and OAc can dramatically impact nucleation and growth kinetics.

To understand the role of OAm and OAc, a series of experiments were carried out where the ratio of the two compounds were varied while keeping the nickel precursor ($Ni(acac)_2$) constant. The ratio of OAm:OAc was varied from 5:1 to 1:5 V:V as well as having solutions of either pure OAm (1:0) or pure OAc (0:1). The molar ratio of each ligand to the Ni precursor ranged from 30:1 down to 6:1 in all cases except the single ligand cases where the ratio (ligand:precursor) would be 38:0. Lastly another two sets of reactions were carried out where the primary alkylamine (OAm) was substituted with a tertiary amine, tri-octylamine (TOA) in the first case, while in the second case, the OAc was substituted by 1-octadecene.

Figure 3.6 show the results from the ligand ratio studies using OAm and OAc. Decreasing the ratio of OAm:OAc from 5:1 that produces multipod morphology, leads to an eventual loss of multipod structure at 2:1 ratio. The ratio of 4:1 and 3:1 do produce multipods, however they are not well defined and as uniform as those produced using a 5:1 ratio. At 2:1, large faceted Ni nanoparticles are formed while at 1:1, there is a mixture of irregularly shaped nanoparticles comprising of nickel and nickel oxide. Reactions where ligand ratios had higher OAc amounts compared to OAm did not produce Ni nanoparticles under the same reaction conditions (including time/number of MW power cycles). This is consisted with the argument that Ni nanoparticle formation requires the reduction of the precursor by OAm, which is a limiting agent at low OAm:OAc ratios, or that the precursor complex formed in excess OAc does not get reduced easily as suggested by Tilley et al.[54]

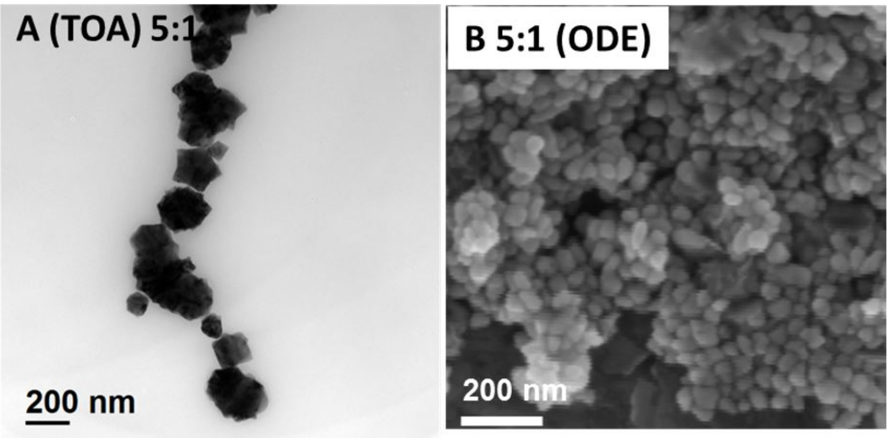

Figure 3.7: (A) Effect of substitution of the primary amine ligand (OAm) for a tertiary amine (TOA) and (B) Effect of substitution of the oleic acid ligand (OAc) for a non-functionalized ligand (1-ODE)on multipod morphology imaged using SEM. Reactions were carried out using a 5:1 ratio of ligands while keeping the Ni(acac)$_2$ concentration at 0.083 M.

Results for a reaction where the OAm was substituted by a tertiary amine, TOA, show that the morphology of the nickel nanoparticle is completely changed as shown in figure 3.7A. The use of TOA with OAc produces irregular nanostructures of varying sizes, with some being faceted. TOA will have a different reduction rate owing to its tertiary amine structure, and possibly have a different surface packing structure on the growing nanoparticle alongside the OAc present. The surface packing would affect accessibility for monomer addition or surface-mediated reduction of precursor. On the other end, elimination of OAc from the reaction leads to loss of multipod morphology loss as shown in figure 3.7B. OAc therefore is a critical component as well in the synthesis of the multipods. To further investigate the ligand effects, absorption spectra of pre-reaction solutions consisting of metal precursor mixed with different ligand ratios were taken (diluted in toluene).

From figure 3.8, it is clearly evident that the nickel complex formed through addition of $Ni(acac)_2$ to solutions with different OAm:OAc ratios is not the same.

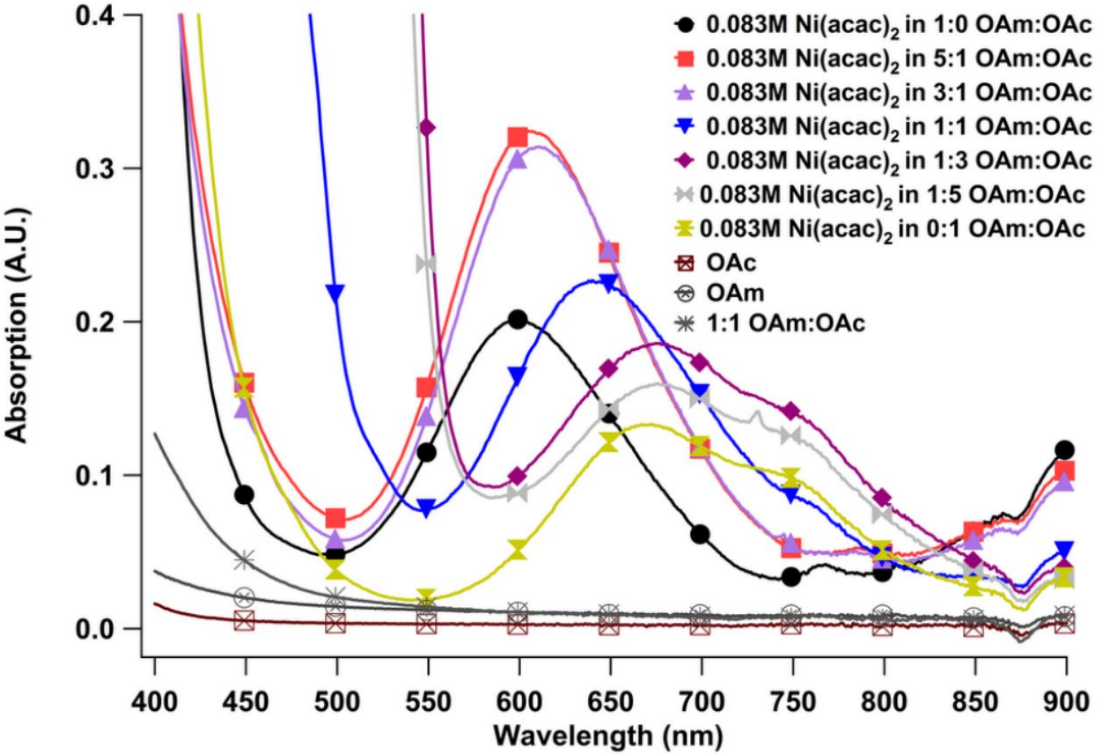

Figure 3.8: Absorption spectra of a 0.083 M $Ni(acac)_2$ solution made in different OAm:OAc ratio pre-reaction solution diluted (3x dilution factor) in toluene. Spectra of OAm only, OAc only, and 1:1 OAm:OAc in toluene is also shown.

The solvents by themselves (or a 1:1 V:V mixture) do not show any absorption features between 500 nm and 900 nm when added to toluene, but the $Ni(acac)_2$ complexes do exhibit features. $Ni(acac)_2$ in pure OAm shows a peak at 600 nm and a possible other peak forming at >900 nm, while $Ni(acac)_2$ in pure OAc exhibits a two-peak absorption feature with peaks at 660 nm and 750 nm. Solutions of the $Ni(acac)_2$ in ratios of the two ligands show characteristics of the complexes made in the individual ligands, however the absorption intensities of the peaks were not simply a weighted sum of the $Ni(acac)_2$ complexes in the two individual ligands. This suggests that the complexes formed in a mixture of OAm and OAc are different.

Obtaining a spectrum of the Ni(acac)$_2$ without any OAm or OAc was possible in polar solvents like water and methanol. Spectra of the Ni(acac)$_2$ complex in water, in MeOH, as well those formed in pure OAm, pure OAc and pure TOA with dilution in toluene is shown in figure 3.9. The spectra of the Ni(acac)$_2$ in water and MeOH were background corrected for the respective solvent.

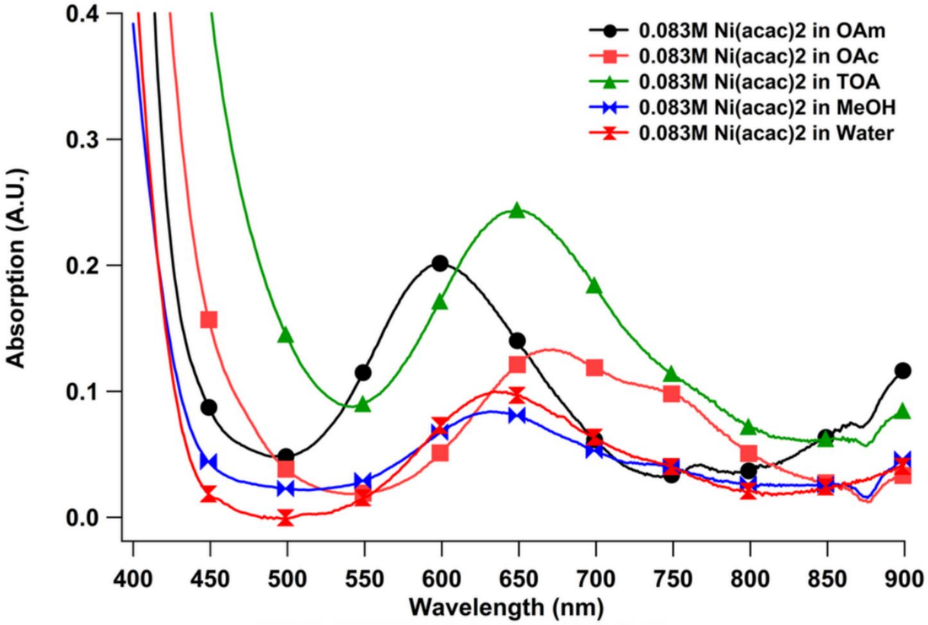

Figure 3.9: Absorption spectra of Ni(acac)$_2$ solutions made with different solvents (water and methanol (MeOH)). Spectra of Ni(acac)$_2$ dissolved in either pure OAm or OAc, and diluted in toluene is shown for comparison.

From this set of spectra in figure 3.9, it is seen that the Ni(acac)$_2$ which is a hydrated complex, in water shows a two-peak feature centered at 640 nm and 750 nm, similar to that in pure MeOH. A blue-shift is observed when complexed with OAm while a red-shift is observed when complexed with OAc. The shift of the 640 nm peak of Ni(acac)$_2$ when complexed with TOA is not as significant as that with OAm, and does appear to be slightly red-shifted. It should be noted here that as these spectra are collected in different solvents (water, MeOH or toluene), peak shifts can also occur when absorption spectra are taken in different solvents.[153] Once again, these results suggest that the OAm and OAc are not merely reducing or capping agents during the reaction, but impact the reaction system even before the reaction has started.

It is surprising that the complexation of OAc and OAm on metal precursors and characterization of the pre-reaction solution to produce nanoparticles has been overlooked considering the extensive use of these two molecules in the nanoparticle synthesis field. It is known that the thermal stability of metal precursors will be affected by the ligand groups[154], which is indicative of binding strength and will therefore also affect reactivity. While the results in this section may not provide a complete picture, it does reveal details about ligand factors affecting nanoparticle growth that supplement the knowledge on the topic. The experimental data advocates a greater attention to understanding the species in the pre-reaction solution if we are to fully understand nanoparticle synthesis pathways. It would be ideal if the pre-reaction solutions could be analyzed easily and quantitatively with more than simple absorption spectroscopy.

3.3.4 Effect of Microwave Vessel Type: Glass versus Silicon Carbide

Microwave-assisted heated reactions as shown in Chapter 2 can be more versatile than convectively-heated reactions as the microwave reactor allows greater control over heating rates and temperature profiles by the use of modulating microwave power and active air-cooling enabled by the system. For efficient microwave heating of reactants, a microwave-transparent vessel is preferred. In certain cases, the use of a microwave-absorbing material like silicon carbide (SiC) for the vessel type in a microwave-assisted reaction may allow for a more-convective like heating behavior but with the ability to ramp up the reaction at a much faster rate than using convective heating. The SiC vessel is not 100% microwave-absorbing however as shown by Ashley et al. but does heat up faster and reduces the MW field penetration by ∼15% compared to a borosilicate vessel (glass).[155] The effect of using a SiC carbide vessel (that would provide a faster heating rate) on nickel multipod evolution was investigated. Reactions in a 10 ml glass vessel and a 10 ml SiC vessel under cycled MW power were compared. The products of the two reactions are shown in figure 3.10.

It can be seen that the reaction in the glass vessel produces multipod structures but the SiC vessel gave rise to a mixture of morphologies, including spherical particles, multipods with short arms and a number of large flat sheet-like structures. Reason for the poor size and shape control in the SiC vessel might be attributed to a thermal gradient created in the SiC vessel from the hot inner surface of the vessel wall to a cooler region in the center of the vessel due to the high thermal conductivity of SiC and lower microwave energy penetration into the solution. The thermal conductivity of SiC would not only heat the vessel fast but allow it to cool down faster in a cycled

MW power heating experiment. As expected, with a lower MW field penetration into the reaction, the effectiveness of tip heating via the 'lightning-rod effect' is reduced in the SiC vessel, leading to the formation of a majority population of spherical nanoparticles.

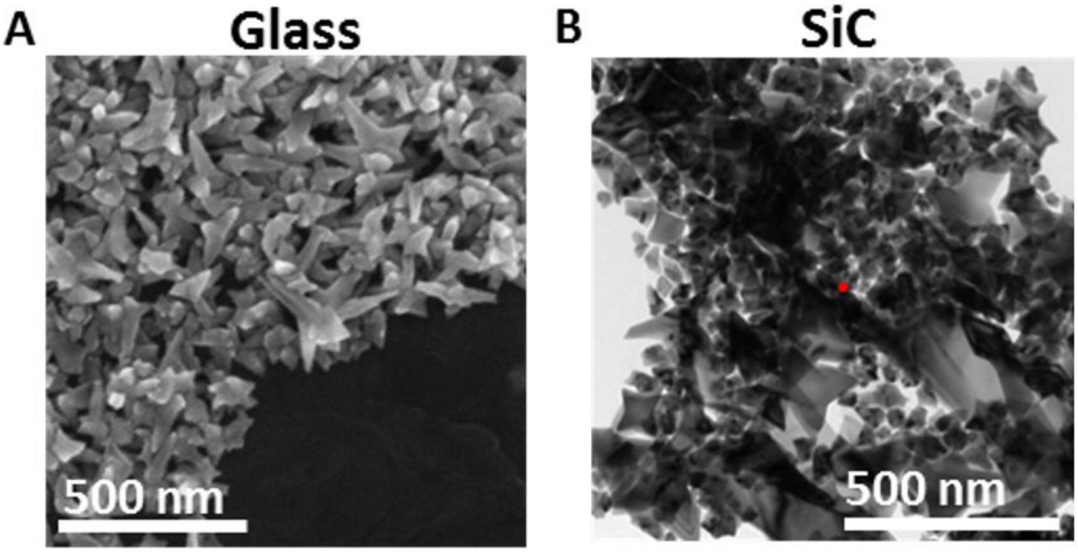

Figure 3.10: (A) SEM of multipod structures formed after reaction in a glass MW vessel and (B) TEM of spherical and sheet-like nanostructures formed after reaction in a SiC MW vessel. Reactions were carried out using a 5:1 V:V ratio of OAm:OAc while keeping the Ni(acac)$_2$ concentration at 0.083 M.

3.3.5 Effect of Stirring Rate on Multipod Evolution

The excitement in the field of anisotropic nanoparticles in the last two decades has led to an in-depth investigation of understanding their growth as summarized in section 1.4.2. As described earlier and shown in this chapter so far, many factors can influence the morphology of nanostructures. One factor that is not well studied is the effect of stirring the reaction solution. Some of the synthesis processes are still not well understood. A handful of papers focus on looking at the specific effect of stirring or agitation on nanoparticle growth.[56–59] Opposite effects are seen in the case of nanorods, where Landman et. al in 2013 show high-frequency stirring produces anisotropic growth of silver nanorods, while Piquemal et. al in 2017 show that stirring rates greater than 150 rounds per minute (rpm) lead to short aspect cobalt nanoparticles with greater structural disordered.[56, 57]. Kaner et. al were the first to show that stirring or shaking leads to nanoparticle collisions and aggregated structures in their work with polyanaline (PANI) nanofibers in 2006 [59], while He et. al emphasize that arrow-head palladium tripods only form in unstirred solutions that allows the formation of a diffusion gradient enabling addition to the nanoparticle tips.[58].

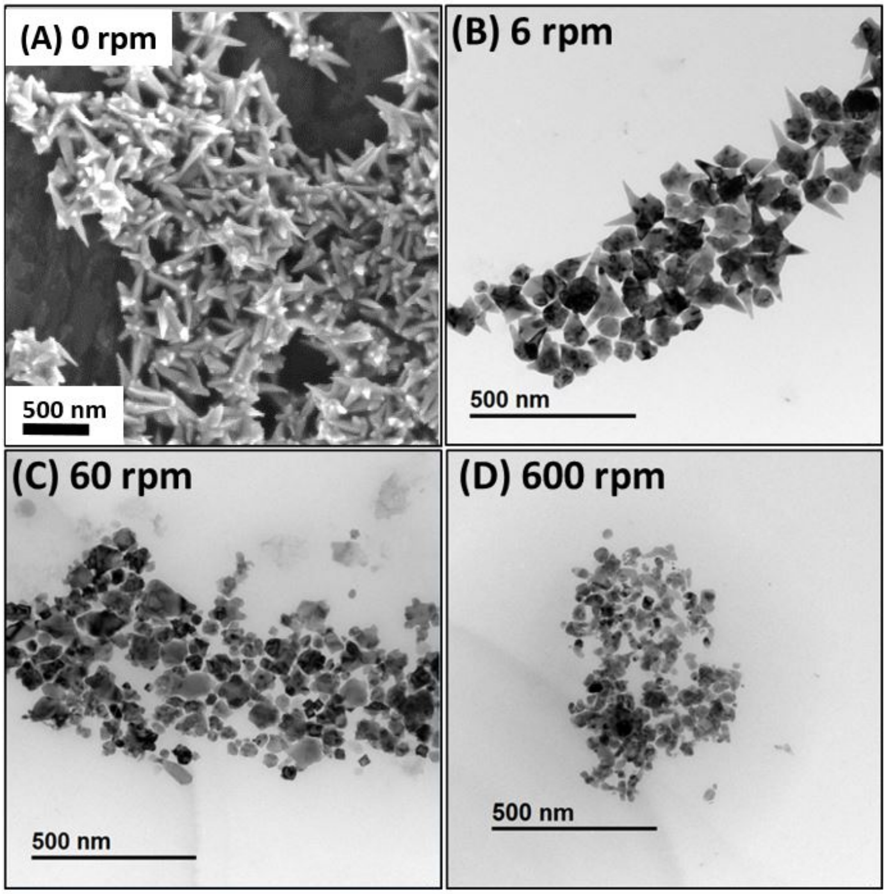

Figure 3.11: Effect of stirring rate on Ni multipod evolution. Particles produced with a stirring rate of (A) 0 rpm, (B) 6 rpm, (C) 60 rpm and (D) 600 rpm and imaged using TEM (except (A)). Reactions were carried out using a 5:1 V:V ratio of OAm:OAc while keeping the $Ni(acac)_2$ concentration at 0.083 M.

The diffusion argument in the work by He et. al in 2015 is based off the work by Murray et. al in 2012 where the shape-directing ability of different metal carbonyls on Pt nanostructures. The growth of several anisotropic structures using reducing of organometallic precursors with dihydrogen gas or carbon monoxide (CO) in literature fail to clearly describe whether the reactions were carried out under agitated conditions or not. As growth of anisotropic structures are typically carried out at low temperatures and take advantage of enabling growth off of certain crystalline facets, it could be presumed retrospectively from the work in Chapter 2 that they were grown under non-agitated conditions. The results of stirring microwave-assisted reactions that produce Ni multipods is shown in this section. Reactions carried out in a 10 ml glass vessel using a 5:1 V:V ratio of OAm:OAc with 0.083 M Ni(acac)$_2$ under cycled MW power (4 cycles of 300W) using different stirring rates produce nanoparticles as shown in figure 3.11. The effect of stirring is significant. As the stirring rate is increased, the formation of multipods decreases and the nanoparticle sizes get smaller. The structures are all multipods with no stirring, while increasing the stirring to 6 rpm leads to a mixture of multipods with large cores and faceted nanoparticles. At 60 rpm, the population of nanoparticles consists of some irregularly shaped structures exhibiting overgrowth and a large population of cubic shaped nanoparticles. At 600 rpm, the nanoparticle population comprise a range of sizes that contain small spherical particles, irregular shaped particles as well as some worm-like structures. The observations suggest that stirring the affects the nucleation and growth process of the multipods.

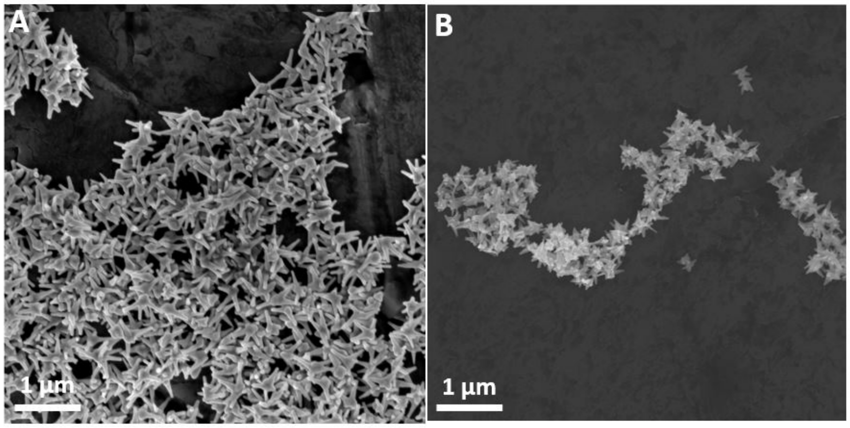

Figure 3.12: SEM of multipod structures formed (A) without stirbar and (B) with a stirbar and stirring rate of 600 rpm in a G30 glass vessel using 300W-8 cycle heating program. Reactions were carried out using a 5:1 V:V ratio of OAm:OAc while keeping the Ni(acac)$_2$ concentration at 0.083 M.

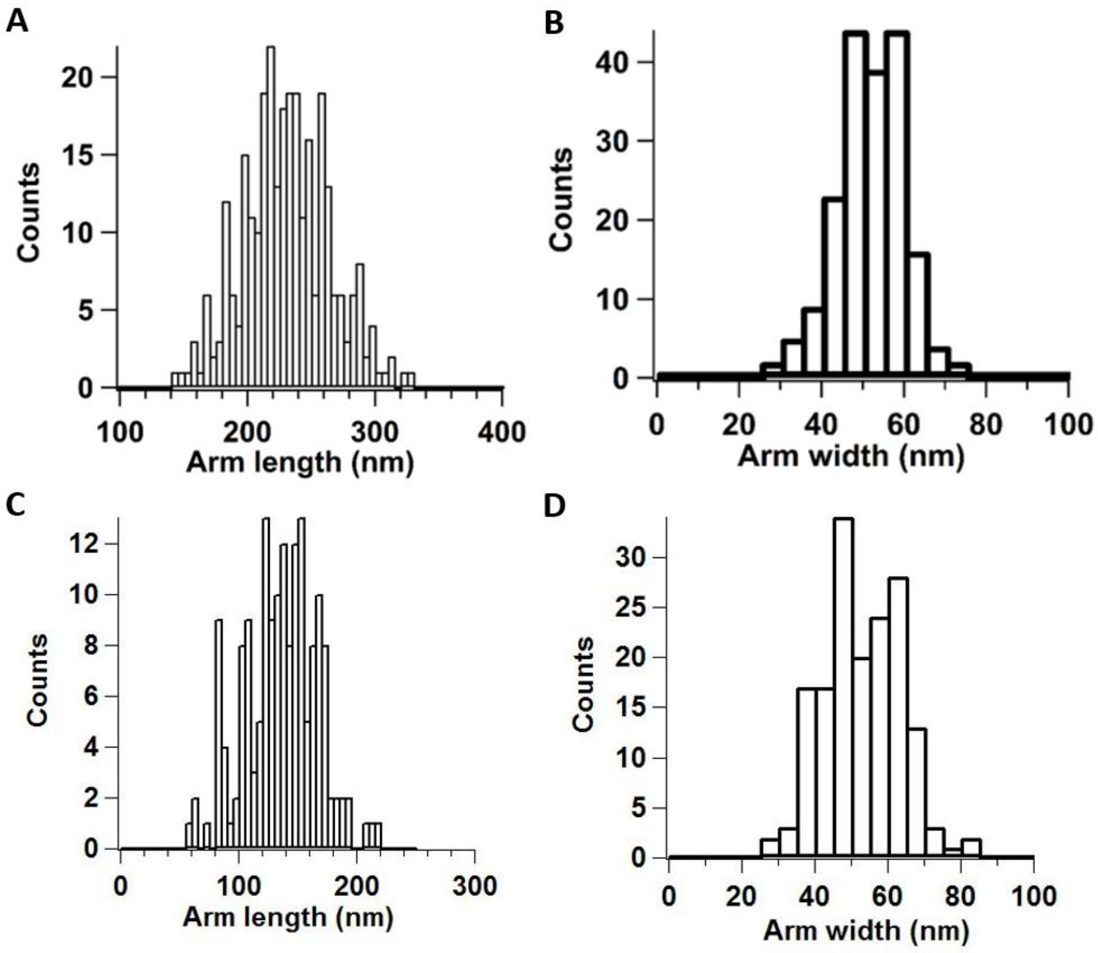

Figure 3.13: Effect of stirring on multipod reaction in a G30 glass vessel using 300W-8 cycle heating program.(A) Arm length and (B) arm width distributions of multipods synthesized without stirbar. (C) Arm length and (D) arm width distributions of multipods synthesized with stirbar and a stirring rate of 600 rpm. Reactions were carried out using a 5:1 V:V ratio of OAm:OAc while keeping the Ni(acac)$_2$ concentration at 0.083 M.

Cubic structures formed even at 60 rpm indicate that the stirring does not change the seed morphology leading to overgrowth and multipod formation but might affect the nucleation rate. If the nucleation rate is increased by increased atomic collision through stirring, the amount of metal precursor left for overgrowth is reduced. This would produce more nanoparticles of smaller sizes. The data collected so far cannot prove whether this is the case, but the question of whether the stirring inhibits multipod morphology through the 'lightning-rod effect' is answered through a second set of experiments carried out in the G30 vessel. The G30 vessel allows the reaction to be carried out for longer using an 8-cycle 300W program without the risk of vial rupture. In figure 3.12, multipod formation is observed with no stirring and with stirring at 600 rpm as well. In the case of the stirred reaction, the multipod structures are however much smaller in size compared to the non-stirred condition. Size analysis of the multipods for this set of reactions is shown in figure 3.13. The average arm length and arm width for the multipods produced with stirring are 135 (± 30) nm and 52 (± 12) nm respectively while those for the un-stirred reaction are 228 (± 33) nm and 51 (± 8.2) nm for arm length and arm width respectively. The multipod arm length under stirred conditions at 600 rpm is approximately half of the arm length under non-stirred conditions while the widths are similar. Assuming complete consumption of precursor, the difference in the sizes imply different number of particles in the two situations.

3.4 Conclusion

While nickel multipod morphology and size distribution is affected by the cycling of MW power, it is one of the many factors at play in the shape-control of the multipods. To deduce the intricate details of the growth mechanism and interplay of all factors, analysis of the complete parameter space is vital. An attempt to fully understand anisotropic Ni multipod growth was made by investigating the concentration of the metal precursor, the choice of metal precursor, the OAm:OAc ratio and the importance of each ligand, the MW vessel type, and the stirring rate of the reaction. Results from the experiments with different concentrations and types of nickel precursor and ligands suggest changes in the kinetics of the reaction which eventually impacts morphology of the resulting nickel nanostructure. Very low or high concentrations of the precursor lead to a loss of anisotropic multipod morphology while the choice of metal precursor complex may add new species to the reaction mixture that may affect shape evolution. Both OAm and OAc were shown to be essential in shaping the nickel nanostructures, and their influence in modifying the initial $Ni(acac)_2$ complex pre-reaction was noted by absorption spectroscopy which impacted the reaction end-products. A more convective style of heating and lower MW penetration in the SiC MW vessel in comparison to glass led to poor morphology control of the multipods. Lastly, the stirring of the reaction was observed to influence the final size of the multipod structure, but did not inhibit multipod formation.

CHAPTER 4

DIELECTRIC PROPERTIES FOR NANOPARTICLE-LOADED POLYMER NANOCOMPOSITES

4.1 Introduction

The development of printable electronics that incorporate components comprised of nanoparticles embedded in polymer matrices requires a uniform nanoparticle dispersion that will not phase segregate under the printing conditions. The incorporation of nanoparticles (<100 nm) to modify polymer properties has been an active area of research for more than a decade.[156–162] Research in the early days focused on the mechanical property enhancements, while more recently the use of nanomaterials in plastics have attracted attention for electronic applications particularly in flexible electronic applications. The dielectric properties of nanoparticle loaded plastic can modify the dielectric properties of polymers for both high and low dielectric applications [163–168] Maintaining low k performance in polymers is critical for insulating electrical interconnects in high-density, high-speed, and high-frequency microelectronic devices, where increased resistance and capacitive coupling in the circuit leads to signal delays and electrical cross-talk at interconnects.[164, 166, 169–172] Contact and non-contact printing of modified inks for two-dimensional printing [173], and adaptation of additive manufacturing based fused deposition modelling (FDM)[174, 175] using nano-polymer blends [176, 177] require that the composite maintains uniformly distributed spherical nanoparticles to avoid a low percolation threshold, increase the dielectric breakdown strength and operational frequency which scales with particle loading, and have minimal impact on the polymer dielectric.[178–180] The impact on the electrical, mechanical, and optical properties of the polymer depends directly on the material type, surface passivation, and degree of dispersion.

For printed electronics, the dielectric properties of the nanocomposite are critical to maintain the low-k properties of the polymer.[169] Studies have shown that incorporation of uniform and small-size nanoparticles in a dielectric insulator matrix such as a polymer, can broaden the operational frequency range of the polymer dielectric, improve its breakdown voltage strength and electromagnetic shielding capability, and improve the mechanical properties as well.[171, 172, 181–184] These studies have shown that incorporation of nano- to micron- sized particles leads to a rise in the dielectric constant with increasing particle volume fraction primarily due to phase segregation[185–188] leading to interfacial polarizations at the particle-polymer interface[187, 189, 190] While the behavior is accounted for using effective medium theory models, the role of phase segregation is not predictable in most cases.[191–194]

This manuscript investigates the use of earth abundant nanoparticles (Ni and Fe_3O_4) in a known low-k dielectric polymer (polystyrene) to investigate the impact on dielectric properties of incorporating Ni andFe_3O_4 nanoparticles sourced from commercial and synthetic methods. The nanoparticles were loaded into 280 kDa polystyrene at increasing volume fractions and analyzed through dielectric spectroscopy, electron microscopy, small angle X-ray, and magnetic measurements to evaluate the particle distribution and dielectric properties as a function of loading level. The study demonstrates that use of synthetically prepared nickel (Ni) and iron oxide (Fe_3O_4) nanoparticles of sizes under 50 nm (diameter) into polystyrene to approximately 50% by weight outperforms commercially sourced materials. The dielectric properties of the studied nanocomposite system show that the properties can be systematically manipulated with incorporation of up to fifteen volume percent loading when synthetically prepared materials are employed. The composites exhibit minimal increase in permittivity and loss tangent. The frequency dependent behavior can be modeled using effective medium theories. The use of surface passivated nanoparticles enhanced the ability to reduce aggregation, allowing uniform blending. The composites were formed into printable filaments without inducing aggregation as evidenced by SEM cross-section analysis. Nanoparticle composites that maintain their dispersity in the filaments are adaptable to FDM manufacturing of flexible electronics.

From an additive manufacturing outlook, the use of well-passivated, smaller nanoparticles leads to better phase dispersity in the polymer and has a lower probability of clogging print heads during FDM printing in comparison to larger sized particle.While nanoparticle-polymer composites using gold, silver and high-k ceramics have been reported[195–197]; the use of earth abundant materials as used in this manuscript is important if scale-up FDM printing methods are to become routine for flexible electronics. The results of the current study are believed to be extendable to other nanoparticle systems whether for optical properties (quantum dots), magnetic properties (nanomagents), or high-k applications (ceramics).

4.2 Materials and Methods

4.2.1 Chemicals

Commercial iron oxide (com-Fe_3O_4) nanopowder 98% (20-30 nm) was purchased from US-Nano and used without further purification. Polystyrene 280 kDa, nickel nanopowder (<100 nm, com-Ni) 99%, nickel acetate tetrahydrate (ni-acac), iron (III) acetylacetonate (fe-acac), oleic acid (OAc), oleylamine (OAm) technical grade 70%, 1-octadecene (1-ODE), tri-octylphosphine (TOP), n-methylpyrrole, toluene, methanol (MeOH), acetone and chloroform were purchased from Sigma Aldrich. The materials were used without further purification.

4.2.2 Synthesis of Nanoparticles

Synthetic Iron Oxide (syn-Fe_3O_4). Spherical, magnetite (11 ± 0.9 nm) nanoparticles passivated by oleic acid/ oleylamine were synthesized by following a previously established route [198]. In brief, 500 mg (0.00142 mol) of fe-acac was dissolved in 18 mL (0.0547 mol) of OAm and 20 mL (0.0628 mol) of OAc. The solution was heated to 180 ° C and 2 mL (0.0225 mol) of n-methylpyrrole was rapidly injected. The temperature was held at 180°C for 30 minutes and then cooled to room temperature. To isolate the Fe_3O_4 from the reaction mixture, MeOH was added until the solution became opaque, and the resultant nanoparticles were removed by applying a magnetic field. The magnetically separated Fe_3O_4 nanoparticles were re-dispersed in toluene, re-precipitated by addition of MeOH, and dried under vacuum.

Synthetic Nickel Nanoparticles (syn-NiNPs). Spherical hcp-Ni (20 nm) nanoparticles, passivated by TOP, were prepared by combining 3.0 g (0.012 mol) of nickel acetate, 72 ml (0.23 mol) of 1-ODE, and 12 ml (0.036 mol) of OAm added to a 250 ml round bottom flask. The solution was degassed under vacuum at 110 °C until no gas evolution was observed and back-filled with N2. To the solution, 5.4 ml (0.012 mol) of TOP was added and the temperature of contents increased to 245 °C. NiNPs were observed to begin forming in solution at 200 °C as observed by the solution color turning black. When the temperature reached 245 °C, the contents were removed from the heating mantle and immediately cooled to room temperature. The reaction was poured into a centrifuge tube and the nickel nanoparticles were precipitated by addition of 10mL toluene followed by 30 ml of methanol. The resulting solution was centrifuged for 5 min. After removing the supernatant, the pellet was redispersed in toluene. To precipitate the NiNPs, excess methanol was added followed by isolation through centrifugation before drying under vacuum.

4.2.3 Nanoparticle-Polystyrene Composite Formation

The nanoparticle-polymer composites were prepared with particle loadings between 0 and 15 volume percent (Table 4.1) by blending chloroform dispersed polystyrene (PS) and nanoparticles dispersed in chloroform with the assistance of sonication at 40 °C. The polymer composite is formed by slow solvent evaporation to form a viscous solution, cast onto a flat glass surface to form a film, and then further dried under vacuum for 24h. To minimize bubble formation in the cured nano-polymer composite film during the vacuum drying step, a multistep drying procedure is followed, wherein initially the sample is heated using an oven from 25 °C to 80 °C (10 °C/hr) over 6h, held at 80 °C for 12 hrs, followed by vacuum drying at 110 °C for 12 hours to fully cure the polymer composite.

To ensure adequate material for dielectric measurements and cross-section analysis by SEM imaging, a 8 mm × 1 mm disc is formed from the above nanoparticle-polymer film by punching $5/16^{th}$ inch disks from the polymer composite, stacking four disks and hot pressing in an aluminum mold at 185 °C degrees at a force of 15,000 pounds for 10 minutes.

4.2.4 Filament Formation

A low volume fraction printable filament for the syn-Ni and com-Ni was prepared by extruding pre-cast and dried nanocomposite film using a Filabot EX2 Filament Extruder operating at 220 °C. The extruded filament was broken up and extruded 3 times to improve homogeneity.

4.2.5 Transmission Electron Microscopy (TEM)

Nanoparticle samples were drop-cast, from toluene dispersion, onto 300 mesh carbon coated copper grids and left to dry under vacuum overnight. The TEM images were recorded using a JEM-ARM200cF electron microscope at 200 kV acceleration voltage.

4.2.6 Scanning Electron Microscopy (SEM)

SEM EDS imaging analysis of cross-sections of the composite cast-film, pressed discs and extruded filament were performed on cleaved samples mounted onto carbon tape and placed on 45°/90° (Ted Pella 16104) low profile aluminum mount to allow cross-section imaging. The mounted samples were carbon coated (4 nm) using a Balzers Mini deposition system MED 010 prior to SEM imaging to prevent charging. SEM imaging was performed on a FEI Nova NanoSEM 400 operating at 20 kV with a spot size of 4.0. The images were collected with an Everhart-Thornley detector (ETD), backscattered electron (BSE) detector or an Oxford INCA X-Sight energy dispersive spectroscopy (EDS) detector. The BSE mode and EDS mapping were used to identify dispersion of nanoparticles within the polymer for the lowest and highest volume fractions of nanoparticles.

4.2.7 Thermogravimetric Analysis (TGA)

TGA was performed on a TA Instruments Q50 thermogravimetric analyzer. The samples were heated at a rate of 10 °C/min from room temperature to 100 °C and held for 5 minutes before continuing to ramp at 10 °C/min to 550 °C. Measurements were performed under nitrogen to prevent further oxidation.

4.2.8 Magnetic Measurements

Magnetic properties were studied with a superconducting quantum interference device (SQUID) magnetometer, MPMS-XL (Quantum Design). Field-dependent magnetization was measured at 300 K, with the applied field varying from 0 T to 1 T and back. Differential Scanning Calorimetry (DSC). Measurements were carried out at the highest loading levels for the nanocomposite using a TA Q250 calorimeter. The samples were subjected to a Heat/Cool/Heat experimental procedure: Ramp at 10 °C/min to 300.00 °C; Ramp at 10 °C/min to 50.00 °C; Ramp at 10 °C/min to 300.00 °C.

4.2.9 Dielectric Spectroscopy

The dielectric spectroscopy was performed on the composite discs (8 mm x 1 mm) on a Novocontrol Impedance Dielectric Spectrometer (Rohde & Schwarz ZVA) and utilized a parallel plate geometry and an Alpha-A modular analyzer to calculate the capacitance and conductivity of each sample. WinDETA software provided the calibration protocols and experimentation setup. The measurements were taken at 1.5 V, for each frequency, and averaged three times for each data point. Measurements were taken over 10 Hz steps over the frequency range chosen.

4.2.10 Powder X-Ray Diffraction (pXRD)

The pXRD patterns for Ni nanoparticles and for all volume percent nanocomposites were acquired on a Rigaku Ultima III diffractometer equipped with a Cu-Kα source. Due to the presence of Fe fluorescence, the Fe_3O_4 composites were analyzed on a PANalyticial Xpert Pro (Cu-Kα source with a filter for removal of iron fluorescence). Data were collected at room temperature, in the 2θ range of $10-80°$.

4.2.11 Small-angle X-ray Scattering (SAXS)

SAXS measurements were performed between 0.1 to 3.7 degrees (2θ) in transmission mode on 8mm × 1mm discs of the nanocomposite using a Bruker Nanostar instrument with a Cu-Kα source ($\lambda = 0.154$ nm). The sample was placed in an aluminum sample holder. Intensity vs. scattering vector (q) plots, where $q = 4\pi/\lambda \sin\theta$, were generated by integrating over a 1 mm × 1 mm area of the detector (600 s averaging time).

4.3 Results and Discussion

Using solution blending methods, Ni and Fe_3O_4 nanoparticles were dispersed in polystyrene (280 kDa) to achieve nanocomposites containing 0 to 15 volume percent (Table 4.1). A volume percentage of 15% is approximately a weight percentage of 50%. Higher loadings were not studied, as the nanocomposite was observed to become brittle above 15 volume percent. Since nanoparticle miscibility in the polystyrene is anticipated to be influenced by the preparative route, the nanoparticles were selected from a commercial (com) and a synthetic (syn) source. It is important to note that the commercial sample is a representative sample but does not represent all possible commercial sources. The sourcing of the com sample was to allow quantities to be obtained at a cost comparable to synthetic preparative routes for the materials under study.

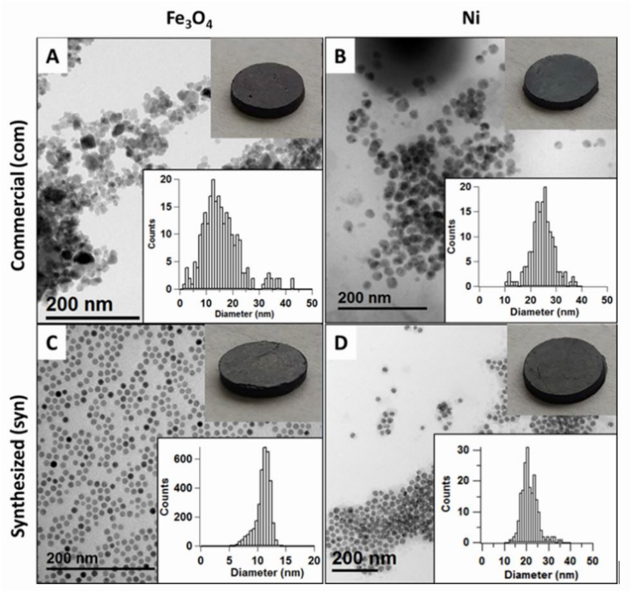

Figure 4.1: TEM size and size distribution of (A) com-Fe_3O_4, (B) com-Ni, (C) syn-Fe_3O_4, and (D) syn-Ni nanoparticles. A disc of the formed composite used in dielectric spectroscopy is shown (insert).

Table 4.1: Properties of the nanoparticles and nanocomposites

	Variant	NP Volume Fractions for composites v_f	NP Diameter (nm) D	Ligand Mass %	Structure	M_s (emu/g) [emu/mol 10^3]
Fe_3O_4	(1) com	0.0137, 0.0266, 0.0935, 0.128	16.8 ± 5.6	7.6	Monoclinic	77.4 [17.9]
	(2) syn	0.0069, 0.0120, 0.0535, 0.109	11.0 ± 0.9	28	Monoclinic	58.3 [13.5]
Ni	(3) com	0.0062, 0.0129, 0.0481, 0.105	24.0 ± 3.3	3.66	Face Centered Cubic (*fcc*)	54.2 [3.18]
	(4) syn	0.0049, 0.0115, 0.0459, 0.0847	23.6 ± 3.2	7.43	Hexagonal Closed Packed (*hcp*)	1 [0.059]

In figure 4.1, TEM of the isolated nanoparticles, size dispersity plots for the nanoparticles, and representative 8 mm x 1 mm nanocomposite discs are shown. Analytical data on the nanoparticles including X-ray powder diffraction, 300 K field sweep magnetization susceptibility plots, and thermogravimetric analysis (TGA) data are provided in figures 4.2, 4.3 and 4.4. The studied Fe_3O_4 nanoparticles exhibit the same crystallographic phase, but comparison of the syn- and com- reveal the commercial samples are non-spherical, exhibit aggregation, and are 50% larger (3.5 times larger volume) in size with a broader size dispersity. The magnetic susceptibility of the com sample is larger consistent with the size difference.[199–203] The Ni nanoparticles are spherical and exhibit nearly identical size and size dispersities; however the com-sample is the strongly magnetic fcc-phase, while the syn-sample is the weakly magnetic hcp-phase (Figure 4.3).

The surface passivation and ligand content are different between the four samples, as measured by thermogravimetric analysis (TGA) (Table 4.1). As shown in figure 4.4, the ligand content from TGA measurements in syn Fe_3O_4 is 28.0 wt% OA/OAm, com Fe_3O_4 is 7.6 wt% polyvinylpyrrolidone (PVP), syn Ni is 7.33 wt% OAm/TOP, and com Ni has $<$ 3.66 wt% ligand content (ligand is proprietary). The commercial variants (com-Ni and com-Fe_3O_4) featured a lower degree of ligand bound to the surface in comparison to the synthesized particles.

The observed polystyrene glass transition temperature (Tg) for the nanocomposites at 0 vol% and at 15 vol% nanoparticle exhibit similar T_g values (Tg = 108 °C) suggesting no impact on the polymer melting behavior (Figure 4.5). The results are consistent with literature on similar sized nanoparticles when dispersed in polymer matrices, where no significant change in Tg is reported.[204–206] The decomposition temperature of the nanocomposite increases with increasing particle loading as shown in figure 4.6. Consistent with this result previous studies have observed an increased thermal stability in nanoparticle loaded polymers. [207–209]

Nanoparticle dispersion in nanocomposite. The nanocomposites shown in inset of Figure 4.1 are uniformly optically dense, exhibit a linear increase in Ms with increasing volume fraction (Figure 4.3), and the pXRD shows a decrease in polystyrenes signal intensity as the concentration of the nanoparticle increases (Figure 4.7). The distribution of the nanoparticles in polystyrene was analyzed using small angle X-ray (Figure 4.8) and cross-sectional SEM-EDS analysis (Figures 4.9 and 4.10).

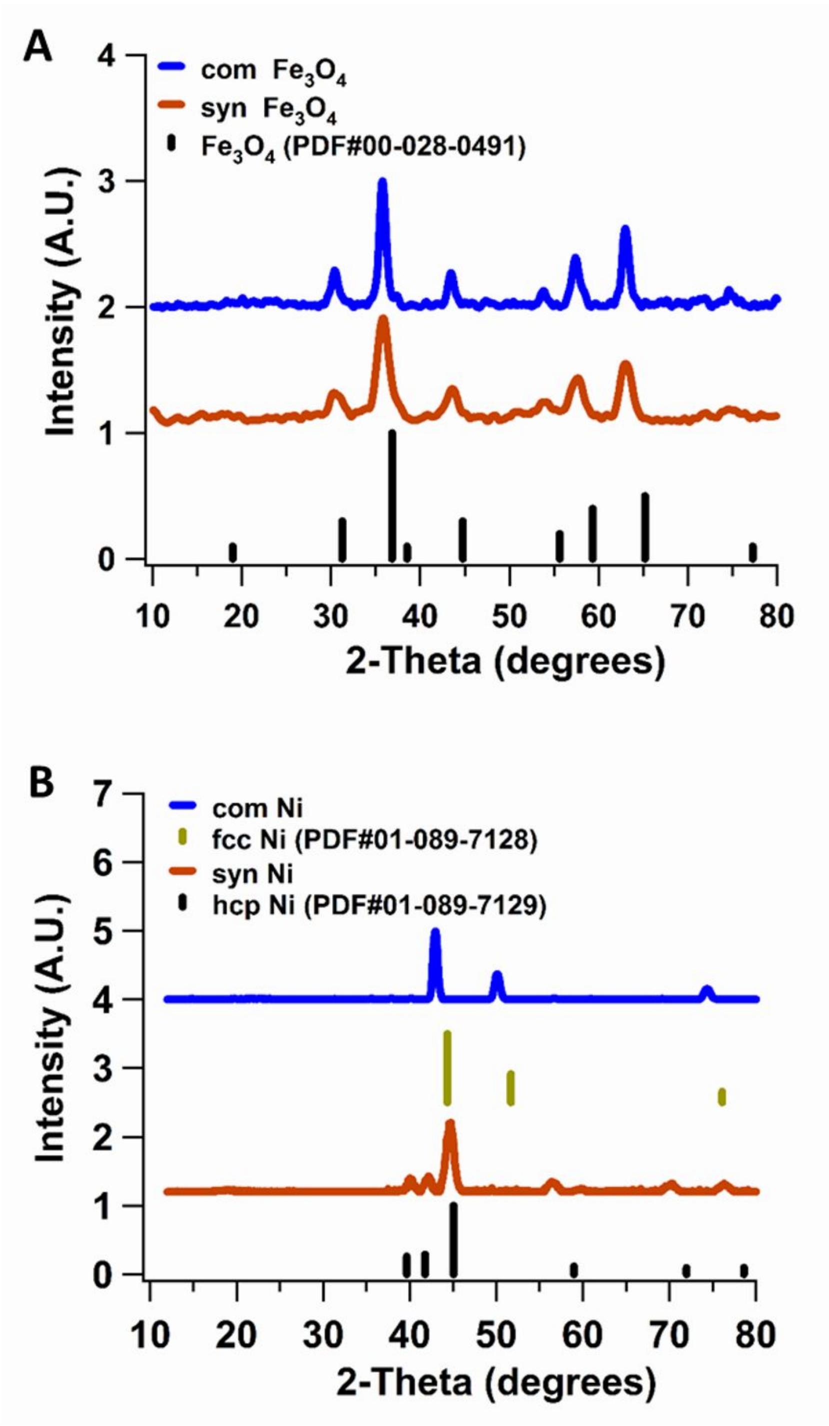

Figure 4.2: Powder X-Ray diffraction (pXRD) characterization of the nanoparticles. (A) Fe_3O_4 nature of iron oxide (syn and com). (B) Face-centered cubic (*fcc*) and hexagonal close-packed (*hcp*) nature of com-Ni and syn-Ni nanoparticles respectively.

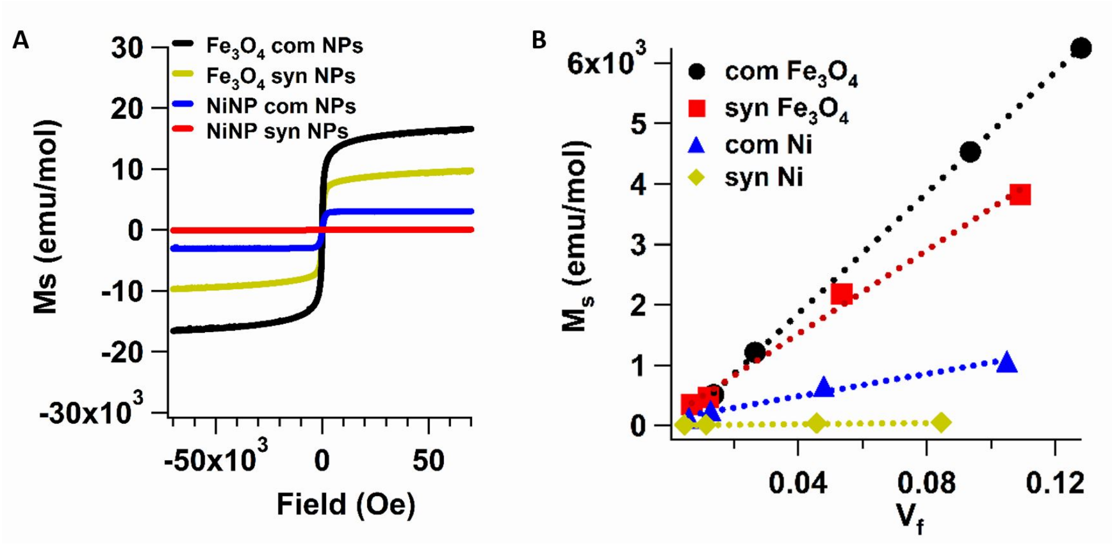

Figure 4.3: Superconducting quantum interference device (SQUID) magnetic measurement data for the saturation magnetization of the nanoparticles (A) and saturation magnetization (M_s) of the polystyrene nanocomposites as a function of nanoparticle volume fraction (B). Synthesized nickel particles were of the *hcp* crystalline variant, which accounted for the ~1 emu/g value.

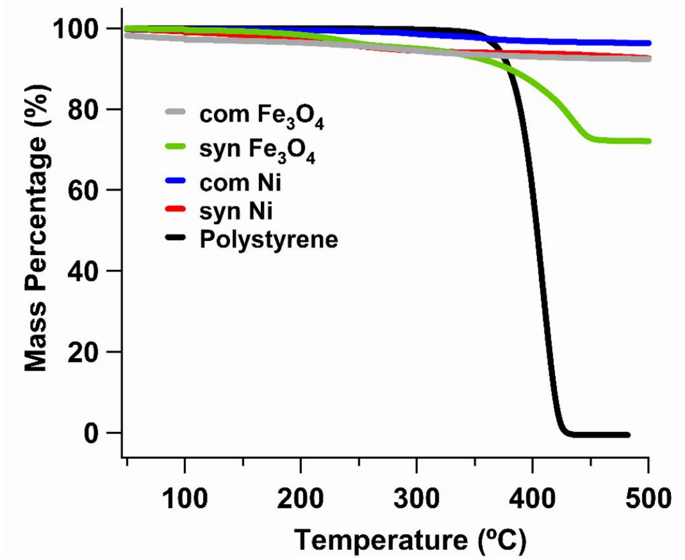

Figure 4.4: TGA analysis of surface ligand functionalization on filler nanoparticles used in study *sans* matrix showing 28, 7.6, 7.4, and 3.7 w/w% ligand mass for synthesized iron oxide, commercial iron oxide, synthesized nickel, and commercial nickel respectively.

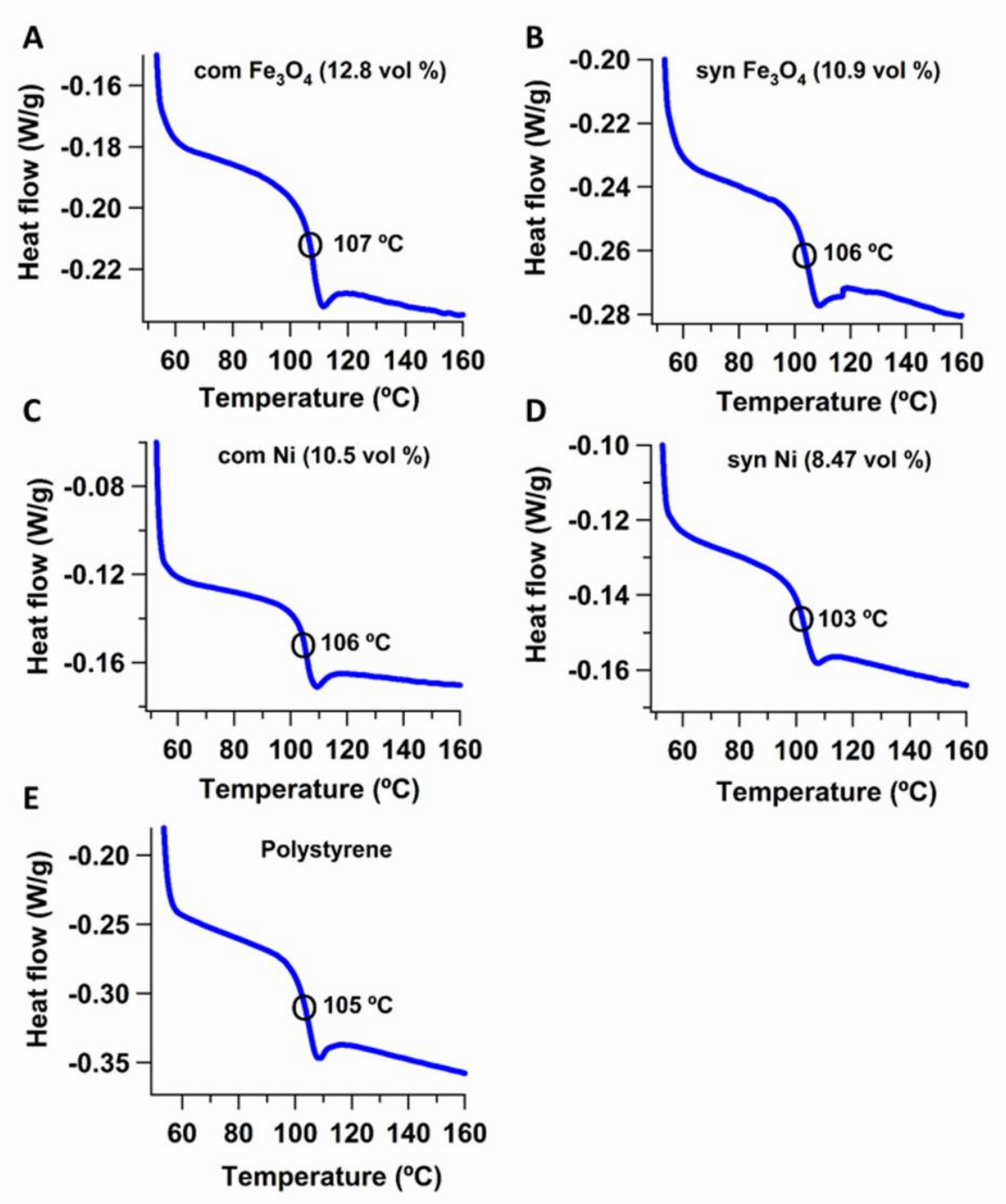

Figure 4.5: DSC thermographs for (a) com-Fe_3O_4, (b) syn-Fe_3O_4, (c) com-Ni and (d) syn-Ni nanocomposites at the highest loading level, and (e) pure polystyrene. The data indicated that there was a minimal change (± 2°C) in glass transition temperature (T_g) of the system upon nanoparticle incorporation.

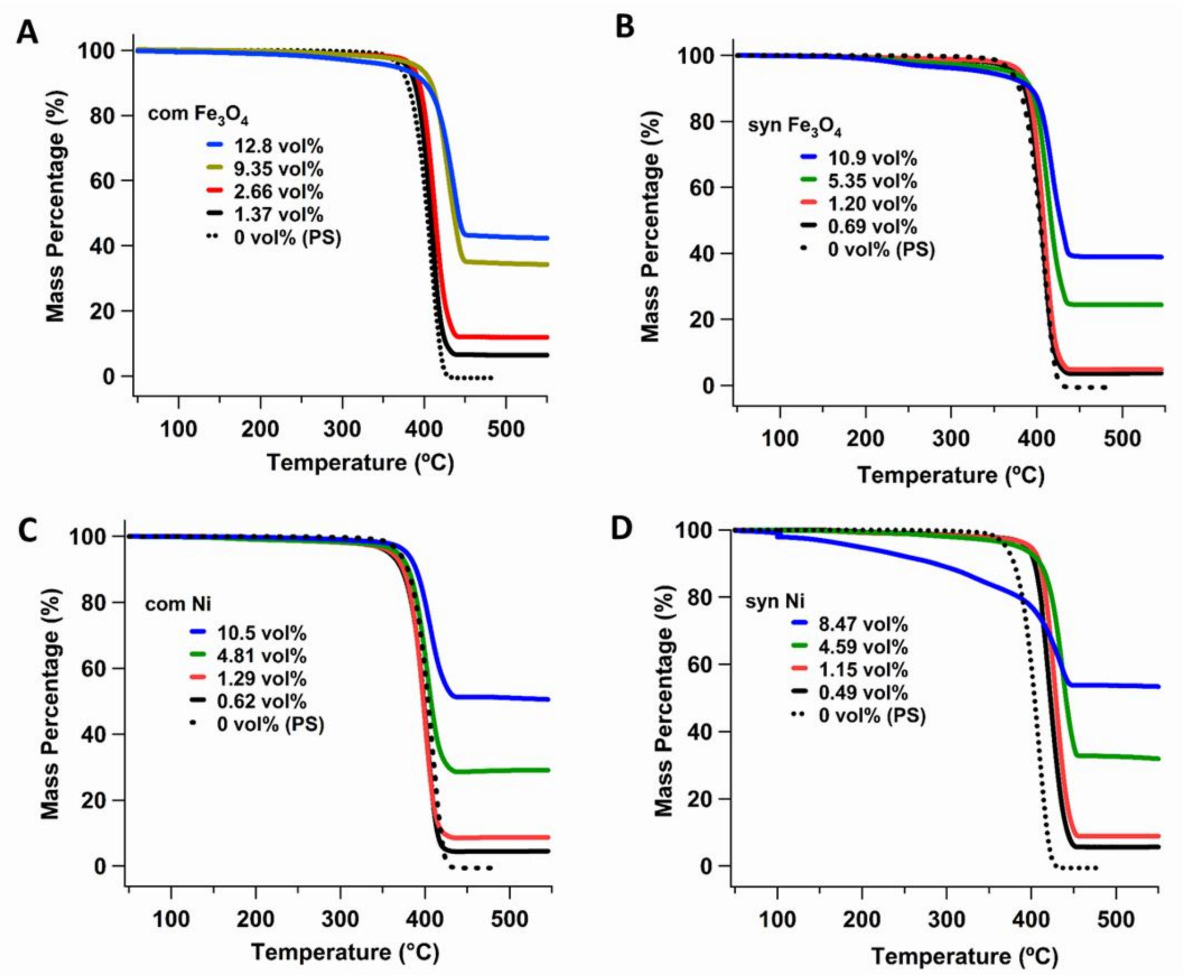

Figure 4.6: Thermogravimetric analysis (TGA) of the composite samples in comparison to pure polystyrene for (a) com-Fe_3O_4, (b) syn-Fe_3O_4, (c) com-Ni and (d) syn-Ni nanocomposites. TGA of the samples suggests that the decomposition temperature of the polystyrene is increased to a small extent as the loading level of particles in the composite increases.

Small Angle X-ray Scattering (SAXS) on the highest and lowest nanoparticle loadings for both the commercial and synthetic samples were performed to investigate the microstructure of the formed composites. Of these samples, only the synthetically prepared materials could be fully analyzed. The nanocomposites formed using syn nanoparticles (Ni and Fe_3O_4) show a clear peak in the I vs. q SAXS plot, which is indicative of ordering of particles on the length scales probed ($2\pi/q$).

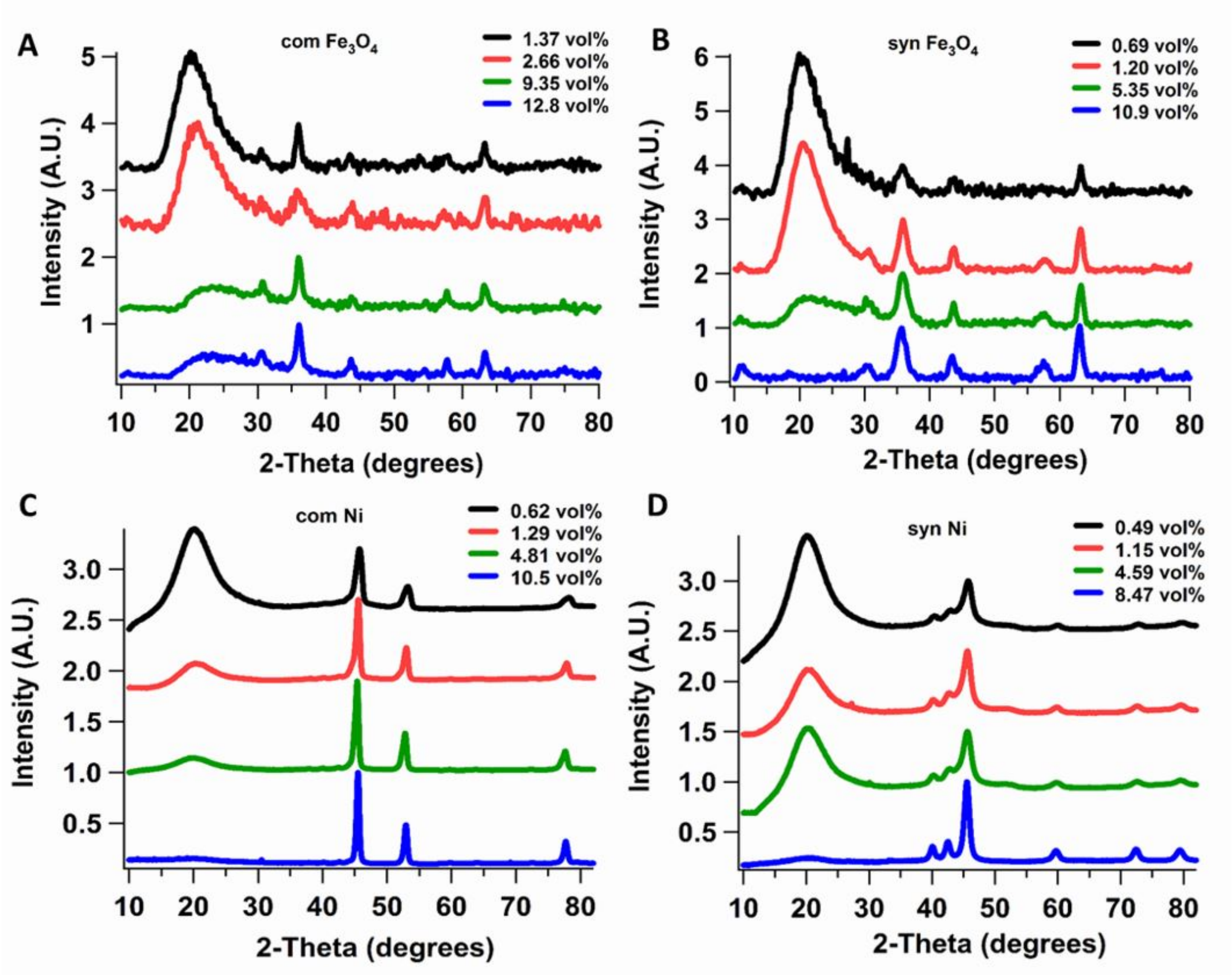

Figure 4.7: pXRD patterns for (a) com-Fe_3O_4, (b) syn-Fe_3O_4 (c) com-Ni and (d) syn-Ni nanocomposites. The peak at 20° corresponds to the polystyrene matrix which decreases as the volume percentage of nanoparticles increases.

From the SAXS data the inter-particle spacing (d) can be can be extracted from the length of the scattering vector q using the lowest angle primary peak (q^*), since $d = 2\pi/q^*$, where $d = 2r + 2l$ (r is nanoparticle radius and l represents the passivant length). In the SAXS data for the syn-Fe_3O_4 (r = 5.5 nm), q^* occurs at a q of 0.25 nm^{-1} (d = 25.1 nm) for the 0.69 vol% and a $q*$ of 0.565 nm-1 (d = 11.1 nm) for the 10.9 vol%. For the syn-Ni samples (r = 12 nm), at the lowest concentration (0.49 vol%) no definable q^* is observed in the q range probed. At high concentration (8.5 vol%) the scattering peak sharpens and occurs at 0.023 nm^{-1} corresponding to d = 27 nm. The I vs.

q SAXS plot (Figure 4.8) for the commercial samples (Ni and Fe_3O_4) do not show any peaks in the scattering pattern resulting in the inability to analyze particles distribution. Earlier studies concluded that phase segregation of the nanoparticles leads to loss of scattering features [210, 211]

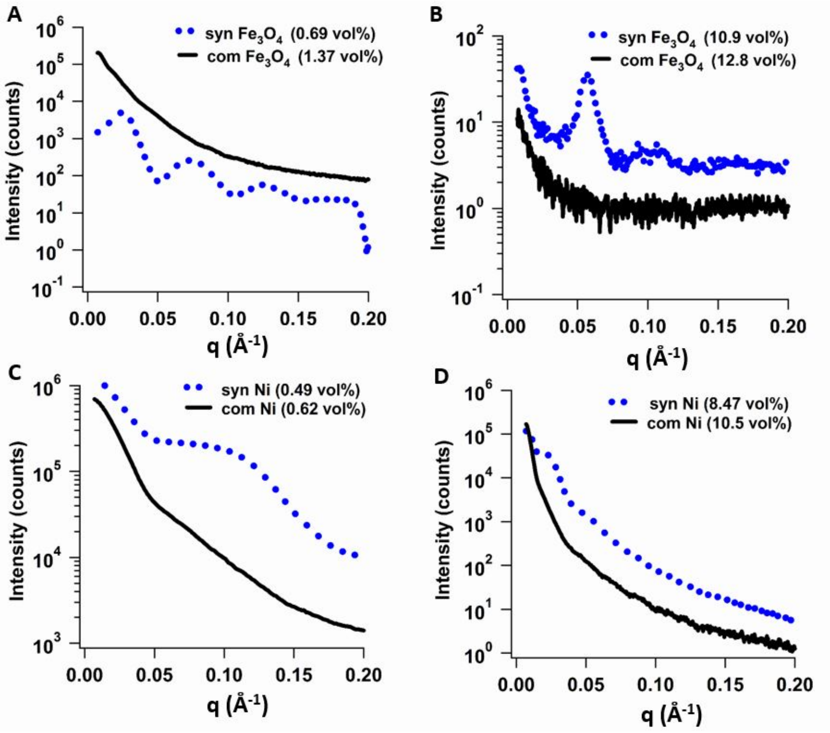

Figure 4.8: I vs. q SAXS data for (A) lowest loading of Fe_3O_4 (com vs. syn), (B) highest loading of Fe_3O_4 (com vs. syn), (C) lowest loading of Ni (com vs. syn), and (D) highest loading of Ni (com vs. syn).

The experimental SAXS data can be interpreted in terms of the degree of dispersion in the polymer when the particle size is considered. The syn-Fe_3O_4 is 11 nm (r = 5.5 nm) with a shell of $2l < 5.6$ nm for the oleylamine (l = 1.5-2.5 nm([212, 213]) /oleic acid (l = 2.8 nm[214]) passivating shell depending on the trans to gauche content in the ligands, surface packing, and degree of passivation. If the Fe_3O_4 is aggregated, we anticipate an inter- particle spacing (d) between 11 and 17 nm.(65) The SAXS data for syn-Fe_3O_4 shows at 10.9 vol%, the interparticle spacing is consistent with a description as being aggregated within the composite.[215] The low concentration (0.69 vol%) syn-Fe_3O_4 sample can be considered on average more disperse based on the larger inter-particle distance observed in the SAXS data. For the Ni sample, the same conclusion can be made since the Ni nanoparticle would be expected to have a minimum inter-particle distance of 30 nm reflecting the syn-Ni diameter 24 nm with a passivant shell of < 6 nm (2l). The measured inter-planar distance of 27 nm in the SAXS data for the 10.5 vol% Ni fits to a model where Ni is aggregated if we assume the primary peak (q^*) is observed.

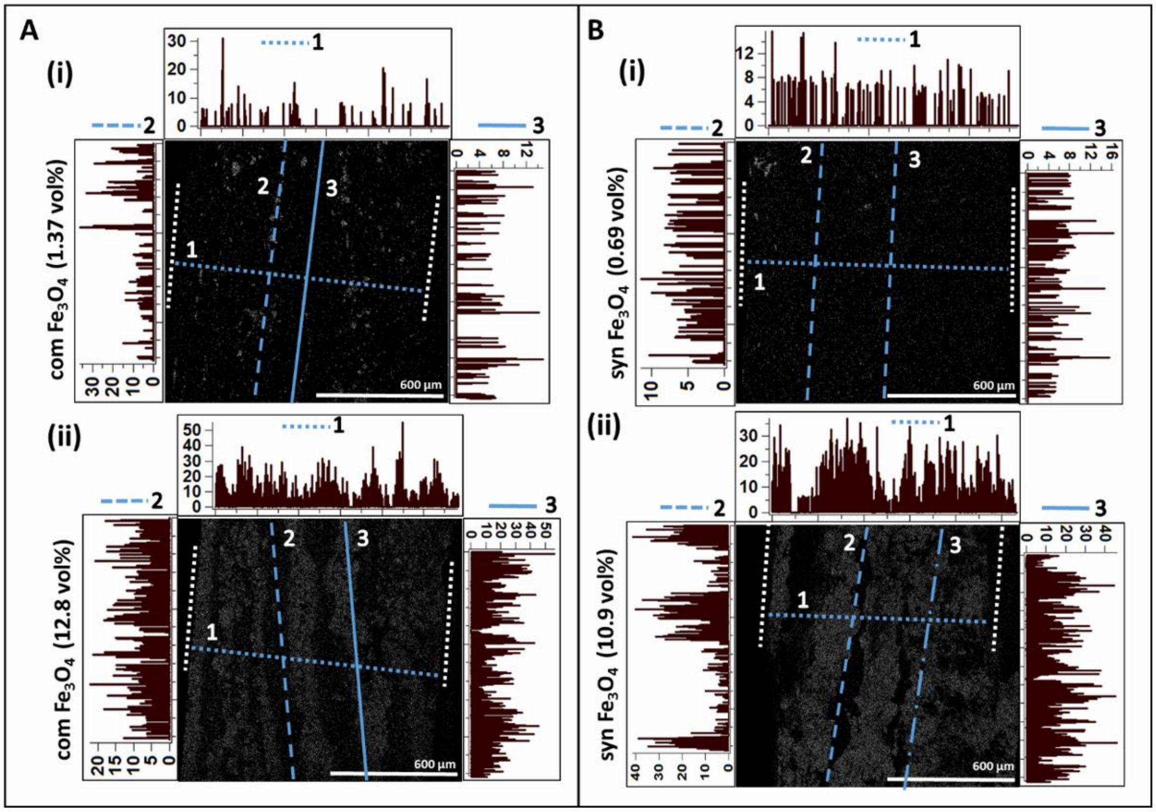

Figure 4.9: Fe Kα SEM-EDS map and line profile scans of nanocomposite discs in various regions for (A) com-Fe_3O_4 and (B) syn-Fe_3O_4. Dashed white lines at the edges indicate the boundaries of the samples.

In Figures 4.9 and 4.10, the SEM-EDS images of the nanocomposites are shown to evaluate the particle dispersity within the composite through elemental distribution. It is believed for the synthetic samples, the particle distribution is random at low concentration and at higher concentrations aggregation arises due to magnetic and electrostatic (Hamaker constant) interactions, in accordance with the SAXS results. The magnetic interactions should dominate the interparticle attraction, as reported for Fe_3O_4 nanoparticles in solution.[216] For the commercial samples poor solubility results in non-statistical distributions. Attempts to analyze individual particle particle

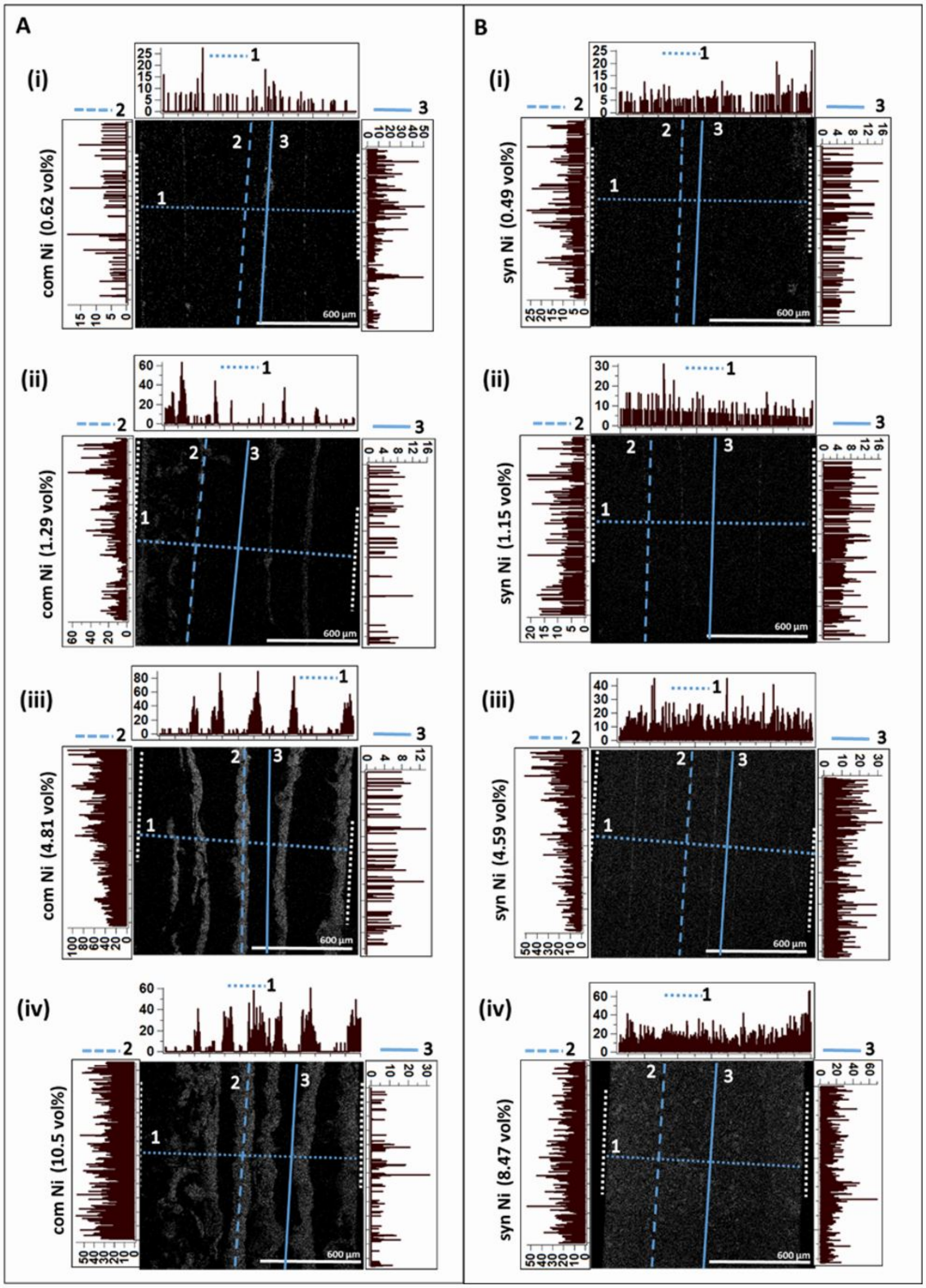

Figure 4.10: Ni Kα SEM-EDS map and line profile scans of pressed nanocomposite samples for all volume fractions of (A) com-Ni and (B) syn-Ni obtained using EDS analysis. Dashed white lines at the edges indicate the boundaries of the samples

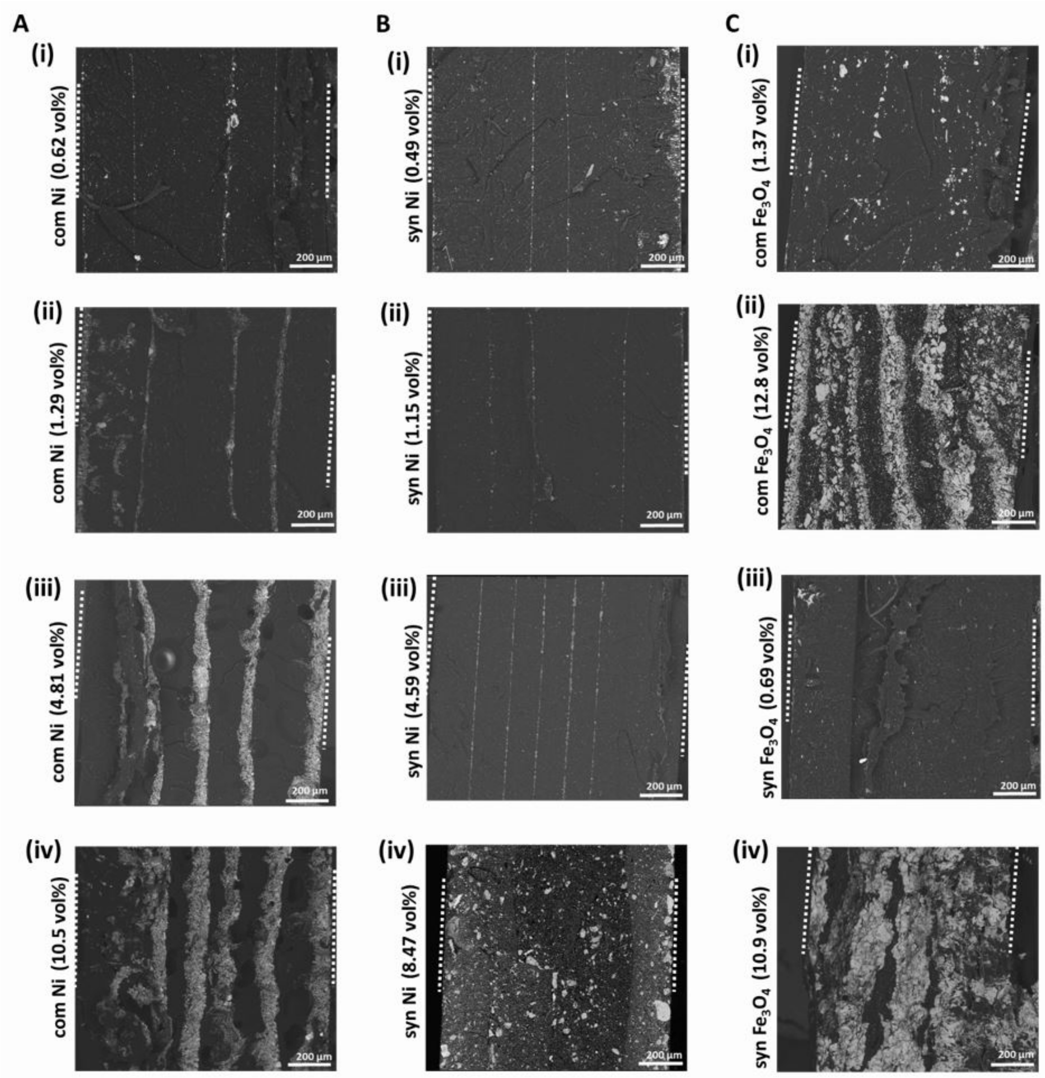

Figure 4.11: BSE data for cross section of pressed sample discs for com-Ni (A i-iv), syn-Ni (B i-iv), com-Fe_3O_4 (C i and ii) and syn-Fe_3O_4 (C iii and iv). Dashed white lines indicate boundaries of sample.

spacing were not performed due to available SEM resolution limits, sample thickness, and the inability to obtain high resolution TEM images of the prepared nanocomposites. In Figures 4.9 and 4.10, the energy dispersive spectroscopy (EDS)-SEM images are shown for the lowest and highest composition com- and syn-Fe_3O_4 and Ni nanocomposites. Back-scattering (BSE) SEM is available in figure 4.11. Inspection of the SEM line scans and images reveal that aggregation and sedimentation occur for all types of nanoparticles with increasing volume fraction in the PS

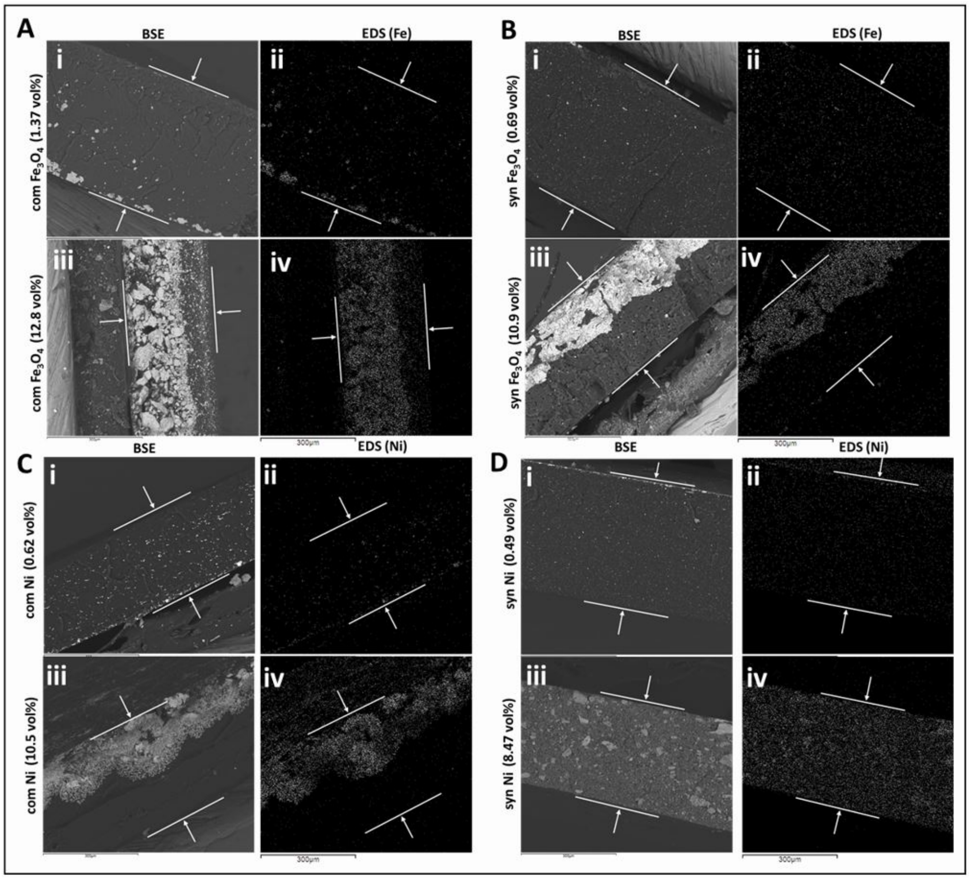

Figure 4.12: BSE and corresponding EDS data for cross-section of cast films for lowest (i and ii) and highest (iii and iv) volume fraction of com-Fe_3O_4 (A), syn-Fe_3O_4 (B), com-Ni (C) and syn-Ni (D). White lines indicate boundaries of film.

composites with the syn- samples showing lower aggregation behavior overall.

A more thorough analysis of the dispersion of Ni in polystyrene can be obtained by imaging the concentration dependent sedimentation (Figure 4.10). The com-Ni samples exhibit visible aggregation (striping) at 0.62 vol%, while the syn-Ni appears to be uniformly dispersed throughout the nanocomposite range studied.

Multiple possible arguments can be made for the difference in behavior including surface passivation differences and magnetic moment differences between the samples. For the nanocomposites it is believed the observed aggregation differences in com and syn reflects primarily the difference in magnetic moment for the samples, as evidenced by the highest magnetic saturation sample, com-Fe_3O_4, exhibiting a higher degree of aggregation than the syn-Fe_3O_4 sample. This is also evident in the Ni samples where the fcc structure (com) shows more significant aggregation than the hcp (syn) structure reflecting their respective moments.

4.3.1 Dielectric Properties

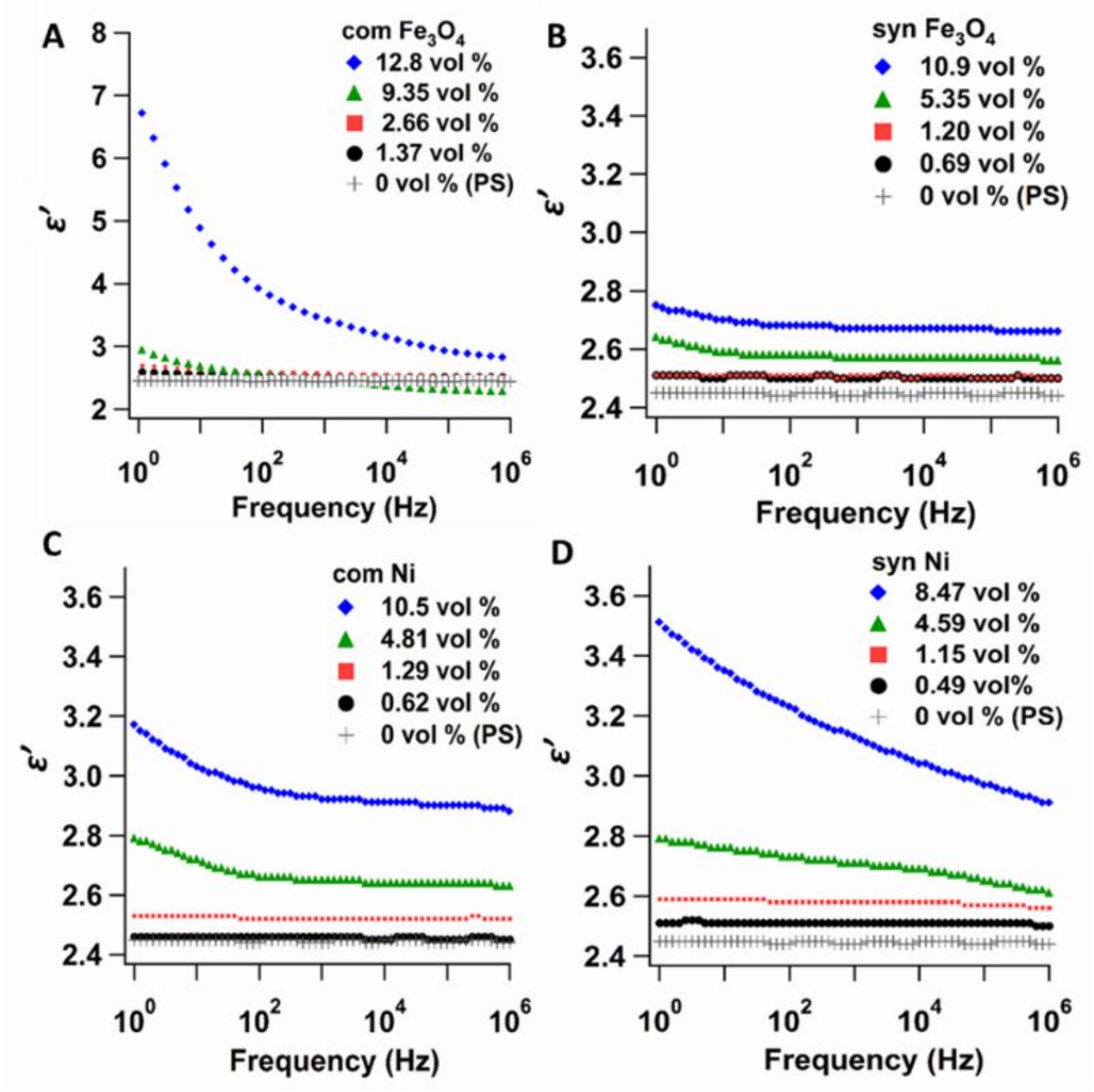

Figure 4.13: Frequency dependent dielectric measurements (0.1 Hz – 1 MHz) of the real permittivity (ϵ') of (A) com-Fe_3O_4, (B) syn-Fe_3O_4 (C) com-Ni and (D) syn-Ni nanocomposites at different particle loadings.

The dielectric properties of the prepared nanocomposites were analyzed by measuring the capacitance of the nanocomposites as a function of frequency to assess the real (ϵ') and imaginary (ϵ'') components of the complex permittivity.[217, 218] In figure 4.13, the frequency dependence of the real permittivity (ϵ') is plotted for the nanocomposites and fit in Figure 4.15 to the Looyenga model. The imaginary permittivity is shown in figure 4.14 and the loss tangent is plotted in Figure 4.17.

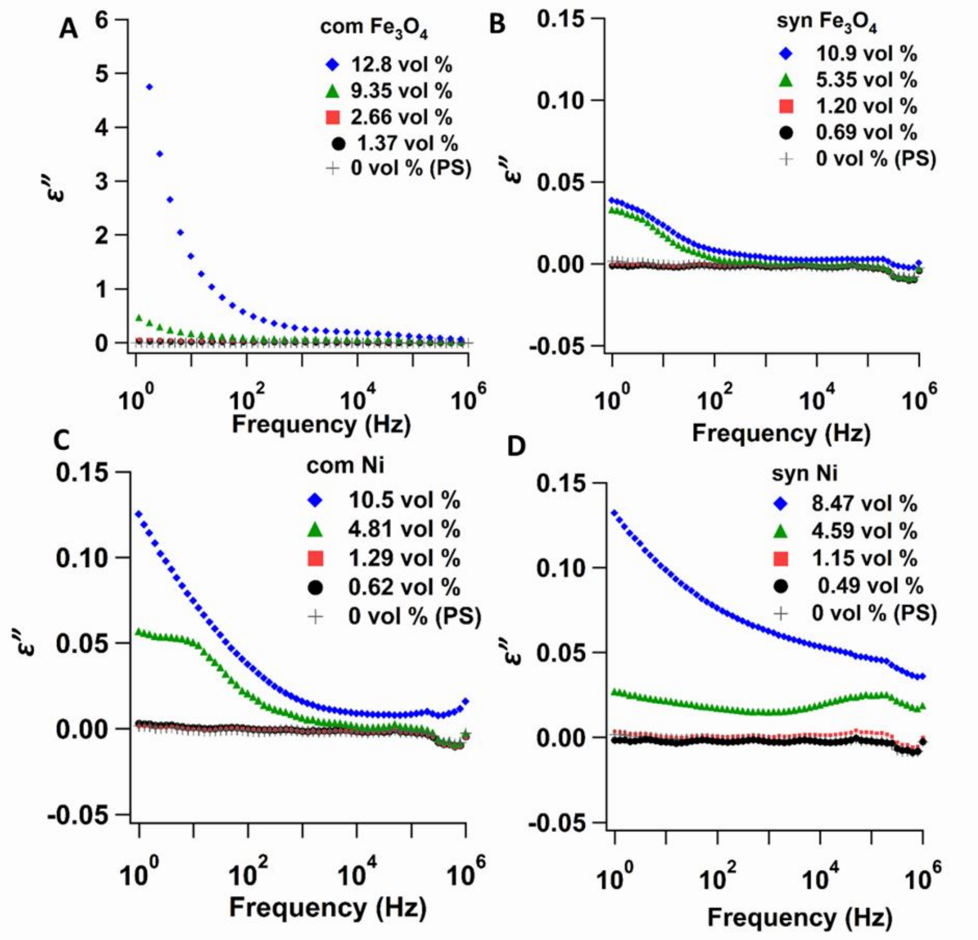

Figure 4.14: Frequency dependent (0.1 Hz - 1 MHz) measurements of the imaginary permittivity (ϵ'') of (a) com-Fe_3O_4, (b) syn-Fe_3O_4 , (c) com-Ni, and (d) syn-Ni nanocomposites.

Real Permittivity. The real permittivity corresponds to the absorptive or storage ability, and is observed to be frequency dependent exhibiting a lower dielectric value with increasing frequency and a positive correlation to particle volume fraction in all four nanocomposite systems (Figure 4.13). The greater increase in the ϵ' for the syn-Ni system versus the com-Ni system can be attributed to the presence of a higher surface passivation level and the polarizable nature of OAm/TOP for syn-Ni. It has been reported that polarizable functional groups respond to electrical fields and enhances the measured ϵ' value at lower frequencies.[219, 220] In comparison, pure polystyrene is frequency independent with a real (ϵ') permittivity of 2.45 consistent with reported values (2.4-2.7).[171, 186, 221]

Earlier nanocomposite studies indicate the dielectric properties of a nanocomposite can be fit by effective medium theories for well-dispersed nanoparticles in the polymer.[222–226] This is achieved when the nanoparticle size is on the order of polymer entanglement regime [187, 189] and the surface passivation leads to miscibility between the phases. The developed dielectric models can be subdivided into three categories depending on the degree of material-material, material-host, material-field interactions (Group 1 vs. Group 2), and shape and orientation effects (Group 3).[225] Dielectric models in Group 1 are used for describing the permittivity frequency response for a non-interacting spherical filler in a matrix. We anticipated that for our nanocomposite system that uses spherical nanoparticles below 50 nm in a low-k host polymer matrix with low volume fractions (<0.15), Group 1 models would fit the best. When the nanomaterials aggregate in the polymer, the dielectric properties cannot be adequately modeled due to the inhomogeneity of the sample.

Comparison of the fits of the real permittivity data at 1 MHz to the various effective medium models are shown in tables 4.2 and 4.3. Inspection of the χ^2 values indicate the analyzed Group 1 and 2 models are within the statistical error. Following from the work of M.C. Arajo et. al, the Looyenga model is used for further analysis and has the lowest χ^2 for the tested models. The real permittivity (ϵ') is fit to the Looyenga effective medium theory, where [227–229]

$$\epsilon' = ((\epsilon'_m)^{1/3}(1 - v_f) + (\epsilon'_f)^{1/3} v_f)^3 \tag{4.1}$$

where ϵ', ϵ'_m, and ϵ'_f corresponds to the real dielectric constant of the composite, matrix and filler respectively, and v_f corresponds to the volume fraction of the nanoparticle. The Looyenga model does not make any shape assumptions for inclusions.[227–229] The ϵ' for the nanocomposites is fit to eqn 4.1, as shown in Figure 4.15. The experimental value for $\mathrm{v}_f = 0.0935$ of the com-Fe_3O_4

($\epsilon' = 2.26$) is below pure polystyrene ($\epsilon'_{\text{m}} = 2.45$) and is believed to be due to the presence of encapsulated bubbles ($\epsilon' = 1$ for air) lowering the observed dielectric value. As such it is treated as an outlier but is included in the data set as it is within one standard deviation. Form the fit, the real permittivity for the nanoparticle filler, ϵ'_f, are 9.34 ± 1.25 (syn-Ni), 7.46 ± 0.78 (com-Ni), 4.12 ± 0.16 (syn-Fe_3O_4), and 5.69 ± 0.65 (com-Fe_3O_4). The values of ϵ'_f and χ^2 for the alternative models (Tables 4.2) are available in table 4.3. The larger value for the Ni samples is consistent with the metallic character of Ni, and consistent with our early analysis of Ni permittivity.[18]

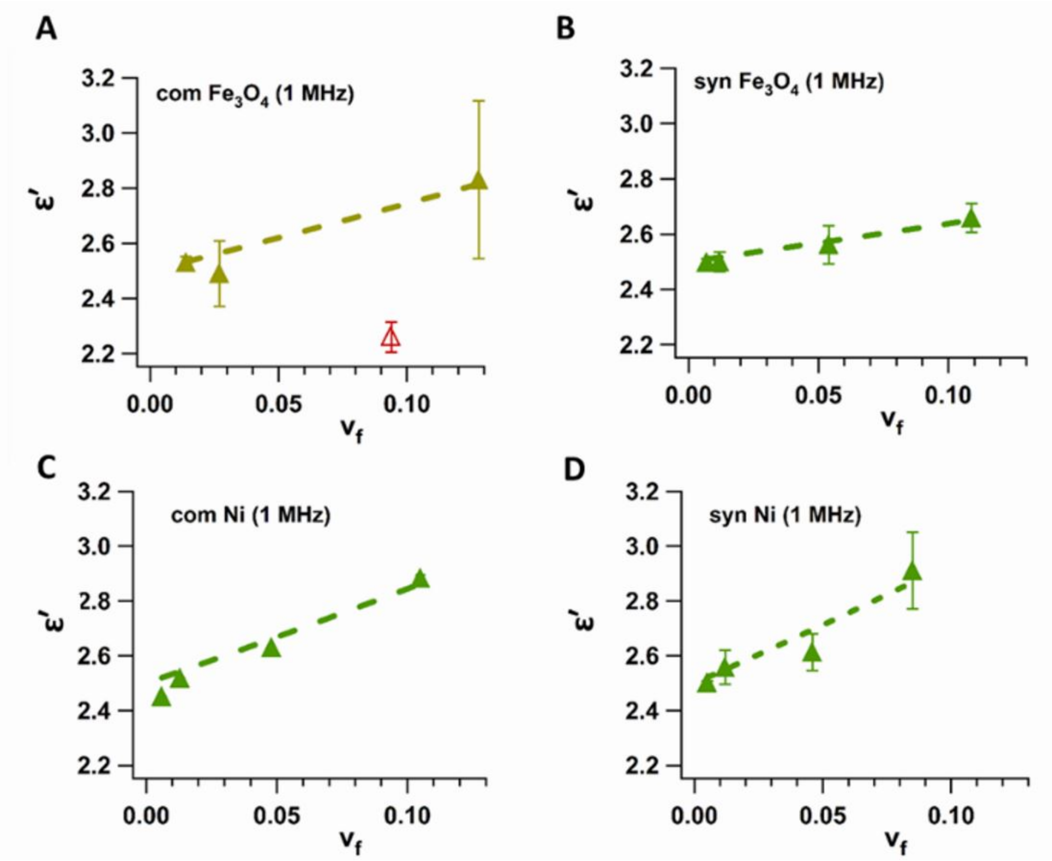

Figure 4.15: The real permittivity (ϵ') of different nanocomposite samples as a function of volume fraction of particles (v_f). Experimental data are the solid symbols while the dashed lines are fits of the Looyenga model to the data. (A) com-Fe_3O_4, (B) syn-Fe_3O_4, (C) com-Ni, and (D) syn-Ni nanocomposites.

Table 4.2: Equations of various models used to fit dielectric real permittivity data

Model (Group)	**Equation**
EMT (1)	$\varepsilon' = \varepsilon'_m(1 - v_f) + \varepsilon'_f v_f$
Maxwell-Garnett (1)	$\varepsilon' = \varepsilon'_m + 3\varepsilon'_m v_f (\frac{\varepsilon'_f - \varepsilon'_m}{\varepsilon'_f + 2\varepsilon'_m - v_f(\varepsilon'_f - \varepsilon'_m)})$
Lichtenecker (1)	$\varepsilon' = e^{((1-v_f)\ln(\varepsilon'_m) + (v_f)\ln(\varepsilon'_m))}$
Sillars (1)	$\varepsilon' = \varepsilon'_m (1 + (\frac{3v_f(\varepsilon'_f - \varepsilon'_m)}{\varepsilon'_f + 2\varepsilon'_m})$
Maxwell-Garnett (with interactions) (2)	$\varepsilon' = \varepsilon'_m(1 + \frac{3v_f\gamma}{1 - v_f\gamma - \frac{2}{3}v_f\gamma\ln(\frac{8+\gamma}{8-2\gamma})})\,; \quad \gamma = \frac{\varepsilon'_f - \varepsilon'_m}{\varepsilon'_f + 2\varepsilon'_m}$
Looyenga (2)	$\varepsilon' = ((\varepsilon'_m)^{1/3}(1 - v_f) + (\varepsilon'_f)^{1/3} v_f)^3$
Yamada (3)	$\varepsilon' = \varepsilon'_m\left(1 + \frac{v_f n'(\varepsilon'_f - \varepsilon'_m)}{n'\varepsilon'_m + (1 - v_f)(\varepsilon'_f - \varepsilon'_m)}\right)$
Van Beek (3)	$\varepsilon' = \varepsilon'_m\left(\frac{\varepsilon'_m + (n(1 - v_f) + \varepsilon'_f)(\varepsilon'_f - \varepsilon'_m)}{\varepsilon'_m + n(1 - v_f)(\varepsilon'_f - \varepsilon'_m)}\right)$
Bergman (3)	$\varepsilon' = \varepsilon'_m + \varepsilon'_f v_f\left(\frac{(\varepsilon'_m - \varepsilon'_f)}{\varepsilon'_f + n(\varepsilon'_m - \varepsilon'_f)}\right)$
Tinga (3)	$\varepsilon' = \varepsilon'_m + \varepsilon'_m v_f\left(\frac{(\varepsilon'_f - \varepsilon'_m)}{\varepsilon'_f + n_f(\varepsilon'_f - \varepsilon'_m) - n_m v_f(\varepsilon'_f - \varepsilon'_m)}\right)$

ε', ε'_m, ε'_f and v_f are the effective real dielectric of nanocomposite, real permittivity of matrix, real permittivity of filler and volume fraction of filler respectively.
n is a depolarization factor and n′ is a shape parameter for models in Group 3 (group denoted in parentheses)
n_m and n_f are factors corresponding to matrix and filler in the Tinga model

Table 4.3: Table showing dielectric data model fitting to real component of permittivity values obtained at 1 MHz using experimental volume fractions, real effective permittivity values of nanocomposites and the real permittivity of polystyrene.

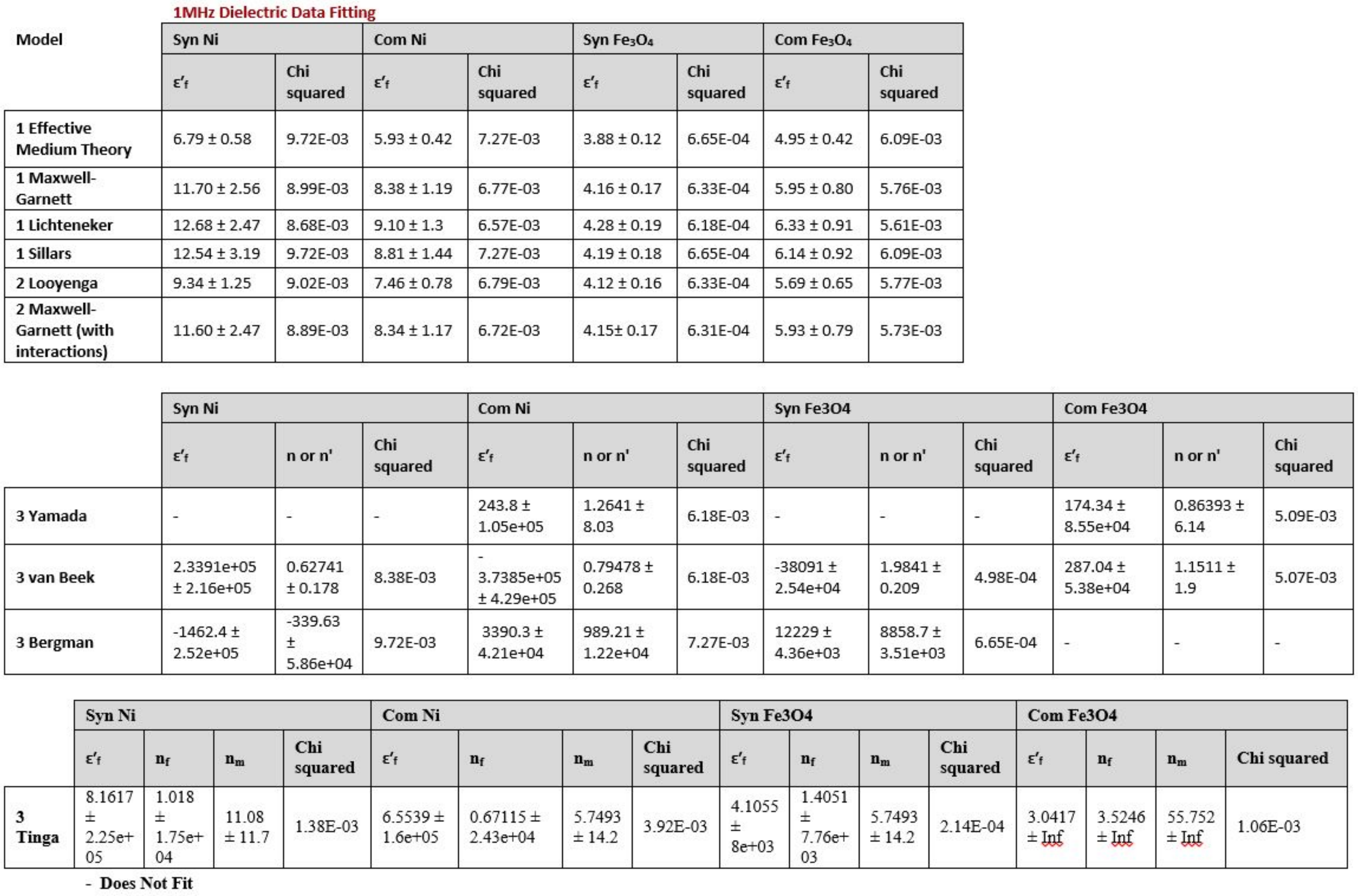

1MHz Dielectric Data Fitting

Model	Syn Ni		Com Ni		Syn Fe_3O_4		Com Fe_3O_4	
	ε'_f	Chi squared	ε'_f	Chi squared	ε'_f	Chi squared	ε'_f	Chi squared
1 Effective Medium Theory	6.79 ± 0.58	9.72E-03	5.93 ± 0.42	7.27E-03	3.88 ± 0.12	6.65E-04	4.95 ± 0.42	6.09E-03
1 Maxwell-Garnett	11.70 ± 2.56	8.99E-03	8.38 ± 1.19	6.77E-03	4.16 ± 0.17	6.33E-04	5.95 ± 0.80	5.76E-03
1 Lichteneker	12.68 ± 2.47	8.68E-03	9.10 ± 1.3	6.57E-03	4.28 ± 0.19	6.18E-04	6.33 ± 0.91	5.61E-03
1 Sillars	12.54 ± 3.19	9.72E-03	8.81 ± 1.44	7.27E-03	4.19 ± 0.18	6.65E-04	6.14 ± 0.92	6.09E-03
2 Looyenga	9.34 ± 1.25	9.02E-03	7.46 ± 0.78	6.79E-03	4.12 ± 0.16	6.33E-04	5.69 ± 0.65	5.77E-03
2 Maxwell-Garnett (with interactions)	11.60 ± 2.47	8.89E-03	8.34 ± 1.17	6.72E-03	4.15± 0.17	6.31E-04	5.93 ± 0.79	5.73E-03

	Syn Ni			Com Ni			Syn Fe3O4			Com Fe3O4		
	ε'_f	n or n'	Chi squared	ε'_f	n or n'	Chi squared	ε'_f	n or n'	Chi squared	ε'_f	n or n'	Chi squared
3 Yamada	-	-	-	243.8 ± 1.05e+05	1.2641 ± 8.03	6.18E-03	-	-	-	174.34 ± 8.55e+04	0.86393 ± 6.14	5.09E-03
3 van Beek	2.3391e+05 ± 2.16e+05	0.62741 ± 0.178	8.38E-03	-3.7385e+05 ± 4.29e+05	0.79478 ± 0.268	6.18E-03	-38091 ± 2.54e+04	1.9841 ± 0.209	4.98E-04	287.04 ± 5.38e+04	1.1511 ± 1.9	5.07E-03
3 Bergman	-1462.4 ± 2.52e+05	-339.63 ± 5.86e+04	9.72E-03	3390.3 ± 4.21e+04	989.21 ± 1.22e+04	7.27E-03	12229 ± 4.36e+03	8858.7 ± 3.51e+03	6.65E-04	-	-	-

	Syn Ni				Com Ni				Syn Fe3O4				Com Fe3O4			
	ε'_f	n_f	n_m	Chi squared	ε'_f	n_f	n_m	Chi squared	ε'_f	n_f	n_m	Chi squared	ε'_f	n_f	n_m	Chi squared
3 Tinga	8.1617 ± 2.25e+05	1.018 ± 1.75e+04	11.08 ± 11.7	1.38E-03	6.5539 ± 1.6e+05	0.67115 ± 2.43e+04	5.7493 ± 14.2	3.92E-03	4.1055 ± 8e+03	1.4051 ± 7.76e+03	5.7493 ± 14.2	2.14E-04	3.0417 ± Inf	3.5246 ± Inf	55.752 ± Inf	1.06E-03

- **Does Not Fit**

Imaginary Permittivity. As shown in figure 4.16, incorporation of synthesized nanoparticles into polystyrene exhibits a linear increase in ϵ'' with increasing volume percentage. The imaginary component of the dielectric for polystyrene is negligible[230], and therefore any change in ϵ'' reflects an increasing contribution from nanoparticle absorptivity. The ϵ'' value for increasing volume fraction of com-Ni and com-Fe_3O_4, where significant sedimentation is observed, scales non-linearly, and can be empirically fit to a power law behavior with n $\sim$ 2. The empirical fit to the power law is speculated to reflect contributions from the highly polarizable groups present in the PVP surface passivation layer of the com-Fe_3O_4. In this case, the passivation layer is non-negligible and therefore the ϵ'' value is anticipated scale as a surface to volume ratio with increasing volume fraction reflecting the ligand layer and greater interfacial polarization. Further studies are underway to evaluate the passivant dependent contributions to the dielectric scaling behavior.

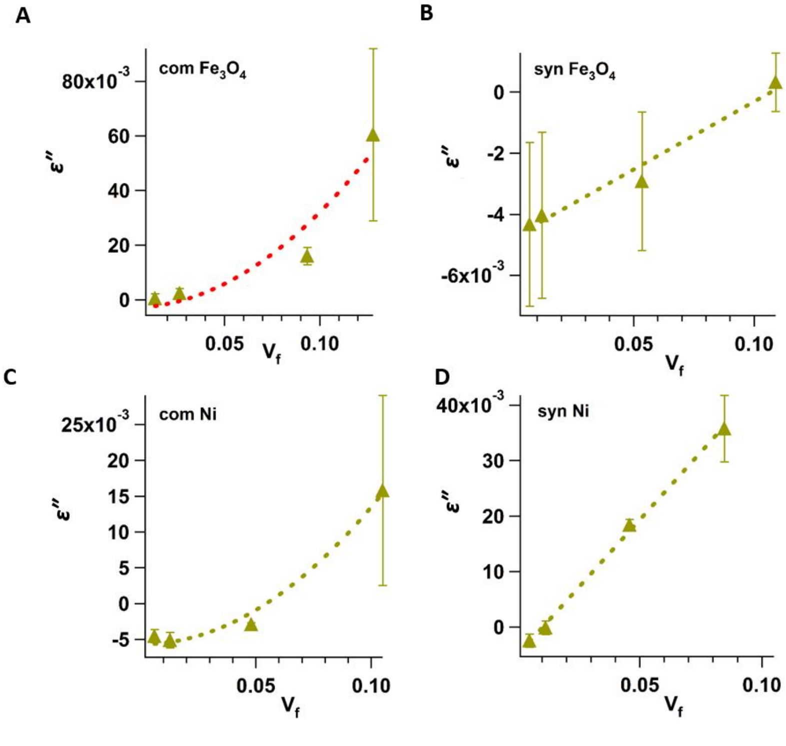

Figure 4.16: Imaginary permittivity (ϵ'') at 1MHz as a function of volume fraction for (a) com-Fe_3O_4, (b) syn-Fe_3O_4, (c) com-Ni and (d) syn-Ni nanocomposites with fitting using a linear (syn- samples) or power law (n=2, for com- samples).

Loss Tangent. In low k applications, the ϵ'' (imaginary dielectric) is an important parameter; however, the loss tangent ($\tan\delta_\epsilon = \epsilon''/\ \epsilon'$) is also critical as the low-k dielectric capacitance influences the performance of the electronic component through heating. The loss tangent, tan δ_ϵ, describes how lossy a material is in terms of dissipation of electrical energy. A low loss material has a tan δ_ϵ below 1.[185, 231] The frequency dependent loss tangent ($\epsilon''/\ \epsilon'$) for the nanocomposites is plotted in Figure 4.17. The nanocomposites are low loss materials over the entire compositional range with the exception of the com-Fe_3O_4 nanocomposite. Both com- samples exhibit the largest frequency sensitivity. At low frequencies, the nanoparticle ligands in the nanocomposite have sufficient time to polarize which is seen in the upward trend in both ϵ' and ϵ'' (Figure 4.14) as the frequency decreases to 0.1 Hz.[186, 232] Electrode polarization could also have led to this observed behavior.[233]

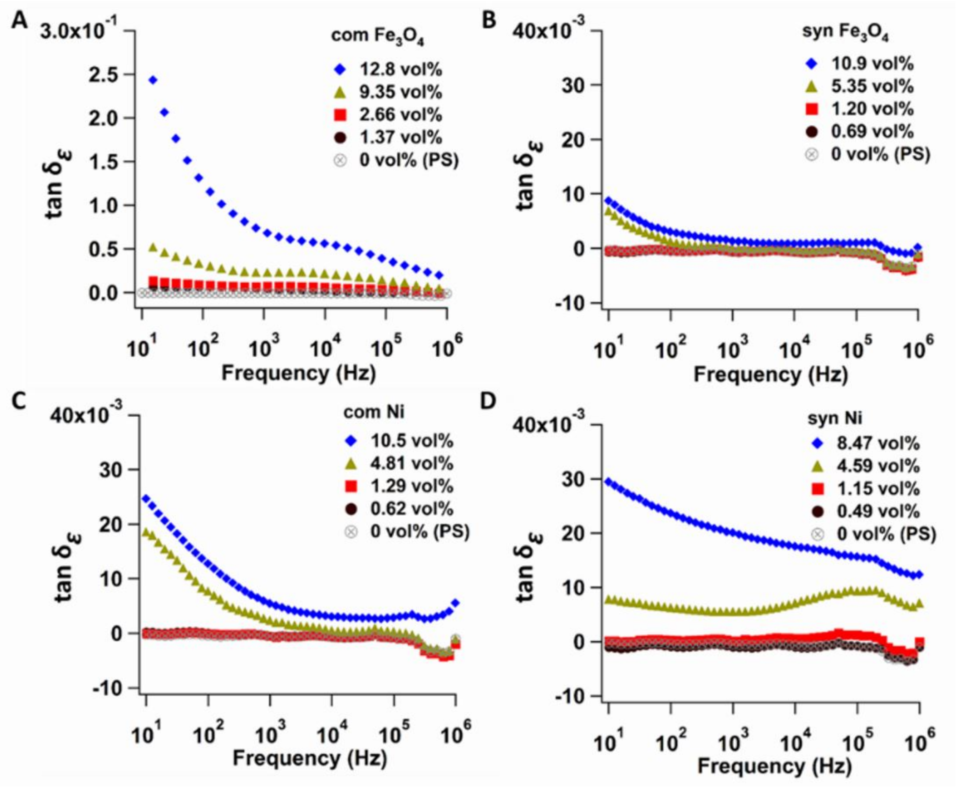

Figure 4.17: Frequency dependent (0.1 Hz 1 MHz) dielectric loss tangent (tan δ_ϵ) of (A) com-Fe_3O_4, (B) syn-Fe_3O_4 , (C) com-Ni, and (D) syn-Ni nanocomposites.

4.3.2 FDM Filament

To evaluate potential FDM printing compatibility, printable filament ($\sim$ 2.5 wt% from TGA analysis of filament) was produced using the low magnetic syn-Ni and the strongly magnetic com-Ni nanoparticles embedded in polystyrene. The filament is formed using a heated extruder to process the film three times yielding a fiber ready for printing applications. Although the fiber was not used in the printer, the cross-sectional distribution of Ni in the fiber was analyzed by SEM. As shown in Figure 4.18, the syn-Ni filament looks black to the eye, while the com-Ni filament appears to be a lighter shade which arises from the better dispersity of the syn-Ni versus com-Ni in the polymer. Cross-section analysis of the filaments indeed show that the overall nanoparticle distribution is more homogenous for the syn-Ni than the com-Ni in both, BSE mode and EDS mode. The application of these fibers for FDM printed low-k insulators in electronic architectures is underway.

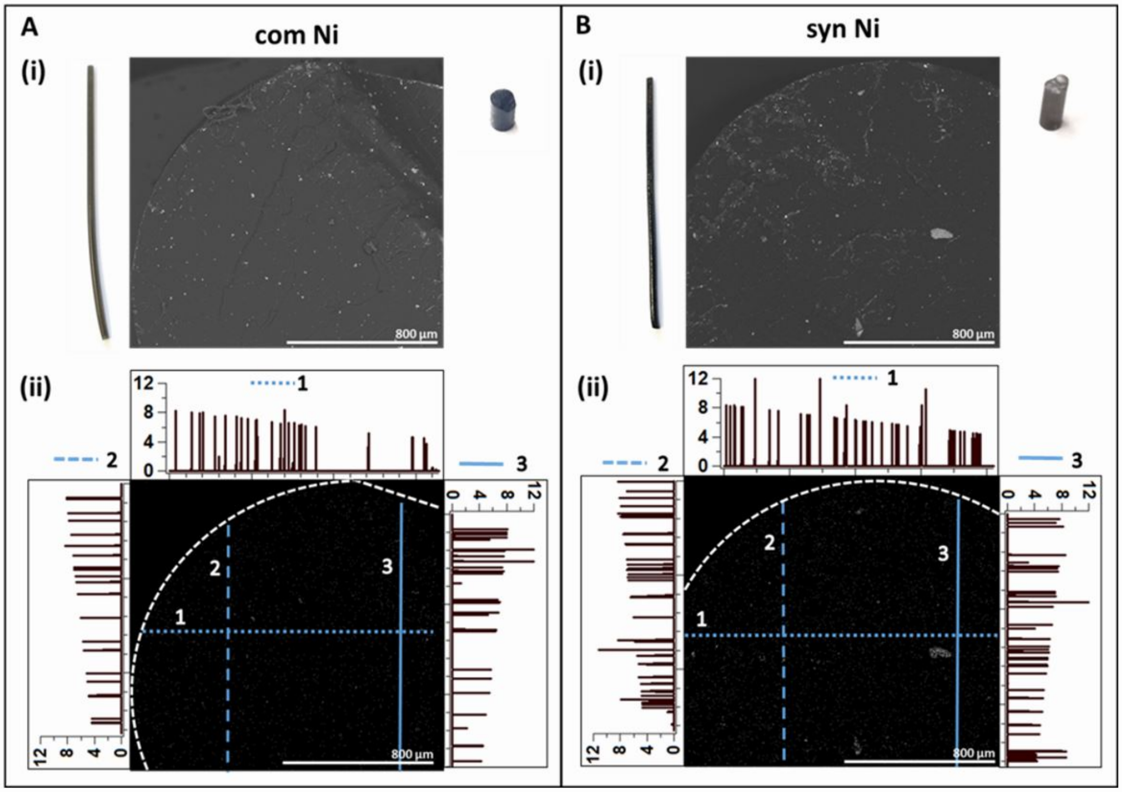

Figure 4.18: Photographs, BSE images and EDS mapping of (A) com-Ni, (B) syn-Ni nanocomposites filaments.

4.4 Conclusion

A systematic investigation into the incorporation of well-characterized monodisperse nanoparticles under 50 nm (diameter) of iron oxide and nickel into polystyrene was carried out in this work. The results demonstrate that the polystyrenene composite could be a viable candidate for a FDM printable materials, when the nanoparticles are uniform. The polymer composites are observed to be well fit to the Looyenga model. The agreement to the Looyenga model reflects the high dispersity of nanoparticles in the polymer, as evidenced by the SEM-EDS cross section analysis.

The data from the current study suggests that one can load polystyrene with small, monodisperse nanoparticles up to 40-50% wt% (10 vol%) and still maintain a low k composite system with low losses even when using a metallic filler like nickel. This is possible when the materials are well formed and passivated. Unlike certain previous work, our results show that incorporating small nanoparticles that have higher surface area compared to micron fillers, did not lead to increased dielectric losses in the nano-composite even when a metallic nickel filler was used. The dielectric components (ϵ' and ϵ'') for the nanocomposite decreased with increasing frequency before reaching a constant value excluding the syn-Ni nanocomposite at the highest volume fraction. As a proof of principle, nanocomposite filaments amenable to FDM printing were produced and shown to maintain their nanoparticle dispersions.

The low loss behavior for the nanocomposites over a wide frequency range for the syn- metallic and metal oxide fillers having small sizes and tight size distributions loaded up to physically attainable limits (50 wt%) was surprising. By comparison to literature the syn-materials all show better performance. The observation of better performance when synthetically prepared materials with well-defined size, size dispersity, and surface passivation are use as polymer fillers to produce low k , low loss materials should provide a new strategy for FDM printed technologies.

CHAPTER 5

ENERGY COUPLING BETWEEN CORE-SHELL NANOPARTICLES AND RED FLUORESCENT DYE MOLECULES

5.1 Introduction

One of the main uses of nanoparticles is in optical applications. The nanoparticles can used as light emitters like quantum dots or can be used as quenchers of light emitted by fluorophores in the vicinity as shown in the case of small gold nanoparticles. The use of the quenching ability of gold nanoparticles has found a range of applications especially in the biomedical field where the interaction of the nanoparticle and a fluorophore can be used to observe turn-on/turn-off events during the detection of an analyte or during the release of a dye-labeled payload in a cell. The distance-dependent non-radiative quenching of a fluorophore with a small gold nanoparticle has proven extremely useful as a biophysical tool for the real-time monitoring of structural changes in RNA and DNA structures.[77–82] The benefit of using a nanoparticle-dye pair for such applications over using a dye-dye pair (where FRET mechanism applies) is the ability to increase the interaction distance well beyond the 10 nm range that FRET can achieve.[15] The nanoparticle can be coupled to more than one acceptor simultaneously [81], or allow multimodal function where the nanoparticle can tether a payload while performing its role as a fluorescent quencher.[79] Lastly, the nanoparticle size can be adjusted to optimize the fluorescence quenching behavior for a particular range of distances being investigated.[74]

While the benefit of small gold nanoparticles is immense, the ability of small AuNPs to efficiently quench dyes that emit in the red wavelengths is poor. This is because the absorptivity of gold in wavelengths above 600 nm drops as the permittivity of the material is lower at those wavelengths (and the LSPR feature is typically around 520 nm).[15, 234] However, the red wavelength upto the near infrared (near-IR) wavelength window is the section in which absorption by biological tissue is minimum, making it a range where optical-based imaging or therapy is beneficial.[97] The absorptivity of gold nanoparticles can be increased in this region by manipulation of the dielectric around the particle. Silica-shelled gold nanoparticles have been shown to have higher absorption in red wavelengths[235], and the distant-dependent quenching behavior for such particles as well as zinc oxide-coated AuNPs has been shown to follow a distance^{-4} model consistent with NSET theory.[92, 93] While this approach could work, to probe biological structures without disrupting their structure or function, the use of smaller sizes of nanoparticles is preferred. A small nanoparticle with long-distance quenching behavior that is biocompatible would be ideal. This is possible by the use of layered core-shell nanoparticles that are designed to absorb more in the wavelengths of interest such as the therapeutic optical window for biological tissue.[101, 236] While core-shell structures are being pursued, the quenching behavior of gold-shelled high permittivity cores have not been studied in great detail to date. One reason for this maybe the challenge in the synthesis of uniform core-shell structures of small sizes and their characterization.[98–100] Theoretical calculations to predict the absorptivity of core-shell structures and experimental UV-vis absorption spectra consistently show that the increase in core permittivity will lead to increase in absorptivity of gold shelled nanoparticles.[101–104]

In this chapter, the synthesis of a core-shell nickel-gold nanoparticle and its ability to quench red dyes is shown. The use of a core material with higher imaginary permittivity as described in section 1.5 can be used to increase the absorptivity of a gold-shelled nanoparticle in red wavelengths.[101, 102] Nickel is known to have stronger absorptivity in the red wavelengths while the use of a gold shell enables biocompatibility and thiol chemistry.[102, 234] The synthesis and characterization of 3.3 nm Ni@Au NPs is shown followed by fluorescent quenching studies of 3.3 nm Ni@Au NPs and 3.5 nm AuNP using two red dyes, ROX and DyLt680. Distance-dependent measurements were carried out by using dye-labeled double-stranded DNA of various lengths for each dye. The emission intensity based studied show the higher quenching efficiency of the Ni@Au NPs compared to the AuNPs, and the quenching behavior fits a inverse forth-power distance curve consistent with the interaction between a nanoparticle and a fluorescent dye.

5.2 Materials and Methods

99% tetrachloauric acid hydrate ($HAuCl_4.xH_20$), 99% nickel acetate tetrahydrate, 1-octadecene, oleylamine (OAm) technical grade 70%, tri-octylphosphine (TOP), toluene, methanol (MeOH), chlorform, agrose, (50x) TAE buffer, sodium cyanide, glycerol, potassium carbonate, tannic acid, bis(p-sulfonatophenyl)phenylphosphine (BSPP), tris(2-carboxyethyl)phosphine (TCEP) hydrochloride, and sodium citrate were purchased from Sigma Aldrich. The materials were used without further purification.

CAAKA peptide was purchased from RS Synthesis LLC and used without further purification. Fluorescent dye-labeled single-stranded deoxyribonucleic acid (ssDNA) with thiol functionalization of different lenghts of base pairs (15bp, 30bp, 45bp and 60bp) were purchased from The Midland Certified Reagent Co. The dyes used for the labeling were ROX and DyLt680 and the sequences are as follows (5' to 3' direction):

(ROX-C6)-CGTTCCGTGTGCATACTGAATTCCGTGTTACTCTTGCCAACCTCG-(C6-thiol)
(DyLt680-C6)-CGTTCCGTGTGCATACTGAATTCCGTGTTACTCTTGCCAACCTCG-(C6
-thiol)
(C6 thiol)-CGAGGTTGGCAAGAGTAACACGGAATTCAGTATGCACACGGAACG
(ROX-C6)-CGTTCCGTGTGCATACTGAATTCCGTGTTA(-C6-thiol)
(DyLt680-C6)-CGTTCCGTGTGCATACTGAATTCCGTGTTA(-C6-thiol)
(thiol-C6)-TAACACGGAATTCAGTATGCACACGGAACG
(ROX-C6-)CGTTCCGTGTGCATA(-C6-thiol)
(DyLt680-C6-)CGTTCCGTGTGCATA(-C6-thiol)
(thiol-C6)TATGCACACGGAACG

5.2.1 Synthesis of Gold Nanoparticles

3.5 nm gold nanoparticles were synthesized by following a literature protocol by Puntes et al.[237]. A 150 ml solution containing sodium citrate (2.2 mM), tannic acid (2.5 mM) and potassium carbonate (150 mM) was added to a round bottom flask at 70°C. A 1 ml solution of 25 mM tetrachloroauric acid was then injected into the vigorously stirring solution and kept for 5 minutes before quenching the reaction in an ice-bath. 100 mg of BSPP was then added to the solution and allowed to stir overnight at room temperature to passivate the surface.

5.2.2 Synthesis of Nickel Nanoparticles

To synthesize the cores, 173 mg of nickel acetate, 7 ml of ODE and 1 ml of OAm were added to a G30 Anton Paar MW vessel sealed with a silicone septum and snap cap. The solution was heated at 100° for 30 min under vacuum before injection of 0.45 ml of TOP to the solution. The vial was back-filled with nitrogen gas before placing it in a Anton Paar Monowave 300 reactor. The solution was heated to 250° in 5 minutes and kept at temperature for 8 min before cooling down to 55°. Nanoparticles were cleaned using magnetic separation in the presence of toluene and excess MeOH. The particles were sonicated in fresh toluene and magnetically separated after addition of excess MeOH. This was done three times before drying them under vacuum.

5.2.3 Synthesis of Nickel-Gold Core-Shell Nanoparticles

40 mg of the nickel nanoparticles were added to 10 ml of chloroform in a round-bottom flask and sonicated till well dispersed. A solution of 85 mg of tetrachloroauric acid, 0.65 ml OAm and 10 ml of chloroform was added to the sonicating solution of nickel nanoparticles in chloroform at 1 ml every 15 minutes. 50 mg of sodium borohydride in 1 ml of cold methanol was added to the reaction 15 minutes after the last addition of the gold salt. This ensures complete reduction of the gold precursor. The reaction was let to sonicate for an additional 30 minutes before magnetic separation. Magnetic separation of the solution as-is led to a fraction of the nanoparticles to be separated, while a second smaller population of nanoparticles were magnetically separated after the addition of excess MeOH. The smaller, magnetic fraction of nanoparticles collected showed a plasmonic feature as expected in the case of a gold-shelled magnetic core, and were used for further experiments. The larger magnetic nanoparticles lacked a plasmon and were not further analyzed.

5.2.4 Phase Transfer of Nickel-Gold Core-Shell to Aqueous Media

5 mg of the Ni@Au nanoparticles were brought up in a 10 ml centrifuge vial with 1 ml of chloroform and kept under stirring using a small stirbar. 10 mg of peptide (CAAKA) dissolved in 1 ml of de-ionized water was added to the stirring solution of Ni@Au in chloroform. The reaction was allowed to stir for 10 minutes during which the nanoparticles phase transferred from the bottom chloroform solution to the top water layer.

5.2.5 Functionalization of Dye-labeled DNA to Nanoparticles

0.5 nmol of single stranded dye-labeled of a given length (15 bp, 30bp or 45bp)and its compliment thiol strand in 20 μl of de-ionized water were pipetted into a 0.6 ml Eppendorf tube. The tube was annnealed at 90° for 2 minutes in an aluminum heat block containing water and allowed to cool to room temperature before the addition of 2 μl of 50 mM TCEP solution (TCEP allows reduction of the dithiol bond in the double-stranded DNA sequence). The solution is allowed to react for 1 h in dark at room temperature before running the solution through a NAP-5 column to remove the excess TCEP which can potentially bind to the nanoparticle surface as well. 25 pmol of nanoparticles (in de-ionized water) is then added to the eluted dye-labeled DNA solution. The nanoparticle-DNA solution is kept to mix in the dark for 48 h after which standard ethanol precipitation protocol allows clean-up of the nanoparticles. This is performed twice to remove excess un-bound DNA after which the pellet is brought up in 200 μl of de-ionized water.

5.2.6 Transmission Electron Microscopy (TEM)and Energy-Dispersive X-ray Spectroscopy (EDS)

Nanoparticle samples were drop-cast, from toluene dispersion, onto 300 mesh carbon coated copper grids and left to dry under vacuum overnight. The TEM images were recorded using a JEM-ARM200cF electron microscope at 200 kV acceleration voltage. The EDS analysis is performed using the EDS detector (EDAX Si(Li) 30mm^2) detector equipped on the TEM system.

5.2.7 Powder X-Ray Diffraction (pXRD)

The pXRD patterns for Ni and gold-shelled Ni nanoparticles were acquired on a Rigaku Ultima III diffractometer equipped with a Cu-K source. Data was collected at room temperature, in the 2θ range of 10-84°.

5.2.8 Magnetic Measurements

Magnetic properties were studied with a superconducting quantum interference device (SQUID) magnetometer, MPMS-XL (Quantum Design). Field-dependent magnetization for nanoparticles was measured at 300 K, with the applied field varying from 0 T to 0.6 T and back down to - 0.2 T.

5.2.9 Thermogravimetric Analysis (TGA)

TGA was performed on a TA Instruments Q50 thermogravimetric analyzer. The samples were heated at a rate of 10 °C/min from room temperature to 100 °C in an alumina pan and held for 5 minutes before continuing to ramp at 10 °C/min to 600 °C). Measurements were performed under nitrogen environment.

5.2.10 X-Ray Fluorescence Spectroscopy (XRF)

XRF analysis of a small amount of the dried gold-shelled Ni nanoparticles was carried out using a Panalytical Epsilon 3 XRF instrument.

5.2.11 UV-Vis Absorption Spectroscopy

Solution absorption spectra for characterization of materials (dye-labeled DNA, nanoparticles, DNA-functionalized nanoparticles) and for quenching studies were taken using a Varian Cary 50 UV-visible spectrophotometer between 200 nm and 900 nm in a 0.3 cm quartz cuvette. A solvent background subtraction was carried out before taking measurments.

5.2.12 Fluorescence Spectroscopy

Solution fluorescence emission spectra for characterization of materials and for quenching studies were taken using a Varian Cary Eclipse spectrophotometer in a 0.3 cm quartz cuvette. Excitation wavelength used for ROX was 580 nm (collection from 590 nm to 800 nm) and for DyLt680 was 680 nm (collection from 690 to 900 nm).

5.2.13 Fluorescent Quenching Studies

The emission spectrum of a 55 μl solution of cleaned up functionalized nanoparticles was measured by absorption and emission spectroscopy before addition of 2 μl 2M dithiothrietol (DTT) (for Ni@Au nanoparticles) or 2 μl 2M sodium cyanide (NaCN) aqueous solution (for AuNPs with BSPP functionalization). Note: DTT was unable to completely release the dye-labeled DNA from the AuNP surface and therefore NaCN was used to etch away the AuNP.

5.2.14 Gel Electrophoresis

Gel electrophoresis was carried out in a horizontal gel box on ice with an applied voltage of 80 V across the terminals (14 cm apart). A 1% agrose gel made using 0.5 g of agrose and 50 ml of 1x TAE buffer was cast with plastic comb and allowed to set. Once the gel was ready, 1x TAE buffer was added to the gel box, after which a mixture of 3:1 V:V ratio of nanoparticle solution and 50% glycerol was pipetted into the wells (20 μl. The gel electrophoresis was started after loading of the wells and allowed to run for 20 min. Photographs of the gel were taken with a cellphone camera at 0, 10 and 20 min.

5.3 Results and Discussion

5.3.1 3.5 nm Gold Nanoparticles

Following the method by Puntes et al., citrate-capped gold nanoparticles of 3.5 nm diameter were synthesized. The weak citrate capping ligand for gold was exchanged with the stronger binding BSPP ligand that ensured long term stability of the nanoparticles for experiments. The TEM of the 3.5 (±0.46) nm nanoparticles and the UV-vis absorption spectra are shown in figure 5.1. The absorption spectra show the characteristic LSPR of gold nanoparticles and the peak maximum for the citrate-capped AuNPs at 507 nm matched the values by Puntes et al. Upon addition of BSPP, a red-shift of the LSPR peak to 517 nm due to the change in surface ligand environment was noted. Gel electrophoresis data of the gold nanoparticles is shown later in 5.9.

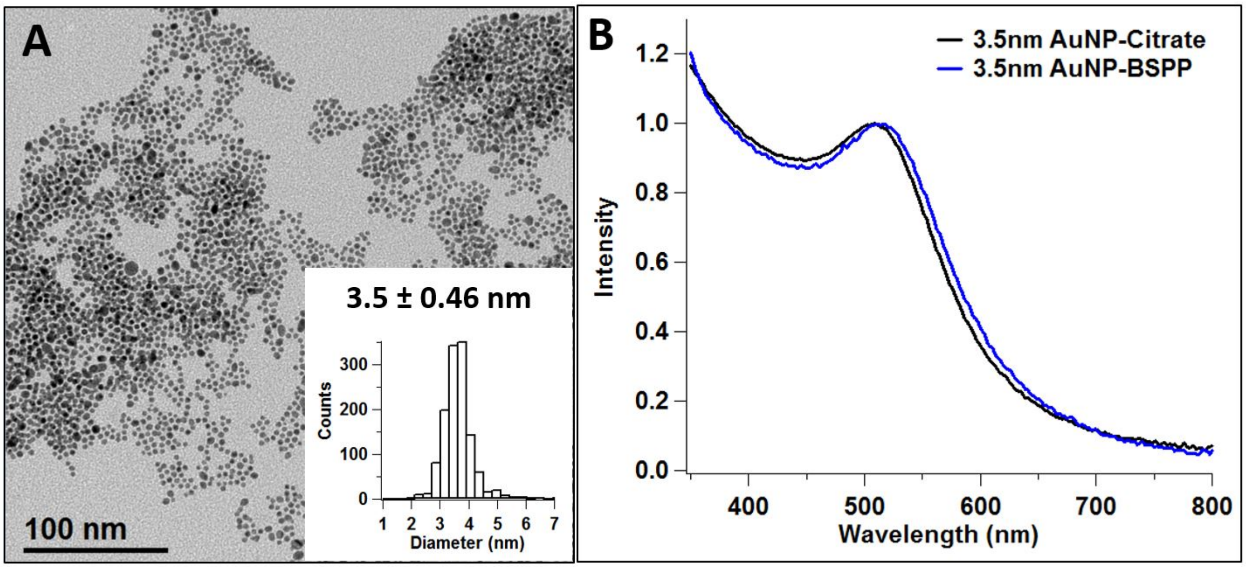

Figure 5.1: (A) TEM of 3.5 nm AuNPs with BSPP functionalization. (B) Solution UV-Vis absorption spectra of 3.5 nm AuNPs with citrate and BSPP functionaliztion.

5.3.2 Nickel and Nickel-Gold Core-Shell Nanoparticles (Ni@Au)

The microwave synthesis of nickel nanoparticles using the nickel (II) acetate precursor, OAm and TOP in 1-ODE resulted in the production of uniform faceted nanoparticles of 22 (±3) nm diameter (figure 5.2A) that had a saturation magnetization moment of ∼15 emu/g and were of face centered cubic crystalline structure from p-XRD measurements (figure 5.3 A and B). The fraction of small plasmonic Ni@Au NPs were found to be of diameter 3.3 nm (±0.7) nm and quite uniform as seen in figure 5.2B. The formation of such small structures can be attributed to the redox chemistry between the gold salt and nickel nanoparticles where the higher reduction potential of gold salt to neutral gold (+1 V) compared to that of Ni^{2+} to Ni^0 would drive the etching reaction. This redox process has been observed previously.[238]

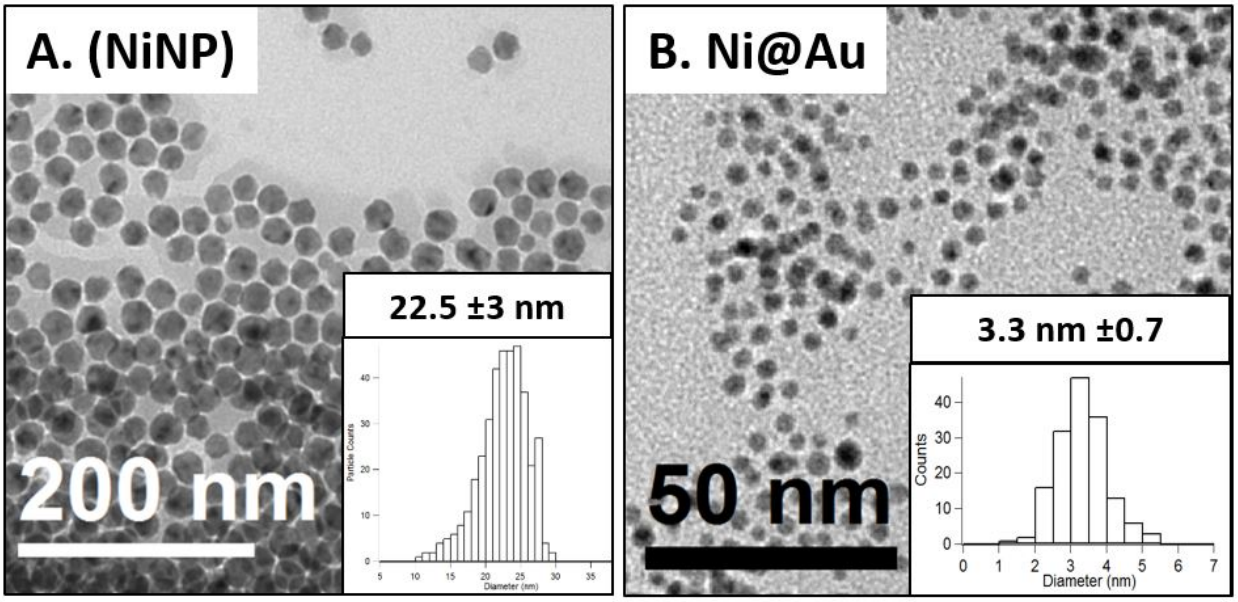

Figure 5.2: TEM of (A) NiNPs and (B) Ni@Au NPs with respective size distributions (insets).

Results from magnetic measurements of the Ni@Au nanoparticles as shown in figure 5.3C confirm the presence of a magnetic material that can be magnetically separated but has a very low saturation magnetization due to the small core size and presence of a dense diamagnetic gold shell which reduces the moment. Powder XRD of the Ni@Au nanoparticles shows a strong (200) peak from the fcc gold shell and the presence of other fcc peaks corresponding to gold and nickel. The strong domination of the powder-XRD by the gold arises from the heavy-atom effect, where gold being much higher in atomic mass, can scatter the X-rays much more than a lighter core.[99] Additionally, the heavier gold being the shell material is able to mask the inner lighter elemental core. This has been observed previously and gives an indication of how well the shelling has taken place.[236] Additionally, if the sample was a mixture of gold and nickel nanoparticles, the intensity of the nickel fcc peaks would not be heavily reduced.

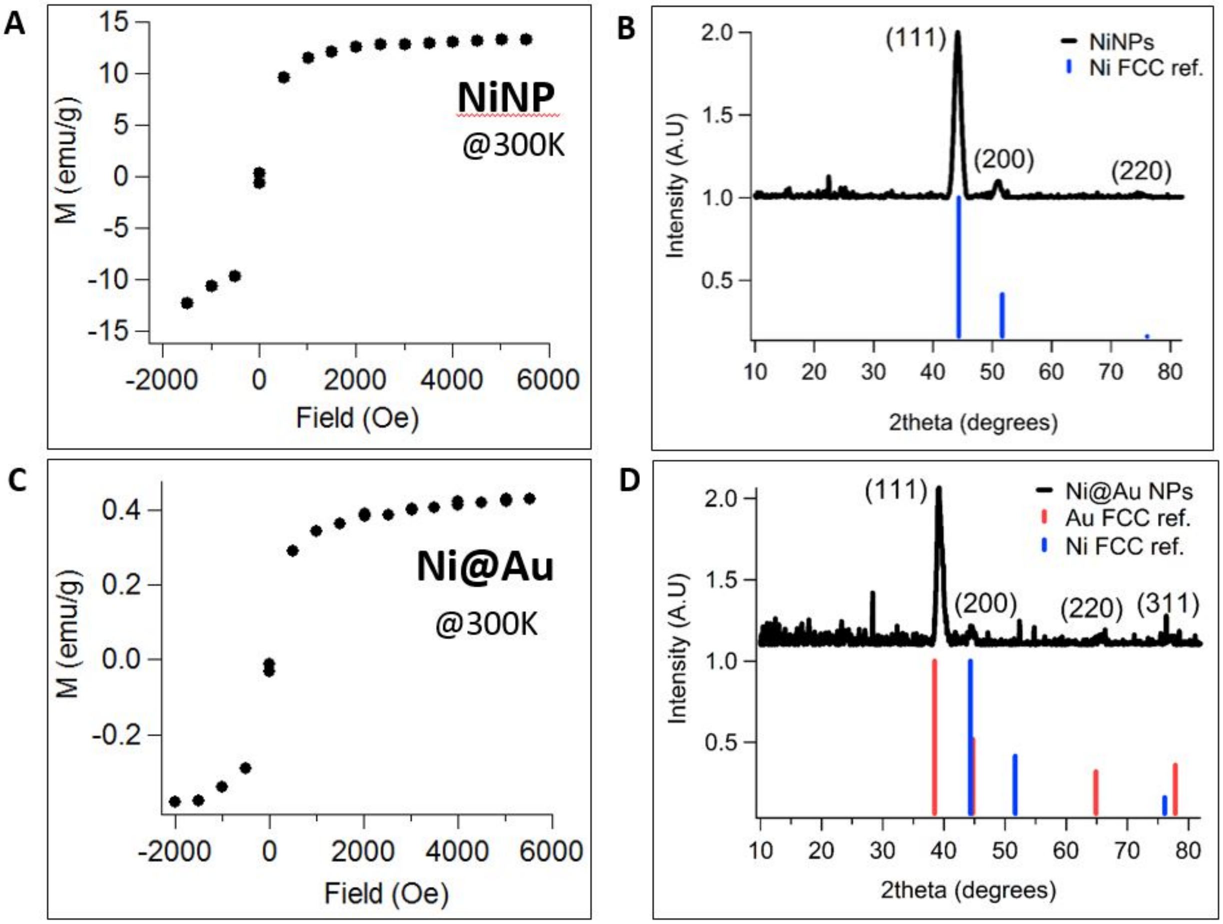

Figure 5.3: (A and C) 300K field-sweep of NiNPs and Ni@Au NPs, and (B and D) p-XRD of NiNPs and Ni@Au NPs.

The magnetic data for 3.3 nm Ni@Au shows a saturation moment of only 0.4 emu/g which is much lower than that for a ∼4 nm NiNP at 300K (2 emu/g) made by Lee et al.[239]. Unfortunately, temperature-dependent magnetic measurements were not obtained on the samples for NiNP and Ni@Au NPs. Analysis of the Ni@Au NPs by EDS during TEM imaging shows the presence of the both Ni and Au in the sample (figure 5.4). Atomic percentage of the Ni and Au in the sample was found to be 35 (±5)% and 65 (±7)% which is in good agreement with XRF analysis (35% for Ni and 60% for Au). Based off the elemental analysis, TEM diameter of the particles, and using densities of the elements, the 3.3 nm Ni@Au structure would be comprised of a 2.1 nm diameter Ni core with a 0.6 nm thick shell of gold. A graphic representing this structure is shown in figure 5.5.

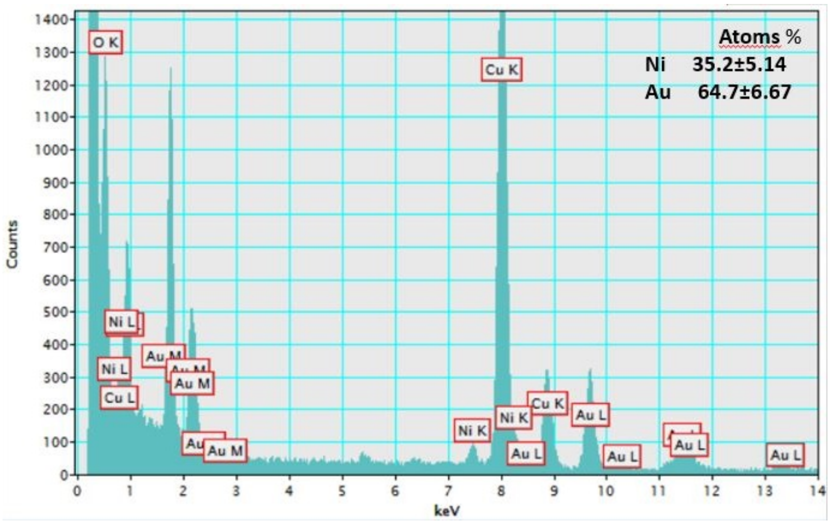

Figure 5.4: EDS spectrum for 3.3 Ni@Au NPs taken during TEM showing the presence of Ni, Au, Cu (from TEM grid), O (trace presence in instrument) and C (from grid and ligands). Quantification of elements was carried out using the Gatan DM3 software that operates the TEM system.

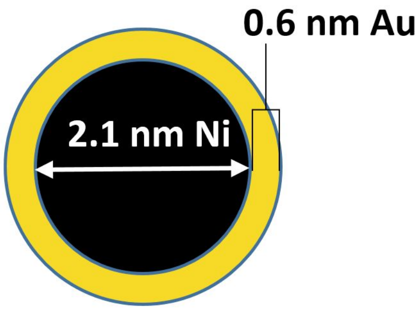

Figure 5.5: Graphic depicting structure of core-shell Ni@Au particle based off of TEM size and XRF/EDS elemental analysis data.

UV-vis absorption spectra of the NiNPs and Ni@Au NPs in toluene as seen in figure 5.6 show the lack of a LSPR feature in the NiNP spectrum in the visible range, but the presence of a LSPR peak is observed in the Ni@Au spectrum indicative of successful shelling with gold. Although not easily distinguishable from a pure gold nanoparticle, the absorption spectrum of Ni@Au shows a slightly broader LSPR feature and shows higher absorptivity in the wavelengths above 550 nm.

5.3.3 Phase-Exchange of Ni@Au Nanoparticles

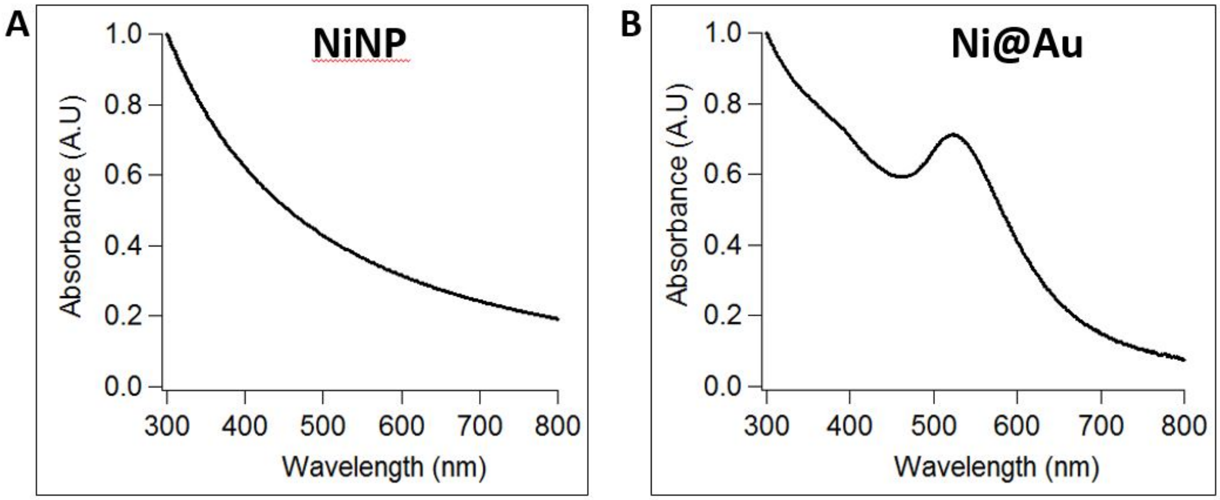

Figure 5.6: UV-vis absorption spectra of (A) NiNPs and (B) Ni@Au NPs in toluene.

Biphasic exchange of the Ni@Au NPs was carried out to make the nanoparticles soluble in water for DNA functionalization.

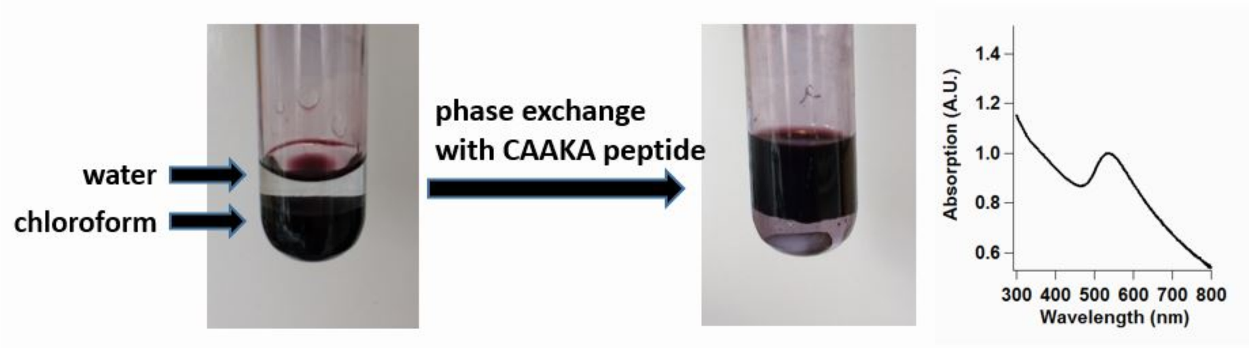

Figure 5.7: Photographs showing biphase exchange of Ni@Au NPs from chloroform to water using peptide (CAAKA) and UV-Vis absorption spectrum of Ni@Au-peptide functionalized NPs in de-ionized water.

This was achieved by the use of a peptide (CAAKA) containing an N-terminus cysteine. The strong affinity of the thiol functional group in the cysteine amino acid can bind to gold surface. An N-terminus cysteine also contains an amine group that can possibly participate in bidendate binding of the cysteine to the gold. As seen in figure 5.7, the nanoparticles move from the bottom chloroform layer to the aqueous layer and maintain the plasmonic absorption feature. The complete transfer of the nanoparticles from the organic layer to the aqueous layer is indicative of gold-shelled nanoparticles and not a mixture of gold and nickel nanoparticles. The nanoparticles were cleaned using ethanol precipitation to remove excess peptide before DNA functionalization.

5.3.4 Optical Properties of Fluorescent Dyes Used in Quenching Experiments

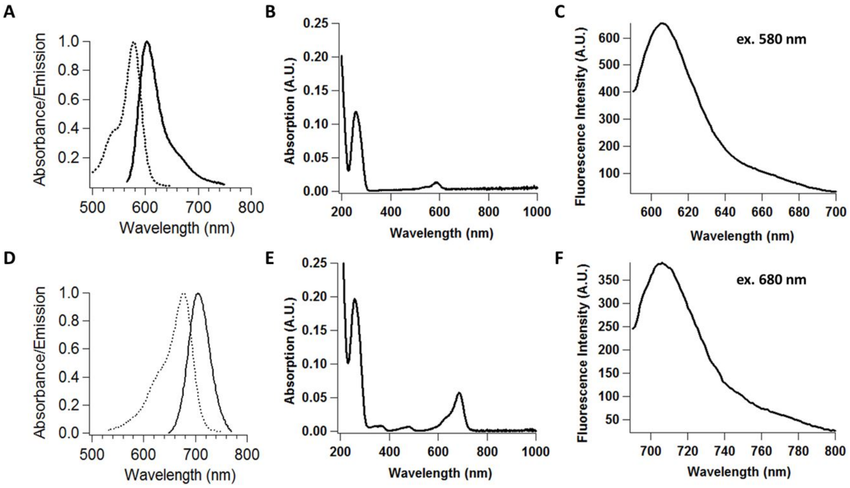

Figure 5.8: (A) Absorption and emission spectra of ROX dye, (B) absorption and (C) emission spectra of a ROX dye-labeled 15bp dsDNA in water, (D) absorption and emission spectra of DyLt680 dye, (E) absorption and (F) emission spectra of a ROX dye-labeled 15bp dsDNA in water.

The two dyes used in the quenching studies are ROX and DyLt680. ROX has an absorption maximum at 575 nm (extinction of 82,000 $cm^{-1}M^{-1}$), an emission maximum of 609 nm, a quantum yield of 0.7 and a lifetime of 4.38 ns.[15] Likewise, DyLt680 has an absorption maximum at 680 nm (extinction of 140,000 $cm^{-1}M^{-1}$), an emission maximum of 710 nm, a quantum yield of 0.21 and a lifetime of 1.68 ns.[15]. The absorption and emission features of the dyes are shown in figure 5.8 A and D. Absorption of 15bp double stranded DNA coupled with ROX and DyLt680 is shown in figure 5.8 B and E respectively, while figure 5.8 C and F show the emission profile for the ROX-labeled DNA (excited at 580 nm) and DyLt680-labeled DNA (excited at 680 nm) respectively. The dyes were chosen based on the knowledge that the ability of pure AuNPs to quench red dyes is limited owing to the poor absorptivity in those wavelengths while the absorptivity of nickel is much higher in the red wavelengths in comparison to gold. It is therefore expected that a core-shell Ni@Au nanoparticle with higher absorptivity in the red wavelengths will quench these dyes to a greater extent than a similar size AuNP.

5.3.5 Gel Electrophoresis

To validate formation of nanoparticl-DNA constructs, gel electrophoresis was carried out with selected samples. Movement of material in a gel is dependent on the size and charge. Nanoparticles with negatively charged ligands will move towards the positive terminal and typically smaller sized nanoparticles move faster than larger bulky structures. In this case, it is expected that nanoparticles functionalized with long DNA strands will move slower in comparison to nanoparticles with only short ligands (peptide or BSPP). The negative charged phosphate backbone of DNA allows the nanoparticles to move towards the positive terminal as well. The results for the gel electrophoresis are shown in figure 5.9. As expected, all samples for DNA-functionalized Ni@Au NPs with different lengths of DNA move in the negative direction along with the peptide-functionalized 3.3 nm Ni@Au and BSPP-functionalized 3.5 nm AuNP. All bands appear to move without significant smearing. The smaller 3.3 nm Ni@Au NPs move faster through the 1% agrose gel when compared to the 3.5 nm AuNPs, and also slightly faster than the DNA-functionalized Ni@Au NPs. Movement of the Ni@Au NPs and DNA-functionalized Ni@Au indicates that the material is not aggregated. The dsDNA functionalized Ni@Au samples are observed to move at a similar rate possibly because the difference in lengths between samples is not enough to allow significant retardation of the band.[240] The Ni@Au with ROX-labeled 15bp dsDNA (band 6) and DyLt680-labeled 15bp dsDNA (band 3) appear to have disappeared because their concentration was low.

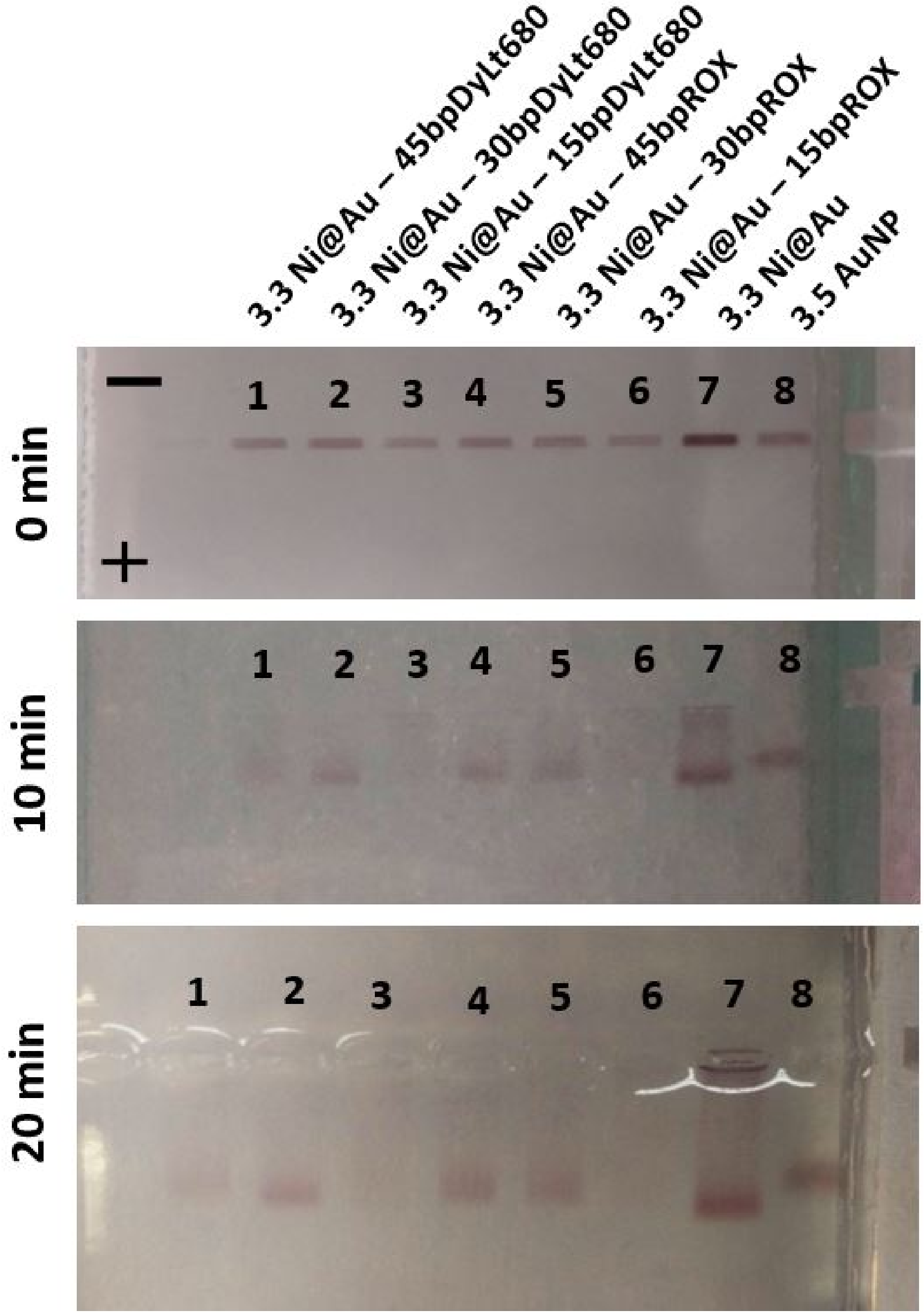

Figure 5.9: Photographs at various time-points of 1% agrose gel loaded with DNA-functionalized Ni@Au nanoparticles along with peptide-functionalized 3.3 nm Ni@Au and BSPP-functionalized 3.5 nm AuNP. The gel electrophoresis was carried out in a 1x TAE buffer over ice with an application of 80V across the gel box (14 cm length).

5.3.6 Fluorescence Quenching of ROX and DyLt680 by AuNPs and Ni@Au NPs

Fluorescent quenching studies to investigate the distant-dependent quenching of a core-shell nickel-gold nanoparticle in comparison to a gold nanoparticle of similar size were carried out by attaching a fluorophore (dye) to the nanoparticles using a rigid spacer of known distance. Based on the Clegg model, double-stranded DNA can be considered rigid for B-DNA under 100 base pairs (bp).[15] The use of dsDNA has been used routinely by the Strouse group to perform distant-dependent quenching studies, and these DNA sequences with terminal dye functionalization are commercially available. In a typical setup, the emission of the nanoparticles functionalized with the dye-labeled nanoparticles are first taken to obtain the quenched emission signal from the sample. The dye-labeled DNA is then detached from the nanoparticle by either out-competing the surface-bound DNA strand with another strongly binding molecule, or by dissolving the nanoparticle using sodium cyanide. Emission measurement on the sample after detachment of the dye-labeled DNA is then taken and gives the unquenched signal. This method allows emission from the same sample before and after quenching, which ensures that the signal is coming from the same number of dye molecules in both cases. It is assumed that after two rounds of ethanol precipitation clean-up post-labeling of nanoparticles, the emission signal coming from the samples is from bound dye-labeled DNA. The quenching percentage can be calculated by taking the fraction of area under the emission curve for the quenched sample over the unquenched sample and subtracting it from 100%. Obtaining the quenching at different distances from the surface allow for plotting of quenching versus distance which can then be fit to a quenching curve. Experiments for the Ni@Au samples with dye-labeled DNA were carried out by addition of excess DTT which successfully released the dye-labeled DNA strands as shown in figures 5.10 and 5.11. The same method unfortunately did not work effectively with the AuNPs and therefore NaCN was used in the quenching studies. The absorption and emission data for the AuNPs functionalized by ROX and DyLt680 using different lengths of DNA is shown in figures 5.12 and 5.13 respectively. It was noted that nanoparticle clean up procedure for these small nanoparticles after DNA-functionalization led to inefficient recovery of material preventing use of higher concentration samples. Despite the use of 20 fold excess mols of dye-labeled DNA during functionalization, loading of the 15bp DNA with either dye was poor compared to other lengths, which could be due to an issue with the material lots ordered.

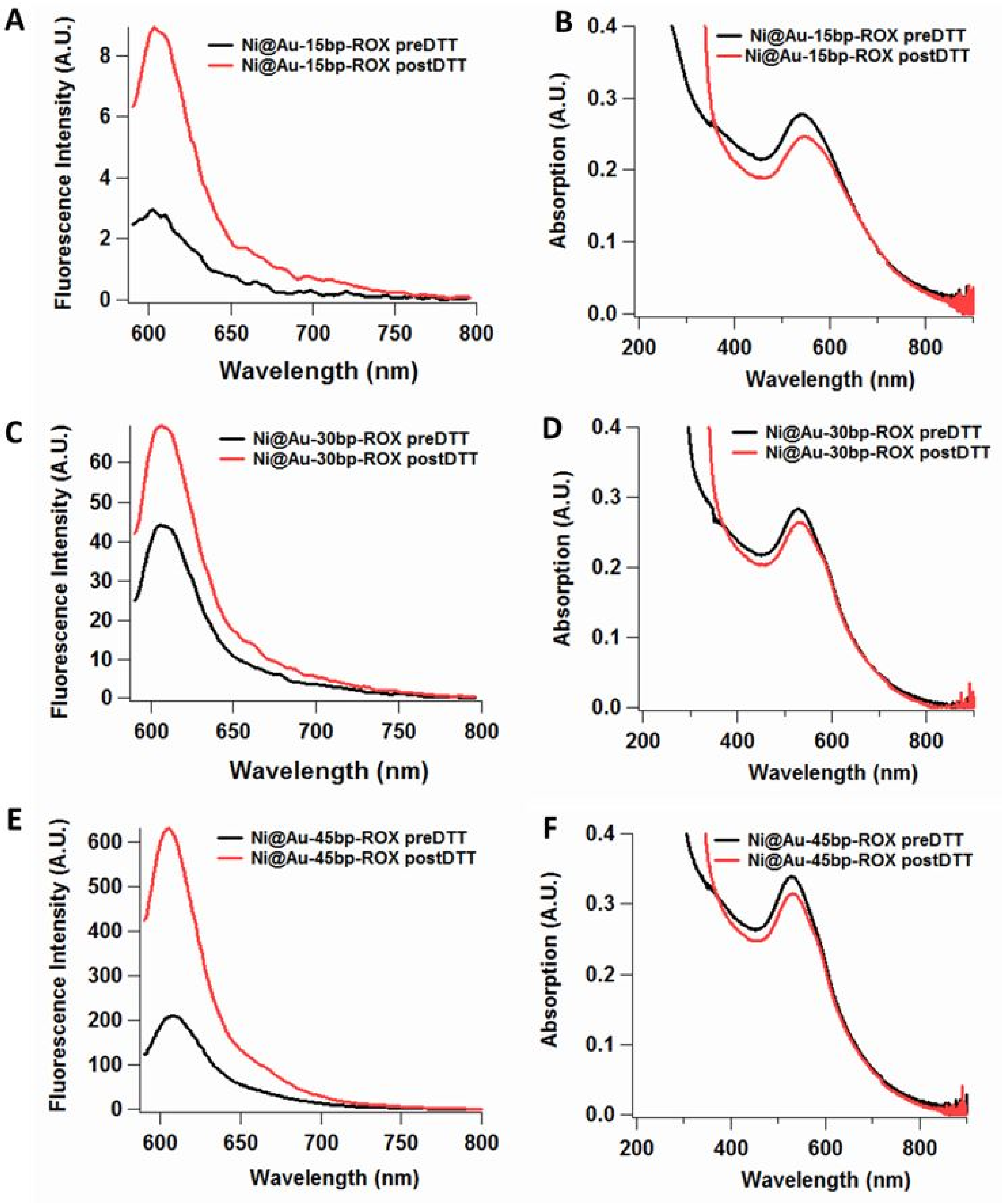

Figure 5.10: Fluorescence emission (A,C,E) and respective absorption (B,D,F) data for 3.3 nm Ni@Au NPs functionalized with different lengths (15bp, 30bp, 45bp) of ROX-labeled dsDNA pre- and post-DTT treatment.

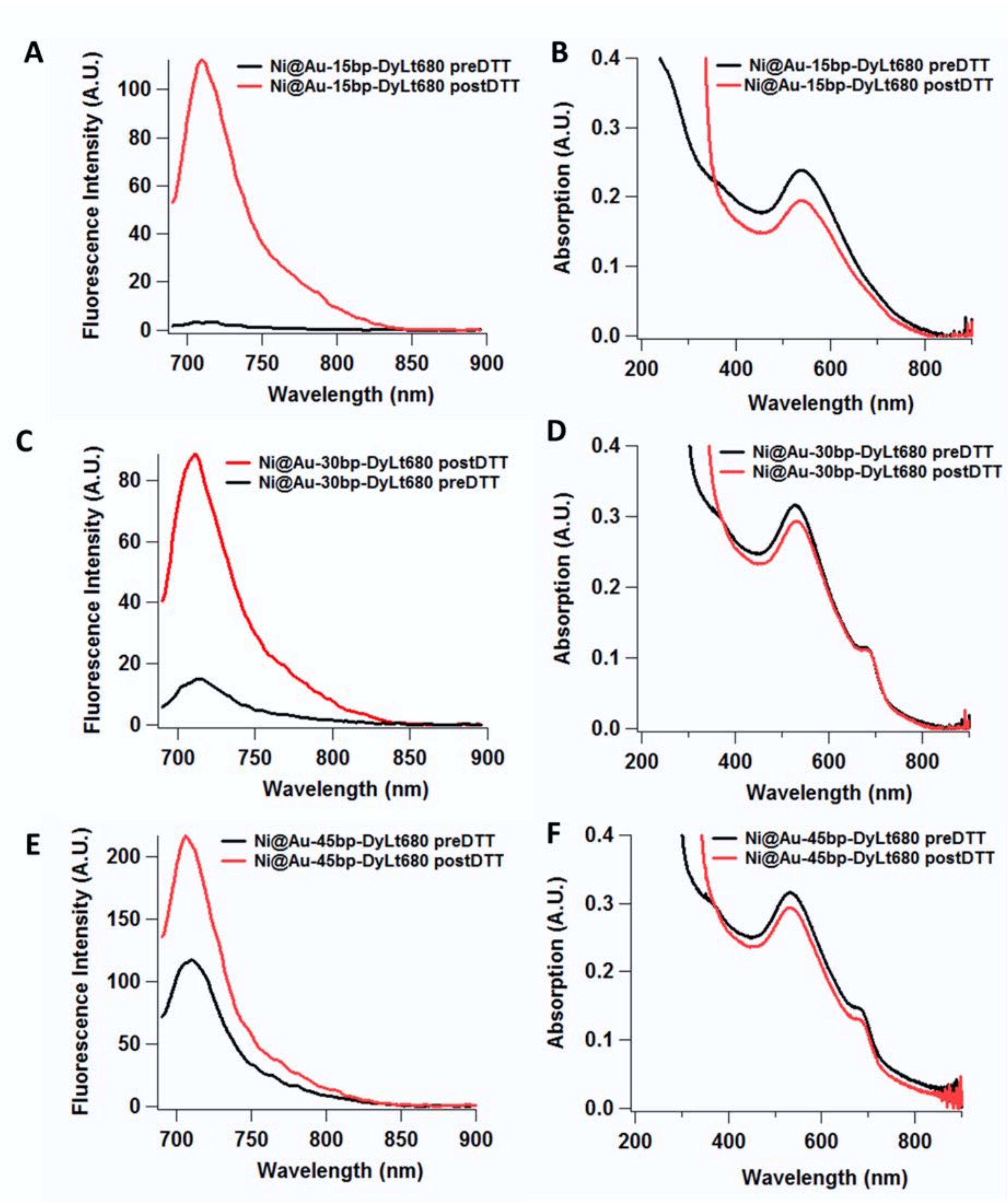

Figure 5.11: Fluorescence emission (A,C,E) and respective absorption (B,D,F) data for 3.3 nm Ni@Au NPs functionalized with different lengths (15bp, 30bp, 45bp) of DyLt680-labeled dsDNA pre- and post-DTT treatment.

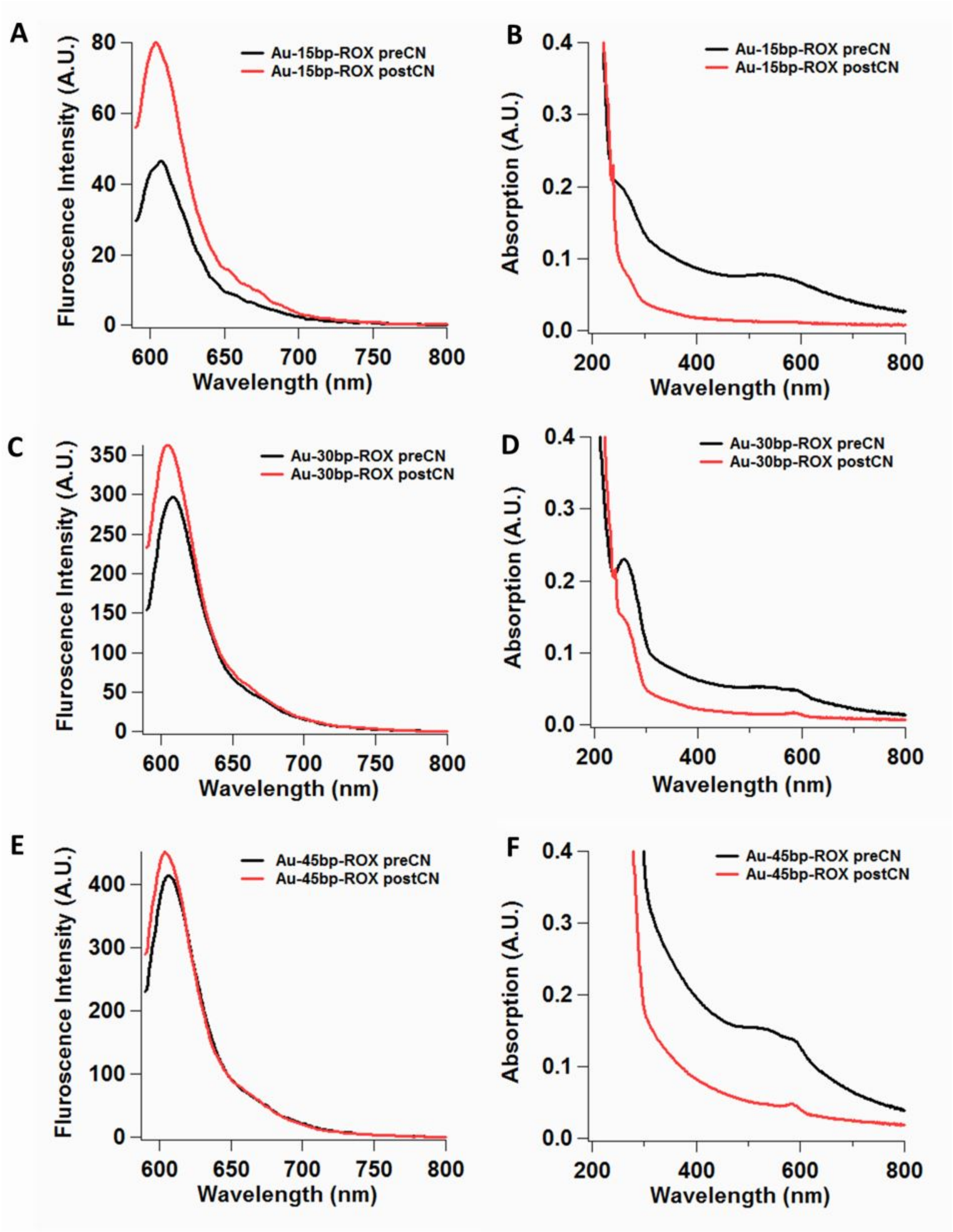

Figure 5.12: Fluorescence emission (A,C,E) and respective absorption (B,D,F) data for 3.5 nm AuNP functionalized with different lengths (15bp, 30bp, 45bp) of ROX-labeled dsDNA pre- and post-CN treatment.

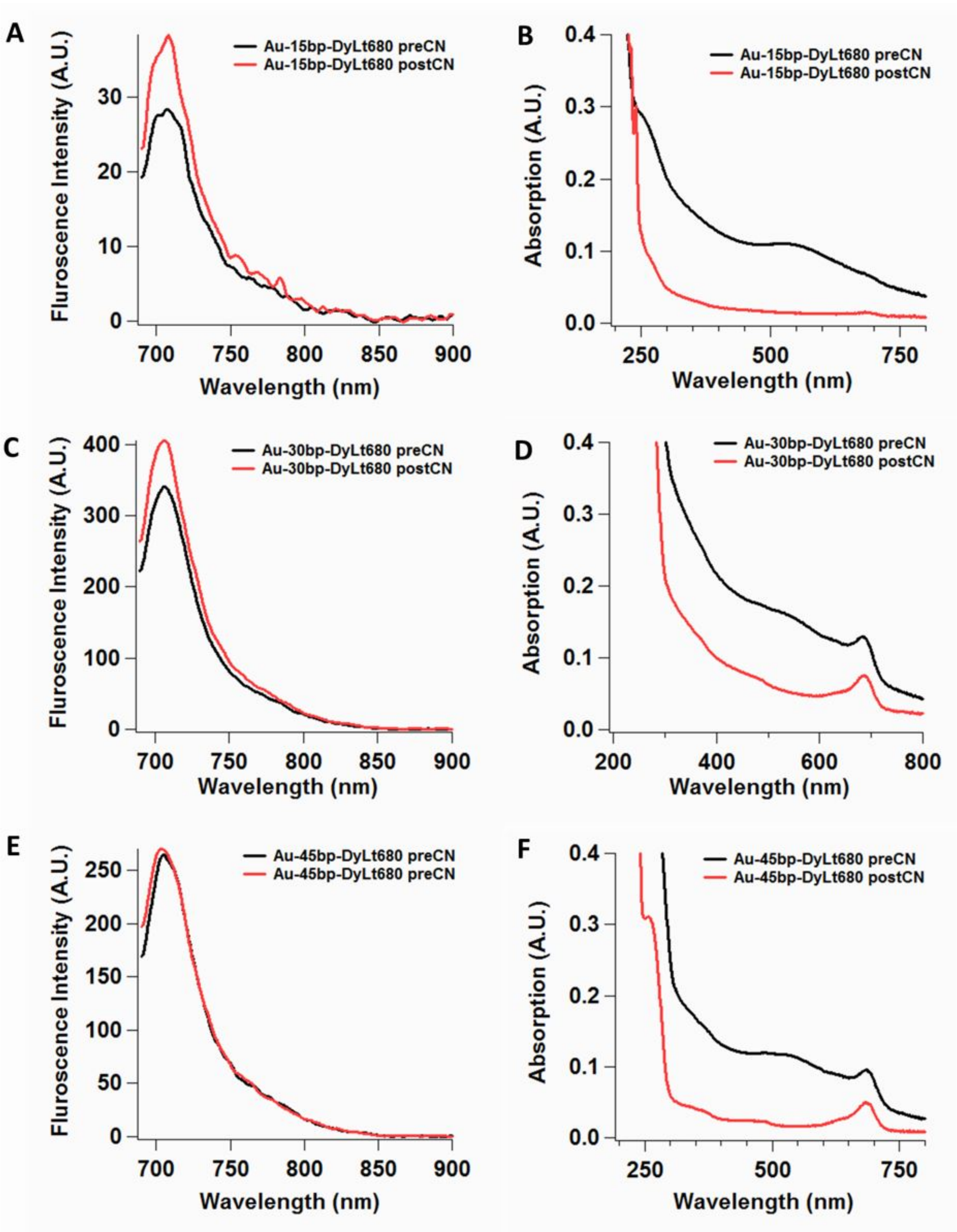

Figure 5.13: Fluorescence emission (A,C,E) and respective absorption (B,D,F) data for 3.5 nm AuNP functionalized with different lengths (15bp, 30bp, 45bp) of DyLt680-labeled dsDNA pre- and post-CN treatment.

Experimental data from the quenching studies clearly show that fluorescence recovery takes place upon addition of DTT in the case of Ni@Au or addition of NaCN in the case of AuNP. This fluorescence recovery decreases as a function of increasing base-pair length of DNA space as expected from distant-dependent quenching. The emission data also shows that quenching of ROX was higher than that of DyLt680 for 3.3 nm Ni@Au and 3.5 nm AuNP as expected. The results are more easily displayed in figure 5.14 where the quenching is plotted as a function of distance in nm.

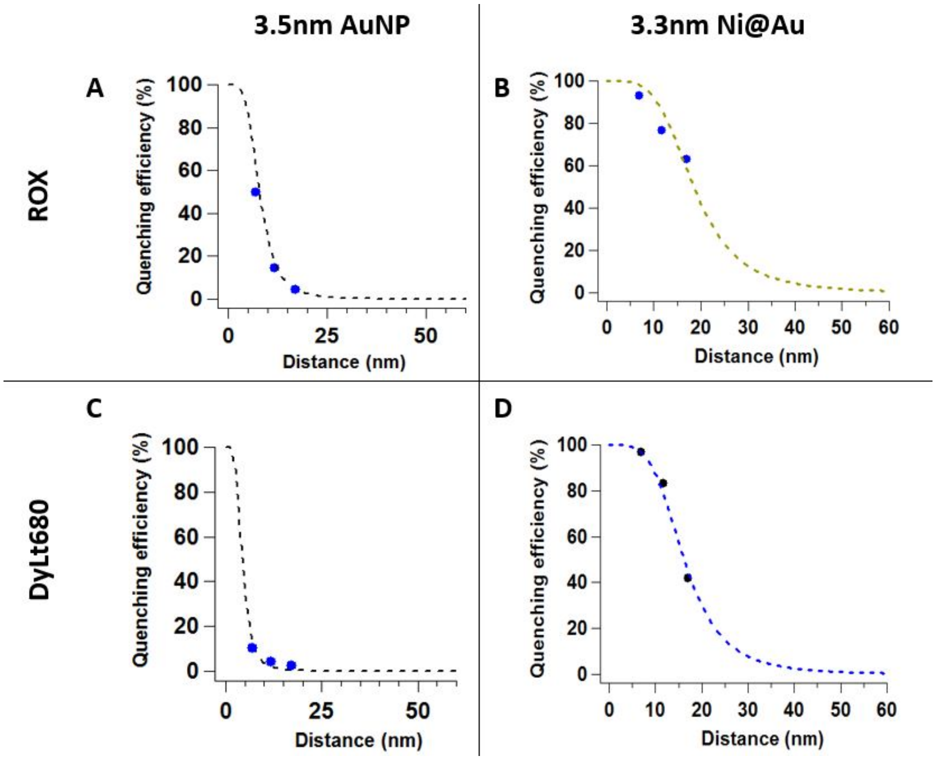

Figure 5.14: Quenching efficiency versus distance curves for experimental data for (A) 3.5 nm AuNP and ROX, (B) 3.3 Ni@Au NP and ROX, (C) 3.5 nm AuNP and DyLt680, and (D) 3.3 nm Ni@Au NP and DyLt680. Dotted lines represent distance^{-4} dependent quenching curves.

The corresponding distances for dsDNA spacers of 15, 30 and 45 base pairs are 6.8, 11.7 and 17.0 nm respectively.[15] The dotted lines represent a quenching curve fit function of the form:

$$Q_{eff} = \frac{1}{1 + \left(\frac{d}{d_0}\right)^4} \tag{5.1}$$

where Q$_{eff}$ is the quenching efficiency given in percentage, d is the distance between the dye and nanoparticle surface, and d$_0$ is the 50% quenching distance at which fluorescence intensity of the dye is 50% quenched by the nanoparticle. It can be observed from the fitting that the quenching behavior can be fit to an NSET model that follows a forth power dependent behavior with respect to distance between the nanoparticle and the dye. The quenching function fitted in Igor Pro 4.0 yielded d$_0$ of 6.27 (± 0.31) nm, 4.04 (± 0.28) nm, 18 (± 1.4) nm, and 16 (± 0.55) nm for 3.5 nm AuNP-ROX, 3.5 nm AuNP-DyLt680, 3.3 nm Ni@Au NP-ROX, and 3.3 nm Ni@Au NP-DyLt680 respectively. The experimental d$_0$ values for the 3.5 nm AuNP are slightly below the predicted value by the size-dependent NSET model: 6.27 nm (experimental) versus 7.97 nm (model) for ROX, and 4.04 nm (experimental) versus 4.3 nm (model) for DyLt680.[15] The experimental d$_0$ for 3.3 nm Ni@Au are significantly greater than the values for the corresponding 3.5 nm AuNP suggesting the absorptive role of the Ni core as well. The imaginary component of the permittivity (ϵ') that corresponds to absorptivity is shown in figure 5.15 for both gold and nickel. The values were obtained from the work by Johnson and Christy.[234] It is clear that Ni has a much higher absorptivity than that of Au for the range of the red dyes.

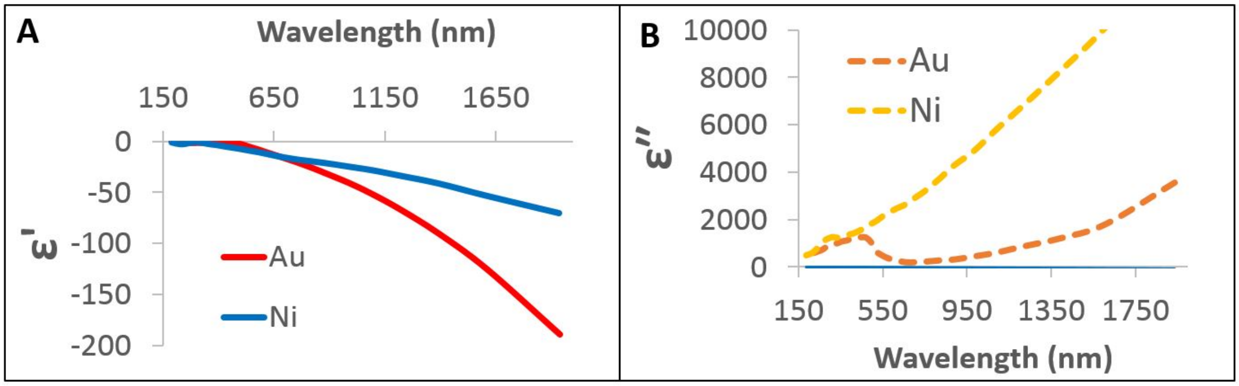

Figure 5.15: (A) Real component of the permittivity for Au and Ni, and (B) imaginary component of the permittivity for Au and Ni. Values obtained from Johnson and Christy.

Modification of the NSET model to account for the dielectric of the core-shell Ni@Au nanoparticle predicted d_0 values of 9.1 nm for ROX and 6.2 nm for DyLt680. These values are greater than that of AuNPs but still lower than the values obtained from the experimental fit.[15] It is possible that the experimental shell thickness calculated is not very accurate or that the model considers absorption to take place within the gold shell only, which might not be the case. Overall, the core-shell nanoparticles do indeed exhibit higher quenching of the red dyes in comparison to gold nanoparticles.

5.4 Conclusion

The role of layered dielectric materials to modify the energy coupling between a nanoparticle and a fluorophore was investigated through the synthesis of a nickel-gold core-shell nanoparticle that was then compared to gold nanoparticles of similar size in fluorescent quenching experiments. The Ni@Au NPs were synthesized by the shelling of NiNPs cores by gold salt in organic media that produced small magnetic and plasmonic nanoparticles. As the nickel core has a high imaginary component, the absorptivity of a gold-shelled nickel core is expected to increased in red wavelengths, and therefore fluorescent quenching of red dyes like ROX and DyLt680 are expected to increase when coupled to Ni@Au nanoparticles in comparison to pure gold nanoparticles. 3.3 nm Ni@Au and 3.5 nm Au nanoparticles were coupled to fluorescent dyes, DyLt680 and ROX using different length (15bp, 30bp and 45bp) dye-labeled double-stranded DNA sequences for quenching studies. The nanoparticles exhibited fourth-power law distance-dependent quenching behavior monitored through emission intensity change between coupled and uncoupled states of nanoparticle and dye. The d_0 of the Ni@Au particles were indeed much higher than that of the AuNP nanoparticles for both dyes and the the nanoparticle quenching behavior predicted by the NSET model was close for the AuNPs, but under-predicted the quenching efficiency of the Ni@Au structures. Reconsideration of the absorptivity of the nanoparticle to include a higher absorption by the core and repeated experiments with possibly different core-shell sizes would help elucidate the difference between the predictive model and experimental results.

CHAPTER 6

CONCLUSION AND OUTLOOK

This research work investigated the synthesis of different nanoparticle systems, the factors that govern their shape and size control which included the influence of microwave energy in promoting faster anisotropic growth. The interaction of these synthesized nanoparticles with electromagnetic radiation was investigated through their incorporation in a dielectric nanocomposite and as quenchers of fluorescent dye molecules.

Chapter 2 investigated how changing the delivery of microwave power from a continuous variable amount to a cycled manner enabled the faster anisotropic growth of nickel multipod arms. The work showed that high-power short-pulses of microwave energy was efficient in creating high aspect ratio arms and promoted more uniform size distributions. The results support a proposed 'lightning-rod mechanism' where the overgrowths of the enlarging nanostructure get much hotter than the rest of the nanoparticle surface during microwave power cycling, promoting faster autocatalytic growth at the tips. The implication of this study suggests that cycled microwave power could provide a faster, efficient and reliable route to creating anisotropic multipod nanostructures. The anisotropic Ni multipods show very high surface area, exhibit aspect ratio coercivity and are currently being used in a collaborate catalysis study. The 'lightning-rod effect' is a matter-electromagnetic wave interaction not specific to a single material, and would apply to other important materials such as Fe, Pd, Pt (for catalysis), Au (for plasmonic-related applications and SERS) as well as hard-magnetic materials where shape anisotropy is quite significant for coercivity. Growing other anisotropic nanostructures using a pulsed microwave energy approach would be the future direction for this research.

Chapter 3 expanded upon the understanding of multipod growth mechanism. As it is known that anisotropic nanoparticles can be grown through convective routes through the manipulation of a number of factors, this chapter investigated how such factors would influence the growth of multipod structures under microwave-assisted heating under a power cycling mode. The growth of anisotropic metallic nanomaterials using microwave-assisted heating is not vastly studied, and this chapter delved further into the topic. The effect of changing the metal precursor type, metal precursor concentration, ligand ratios and types, as well as stirring rate is shown to affect the evolution of the multipod structure. The experimental results from the metal precursor concentration studies show that nucleation and growth kinetics are affected to the extent that nanoparticle shape is affected. Concentration of metal precursor therefore provides another handle to control shape. By changing the ligand ratio of oleylamine and oleic acid, the nickel nanoparticle shape is also modified, possibly due to the formation of different starting precursor complexes as observed in the UV-Vis absorption spectra pre-reaction. The ligands in solution therefore not only act as reducing agents and capping agents, but interact with the precursor and produce a complex at the begin that can behave differently. Two other parameters were investigated: microwave vessel type (SiC versus glass) and the stirring rate. The SiC being a better microwave absorber than glass, led to poor multipod formation, producing a mixture of sheet-like structures and spherical nanoparticles. This could potentially arise from the differential temperature at the hot SiC vessel walls versus the interior. Stirring of the reaction solution that produces multipods was seen to disrupt the anisotropic growth process. However the reaction in the larger microwave reaction vessel showed that even with a high stirring rate, multipods could be formed, but of a smaller aspect ratio than those without any stirring. The experiments in this section show that multipod evolution is a complex process, and can be drastically affected through small perturbations. This further supports the argument that reactions conditions that produce multipod structures for a certain material may not always easily translate to other materials, and may need an optimization of multiple parameters. The next steps for the research work in this chapter would be an in-depth investigation of how stirring affects the nucleation and growth process of the Ni multipods, and in developing a predictable model on how to control anisotropic growth of a material.

Chapter 4 focused on incorporation of small metallic (hcp Ni and fcc Ni) and/or magnetic (fcc Ni, Fe_3O_4) nanoparticles in a dielectric polymer (polystyrene), and investigated how the physical properties (dielectric, magnetic, thermal stability) of the material can be tuned. Such nanocomposites materials have applications in 3-D printable dielectric material and light-weight EMI shielding. The properties of nanocomposites incorporating well-characterized synthesized nanoparticle fillers versus nanocomposites incorporating commercially available nanoparticles were compared. The composites with different loading level of nanoparticle filler were shown to exhibit low k and low loss properties in all cases even at high loading levels (50%) except the system with commercial Fe_3O_4 nanoparticle filler. This was attributed to the incompatible and highly polarizable PVP ligand that passivated the commercial Fe_3O_4 nanoparticles. By fitting the dielectric data (real component of permittivity) of the nanocomposites as a function of volume fraction to existing effective medium theory models, it was possible to find the dielectric constant of the filler nanoparticles and show that the systems can fit models where particle-particle interaction is not present. The dielectric losses (imaginary component of permittivity) as a function of volume fraction show that the nanocomposities with synthesized nanoparticles show lower losses that scale linearly with loading level while the commercial nanoparticle-filled nanocomposites show higher losses that scale as a power law (n = 2). Particle distribution analysis using SEM revealed that the composites with higher saturation magnetization had a tendency to aggregate during solution casting of nanocomposite films, however the SAXS data suggests that the composites with synthesized nanoparticles have some ordering with the presence of peak features in the SAXS unlike the nanocomposite materials with commercial nanoparticles that showed featureless SAXS patterns. The layered nanocomposite structure (formed from the stacking of 4-5 cast films)used in the dielectric spectroscopy studies does not critically affect the response of the material. The results show that using high-surface area nanoparticles in a polymer can still allow maintenance of low-k and low loss properties while incorporating magnetic and thermal stability benefits. Evaluating the EMI shielding, dielectric breakdown strength and printability of these nanocomposites is the next logical step. Additionally, developing EMI shielding nanocomposites with anisotropic magnetic Ni multipod filler material would improve the electromagnetic shielding ability from shape-effects and possibly allow the tuning of shielding effectiveness in different frequencies ranges.

The interaction of small core-shell nanostructures in a surface transfer energy process was investigated in Chapter 5. This was achieved by the synthesis of 3.3 nm diameter nickel-gold core-shell nanoparticles which were then coupled to a red dyes, ROX (emisson max 609 nm) and a far-red dye, DyLt680 (emission max 710 nm) using different lengths of double-stranded DNA. Characterization of the core-shell structure by UV-Vis spectroscopy, XRD, EDS/XRF magnetic methods and ligand exchange indicate the formation of a gold-shelled nickel nanoparticle. The quenching studying using fluorescence emission intensity changes between a conjugated dye-nanoparticle system and a non-conjugated system achieved using cyanide etching of the nanoparticle showed distant-dependent quenching behavior. The results show a fourth-power law (with respect to distance) surface-energy transfer behavior for the core-shell structures, and the quenching efficiency was much higher than a solid gold nanoparticle (3.5 nm). The d_0 for the 3.3 nm nickel-gold nanoparticle was found to be ∼18 nm for the ROX dye while that for the DyLt680 was to be ∼16 nm. These values are much higher than that of a 3.5 nm gold nanoparticle that had values of ∼8 nm for the ROX dye while that for the DyLt680 was to be ∼4.3 nm. The higher absorptivity of the core-shell structure with a core comprising of nickel is anticipated as the absorptivity of nickel in the wavelengths above 600 nm is higher than that of gold, known from the dielectric data for the two materials. The d_0 values for the gold nanoparticle are close to that predicted by the size-dependent NSET model but the values of the core-shell structure are under-predicted with the modified size-dependent NSET model that uses the dielectric of a core-shell structure. This under-prediction might arise as the model still assumes that the non-radiative transfer primarily takes place to only the outer gold shell. [15] It is possible that the core absorptivity is not accurately modeled or that the experimental thickness of the thin gold shell is inaccurate. A better approach to evaluate the accurate quenching behavior would be to use fluorescent lifetime analysis. However if the quenching efficiency of the core-shell structure is high, the shortened lifetime might be a challenge to detect without a fast lifetime system. Furthermore, studies with use of different core-shell ratios and use of different metal core-materials would expand the scope of the project and provide a more robust set of results to validate the distant-dependent behavior for core-shell nanostructures.

APPENDIX A

COPYRIGHT PERMISSION

Permission for content used in Chapter 2 of this dissertation.

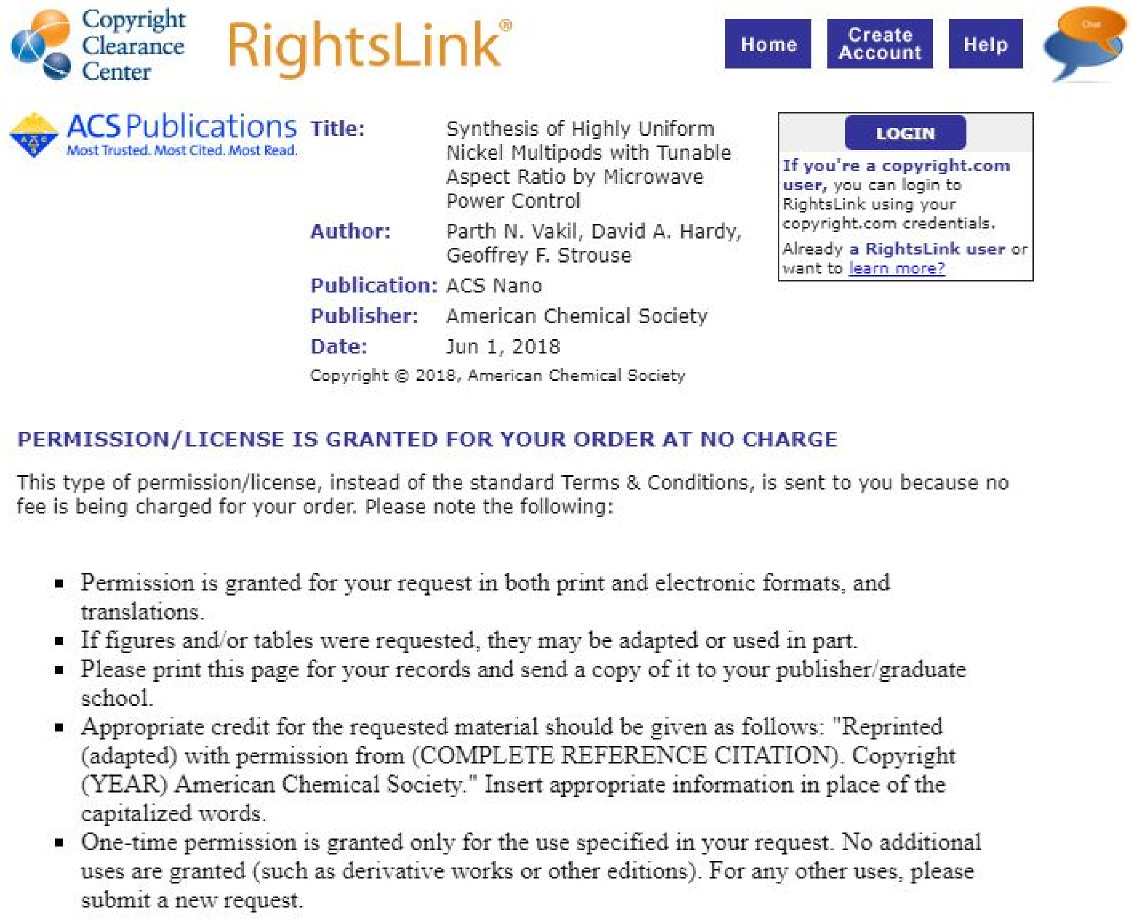

Title: Synthesis of Highly Uniform Nickel Multipods with Tunable Aspect Ratio by Microwave Power Control

Author: Parth N. Vakil, David A. Hardy, Geoffrey F. Strouse

Publication: ACS Nano

Publisher: American Chemical Society

Date: Jun 1, 2018

Copyright © 2018, American Chemical Society

If you're a copyright.com user, you can login to RightsLink using your copyright.com credentials.

Already **a RightsLink user** or want to learn more?

PERMISSION/LICENSE IS GRANTED FOR YOUR ORDER AT NO CHARGE

This type of permission/license, instead of the standard Terms & Conditions, is sent to you because no fee is being charged for your order. Please note the following:

- Permission is granted for your request in both print and electronic formats, and translations.
- If figures and/or tables were requested, they may be adapted or used in part.
- Please print this page for your records and send a copy of it to your publisher/graduate school.
- Appropriate credit for the requested material should be given as follows: "Reprinted (adapted) with permission from (COMPLETE REFERENCE CITATION). Copyright (YEAR) American Chemical Society." Insert appropriate information in place of the capitalized words.
- One-time permission is granted only for the use specified in your request. No additional uses are granted (such as derivative works or other editions). For any other uses, please submit a new request.

BIBLIOGRAPHY

[1] Nathan D. Burrows, Ariane M. Vartanian, Nardine S. Abadeer, Elissa M. Grzincic, Lisa M. Jacob, Wayne Lin, Ji Li, Jordan M. Dennison, Joshua G. Hinman, and Catherine J. Murphy. Anisotropic nanoparticles and anisotropic surface chemistry. *The Journal of Physical Chemistry Letters*, 7(4):632–641, 2016. PMID: 26817922.

[2] Hector Barron, George Opletal, Richard Tilley, and Amanda S Barnard. Predicting the role of seed morphology in the evolution of anisotropic nanocatalysts. *Nanoscale*, 9(4):1502–1510, 2017.

[3] Yadong Yin and A Paul Alivisatos. Colloidal nanocrystal synthesis and the organic–inorganic interface. *Nature*, 437(7059):664, 2004.

[4] Zhaohui Wu, Shuanglei Yang, and Wei Wu. Shape control of inorganic nanoparticles from solution. *Nanoscale*, 8(3):1237–1259, 2016.

[5] Eric J Lerner. Biomimetic nanotechnology. *Industrial Physicist*, 10(4):16–19, 2004.

[6] Fern Wickson. Narratives of nature and nanotechnology. *Nature nanotechnology*, 3(6):313, 2008.

[7] Yang T Cheng, DE Rodak, CA Wong, and CA Hayden. Effects of micro-and nano-structures on the self-cleaning behaviour of lotus leaves. *Nanotechnology*, 17(5):1359, 2006.

[8] Shichao Niu, Bo Li, Zhengzhi Mu, Meng Yang, Junqiu Zhang, Zhiwu Han, and Luquan Ren. Excellent structure-based multifunction of morpho butterfly wings: a review. *Journal of Bionic Engineering*, 12(2):170–189, 2015.

[9] Lei Jiang, Yong Zhao, and Jin Zhai. A lotus-leaf-like superhydrophobic surface: a porous microsphere/nanofiber composite film prepared by electrohydrodynamics. *Angewandte Chemie*, 116(33):4438–4441, 2004.

[10] Olivier Poncelet, Guillaume Tallier, Priscilla Simonis, Alain Cornet, and Laurent A Francis. Synthesis of bio-inspired multilayer polarizers and their application to anti-counterfeiting. *Bioinspiration & biomimetics*, 10(2):026004, 2015.

[11] S Anu Mary Ealia and MP Saravanakumar. A review on the classification, characterisation, synthesis of nanoparticles and their application. In *IOP Conference Series: Materials Science and Engineering*, volume 263, page 032019. IOP Publishing, 2017.

[12] Vasudevanpillai Biju, Tamitake Itoh, Abdulaziz Anas, Athiyanathil Sujith, and Mitsuru Ishikawa. Semiconductor quantum dots and metal nanoparticles: syntheses, optical properties, and biological applications. *Analytical and bioanalytical chemistry*, 391(7):2469–2495, 2008.

[13] Kenneth J Klabunde and Ryan Richards. *Nanoscale materials in chemistry*, volume 1035. Wiley Online Library, 2001.

[14] Luis J Mendoza Herrera, David Munetón Arboleda, Daniel C Schinca, and Lucía B Scaffardi. Determination of plasma frequency, damping constant, and size distribution from the complex dielectric function of noble metal nanoparticles. *Journal of Applied Physics*, 116(23):233105, 2014.

[15] Ryan A. Riskowski. *Theory and Applications of Surface Energy Transfer for 2-20 Nm Diameter Metal Nanoparticles*. PhD thesis, Florida State University, 2016.

[16] Vicky V Mody, Rodney Siwale, Ajay Singh, and Hardik R Mody. Introduction to metallic nanoparticles. *Journal of Pharmacy and Bioallied Sciences*, 2(4):282, 2010.

[17] Rosalynn Quiñones, Aparna Raman, and Ellen S Gawalt. Functionalization of nickel oxide using alkylphosphonic acid self-assembled monolayers. *Thin Solid Films*, 516(23):8774–8781, 2008.

[18] Bridgett Ashley, Parth N. Vakil, Brian B. Lynch, Christopher M. Dyer, Joseph B. Tracy, Jeffery Owens, and Geoffrey F. Strouse. Microwave enhancement of autocatalytic growth of nanometals. *ACS Nano*, 11(10):9957–9967, 2017.

[19] Aaron C Johnston-Peck, Junwei Wang, and Joseph B Tracy. Synthesis and structural and magnetic characterization of ni (core)/nio (shell) nanoparticles. *ACS nano*, 3(5):1077–1084, 2009.

[20] An-Hui Lu, E emsp14L Salabas, and Ferdi Schüth. Magnetic nanoparticles: synthesis, protection, functionalization, and application. *Angewandte Chemie International Edition*, 46(8):1222–1244, 2007.

[21] Abolfazl Akbarzadeh, Mohammad Samiei, and Soodabeh Davaran. Magnetic nanoparticles: preparation, physical properties, and applications in biomedicine. *Nanoscale research letters*, 7(1):144, 2012.

[22] RH Kodama. Magnetic nanoparticles. *Journal of magnetism and magnetic materials*, 200(1-3):359–372, 1999.

[23] David J Carnevale. *Understanding Magnetic Exchange Behavior in Core@Shell Nanoparticles*. PhD thesis, Florida State University, 2017.

[24] Bridgett A Ashley. *Understanding the Microwave in Microwave Chemistry.* PhD thesis, Florida State University, 2017.

[25] Paul A Kohl. Low–dielectric constant insulators for future integrated circuits and packages. *Annual review of chemical and biomolecular engineering*, 2:379–401, 2011.

[26] John B Pendry, AJ Holden, WJ Stewart, and I Youngs. Extremely low frequency plasmons in metallic mesostructures. *Physical review letters*, 76(25):4773, 1996.

[27] Noboru Yoshikawa. Fundamentals and applications of microwave heating of metals. *Journal of Microwave Power and Electromagnetic Energy*, 44(1):4–13, 2010.

[28] Satnam Singh, Dheeraj Gupta, Vivek Jain, and Apurbba K Sharma. Microwave processing of materials and applications in manufacturing industries: A review. *Materials and Manufacturing Processes*, 30(1):1–29, 2015.

[29] Radha Raman Mishra and Apurbba Kumar Sharma. Microwave–material interaction phenomena: heating mechanisms, challenges and opportunities in material processing. *Composites Part A: Applied Science and Manufacturing*, 81:78–97, 2016.

[30] Daan P Sprünken, Hiroo Omi, Kazuaki Furukawa, Hiroshi Nakashima, Ilya Sychugov, Yoshihiro Kobayashi, and Keiichi Torimitsu. Influence of the local environment on determining aspect-ratio distributions of gold nanorods in solution using gans theory. *The Journal of Physical Chemistry C*, 111(39):14299–14306, 2007.

[31] Timothy J Merkel, Kevin P Herlihy, Janine Nunes, Ryan M Orgel, Jason P Rolland, and Joseph M DeSimone. Scalable, shape-specific, top-down fabrication methods for the synthesis of engineered colloidal particles. *Langmuir*, 26(16):13086–13096, 2009.

[32] Shei Sia Su and Isaac Chang. Review of production routes of nanomaterials. In *Commercialization of Nanotechnologies–A Case Study Approach*, pages 15–29. Springer, 2018.

[33] Andrea R Tao, Susan Habas, and Peidong Yang. Shape control of colloidal metal nanocrystals. *small*, 4(3):310–325, 2008.

[34] Xun Wang, Jing Zhuang, Qing Peng, and Yadong Li. A general strategy for nanocrystal synthesis. *Nature*, 437(7055):121, 2005.

[35] Nguyen TK Thanh, N Maclean, and S Mahiddine. Mechanisms of nucleation and growth of nanoparticles in solution. *Chemical reviews*, 114(15):7610–7630, 2014.

[36] Jörg Polte. Fundamental growth principles of colloidal metal nanoparticles–a new perspective. *CrystEngComm*, 17(36):6809–6830, 2015.

[37] Lydia Bahrig, Stephen G Hickey, and Alexander Eychmüller. Mesocrystalline materials and the involvement of oriented attachment–a review. *CrystEngComm*, 16(40):9408–9424, 2014.

[38] Murielle A Watzky and Richard G Finke. Transition metal nanocluster formation kinetic and mechanistic studies. a new mechanism when hydrogen is the reductant: slow, continuous nucleation and fast autocatalytic surface growth. *Journal of the American Chemical Society*, 119(43):10382–10400, 1997.

[39] Tung-Han Yang, Shan Zhou, Kyle D. Gilroy, Legna Figueroa-Cosme, Yi-Hsien Lee, Jenn-Ming Wu, and Younan Xia. Autocatalytic surface reduction and its role in controlling seed-mediated growth of colloidal metal nanocrystals. *Proceedings of the National Academy of Sciences*, page 201713907, 2017.

[40] Bridgett Ashley, Christopher M. Dyer, Jeffery Owens, and Geoffrey F. Strouse. Influence of microwave frequency and power on nanometal growth. *The Journal of Physical Chemistry C*, 2018.

[41] Lucian Bentea, Murielle A Watzky, and Richard G Finke. Sigmoidal nucleation and growth curves across nature fit by the finke–watzky model of slow continuous nucleation and autocatalytic growth: explicit formulas for the lag and growth times plus other key insights. *The Journal of Physical Chemistry C*, 121(9):5302–5312, 2017.

[42] Chen Mei, Wu Binghui, Yang Jing, and Zheng Nanfeng. Small adsorbateassisted shape control of pd and pt nanocrystals. *Advanced Materials*, 24(7):862–879, 2012.

[43] Nanjing Hao, Yuan Nie, Amogha Tadimety, Andrew B Closson, and John XJ Zhang. Microfluidics-mediated self-template synthesis of anisotropic hollow ellipsoidal mesoporous silica nanomaterials. *Materials Research Letters*, 5(8):584–590, 2017.

[44] LD Marks and L Peng. Nanoparticle shape, thermodynamics and kinetics. *Journal of Physics: Condensed Matter*, 28(5):053001, 2016.

[45] Yawen Wang, Jiating He, Cuicui Liu, Wen Han Chong, and Hongyu Chen. Thermodynamics versus kinetics in nanosynthesis. *Angewandte Chemie International Edition*, 54(7):2022–2051, 2015.

[46] Yiying Wu, Tsachi Livneh, You Xiang Zhang, Guosheng Cheng, Jianfang Wang, Jing Tang, Martin Moskovits, and Galen D Stucky. Templated synthesis of highly ordered mesostructured nanowires and nanowire arrays. *Nano Letters*, 4(12):2337–2342, 2004.

[47] Pierre Cheyssac, M Sacilotti, and G Patriarche. Vapor-liquid-solid mechanisms: Challenges for nanosized quantum cluster/dot/wire materials. *Journal of applied physics*, 100(4):044315, 2006.

[48] Nikos Liakakos, Benoit Cormary, Xiaojian Li, Pierre Lecante, Marc Respaud, Laurent Maron, Andrea Falqui, Alessandro Genovese, Laure Vendier, Spyros Koinis, et al. The big impact of a small detail: cobalt nanocrystal polymorphism as a result of precursor addition rate during stock solution preparation. *Journal of the American Chemical Society*, 134(43):17922–17931, 2012.

[49] Alec P. LaGrow, Soshan Cheong, John Watt, Bridget Ingham, Michael F. Toney, David A. Jefferson, and Richard D. Tilley. Can polymorphism be used to form branched metal nanostructures? *Advanced Materials*, 25(11):1552–1556, 2013.

[50] Alexander N. Chen, Mattea M. Scanlan, and Sara E. Skrabalak. Surface passivation and supersaturation: Strategies for regioselective deposition in seeded syntheses. *ACS Nano*, 11(12):12624–12631, 2017. PMID: 29164855.

[51] Nancy Ortiz and Sara E Skrabalak. Manipulating local ligand environments for the controlled nucleation of metal nanoparticles and their assembly into nanodendrites. *Angewandte Chemie International Edition*, 51(47):11757–11761, 2012.

[52] Xi Yin, Miao Shi, Jianbo Wu, Yung-Tin Pan, Danielle L. Gray, Jeffery A. Bertke, and Hong Yang. Quantitative analysis of different formation modes of platinum nanocrystals controlled by ligand chemistry. *Nano letters*, 17(10):6146–6150, 2017.

[53] Simona E Hunyadi Murph, Catherine J Murphy, Austin Leach, and Kenneth Gall. A possible oriented attachment growth mechanism for silver nanowire formation. *Crystal Growth & Design*, 15(4):1968–1974, 2015.

[54] John Watt, Soshan Cheong, Michael F. Toney, Bridget Ingham, James Cookson, Peter T. Bishop, and Richard D. Tilley. Ultrafast growth of highly branched palladium nanostructures for catalysis. *ACS Nano*, 4(1):396–402, 2009.

[55] Zheng Fang, Yuliang Zhang, Feifei Du, and Xinhua Zhong. Growth of anisotropic platinum nanostructures catalyzed by gold seed nanoparticles. *Nano Research*, 1(3):249–257, 2008.

[56] Mahmoud A Mahmoud, Mostafa A El-Sayed, Jianping Gao, and Uzi Landman. High-frequency mechanical stirring initiates anisotropic growth of seeds requisite for synthesis of asymmetric metallic nanoparticles like silver nanorods. *Nano letters*, 13(10):4739–4745, 2013.

[57] K Mrad, F Schoenstein, HTT Nong, E Anagnostopoulou, A Viola, L Mouton, S Mercone, C Ricolleau, N Jouini, M Abderraba, et al. Control of the crystal habit and magnetic properties of co nanoparticles through the stirring rate. *CrystEngComm*, 19(25):3476–3484, 2017.

[58] Na Su, Xueying Chen, Bin Yue, and Heyong He. Formation of palladium concave nanocrystals via auto-catalytic tip overgrowth by interplay of reduction kinetics, concentration gradient and surface diffusion. *Nanoscale*, 8(16):8673–8680, 2016.

[59] Dan Li and Richard B Kaner. Shape and aggregation control of nanoparticles: not shaken, not stirred. *Journal of the American Chemical Society*, 128(3):968–975, 2006.

[60] Xiaowei Teng and Hong Yang. Synthesis of platinum multipods: an induced anisotropic growth. *Nano letters*, 5(5):885–891, 2005.

[61] Idalia Bilecka and Markus Niederberger. Microwave chemistry for inorganic nanomaterials synthesis. *Nanoscale*, 2(8):1358–1374, 2010.

[62] Tsuji Masaharu. Microwaveassisted synthesis of metallic nanomaterials in liquid phase. *ChemistrySelect*, 2(2):805–819, 2017.

[63] Manoj B Gawande, Sharad N Shelke, Radek Zboril, and Rajender S Varma. Microwave-assisted chemistry: synthetic applications for rapid assembly of nanomaterials and organics. *Accounts of chemical research*, 47(4):1338–1348, 2014.

[64] David J Carnevale, Michael Shatruk, and Geoffrey F Strouse. Ligand passivated core–shell fept@ co nanomagnets exhibiting enhanced energy product. *Chemistry of Materials*, 28(15):5480–5487, 2016.

[65] Claire M. Cobley, Sara E. Skrabalak, Dean J. Campbell, and Younan Xia. Shape-controlled synthesis of silver nanoparticles for plasmonic and sensing applications. *Plasmonics*, 4(2):171–179, 2009.

[66] Jing Sun, Wenlong Wang, and Qinyan Yue. Review on microwave-matter interaction fundamentals and efficient microwave-associated heating strategies. *Materials*, 9(4), 2016.

[67] P. P. Rajeev, P. Ayyub, S. Bagchi, and G. Ravindra Kumar. Nanostructures, local fields, and enhanced absorption in intense lightmatter interaction. *Optics letters*, 29(22):2662–2664, 2004.

[68] R. F. Zhuo, L. Qiao, H. T. Feng, J. T. Chen, D. Yan, Z. G. Wu, and P. X. Yan. Microwave absorption properties and the isotropic antenna mechanism of zno nanotrees. *Journal of Applied Physics*, 104(9):094101, 2008.

[69] P. F. Liao and A. Wokaun. Lightning rod effect in surface enhanced raman scattering. *The Journal of Chemical Physics*, 76(1):751–752, 1982.

[70] Yongcun Li, Feng Xu, Xiaofang Hu, Yunbo Luan, Zhijun Han, and Zhiyong Wang. Focusing effect of electromagnetic fields and its influence on sintering during the microwave processing of metallic particles. *Journal of Materials Research*, 30(23):3663–3670, 2015.

[71] Zhao Hongtao, Han Xijiang, Zhang Lifang, Wang Gangyi, Wang Chao, Li Xueai, and Xu Ping. Controlled synthesis and morphology-dependent electromagnetic properties of nickel nanostructures by -ray irradiation technique. *Radiation Physics and Chemistry*, 80(3):390–393, 2011.

[72] Panikkanvalappil R. Sajanlal, Theruvakkattil S. Sreeprasad, Akshaya K. Samal, and Thalappil Pradeep. Anisotropic nanomaterials: structure, growth, assembly, and functions. *Nano Reviews*, 2(1):5883, 2011.

[73] Xiaocui Wang, Guohua Li, Yu Ding, and Shuqing Sun. Understanding the photothermal effect of gold nanostars and nanorods for biomedical applications. *RSC Advances*, 4(57):30375–30383, 2014.

[74] Christopher J Breshike, Ryan A Riskowski, and Geoffrey F Strouse. Leaving forster resonance energy transfer behind: Nanometal surface energy transfer predicts the size-enhanced energy coupling between a metal nanoparticle and an emitting dipole. *The Journal of Physical Chemistry C*, 117(45):23942–23949, 2013.

[75] Mani Prabha Singh and Geoffrey F Strouse. Involvement of the lspr spectral overlap for energy transfer between a dye and au nanoparticle. *Journal of the American Chemical Society*, 132(27):9383–9391, 2010.

[76] Travis Jennings and Geoffrey Strouse. Past, present, and future of gold nanoparticles. In *Bio-Applications of Nanoparticles*, pages 34–47. Springer, 2007.

[77] Mani Prabha Singh, Travis L Jennings, and Geoffrey F Strouse. Tracking spatial disorder in an optical ruler by time-resolved nset. *The Journal of Physical Chemistry B*, 113(2):552–558, 2008.

[78] Megan E Muroski, Thomas J Morgan Jr, Cathy W Levenson, and Geoffrey F Strouse. A gold nanoparticle pentapeptide: gene fusion to induce therapeutic gene expression in mesenchymal stem cells. *Journal of the American Chemical Society*, 136(42):14763–14771, 2014.

[79] Megan E Muroski, Joshua M Kogot, and Geoffrey F Strouse. Bimodal gold nanoparticle therapeutics for manipulating exogenous and endogenous protein levels in mammalian cells. *Journal of the American Chemical Society*, 134(48):19722–19730, 2012.

[80] Rachel E Armstrong, Ryan A Riskowski, and Geoffrey F Strouse. Nanometal surface energy transfer optical ruler for measuring a human telomere structure. *Photochemistry and photobiology*, 91(3):732–738, 2015.

[81] Ryan A Riskowski, Rachel E Armstrong, Nancy L Greenbaum, and Geoffrey F Strouse. Triangulating nucleic acid conformations using multicolor surface energy transfer. *ACS nano*, 10(2):1926–1938, 2016.

[82] Jelani Griffin, Anant Kumar Singh, Dulal Senapati, Patsy Rhodes, Kanieshia Mitchell, Brianica Robinson, Eugene Yu, and Paresh Chandra Ray. Size-and distance-dependent nanoparticle surface-energy transfer (nset) method for selective sensing of hepatitis c virus rna. *Chemistry-A European Journal*, 15(2):342–351, 2009.

[83] TL Jennings, MP Singh, and GF Strouse. Fluorescent lifetime quenching near d= 1.5 nm gold nanoparticles: probing nset validity. *Journal of the American Chemical Society*, 128(16):5462–5467, 2006.

[84] Riccardo Ferrando, Julius Jellinek, and Roy L Johnston. Nanoalloys: from theory to applications of alloy clusters and nanoparticles. *Chemical reviews*, 108(3):845–910, 2008.

[85] Ankit Agrawal, Shin Hum Cho, Omid Zandi, Sandeep Ghosh, Robert W Johns, and Delia J Milliron. Localized surface plasmon resonance in semiconductor nanocrystals. *Chemical reviews*, 118(6):3121–3207, 2018.

[86] Rajib Ghosh Chaudhuri and Santanu Paria. Core/shell nanoparticles: classes, properties, synthesis mechanisms, characterization, and applications. *Chemical reviews*, 112(4):2373–2433, 2011.

[87] Richard D Averitt, Sarah L Westcott, and Naomi J Halas. Linear optical properties of gold nanoshells. *JOSA B*, 16(10):1824–1832, 1999.

[88] Steven J Oldenburg, Joseph B Jackson, Sarah L Westcott, and NJ Halas. Infrared extinction properties of gold nanoshells. *Applied Physics Letters*, 75(19):2897–2899, 1999.

[89] Felicia Tam, Glenn P Goodrich, Bruce R Johnson, and Naomi J Halas. Plasmonic enhancement of molecular fluorescence. *Nano letters*, 7(2):496–501, 2007.

[90] Hui Wang, Daniel W Brandl, Fei Le, Peter Nordlander, and Naomi J Halas. Nanorice: a hybrid plasmonic nanostructure. *Nano letters*, 6(4):827–832, 2006.

[91] Nardine S Abadeer, Marshall R Brennan, William L Wilson, and Catherine J Murphy. Distance and plasmon wavelength dependent fluorescence of molecules bound to silica-coated gold nanorods. *ACS nano*, 8(8):8392–8406, 2014.

[92] Philipp Reineck, Daniel Gómez, Soon Hock Ng, Matthias Karg, Toby Bell, Paul Mulvaney, and Udo Bach. Distance and wavelength dependent quenching of molecular fluorescence by au@ sio2 core–shell nanoparticles. *ACS nano*, 7(8):6636–6648, 2013.

[93] Krishna Kanta Haldar, Tapasi Sen, and Amitava Patra. Au@ zno core- shell nanoparticles are efficient energy acceptors with organic dye donors. *The Journal of Physical Chemistry C*, 112(31):11650–11656, 2008.

[94] Hsing-Hui Lin and I-Chia Chen. Study of the interaction between gold nanoparticles and rose bengal fluorophores with silica spacers by time-resolved fluorescence spectroscopy. *The Journal of Physical Chemistry C*, 119(47):26663–26671, 2015.

[95] Jeffrey N Anker, W Paige Hall, Olga Lyandres, Nilam C Shah, Jing Zhao, and Richard P Van Duyne. Biosensing with plasmonic nanosensors. *Nature materials*, 7(6):442, 2008.

[96] Jit Kang Lim, Sara A Majetich, and Robert D Tilton. Stabilization of superparamagnetic iron oxide core- gold shell nanoparticles in high ionic strength media. *Langmuir*, 25(23):13384–13393, 2009.

[97] Ezequiel R Encina and Eduardo A Coronado. Size optimization of iron oxide@ noble metal core–shell nanohybrids for photothermal applications. *The Journal of Physical Chemistry C*, 120(10):5630–5639, 2016.

[98] Junfeng Wang, Xuezhong Wu, Chongwen Wang, Zhen Rong, Hongmei Ding, Hui Li, Shaohua Li, Ningsheng Shao, Peitao Dong, Rui Xiao, et al. Facile synthesis of au-coated magnetic nanoparticles and their application in bacteria detection via a sers method. *ACS applied materials & interfaces*, 8(31):19958–19967, 2016.

[99] Lingyan Wang, Lingyan Wang, Jin Luo, Quan Fan, Masatsugu Suzuki, Itsuko S Suzuki, Mark H Engelhard, Yuehe Lin, Nam Kim, Jian Q Wang, et al. Monodispersed core- shell fe3o4@ au nanoparticles. *The Journal of Physical Chemistry B*, 109(46):21593–21601, 2005.

[100] Yujun Song, Jie Ding, and Yinghui Wang. Shell-dependent evolution of optical and magnetic properties of co@ au core–shell nanoparticles. *The Journal of Physical Chemistry C*, 116(20):11343–11350, 2012.

[101] Rizia Bardhan, Nathaniel K Grady, Tamer Ali, and Naomi J Halas. Metallic nanoshells with semiconductor cores: optical characteristics modified by core medium properties. *ACS nano*, 4(10):6169–6179, 2010.

[102] Carly S Levin, Cristina Hofmann, Tamer A Ali, Anna T Kelly, Emilia Morosan, Peter Nordlander, Kenton H Whitmire, and Naomi J Halas. Magnetic- plasmonic core- shell nanoparticles. *ACS nano*, 3(6):1379–1388, 2009.

[103] Elise Anne Chaffin, Saheel Bhana, Ryan Timothy OConnor, Xiaohua Huang, and Yongmei Wang. Impact of core dielectric properties on the localized surface plasmonic spectra of gold-coated magnetic core–shell nanoparticles. *The Journal of Physical Chemistry B*, 118(49):14076–14084, 2014.

[104] Elyahb Allie Kwizera, Elise Chaffin, Xiao Shen, Jingyi Chen, Qiang Zou, Zhiming Wu, Zheng Gai, Saheel Bhana, Ryan OConnor, Lijia Wang, et al. Size-and shape-controlled synthesis and properties of magnetic–plasmonic core–shell nanoparticles. *The Journal of Physical Chemistry C*, 120(19):10530–10546, 2016.

[105] Xiaozheng Xue, Viktor Sukhotskiy, and Edward P Furlani. Optimization of optical absorption of colloids of sio 2@ au and fe 3 o 4@ au nanoparticles with constraints. *Scientific reports*, 6:35911, 2016.

[106] Noktan M. Alyami, Alec P. LaGrow, Dalaver H. Anjum, Chao Guan, Xiao-He Miao, Lutfan Sinatra, Ding-Jier Yuan, Omar F. Mohammed, Kuo-Wei Huang, and Osman M. Bakr. Synthesis and characterization of branched fcc/hcp ruthenium natannostructures and their catalytic activity in ammonia borane hydrolysis. *Crystal Growth & Design*, 2018.

[107] Mingshang Jin, Hui Zhang, Zhaoxiong Xie, and Younan Xia. Palladium concave nanocubes with highindex facets and their enhanced catalytic properties. *Angewandte Chemie International Edition*, 50(34):7850–7854, 2011.

[108] Hongjing Wang, Shuli Yin, Yinghao Li, Hongjie Yu, Chunjie Li, Kai Deng, You Xu, Xiaonian Li, Hairong Xue, and Liang Wang. One-step fabrication of tri-metallic pdcuau nanothorn assemblies as an efficient catalyst for oxygen reduction reaction. *Journal of Materials Chemistry A*, 2018.

[109] John Watt, Soshan Cheong, and Richard D. Tilley. How to control the shape of metal nanostructures in organic solution phase synthesis for plasmonics and catalysis. *Nano Today*, 8(2):198–215, 2013.

[110] Rong He, You-Cheng Wang, Xiaoyong Wang, Zhantong Wang, Gang Liu, Wei Zhou, Longping Wen, Qunxiang Li, Xiaoping Wang, Xiaoyuan Chen, Jie Zeng, and J. G. Hou. Facile synthesis of pentacle goldcopper alloy nanocrystals and their plasmonic and catalytic properties. *Nature Communications*, 5:4327, 2014.

[111] Jiawei Zhang, Qin Kuang, Yaqi Jiang, and Zhaoxiong Xie. Engineering high-energy surfaces of noble metal nanocrystals with enhanced catalytic performances. *Nano Today*, 11(5):661–677, 2016.

[112] Peter Strasser, Manuel Gliech, Stefanie Kuehl, and Tim Moeller. Electrochemical processes on solid shaped nanoparticles with defined facets. *Chemical Society Reviews*, 2018.

[113] Shuiping Luo and Pei Kang Shen. Concave platinumcopper octopod nanoframes bounded with multiple high-index facets for efficient electrooxidation catalysis. *ACS Nano*, 11(12):11946–11953, 2017.

[114] Enyi Ye, Michelle D. Regulacio, Shuang-Yuan Zhang, Xian Jun Loh, and Ming-Yong Han. Anisotropically branched metal nanostructures. *Chemical Society Reviews*, 44(17):6001–6017, 2015.

[115] Zhenming Cao, Qiaoli Chen, Jiawei Zhang, Huiqi Li, Yaqi Jiang, Shouyu Shen, Gang Fu, Bang-an Lu, Zhaoxiong Xie, and Lansun Zheng. Platinum-nickel alloy excavated nano-multipods with hexagonal close-packed structure and superior activity towards hydrogen evolution reaction. *Nature Communications*, 8:15131, 2017. 28436494[pmid] Nat Commun.

[116] Younan Xia, Yujie Xiong, Byungkwon Lim, and Sara E. Skrabalak. Shapecontrolled synthesis of metal nanocrystals: Simple chemistry meets complex physics? *Angewandte Chemie International Edition*, 48(1):60–103, 2009.

[117] Rebecca G. Weiner, Christopher J. DeSantis, Mariana B. T. Cardoso, and Sara E. Skrabalak. Diffusion and seed shape: Intertwined parameters in the synthesis of branched metal nanostructures. *ACS Nano*, 8(8):8625–8635, 2014.

[118] Xiaowei Teng and Hong Yang. Synthesis of platinum multipods: an induced anisotropic growth. *Nano letters*, 5(5):885–891, 2005.

[119] Meital Shviro and David Zitoun. Nickel nanocrystals: fast synthesis of cubes, pyramids and tetrapods. *Rsc Advances*, 3(5):1380–1387, 2013.

[120] Byungkwon Lim and Younan Xia. Metal nanocrystals with highly branched morphologies. *Angewandte Chemie International Edition*, 50(1):76–85, 2011.

[121] Naween Dahal, Stephany Garcia, Jiping Zhou, and Simon M Humphrey. Beneficial effects of microwave-assisted heating versus conventional heating in noble metal nanoparticle synthesis. *ACS nano*, 6(11):9433–9446, 2012.

[122] Pranaw Kunal, Emily J Roberts, Carson T Riche, Karalee Jarvis, Noah Malmstadt, Richard L Brutchey, and Simon M Humphrey. Continuous flow synthesis of rh and rhag alloy nanoparticle catalysts enables scalable production and improved morphological control. *Chemistry of Materials*, 29(10):4341–4350, 2017.

[123] Qinghe Liu, Xianhui Xu, Weixing Xia, Renchao Che, Chen Chen, Qi Cao, and Jingang He. Dependency of magnetic microwave absorption on surface architecture of co20ni80 hierarchical structures studied by electron holography. *Nanoscale*, 7(5):1736–1743, 2015.

[124] Chao Wang, Xijiang Han, Ping Xu, Jingyu Wang, Yunchen Du, Xiaohong Wang, Wu Qin, and Tao Zhang. Controlled synthesis of hierarchical nickel and morphology-dependent electromagnetic properties. *The Journal of Physical Chemistry C*, 114(7):3196–3203, 2010.

[125] Chao Wang, Surong Hu, Xijiang Han, Wen Huang, and Lunfu Tian. Controlled synthesis and microwave absorption property of chain-like co flower. *PLOS ONE*, 8(2):e55928, 2013.

[126] Zhenguo An, Shunlong Pan, and Jingjie Zhang. Synthesis and tunable assembly of spear-like nickel nanocrystallites: From urchin-like particles to prickly chains. *The Journal of Physical Chemistry C*, 113(4):1346–1351, 2009.

[127] Muhammad Imran Din and Aneela Rani. Recent advances in the synthesis and stabilization of nickel and nickel oxide nanoparticles: A green adeptness. *International Journal of Analytical Chemistry*, 2016:3512145, 2016. 27413375[pmid] Int J Anal Chem.

[128] Sarah Z. Tasker, Eric A. Standley, and Timothy F. Jamison. Recent advances in homogeneous nickel catalysis. *Nature*, 509:299, 2014.

[129] Francisco Alonso, Paola Riente, and Miguel Yus. Nickel nanoparticles in hydrogen transfer reactions. *Accounts of Chemical Research*, 44(5):379–391, 2011.

[130] Vivek Polshettiwar, Babita Baruwati, and Rajender S. Varma. Nanoparticle-supported and magnetically recoverable nickel catalyst: a robust and economic hydrogenation and transfer hydrogenation protocol. *Green Chemistry*, 11(1):127–131, 2009.

[131] Sophie Carenco, Cedric Boissiere, Lionel Nicole, Clment Sanchez, Pascal Le Floch, and Nicolas Mzailles. Controlled design of size-tunable monodisperse nickel nanoparticles. *Chemistry of Materials*, 22(4):1340–1349, 2010.

[132] Ying-Jie Zhu and Feng Chen. Microwave-assisted preparation of inorganic nanostructures in liquid phase. *Chemical reviews*, 114(12):6462–6555, 2014.

[133] Zhi Chen, Dai Mochizuki, and Yuji Wada. Precisely controlled synthesis of metal nanoparticles under microwave irradiation. *Microwaves in Nanoparticle Synthesis: Fundamentals and Applications*, pages 145–183, 2013.

[134] Helen J Kitchen, Simon R Vallance, Jennifer L Kennedy, Nuria Tapia-Ruiz, Lucia Carassiti, Andrew Harrison, A Gavin Whittaker, Timothy D Drysdale, Samuel W Kingman, and Duncan H Gregory. Modern microwave methods in solid-state inorganic materials chemistry: from fundamentals to manufacturing. *Chemical reviews*, 114(2):1170–1206, 2014.

[135] Stefanos Mourdikoudis, Vincent Colliere, Catherine Amiens, Pierre Fau, and Myrtil L. Kahn. Metalorganic pathways for anisotropic growth of a highly symmetrical crystal structure: Example of the fcc ni. *Langmuir*, 29(44):13491–13501, 2013.

[136] Fei Ma, Ji Ma, Juanjuan Huang, and Jiangong Li. The shape dependence of magnetic and microwave properties for ni nanoparticles. *Journal of Magnetism and Magnetic Materials*, 324(2):205–209, 2012.

[137] James D. Hoefelmeyer, Krisztian Niesz, Gabor A. Somorjai, and T. Don Tilley. Radial anisotropic growth of rhodium nanoparticles. *Nano letters*, 5(3):435–438, 2005.

[138] P. Davide Cozzoli, Etienne Snoeck, Miguel Angel Garcia, Cinzia Giannini, Antonietta Guagliardi, Antonio Cervellino, Fabia Gozzo, Antonio Hernando, Klaus Achterhold, Nelica Ciobanu, Fritz G. Parak, Roberto Cingolani, and Liberato Manna. Colloidal synthesis and characterization of tetrapod-shaped magnetic nanocrystals. *Nano letters*, 6(9):1966–1972, 2006.

[139] Qing Song and Z John Zhang. Shape control and associated magnetic properties of spinel cobalt ferrite nanocrystals. *Journal of the American Chemical Society*, 126(19):6164–6168, 2004.

[140] Taeghwan Hyeon. Chemical synthesis of magnetic nanoparticles. *Chemical Communications*, (8):927–934, 2003.

[141] Keith P Donegan, Jeffrey F Godsell, Joseph M Tobin, Justin P O'Byrne, David J Otway, Michael A Morris, Saibal Roy, and Justin D Holmes. Microwave-assisted synthesis of icosahedral nickel nanocrystals. *CrystEngComm*, 13(6):2023–2028, 2011.

[142] Pengwei Li, Ning Wang, and Rongming Wang. Flower-like nickel nanocrystals: Facile synthesis, shape evolution, and their magnetic properties. *European Journal of Inorganic Chemistry*, 2010(15):2261–2265, 2010.

[143] Xianluo Hu and Jimmy C Yu. High-yield synthesis of nickel and nickel phosphide nanowires via microwave-assisted processes. *Chemistry of Materials*, 20(21):6743–6749, 2008.

[144] Xuemin He, Wei Zhong, Chak-Tong Au, and Youwei Du. Size dependence of the magnetic properties of ni nanoparticles prepared by thermal decomposition method. *Nanoscale research letters*, 8(1):446, 2013.

[145] Chen Zhi, Mochizuki Dai, and Wada Yuji. *Precisely Controlled Synthesis of Metal Nanoparticles under Microwave Irradiation*, chapter 7, pages 145–183. Wiley-Blackwell, 2013.

[146] Wei Xu, Kong Yong Liew, Hanfan Liu, Tao Huang, Chuntao Sun, and Yanxi Zhao. Microwave-assisted synthesis of nickel nanoparticles. *Materials letters*, 62(17-18):2571–2573, 2008.

[147] Jeffrey A Gerbec, Donny Magana, Aaron Washington, and Geoffrey F Strouse. Microwave-enhanced reaction rates for nanoparticle synthesis. *Journal of the American Chemical Society*, 127(45):15791–15800, 2005.

[148] Stefanos Mourdikoudis and Luis M Liz-Marzán. Oleylamine in nanoparticle synthesis. *Chemistry of Materials*, 25(9):1465–1476, 2013.

[149] Yanyun Ma, Jie Zeng, Weiyang Li, Maureen McKiernan, Zhaoxiong Xie, and Younan Xia. Seed-mediated synthesis of truncated gold decahedrons with a aucl/oleylamine complex as precursor. *Advanced materials*, 22(17):1930–1934, 2010.

[150] Ki Min Nam, Jae Ha Shim, Hosung Ki, Sang-Il Choi, Gaehang Lee, Jae Kwon Jang, Younghun Jo, Myung-Hwa Jung, Hyunjoon Song, and Joon T Park. Single-crystalline hollow face-centered-cubic cobalt nanoparticles from solid face-centered-cubic cobalt oxide nanoparticles. *Angewandte Chemie International Edition*, 47(49):9504–9508, 2008.

[151] Richard Anthony Harris, Poslet Morgan Shumbula, and Hendriette van der Walt. Analysis of the interaction of surfactants oleic acid and oleylamine with iron oxide nanoparticles through molecular mechanics modeling. *Langmuir*, 31(13):3934–3943, 2015.

[152] Wenbo Bu, Zhenxing Chen, Feng Chen, and Jianlin Shi. Oleic acid/oleylamine cooperative-controlled crystallization mechanism for monodisperse tetragonal bipyramid nala (moo4) 2 nanocrystals. *The Journal of Physical Chemistry C*, 113(28):12176–12185, 2009.

[153] Mihaela Homocianu et al. Solvent effects on the electronic absorption and fluorescence spectra. *Journal of Advanced Research in Physics*, 2(1), 2011.

[154] Qing Song, Yong Ding, Zhong Lin Wang, and Z John Zhang. Tuning the thermal stability of molecular precursors for the nonhydrolytic synthesis of magnetic mnfe2o4 spinel nanocrystals. *Chemistry of Materials*, 19(19):4633–4638, 2007.

[155] Bridgett Ashley, Derek D Lovingood, Yu-Che Chiu, Hanwei Gao, Jeffery Owens, and Geoffrey F Strouse. Specific effects in microwave chemistry explored through reactor vessel design, theory, and spectroscopy. *Physical Chemistry Chemical Physics*, 17(41):27317–27327, 2015.

[156] Anna C. Balazs, Todd Emrick, and Thomas P. Russell. Nanoparticle polymer composites: Where two small worlds meet. *Science*, 314(5802):1107–1110, 2006.

[157] Farzana Hussain, Mehdi Hojjati, Masami Okamoto, and Russell E. Gorga. Review article: Polymer-matrix nanocomposites, processing, manufacturing, and application: An overview. *Journal of Composite Materials*, 40(17):1511–1575, 2006.

[158] Damien M Marquis, Eric Guillaume, and Carine Chivas-Joly. Properties of nanofillers in polymer. In *Nanocomposites and polymers with analytical methods*. InTech, 2011.

[159] Yusuke Imai. *Inorganic Nano-fillers for Polymers*. Springer Berlin Heidelberg, Berlin, Heidelberg, 2014.

[160] Monika upov, Grayna Simha Martynkov, and Karla Barabaszov. Effect of nanofillers dispersion in polymer matrices: a review. *Science of Advanced Materials*, 3(1):1–25, 2011.

[161] Richard A Vaia and John F Maguire. Polymer nanocomposites with prescribed morphology: going beyond nanoparticle-filled polymers. *Chemistry of Materials*, 19(11):2736–2751, 2007.

[162] Shanghua Li, Meng Meng Lin, Muhammet S. Toprak, Do Kyung Kim, and Mamoun Muhammed. Nanocomposites of polymer and inorganic nanoparticles for optical and magnetic applications. *Nano Reviews*, 1:10.3402/nano.v1i0.5214, 2010.

[163] L. A. Ramajo, A. A. Cristbal, P. M. Botta, J. M. Porto Lpez, M. M. Reboredo, and M. S. Castro. Dielectric and magnetic response of fe3o4/epoxy composites. *Composites Part A: Applied Science and Manufacturing*, 40(4):388–393, 2009.

[164] He Seung, Albert S, Kyung-Youl Baek, and Seung Sang. Low dielectric materials for microelectronics. *Intech Open*, 2012.

[165] M. R. Vengatesan, S. Devaraju, K. Dinakaran, and M. Alagar. Sba-15 filled polybenzoxazine nanocomposites for low-k dielectric applications. *Journal of Materials Chemistry*, 22(15):7559, 2012.

[166] Benjamin D. Hatton, Kai Landskron, William J. Hunks, Mark R. Bennett, Donna Shukaris, Douglas D. Perovic, and Geoffrey A. Ozin. Materials chemistry for low-k materials. *Materials Today*, 9(3):22–31, 2006.

[167] M. Lis, M. Plaut, A. Zai, D. Cipolle, J. Russo, and T. Fedynyshyn. High performance, 3d-printable dielectric nanocomposites for millimeter wave devices. *ACS Appl Mater Interfaces*, 8(49):34019–34026, 2016.

[168] Richard Farrell, Tandra Goshal, Uros Cvelbar, Nikolay Petkov, and Michael A. Morris. Advances in ultra low dielectric constant ordered porous materials. *The Electrochemical Society Interface*, pages 39–46, 2011.

[169] H. Treichel, G. Ruhl, P. Ansmann, R. Wrl, Ch Mller, and M. Dietlmeier. Low dielectric constant materials for interlayer dielectric: (invited paper). *Microelectronic Engineering*, 40(1):1–19, 1998.

[170] D. Shamiryan, T. Abell, F. Lacopi, and K. Maex. Low-k dielectric materials. *Materials Today*, pages 34–39, 2004.

[171] Peter Barber, Shiva Balasubramanian, Yogesh Anguchamy, Shushan Gong, Arief Wibowo, Hongsheng Gao, Harry J. Ploehn, and Hans-Conrad zur Loye. Polymer composite and nanocomposite dielectric materials for pulse power energy storage. *Materials*, pages 1697–1733, 2009.

[172] Toshikatsu Tanaka, GC Montanari, and R Mulhaupt. Polymer nanocomposites as dielectrics and electrical insulation-perspectives for processing technologies, material characterization and future applications. *IEEE transactions on Dielectrics and Electrical Insulation*, 11(5):763–784, 2004.

[173] S. Khan, L. Lorenzelli, and R. S. Dahiya. Technologies for printing sensors and electronics over large flexible substrates: A review. *IEEE Sensors Journal*, 15(6):3164–3185, 2015.

[174] Pylin Sarobol, Adam Cook, Paul G. Clem, David Keicher, Deidre Hirschfeld, Aaron C. Hall, and Nelson S. Bell. Additive manufacturing of hybrid circuits. *Annual Review of Materials Research*, 46(1):41–62, 2016.

[175] Giovanni Postiglione, Gabriele Natale, Gianmarco Griffini, Marinella Levi, and Stefano Turri. Conductive 3d microstructures by direct 3d printing of polymer/carbon nanotube nanocomposites via liquid deposition modeling. *Composites Part A: Applied Science and Manufacturing*, 76:110–114, 2015.

[176] Sung-Yueh Wu, Chen Yang, Wensyang Hsu, and Liwei Lin. 3d-printed microelectronics for integrated circuitry and passive wireless sensors. *Microsystems & Nanoengineering*, 1:15013, 2015.

[177] Corey Shemelya, Luis Banuelos-Chacon, Adrian Melendez, Craig Kief, David Espalin, Ryan Wicker, Gijs Krijnen, and Eric MacDonald. Multi-functional 3d printed and embedded sensors for satellite qualification structures. In *SENSORS, 2015 IEEE*, pages 1–4. IEEE, 2015.

[178] Maheswar Panda, V. Srinivas, and A. K. Thakur. On the question of percolation threshold in polyvinylidene fluoride/nanocrystalline nickel composites. *Applied Physics Letters*, 92(13):132905, 2008.

[179] Eduardo do Nascimento, Airton Ramos, Dario Windmoller, Pau Reig Rodrigo, Roberto Teruel Juanes, Amparo Ribes Greus, Vicente Amig Borrs, and Luiz Antnio Ferreira Coelho. Breakdown, free-volume and dielectric behavior of the nanodielectric coatings based on epoxy/metal oxides. *Journal of Materials Science: Materials in Electronics*, 27(9):9240–9254, 2016.

[180] Anju Toor, Hongyun So, and Albert P. Pisano. Improved dielectric properties of polyvinylidene fluoride nanocomposite embedded with poly(vinylpyrrolidone)-coated gold nanoparticles. *ACS applied materials & interfaces*, 9(7):6369–6375, 2017.

[181] Scott P Fillery, Hilmar Koerner, Lawrence Drummy, Erik Dunkerley, Michael F Durstock, Daniel F Schmidt, and Richard A Vaia. Nanolaminates: increasing dielectric breakdown strength of composites. *ACS applied materials & interfaces*, 4(3):1388–1396, 2012.

[182] DR Paul and Lioyd M Robeson. Polymer nanotechnology: nanocomposites. *Polymer*, 49(15):3187–3204, 2008.

[183] Penghao Hu, Yang Shen, Yuhan Guan, Xuehui Zhang, Yuanhua Lin, Qiming Zhang, and CeWen Nan. Topologicalstructure modulated polymer nanocomposites exhibiting highly enhanced dielectric strength and energy density. *Advanced Functional Materials*, 24(21):3172–3178, 2014.

[184] Fadzidah Mohd Idris, Mansor Hashim, Zulkifly Abbas, Ismayadi Ismail, Rodziah Nazlan, and Idza Riati Ibrahim. Recent developments of smart electromagnetic absorbers based polymer-composites at gigahertz frequencies. *Journal of Magnetism and Magnetic Materials*, 405:197–208, 2016.

[185] Jianwen Xu and C. P. Wong. Low-loss percolative dielectric composite. *Applied Physics Letters*, 87(8):082907, 2005.

[186] Liang Zhang, Shuo Chen, Shuai Yuan, Dongrui Wang, Peng-Hao Hu, and Zhi-Min Dang. Low dielectric loss and weak frequency dependence of dielectric permittivity of the ceo2/polystyrene nanocomposite films. *Applied Physics Letters*, 105(5):052905, 2014.

[187] M. Roy, J. K. Nelson, R. K. MacCrone, L. S. Schadler, C. W. Reed, and R. Keefe. Polymer nanocomposite dielectrics-the role of the interface. *IEEE transactions on Dielectrics and Electrical Insulation*, 12(4):629–643, 2005.

[188] Toshikatsu Tanaka. Dielectric nanocomposites with insulating properties. *IEEE transactions on Dielectrics and Electrical Insulation*, 12(5):914–928, 2005.

[189] Sung-Dong Cho, Sang-Yong Lee, Jin-Gul Hyun, and Kyung-Wook Paik. Comparison of theoretical predictions and experimental values of the dielectric constant of epoxy/batio3 composite embedded capacitor films. *Journal of Materials Science: Materials in Electronics*, 16(2):77–84, 2005.

[190] G. Polizos, E. Tuncer, V. Tomer, I. Sauers, C. A. Randall, and E. Manias. Dielectric spectroscopy of polymer-based nanocomposite dielectrics with tailored interfaces and structured spatial distribution of fillers. In *Nanoscale Spectroscopy with Applications*, pages 93–130. CRC Press, 2013.

[191] Polycarpos Pissis, Daniel Fragiadakis, Athanasios Kanapitsas, and Kostas Delides. Broadband dielectric relaxation spectroscopy in polymer nanocomposites. *Macromolecular Symposia*, 265(1):12–20, 2008.

[192] Moran Wang and Ning Pan. Predictions of effective physical properties of complex multiphase materials. *Materials Science and Engineering: R: Reports*, 63(1):1–30, 2008.

[193] N. Jayasundere and B. V. Smith. Dielectric constant for binary piezoelectric 03 composites. *Journal of Applied Physics*, 73(5):2462–2466, 1993.

[194] Holcman Vladimr and Liedermann Karel. New mixing rule of polymer composite systems. *WSEAS Transactions on Electronics*, (9), 2007.

[195] Alexander Kamyshny and Shlomo Magdassi. Conductive nanomaterials for printed electronics. *Small*, 10(17):3515–3535, 2014.

[196] Michael G Todd and Frank G Shi. Complex permittivity of composite systems: A comprehensive interphase approach. *IEEE transactions on Dielectrics and Electrical Insulation*, 12(3):601–611, 2005.

[197] Pulickel M Ajayan, Linda S Schadler, and Paul V Braun. *Nanocomposite science and technology*. John Wiley & Sons, 2006.

[198] Yiwei Tan, Zhongbin Zhuang, Qing Peng, and Yadong Li. Room-temperature soft magnetic iron oxide nanocrystals: Synthesis, characterization, and size-dependent magnetic properties. *Chemistry of Materials*, 20(15):5029–5034, 2008.

[199] L. Nicolais and G. Carotenuto. *Metal-Polymer Nanocomposites*. Wiley, 2004.

[200] Chao Liu and Z. John Zhang. Size-dependent superparamagnetic properties of mn spinel ferrite nanoparticles synthesized from reverse micelles. *Chemistry of Materials*, 13(6):2092–2096, 2001.

[201] Young-wook Jun, Jung-wook Seo, and Jinwoo Cheon. Nanoscaling laws of magnetic nanoparticles and their applicabilities in biomedical sciences. *Accounts of Chemical Research*, 41(2):179–189, 2008.

[202] Jens Baumgartner, Luca Bertinetti, Marc Widdrat, Ann M. Hirt, and Damien Faivre. Formation of magnetite nanoparticles at low temperature: From superparamagnetic to stable single domain particles. *PLOS ONE*, 8(3):1–6, 03 2013.

[203] Shouhu Xuan, Yi-Xiang J. Wang, Jimmy C. Yu, and Ken Cham-Fai Leung. Tuning the grain size and particle size of superparamagnetic fe3o4 microparticles. *Chemistry of Materials*, 21(21):5079–5087, 2009.

[204] S. Chandran, J. K. Basu, and M. K. Mukhopadhyay. Variation in glass transition temperature of polymer nanocomposite films driven by morphological transitions. *J Chem Phys*, 138(1):014902, 2013.

[205] Benjamin J Ash, Richard W Siegel, and Linda S Schadler. Glasstransition temperature behavior of alumina/pmma nanocomposites. *Journal of Polymer Science Part B: Polymer Physics*, 42(23):4371–4383, 2004.

[206] Linda S Schadler, Sanat K Kumar, Brian C Benicewicz, Sarah L Lewis, and Shane E Harton. Designed interfaces in polymer nanocomposites: A fundamental viewpoint. *MRS bulletin*, 32(4):335–340, 2007.

[207] Thomas Hanemann and Dorothe Vinga Szab. Polymer-nanoparticle composites: From synthesis to modern applications. *Materials*, 3(6):3468, 2010.

[208] Z. H. Mbhele, M. G. Salemane, C. G. C. E. van Sittert, J. M. Nedeljkovi, V. Djokovi, and A. S. Luyt. Fabrication and characterization of silverpolyvinyl alcohol nanocomposites. *Chemistry of Materials*, 15(26):5019–5024, 2003.

[209] Serguei M. Lebedev, Olga S. Gefle, and Serguei N. Tkachenko. Metal-polymer pvdf/nickel composites and evaluation of their dielectric and thermal properties. *Journal of Electrostatics*, 68(2):122–127, 2010.

[210] Tao Li, Andrew J Senesi, and Byeongdu Lee. Small angle x-ray scattering for nanoparticle research. *Chemical reviews*, 116(18):11128–11180, 2016.

[211] Qiang Lan, Lorraine F Francis, and Frank S Bates. Silica nanoparticle dispersions in homopolymer versus block copolymer. *Journal of Polymer Science Part B: Polymer Physics*, 45(16):2284–2299, 2007.

[212] Alexandre Kisner. *Ultrathin gold nanowires: chemistry, electrical characterization and application to sense cellular biology*, volume 24. Forschungszentrum Jlich, 2013.

[213] Zhongwu Wang, Xiao-Dong Wen, Roald Hoffmann, Jae Sung Son, Ruipeng Li, Chia-Chen Fang, Detlef-M. Smilgies, and Taeghwan Hyeon. Reconstructing a solid-solid phase transformation pathway in cdse nanosheets with associated soft ligands. *Proceedings of the National Academy of Sciences*, 107(40):17119–17124, 2010.

[214] Eva R Garland, Elias P Rosen, Laura I Clarke, and Tomas Baer. Structure of submonolayer oleic acid coverages on inorganic aerosol particles: evidence of island formation. *Physical Chemistry Chemical Physics*, 10(21):3156–3161, 2008.

[215] Dan Wang, Bingbing Lin, Taipeng Shen, Jun Wu, Fuhua Hao, Chunchao Xia, Qiyong Gong, Huiru Tang, Bin Song, and Hua Ai. Control of the interparticle spacing in superparamagnetic iron oxide nanoparticle clusters by surface ligand engineering. *Chinese Physics B*, 25(7):077504, 2016.

[216] Bertrand Faure, German Salazar-Alvarez, and Lennart Bergstrom. Hamaker constants of iron oxide nanoparticles. *Langmuir*, 27(14):8659–8664, 2011.

[217] Fritz Wolter and Fritz Thom. A parallel-plate capacitor used to determine the complex permittivity of supercooled aqueous solutions in the 1 mhz range. *Measurement Science Technology*, 7:969–975, 1996.

[218] T. T. Grove, M. F. Masters, and R. E. Miers. Determining dielectric constants using a parallel plate capacitor. *American Journal of Physics*, 73(1):52–56, 2005.

[219] Joseph V. Mantese, Adolph L. Micheli, Dennis F. Dungan, Richard G. Geyer, James BakerJarvis, and John Grosvenor. Applicability of effective medium theory to ferroelectric/ferrimagnetic composites with composition and frequencydependent complex permittivities and permeabilities. *Journal of Applied Physics*, 79(3):1655–1660, 1996.

[220] X. L. Dong, X. F. Zhang, H. Huang, and F. Zuo. Enhanced microwave absorption in ni/polyaniline nanocomposites by dual dielectric relaxations. *Applied Physics Letters*, 92(1):013127, 2008.

[221] Maurizio Crippa, Alberto Bianchi, Davide Cristofori, Massimiliano D'Arienzo, Franco Merletti, Franca Morazzoni, Roberto Scotti, and Roberto Simonutti. High dielectric constant rutilepolystyrene composite with enhanced percolative threshold. *Journal of Materials Chemistry C*, 1(3):484–492, 2013.

[222] J. A. Reynolds and J. M. Hough. Formulae for dielectric constant of mixtures. *Proceedings of the Physical Society. Section B*, 70(8):769, 1957.

[223] A. H. Sihvola and J. A. Kong. Effective permittivity of dielectric mixtures. *IEEE Transactions on Geoscience and Remote Sensing*, 26(4):420–429, 1988.

[224] F. Carpi and D. D. Rossi. Improvement of electromechanical actuating performances of a silicone dielectric elastomer by dispersion of titanium dioxide powder. *IEEE transactions on Dielectrics and Electrical Insulation*, 12(4):835–843, 2005.

[225] M. Carvalho Arajo, C. M. Costa, and S. Lanceros-Mndez. Evaluation of dielectric models for ceramic/polymer composites: Effect of filler size and concentration. *Journal of Non-Crystalline Solids*, 387:6–15, 2014.

[226] M Ezzat, NA Sabiha, and M Izzularab. Accurate model for computing dielectric constant of dielectric nanocomposites. *Applied Nanoscience*, 4(3):331–338, 2014.

[227] D. C. Dube. Study of landau-lifshitz-looyenga's formula for dielectric correlation between powder and bulk. *Journal of Physics D: Applied Physics*, 3(11):1648, 1970.

[228] Enis Tuncer. The landau-lifshitz/looyenga dielectric mixture expression and its self-similar fractal nature. *arXiv preprint cond-mat/0503750*, 2005.

[229] Maik Scheller, Christian Jansen, and Martin Koch. Applications of effective medium theories in the terahertz regime. In *Recent Optical and Photonic Technologies*. InTech, 2010.

[230] R. K. Goyal, P. A. Jagadale, and U. P. Mulik. Thermal, mechanical, and dielectric properties of polystyrene/expanded graphite nanocomposites. *Journal of Applied Polymer Science*, 111(4):2071–2077, 2009.

[231] A. K. Jonscher. Low-loss dielectrics. *Journal of materials science*, 34(13):3071–3082, 1999.

[232] Mayumi Hyuga, Toshikatsu Tanaka, Yoshimichi Ohki, Takahiro Imai, Miyuki Harada, and Mitsukazu Ochi. Correlation between mechanical and dielectric relaxation processes in epoxy resin composites with nano-and micro-fillers. *IEEJ Transactions on Fundamentals and Materials*, 131:1041–1047, 2011.

[233] C. V. Chanmal. *Dielectric relaxations in PVDF/BaTiO3 nanocomposites*, volume 2. 2008.

[234] Peter B Johnson and R-W$_-$ Christy. Optical constants of the noble metals. *Physical review B*, 6(12):4370, 1972.

[235] Luis M Liz-Marzán, Michael Giersig, and Paul Mulvaney. Synthesis of nanosized gold- silica core- shell particles. *Langmuir*, 12(18):4329–4335, 1996.

[236] Zhichuan Xu, Yanglong Hou, and Shouheng Sun. Magnetic core/shell fe3o4/au and fe3o4/au/ag nanoparticles with tunable plasmonic properties. *Journal of the American Chemical Society*, 129(28):8698–8699, 2007.

[237] Jordi Piella, Neus G Bastus, and Victor Puntes. Size-controlled synthesis of sub-10-nanometer citrate-stabilized gold nanoparticles and related optical properties. *Chemistry of Materials*, 28(4):1066–1075, 2016.

[238] Qianqian Ding, Yongmei Ma, Yingjie Ye, Liangbao Yang, and Jinhuai Liu. A simple method to prepare the magnetic ni@ au core-shell nanostructure for the cycle surface enhanced raman scattering substrates. *Journal of Raman Spectroscopy*, 44(7):987–993, 2013.

[239] Yoontae Jeon, Gang Ho Lee, Jeunghee Park, Bongsoo Kim, and Yongmin Chang. Magnetic properties of monodisperse nih x nanoparticles and comparison to those of monodisperse ni nanoparticles. *The Journal of Physical Chemistry B*, 109(25):12257–12260, 2005.

[240] Colin J Loweth, W Brett Caldwell, Xiaogang Peng, A Paul Alivisatos, and Peter G Schultz. Dna-based assembly of gold nanocrystals. *Angewandte Chemie International Edition*, 38(12):1808–1812, 1999.

BIOGRAPHICAL SKETCH

EDUCATION

Ph.D. in Materials Chemistry August 2018

Florida State University, Tallahassee, FL

Thesis: Nanoparticle-Electromagnetic Radiation Interactions: Implications and Applications

Advisor: Dr. Geoffrey F. Strouse

M.S. in Chemistry December 2015

Florida State University, Tallahassee, FL

B.A.Sc. in Engineering Science - Major in Nanoengineering June 2012

University of Toronto, Toronto, ON

RESEARCH EXPERIENCE

Graduate Research Assistant **Aug 2016 - Present**

Strouse Lab, Florida State University, FL

- Successfully synthesized various nanoparticles (Au/Ni/Pd/Fe_3O_4/ZnO/core-shell) and modified their surface with shelling (Au/SiO2/Ni) or ligands/peptides/DNA
- Developed a new method using microwave-assisted heating to control nanoparticle morphology that resulted in a patent (patent application submitted)
- Investigated energy transfer processes between nanoparticles and fluorescent dyes/lanthanide ions using UV-Vis absorbance, fluorescence emission and lifetime spectroscopy
- Modified gold nanoparticles with peptides and DNA, grew and transformed bacteria for plasmids, cultured and transfected cells, stained and imaged cells (nano-biotechnology project)
- Led collaboration with a national laboratory (NETL) on a catalysis project, with chemical engineers on a 3D-printable low-k dielectric polymer, and with a medical school group on gene-functionalized nanoparticles

- Characterized materials using thermal analysis (TGA, DSC), magnetic method (SQUID), microscopy (TEM, SEM, light, confocal, fluorescence), scattering (pXRD, SAXS, DLS), spectroscopy (FTIR, UV-Vis, EDS, fluorescence/PL, dielectric), gel electrophoresis and mechanical testing (DMA, rheology)
- Trained other students (graduate and undergraduate) and a postdoctoral scientists on multiple instruments and experimental techniques
- Reviewed scientific publications, designed experimental plans and assisted in writing research grants (NIH & NSF)
- Presented findings at conferences (posters and talks), resulted in several publications (1st author and 2nd author papers in ACS Nano published, one 1st author paper in review, two 1st author papers in preparation, and a provisional patent (submitted))

Research Assistant **Sep 2011 - Apr 2012**

Adv. Pharmaceutics & Drug Delivery Lab,University of Toronto, ON

- Developed and evaluated theranostic nanoparticle formulations for detection and treatment of breast cancer
- Incorporated imaging (quantum dot) and chemotherapeutic (mitomycin C and doxorubicin) modalities into a single polymer nanoparticle formulation for undergraduate thesis
- Synthesized quantum dots, ester-based nanoparticles and characterized systems using various methods (DLS sizing, zeta potential, fluorescence, UV-Vis, partition assay)
- Optimized formulation and performed drug release studies

Research Assistant **May 2011 - Aug 2012**

Nanobioengineering Lab, McGill University, QC

- Designed 28 prototype silicon pins and microfabricated them in a cleanroom facility (McGill Nanotools Microfab) to optimize existing contact-printing system, and identified other problems in existing setup
- Tested pins with a microplotter using a co-localization ELISA assay and fluorescence scanner
- Some designs outperformed old pins by producing fluorescent spots with better signal quality, reduced substrate damage and higher reproducibility

Co-Op Student **Sep 2010 - Apr 2011**

Analytical R$D Platform, Biochemistry Dept., Sanofi Pasteur Limited, ON

- Monitored vaccine components using biophysical techniques (FT-IR, CD and Fluorescence) and established standard operating protocols (SOPs) for different projects
- Trained and guided a new intern student, and successfully completed immunology courses offered
- Underwent training for Good Laboratory Practices (GMP), Good Manufacturing Practices (GMP) and Good Documentation Practices (GDP)
- Contributed to top 10 global priority projects for Sanofi Pasteur and efforts contributed to a conference presentation

Research Assistant **May 2010 - Aug 2010**

Stem Cell Bioengineering Lab, University of Toronto, ON

- Developed a deep UV lithography micropatterning technique to pattern cardiac cell lines
- Evaluated feasibility of upscaling the method to a 96-well plate format for high throughput studies in an efficient and economical method
- Performed cell culturing, immunohistochemistry and live-cell assays to test out micropatterning effects

Research Assistant **May 2009 - Jul 2009**

Erb Group (Materials Science Engineering Dept.), University of Toronto, ON

- Successfully collected research data on how nanostructures are formed on the butterfly eye that aids to design of new processes for anti-reflective coatings
- Gathered in-depth information on biological structure and function of *Nymphalis Antiopa* compound eye
- Presented findings and helped establish future research approach to material design for the Erb Group

TEACHING EXPERIENCE

Graduate Teaching Assistant **Aug 2012 - Jul 2016**

Dept. of Chemistry and Biochemistry, Florida State University, FL

- Taught 30-80 students in General Chemistry I and II (recitation and lab), Chemistry for non-majors (lab), Organic Chemistry (lab) and Honors Chemistry (lab)
- Reviewed chemistry topics and practice problems in recitation classes (30 students/class)
- Reviewed laboratory techniques and experiments, monitored and assisted students during lab, and ensured safety during experiments (24 students/ section)
- Successfully helped multiple students understand their homework and lab experiments during office hours each week, and showed them how to use Microsoft Excel efficiently

Mentor (Directed Individual Study) **May 2015 - Apr 2018**

Dept. of Chemistry and Biochemistry, Florida State University, FL

- Mentored 4 undergraduate chemistry / chemical engineering students for different nanoparticle projects that involved nanoparticle and application during May-Aug 2015, Sep-Dec 2015, Jan-Apr 2017, Feb-Apr 2018
- Student learned to successful synthesize nanoparticles (incld. microwave-based synthesis), characterize them (pXRD, FTIR, UV-Vis absorbance and fluorescence spectroscopy, gel electrophoresis), and modify their surface/ perform ligand exchange
- Guided students on how to design experiments, troubleshoot problems and interpret/analyze data
- Taught students about Nanometal Surface Energy Transfer (NSET), magnetism, anisotropic metallic nanostructures and applications to various problems including understanding biological structures, drug delivery, catalysis and photothermal therapy
- Students presented their project and learning experience through poster sessions/talks at FSU

PUBLICATIONS

- "Synthesis of Highly Uniform Nickel Multipods with Tunable Aspect Ratio by Microwave Power Control." **Vakil PN**, Hardy DA, Strouse GF. (2018) *ACS Nano*, 12, 6784-6793. DOI:10.1021/acsnano.8b01992
- "Microwave Enhancement of Autocatalytic Growth of Nanometals." Ashley BA, **Vakil PN**, Lynch BB, Dyer CM, Tracy JB, Strouse GF. (2017) *ACS Nano*, 11, 9957-9967. DOI:10.1021/acsnano.7b04040

- “Dielectric Properties for Nanocomposites Comparing Commercial and Synthetic Ni and Fe3o4 Loaded Polystyrene .” **Vakil PN**, Muhammed F, Hardy DA, Dickens TJ, Ramakrishnan S, Strouse GF. *ACS Omega. In review*

- “Elucidating Factors Controlling Nickel Multipods Growth: Precursor and Ligand Concentrations and Choices, Microwave Vessel Type and Stirring Rates.” **Vakil PN**, Hardy DA, Strouse GF. *Chemistry of Materials. In preparation*

- “Highly Quenching Nickel-Gold Core-Shell Magnetic Plasmonic Nanoparticles.” **Vakil PN**, Strouse GF. *Journal of Physical Chemistry C. In preparation*

- “Fe_3O_4@Au-Peptide Conjugates for Optical and Magnetic Tracking in Gliosarcoma Cells.” Carnevale KJF, **Vakil PN**, Woo LJ, Kalinsky M, Dias A, Rosenberg J, Levenson CW, Strouse GF. *Journal of the American Chemical Society. In preparation*

PATENTS

- “Nickel multipod nanostructures and methods” **Vakil PN** and Strouse GF. U.S. Provisional Application No. 62/646,055

PRESENTATIONS

- **Vakil PN**, Hardy DA, Strouse GF, “Synthesis of highly Uniform nickel multipods with tunable aspect ratio by microwave-power control. Florida Council of Graduate Schools, Tallahassee, FL. April 20, 2018 (Poster)

- **Vakil PN**, Strouse GF, “Pulsed microwave energy: A kinetic control approach to highly branched nickel multipod nanostructures. 255th ACS National Meeting, New Orleans, LA. March 22, 2018 (Talk)

- **Vakil PN**, Muhammed F, Ramakrishnan S, Strouse GF, “Magnetic and dielectric properties of potential 3D printable low-k dielectric nanocomposites: Nickel/iron oxide loaded polystyrene”. 2017 Southeast Regional ACS Meeting. Charlotte, NC. November 8, 2017 (Talk)

- **Vakil PN**, Strouse GF, “Distance- and dye-dependent quenching behavior of magnetic (nickel or iron oxide) core- gold shell nanoparticles”. 254th ACS National Meeting, Washington, DC. August 23, 2017 (Talk)

- **Vakil PN**, Strouse GF, “Highly quenching nickel-gold core-shell magnetic plasmonic nanoparticles for biosensing”. 253rd ACS National Meeting, San Francisco, CA. April 3-5, 2017 (Talk & Poster)

  Vakil PN, Ashley BA, Strouse GF, “Multipod nickel nanostructures: Synthesis, characterization and applications.” 2016 Southeast Regional ACS Meeting. Columbia, SC. October 25, 2016. (Talk)

- **Vakil PN**, Ashley BA, Strouse GF, “Multipod nickel nanostructures: Synthesis, characterization and applications.” 252nd ACS National Meeting. Philadelphia, PA. August 21, 2016. (Poster)

- **Vakil PN**, Strouse GF, ”Nickel Nanoparticles: Synthesis, EMI shielding polycomposites and energy coupling.” Chemistry Materials Seminar at Florida State University. Tallahassee, FL. April 21, 2016. (Talk)

- **Vakil PN**, Strouse GF, ”Biofunctionalized Gold Nanoparticles for Somatic Gene Therapy.” Chemistry Materials Seminar at Florida State University. Tallahassee, FL. October 31, 2013. (Talk)

- Muroski ME, Morgan TJ, Fredrickson KJ, **Vakil PN**, A Derkazalli, CW Levenson, Strouse GF, ”Nanoparticle assisted genetic engineering for protein expression in human mesenchymal stem cells.” 3rd Annual FSU Life Sciences Symposium: Modeling Human Disease. Tallahassee, FL. 14-15 February 2013. (Poster)

- Kirkitadze M, Dhaliwal S, Hu J, **Vakil PN**, Williams W, Remi E, Blackburn N, Carpick B, ”Biophysical Characterization of a PEGylated Monoclonal Antibody.” Poster and Podium session presented at 8th Annual Essential Protein Engineering Summit - Analytical Stream, Biophysical & Biochemical Characterization of Biotherapeutics. Boston, MA. 30 Apr 4 May 2011.

AWARDS AND HONORS

- Spring 2018 ACS National Meeting GSSPC Travel Award, Florida State University 2018
- Graduate Student Excellence in Visual Arts Award Finalist, Florida State University 2018
- American Chemical Society Membership 2016 - Present
- Golden Key International Honor Society Membership 2014 - Present

- Art in STEM Competition Finalist 2015, 2016, 2018
- FSU Global Citizen Award 2013-2014 Winner (& Nominee for 2012-2013) 2014
- Graduate Admission Award, Florida State University 2012
- NSERC Award for Nanoscience & Nanotechnology 2010
- Undergraduate Nanotechnology Network Research Award 2009
- Faculty of App. Science and Eng. Admission Scholarship, University of Toronto 2007

SKILLS

Research Expertise: Magnetic/Metallic/Plasmonic/Core-Shell Nanoparticles, Microwave Chemistry, Energy Transfer (FRET, NSET, LRET) and Biosensors, Bionanotechnology, Polymer Nanocomposites, Plasmonics, Additive Manufacturing, 3D Printing, Colloidal Chemistry, Materials Chemistry, Surface Chemistry, Analytical Chemistry

Instrumentation and Techniques: Analytical Biophysics, Nanocomposites, Dielectrics, Additive Manufacturing, 3D printing, Transmission Electron Microscopy (TEM), Powder X-Ray Diffraction (pXRD), Scanning Electron Microscopy (SEM), Energy Dispersive X-Ray Spectroscopy (EDX/EDS), Small Angle X-Ray Scattering (SAXS), Thermogravimetric Analysis (TGA), Differential Scanning Calorimetry (DSC), FT-IR Spectroscopy, Circular Dichroism (CD), Dynamic Light Scattering (DLS), Zeta Potential, Cyclic Voltammetry (CV), UV-Vis-NIR Absorption Spectroscopy, Fluorescence Spectroscopy, Photoluminescence Lifetime Spectroscopy, Dynamic Mechanical Analysis (DMA), Rheology, UV Lithography, Micropatterning, Microfabrication

Synthesis skills: Nanoparticle Synthesis, Nanoparticle Modification, Nanoparticle Shelling, Ligand Exchange, Surface Modification, Phase Exchange, Microwave-Assisted Synthesis, Nanocomposite Preparation, Handling Dry Glove Box

Biology-related: Growth and Transformation of Bacteria, Plasmid Extraction, Linearization and Conjugation, DNA Handling, Growth, Maintenance, Staining and Observation of Cell Lines, Use of Cell Counter, Hemocytometer, Light Microscopy, Confocal Laser Scanning Microscopy (LCSM), Conjugation Of Peptides and DNA To Gold Nanoparticles, Transfection with Nanoparticles, Gel Electrophoresis, Drug Delivery, Biomaterials, Bioengineering, Cancer Research, Biosafety, Formulation, Drug Release Studies, Co-Localization ELISA Assay, Cell Culture Software: Igor Pro 4.0, OriginPro 8.5, Chembiodraw, Pymol, Image J, Endnote, Microsoft Office, Vectorworks, Clewin, Google Sketch-Up, Adobe Lightroom, LaTex, C, C++, Verilog, Assembly Language, Scripting For Clewin and OpenSCAD, Programming

Personality / Interpersonal / Industry: Research Project Management, Interpersonal Skills, Photography, Organizing, Proactivity, Positive Attitude, Mentorship, Team Leadership, Scientific Writing, Data Collection and Analysis, Leadership, Teamwork, Project Management, University Teaching, Quantitative Analysis, Presentation, Communication, Troubleshooting, Problem Solving, Analytical thinking, Innovative, Creative, Self-driven, Statistical analysis, Data fitting, Good Laboratory Practices (GMP), Good Manufacturing Practices (GMP), Good Documentation Practices (GDP), Standard Operating Protocols (SOPs), R&D, Literature Reviews, Chemical Engineering, Data Analysis, Science, Nanotechnology, Research, Biochemistry, Chemistry, Laboratory, Biotechnology, Lifesciences, Characterization, Biomedical Engineering, Materials Science, Stem Cells, Healthcare, Engineering Design, Nanomaterials, Laboratory Skills, Nanoparticles

Language: English (native), Gujarati (native), Hindi (advanced), Marathi (intermediate), Swahili (intermediate), French (beginner)